Modelling and Control of Integrated Photovoltaic-Module and Converter Systems for Partial Shading Operation Using Artificial Intelligence

Benjamin Vui Ping Chong

Submitted in accordance with the requirements for the degree of
Doctor of Philosophy

The University of Leeds
School of Mechanical Engineering/School of Electronic & Electrical Engineering

October, 2010

Intellectual Property and Publication Statements

The candidate confirms that the work submitted is his own, except where work which has formed part of jointly-authored publications has been included. The contribution of the candidate and the other authors to this work has been explicitly indicated below. The candidate confirms that appropriate credit has been given within the thesis where reference has been made to the work of others.

Some of the work presented in Chapter 3 of this thesis has been published or submitted for publication in the following articles:

- Chong, B., Zhang, L., and Dehghani, A., "Optimal Design of Ćuk Step-Up Converter for Photovoltaic Energy Systems", 5th International Conference on Power Electronics, Machines and Drives, Brighton, UK, 2010, pp. 1 – 6.
- Chong, B.V.P., Zhang, L., and Dehghani, A., "Analysis of a Step-down Ćuk Converter in continuous and Discontinuous Operating Conditions", 4th International Conference on Power Electronics, Machine and Drives (PEMD), York, UK, 2008, pp. 189-193.

The work contained within the above publications which is directly attributable to the candidate includes the converter design, simulation, experimental work and the preparation of the articles. The work directly attributable to other authors include the editing of the articles.

Acknowledgements

The author would like to express his heartfelt gratitude to his supervisor, Dr Li Zhang for her guidance, support, and encouragement throughout his PhD study. Her sage advice, constructive criticism, and useful suggestions have assisted the writing of this thesis in innumerable ways. Above all, her energy and enthusiasm in research have greatly inspired the author to contribute such a high-quality work for this thesis. The author would also like to offer his sincere gratitude to his other supervisor, Dr Abbas Dehghani, for his continuous support throughout his PhD work.

Appreciation goes to Michael Waite for his help and discussion on the implementation of the practical converter circuits. The author is also grateful to Dr Neil J McEwan for allocating his valuable time to review this thesis and provide insightful feedback. Thanks are also extended to the School of Mechanical Engineering and School of Electronic/Electrical Engineering for providing their financial means and laboratory facilities.

The author is greatly indebted to his father whose career in the power engineering area has inspired the work contributed to this thesis, and to his mother whose prayer and encouragement have helped him sailing through his PhD study.

The author also wishes to convey his love and gratitude to his partner, all his beloved family members and his friends for their understanding and endless love provided through the duration of his study.

Finally, the author would like to dedicate this thesis specially to his grandmother who passed away in June 2009.

Abstract

The thesis has three main themes: analysis and optimal design of Ćuk DC-DC converters; integration of Ćuk DC-DC converters with photovoltaic (PV) modules to improve operation during partial shading; and an artificial intelligence model for the PV module, permitting an accurate maximum power point (MPP) tracking in the integrated system.

The major contribution of the thesis is the control of an integrated photovoltaic module and DC-DC converter configuration for obtaining maximum power generation under non-uniform solar illumination. In place of bypass diodes, the proposed scheme embeds bidirectional Ćuk DC-DC converters within the serially connected PV modules. A novel control scheme for the converters has been developed to adjust their duty ratios, enabling all the PV modules to operate at the MPPs corresponding to individual lighting conditions.

A detailed analysis of a step-down Ćuk converter has been carried out leading to four transfer functions of the converter in two modes, namely variable input - constant output voltage, and variable output - constant input voltage. The response to switch duty ratio variation is shown to exhibit a non-minimum phase feature. A novel scheme for selecting the circuit components is developed using the criteria of suppressing input current and output voltage ripple percentages at a steady state, and minimising the time integral of squared transient response errors. The designed converter has been tested in simulation and in practice, and has been shown to exhibit improved responses in both operating modes.

A Neuro-Fuzzy network has been applied in modelling the characteristics of a PV module. Particle-Swarm-Optimisation (PSO) has been employed for the first time as the training algorithm, with which the tuning speed has been improved. The resulting model has optimum compactness and interpretability and can predict the MPPs of individual PV modules in real time. Experimental data have confirmed its improved accuracy. The tuned Neuro-Fuzzy model has been applied to a practical PV power generation system for MPP control. The results have shown an average error of 1.35% compared with the maximum extractable power of the panel used.

The errors obtained, on average, are also about four times less than those using the genetic-algorithm-based model proposed in a previous research.

All the techniques have been incorporated in a complete simulation system consisting of three PV panels, one boost and two bidirectional Ćuk DC-DC converters. This has been compared under the same weather conditions as the conventional approach using bypass diodes. The results have shown that the new system can generate 32% more power.

Contents

List of Figures

List of Tables

List of Symbols

α – the seriousness of unequal insolations between two identical PV modules

ζ – Damping ratio

Λ_1 – Acceleration coefficient for the cognitive term used in the PSO algorithm

Λ_2 – Acceleration coefficient for the social term used in the PSO algorithm

ξ_{INT} – Constraint factor used interpretability measure

$\varphi_{max(lead)}$ – Maximum phase contributed by phase lead compensator (°)

Ω – Inertia Factor for PSO algorithm

ω_c – Crossover frequency (radians / second)

ω_L – Breakpoint frequency of lag compensator (radians / second)

$\omega_{max(lead)}$ – Frequency at which $\varphi_{max(lead)}$ is obtained (radians / second)

A – Cell ideality factor from the ideal p-n characteristics

AV_{DD} – Positive supply for dsPIC (V)

AV_{SS} – Ground for dsPIC (V)

C_n – Intermediate capacitor for a Ćuk converter (F)

E_G – Band gap energy (eV)

FF_p – Fitness function value

f_s – Switching frequency of a DC-DC converter (Hz)

G – Solar insolation (mW/cm^2)

gbest – Position of the global best particle in the PSO algorithm

$G_{ik}(s)$ – Control-to-input voltage transfer function

$G_{io}(s)$ – Output-to-input voltage transfer function

$G_{oi}(s)$ – Input-to-output voltage transfer function

$G_{ok}(s)$ – Control-to-output voltage transfer function

$H(s)$ – Transfer function for the overall controller

$H_{lag}(s)$ – Transfer function for the lag compensator

$H_{lead}(s)$ – Transfer function for the lead compensator

I_{in} – Current flowing into the input terminal of a DC-DC converter (A)

$I_{OB(DDCM)}$ – Boundary current between DDCM and CCM (A)

$I_{OB(DCVM)}$ – Boundary current between DCVM and CCM (A)

I_{out} – Current flowing from the output terminal of a DC-DC converter (A)

I_o – Reverse saturation current (A)

I_{ph} – Light generated current (A)

I_{PV} – Current flowing from a PV generator (A)

K – Duty cycle of DC-DC converter

K_A – Weighting factor for accuracy measure

K_C – Weighting factor for compactness measure

K_I – Weighting factor for interpretability measure

K_t – Boltzmann's constant (=1.380658 × 10^{-23})

MA – Performance index for accuracy measure

MC – Performance index for compactness measure

MI – Performance index for interpretability measure

N_{lead} – Scalar gain for the lead compensator

n_p – Number of PV cells connected in parallel

n_s – Number of PV cells connected in series

pbest – Personal best position of a particle in the PSO algorithm

P_{PV} – Output power of a PV generator (W)

q – Electron charge (=1.6 × 10^{-19}C)

$rand_1$ – Stochastic variable for the cognitive term used in the PSO algorithm

$rand_2$ – Stochastic variable for the social term used in the PSO algorithm

R_{PV} – The slope of the I–V characteristic of a PV module

R_s – Series ohmic resistance of a PV cell (Ω)

R_{sh} – Shunt ohmic resistance of a PV cell (Ω)

T_a – Ambient temperature (°C)

T_c – Cell temperature (°C)

V_{bus} – DC bus voltage (V)

V_{cn} – Voltage across capacitor C_n (V)

V_i – Voltage across input terminal of a DC-DC converter (V)

V_o – Voltage across output terminal of a DC-DC converter (V)

V_{PV} – Voltage across a PV generator (V)

List of Abbreviations

AC – Alternating Current

ADC – Analogue to Digital Converter

ALU – Arithmetic Logic Unit

CCM – Continuous Conduction Mode

DC – Direct Current

DCR – DC resistance

DCM – Discontinuous Conduction Mode

DCVM – Discontinuous Capacitor Voltage Mode

DDCM – Discontinuous Diode Current Mode

DSP – Digital Signal Processor

ESR – Equivalent Series Resistance

GA – Genetic Algorithm

I-V – Current - Voltage

ICD2 – In-circuit Debugger 2

MF – Membership Function

MPP – Maximum Power Point

MSE – Mean Square Error

P-V – Power - Voltage

P&O – Perturbation and Observation

P+I – Proportional and Integral

PM – Phase Margin

PSO – Particle Swarm Optimization

PWM – Pulse Width Modulation

PV – Photovoltaic

RMSE – Root Mean Square Error

TS – Takagi-Sugeno

Chapter 1
Introduction and Literature Review

1.1 Photovoltaic (PV) Energy Systems and their Challenges

The continuing depletion of the world's oil reserves and increasing concern over the environmental impact of the escalating use of fossil fuels around world give rise to an urgent need to establish electricity generation from renewable energy sources. Electric power generation through photovoltaic (PV) effect has recently gained much attention recently because it is "environmentally friendly", free and abundant. Moreover, PV energy has experienced a steady growth rate for the last 10 years, and, among all the renewable energy sources, it is anticipated to be the major contributor to electricity generation by 2040 [1].

Figure 1.1 summarizes the development of PV technology over the last 60 years [2 – 10]. Due to high fabrication cost, the earliest PV energy systems were only found in space applications [2]. However in the 1980s, the growing semiconductor industry helped drive down the cost of a PV energy system, making it an economically viable power source for utility, commercial and residential applications by the turn of the century.

However with the current trend of integrating PV generators into buildings, houses and many other structures in built-up areas, the probability of partial shading by trees, surrounding structures or even birds can be very high, around 41% for residential PV systems [11]. Under these conditions, there is an electrical mismatch between PV generators resulting in the power dissipation in the shaded or damaged PV cells, raising the cell temperature. If this occurs continuously, the accumulated heat may lead to thermal breakdown in cells and hence a reduced power output [5]. One well-established technique for protecting shaded cells from thermal destruction is to use protection diodes which were included in most commercial PV modules by the mid 1990s [5]. For most of these products, a bypass diode is connected across 18 to 20 serially-connected PV cells, and each series string is protected by a blocking diode as referred to in Figure 1.1 [6]. Nevertheless, these methods still lead to a significant reduction in power output which can be as high as 70% [12].

Recently, a completely different approach to the method described above has been proposed. The rationale for this different approach is to embed DC-DC converters in the PV system, which is claimed to be able to overcome the problem of partial shading [8 – 10]. The key challenge for this scheme lies in choosing adequate system structure and control schemes which are the themes of this thesis.

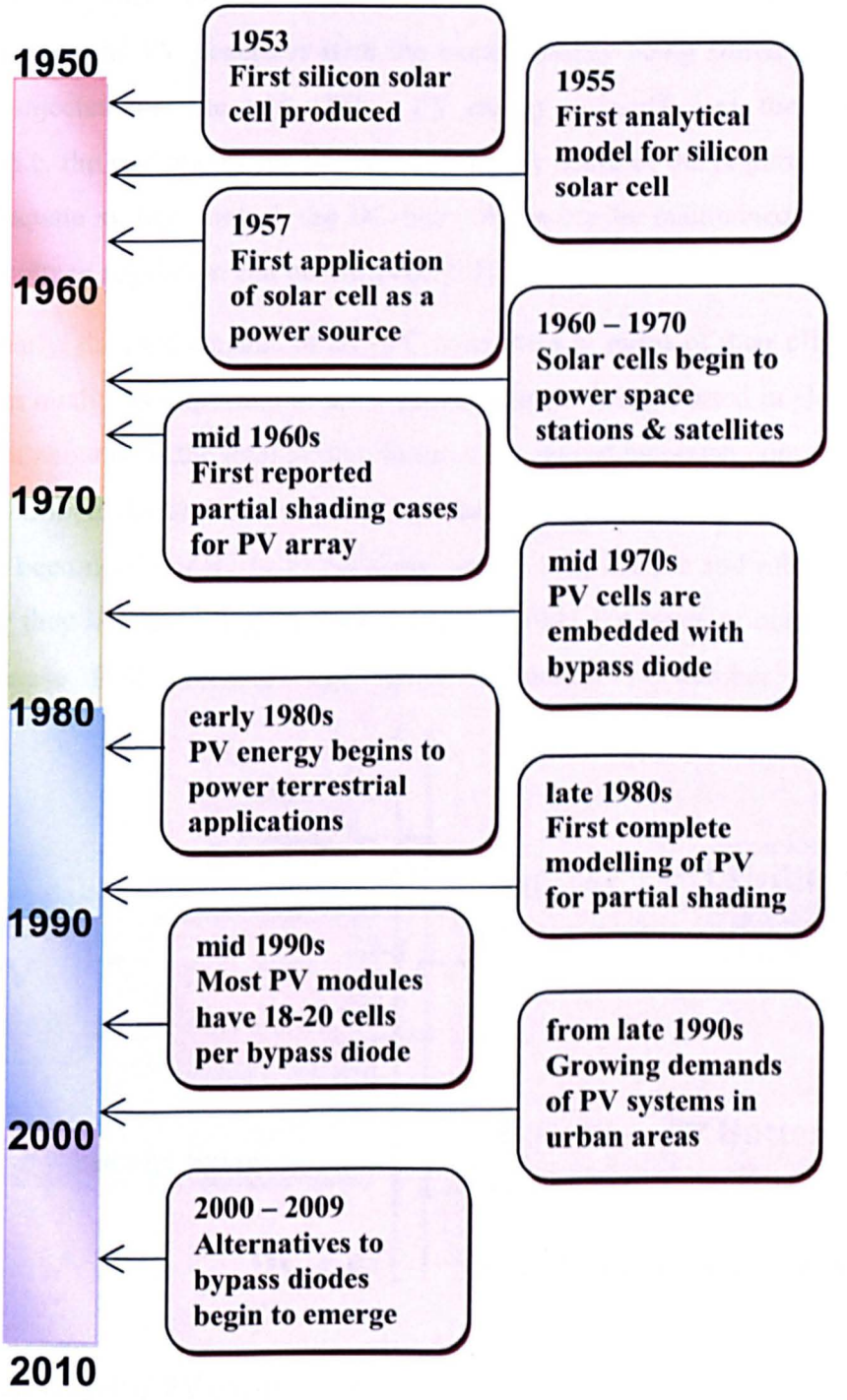

Figure 1.1 Development of photovoltaic technology

1.2 Power Electronic Converters for PV Systems

As illustrated in the block diagram of Figure 1.2, a PV system consists of an array of PV modules, which are linked to the DC-bus by a DC-DC converter. The latter functions as a power conditioner in two aspects; it matches the terminal voltage of the PV array to that of the DC-bus, and controls the PV generator to maximize its power output. When there is surplus PV power, the DC load is supplied from the PV generator with the excess energy being stored in the battery bank or injected into the grid. When PV energy is insufficient, the other power sources (i.e. the grid and/or the battery) can supply some of the required DC power. With adequate system control, the DC-bus voltage can be maintained at a constant and PV voltage regulation can be achieved [13].

Clearly, the performance of DC-DC converters in terms of their efficiency and waveform quality is important to a PV power system. It is reported in Germany and Japan that about 66% the total system failures are caused by power converter defects [14, 15]. Conventional converters such as buck or boost types, as shown in Figure 1.3 have been used widely in PV systems, due to their simple and robust structure. However they introduce high current ripples in either the input or output terminals which cause EMI problems and lower efficiency. A number of emerging

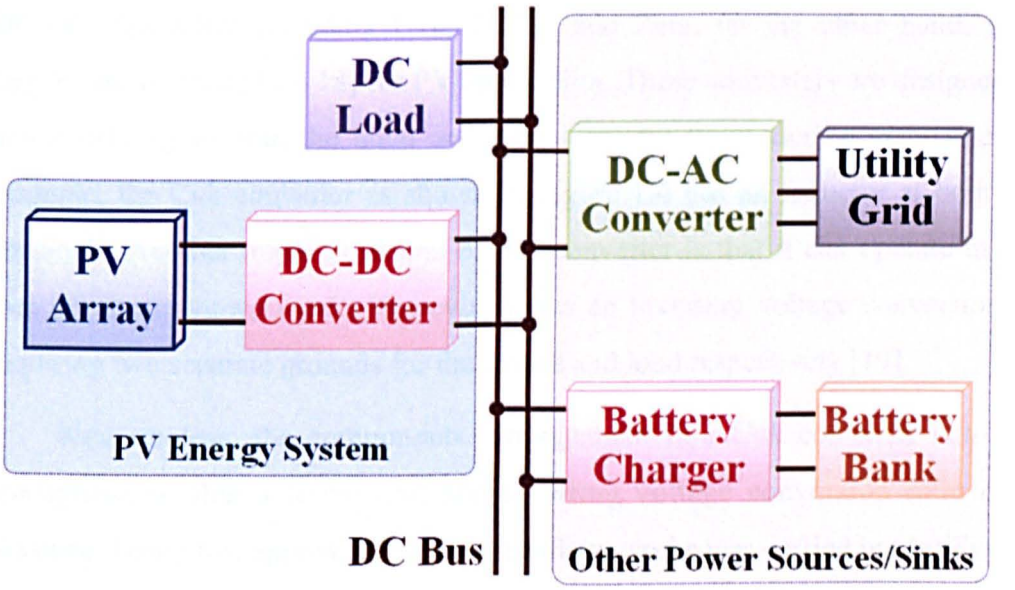

Figure 1.2 A typical PV energy system

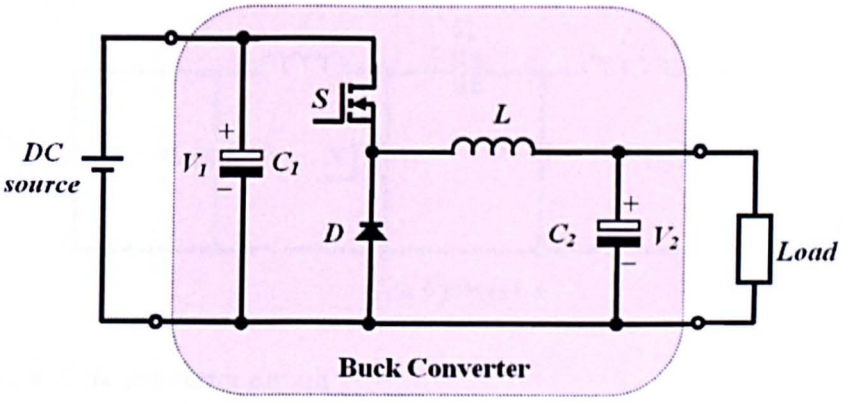

(a) Buck converter

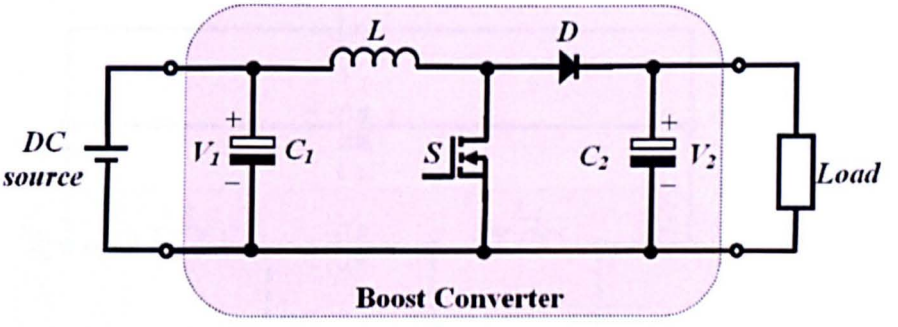

(b) Boost converter

Figure 1.3 Conventional converter configurations

DC-DC converters including Ćuk, SEPIC and Zeta, on the other hand, remain largely unexplored [16 – 18] for PV application. These converters are designed such that continuity in both the input and output current flows can be maintained. For example, the Ćuk converter as shown in Figure 1.4 has an inductor at both of its terminals. Another major attraction of this converter is that it can operate in either step-up or step-down mode. However, it has an inverting voltage conversion ratio requiring two separate grounds for the source and load respectively [19].

Nevertheless, the components' arrangement in a Ćuk converter can be re-configured so that a linear and non-inverting voltage conversion ratio can be obtained. Using this approach, one of the earliest works was carried out by Tymerski who introduced a new topology functioning as a Ćuk step-down converter [20]. Zhang *et al.* then described further that this topology can be derived by connecting the voltage source across X-Y terminal instead of X-W terminal, as shown in Figure 1.5 [21]. Similarly, the load of a Ćuk converter can be connected across the X-Y

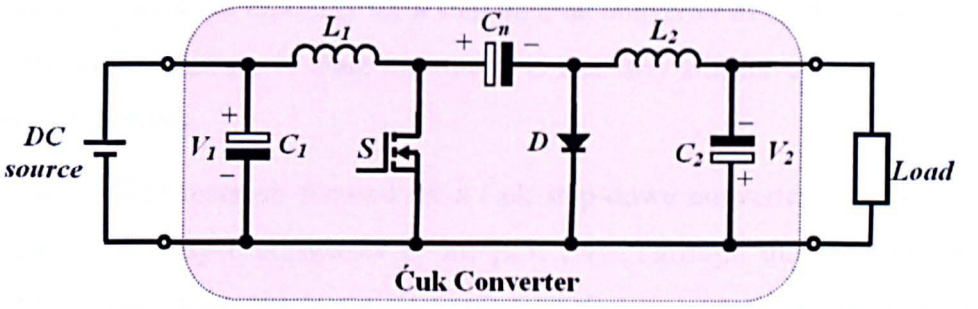

Figure 1.4 Ćuk converter circuit

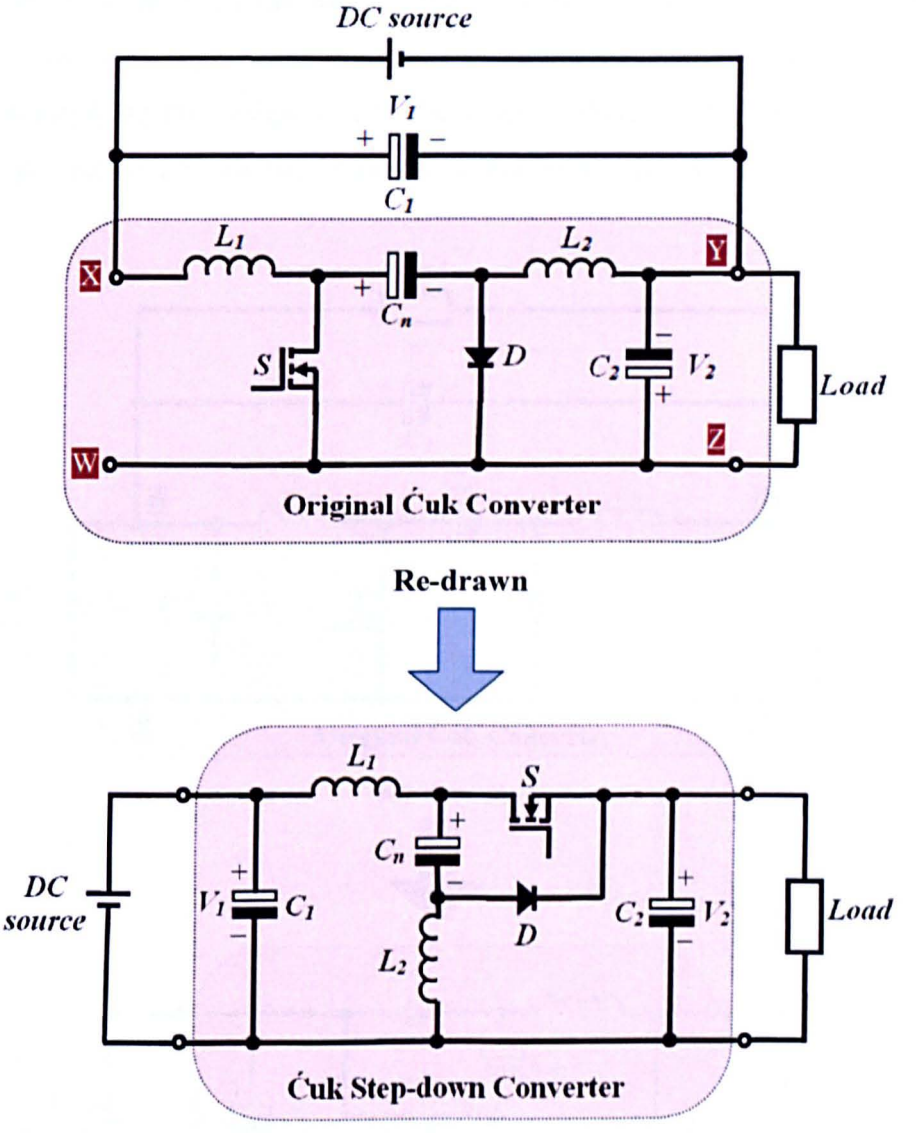

Figure 1.5 Ćuk step-down converter circuit

terminals to obtain the topology for a step-up Ćuk converter as shown in Figure 1.6 [22]. The key advantage of these converters is that they still have continuous input and output currents.

The earliest research focused on a Ćuk step-down converter and its analysis was carried out by Pietkiewicz *et al.* [23, 24]. Through unified topological modelling, their work led to the derivation of the converter duty-ratio-to-output voltage transfer function. The converter was found to be exhibiting the transient features of a forth order system. Hence, their work also involved the development of the converter circuit such that two of the systems poles can be cancelled by the system zeros. This enables the converter to be approximated by a second order system, simplifying the design of a closed-loop feedback controller. However this requires precise values for the converter components. In addition, the modelling

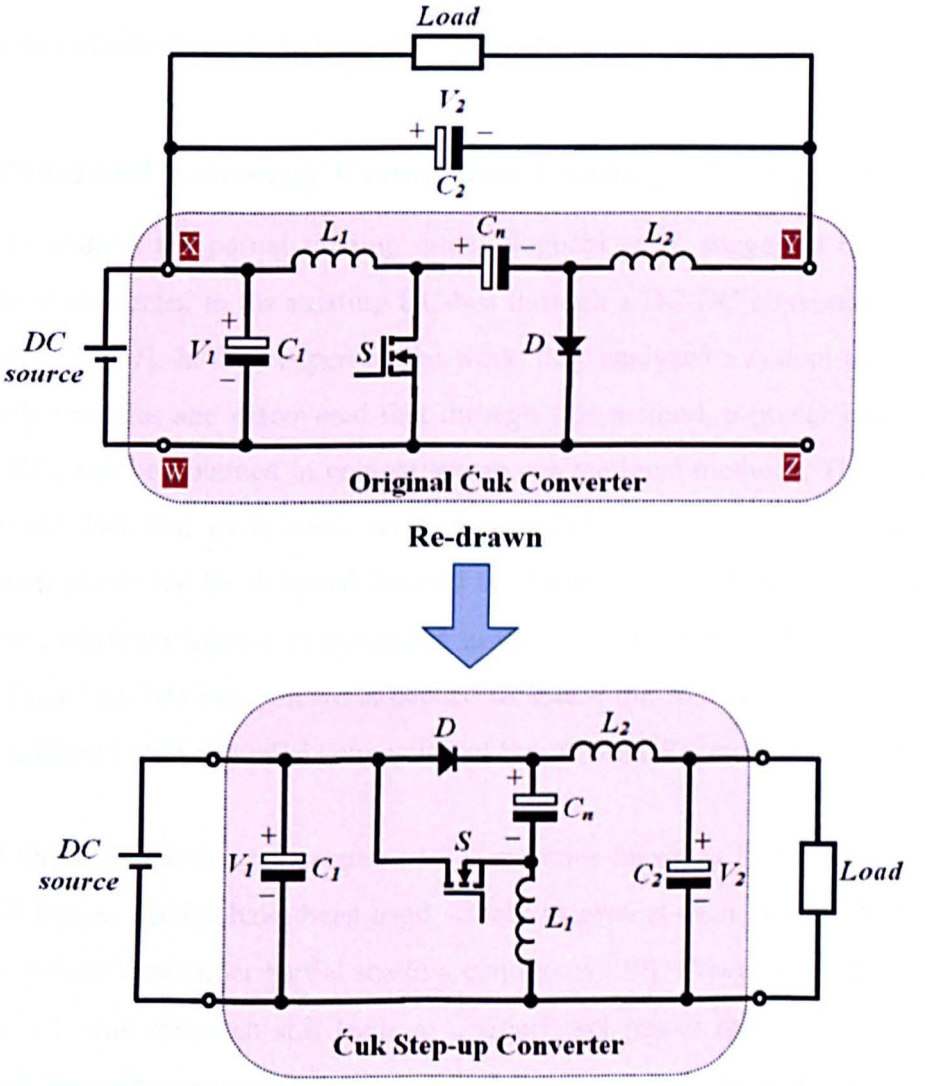

Figure 1.6 Ćuk step-up converter circuit

method employed is cumbersome and requires a rather complex manipulation of various parameters, including the admittances and impedances of the circuit.

Xu carried out a similar analysis for this converter using a simpler approach based on the time average equivalent circuit [25]. The model derived can be implemented readily in simulation software such as SPICE and MATLAB-Simulink. Moreover, another transfer function was derived to depict the output voltage response due to input voltage variations that may occur resulting from the adjustment of the converter duty cycle. This is essential for the design of a converter supplied by a non-linear power source such as a PV generator.

More recently, Babu *et al.* employed the transfer function models to design a one-step ahead predictive controller in regulating the converter output voltage [26]. This was based on the pre-defined reference value for the inductor current. The key attraction of this controller is that stable transient performance can still be obtained even when the there are disturbances, either in the supply, or the load.

1.3 Panel and Converter Connection Topologies for PV Generators

To address the partial shading issue, Noguchi *et al.* suggested that each PV module is connected to the existing DC-bus through a DC-DC converter, as shown in Figure 1.7 [27]. In their experimental work, they analyzed a system consisting of three PV modules and discovered that through this method, a power increment of about 40% can be obtained in comparison to conventional methods. This is mainly due to the fact that each converter can be independently controlled and hence, maximum power can be extracted from all the modules even when some are shaded. However, when the system is connected to the AC consumer loads through power inverters, a high DC bus voltage is needed to match the AC side voltage; this may not be achieved with a parallel connection of low-voltage PV modules [13, 28].

Therefore, a series connection of PV modules becomes highly desirable and external bypass diodes have been used widely to protect each module from being thermally destroyed under partial shading conditions [29]. However, as discussed in Section 1.1, this approach still leads to a significant power reduction. A different approach, through incorporation of additional converters, has the potential to address

the partial shading issues adequately. Using this approach, two topologies have been proposed by the researchers [8, 9, 10, 30]. The first comprises one or several cascaded converters as shown in Figure 1.8. To further raise up the terminal voltage, Femia *et al.* and Bratcu *et al.* proposed to use the boost type of converter that can be controlled independently [10, 30]. The key feature in this topology is that it does not require bidirectional converters. However, it requires a continuous power flow

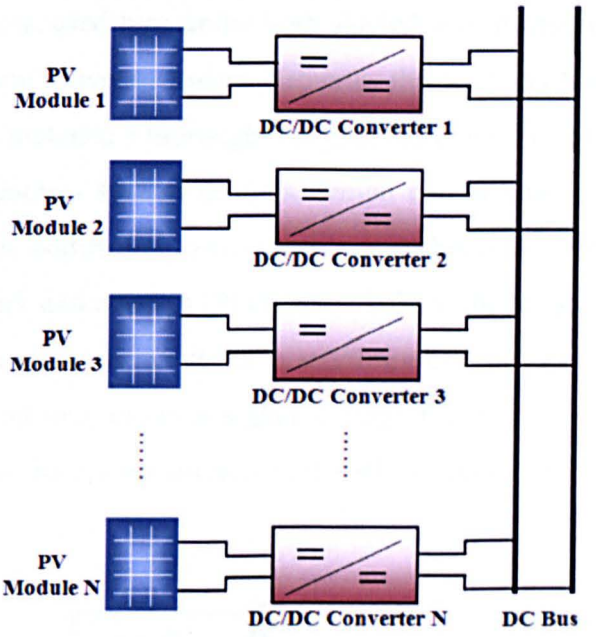

Figure 1.7 One converter per PV module configuration

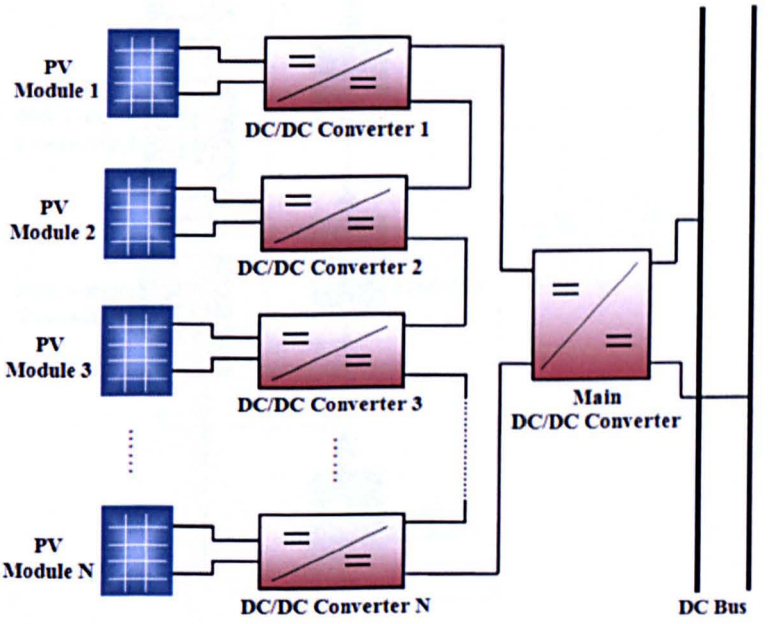

Figure 1.8 Cascaded converter configuration for serially connected PV modules

around the circuit, even when there is no shading. Moreover, the operating duty ratios for the converters depend on both the steady-state operating points of PV currents, and voltages.

The second topology is the integrated converters, as shown in Figure 1.9 which, on the other hand, are required to operate in a bidirectional mode. They still become a desirable choice as the current flowing through the converter is much less than that in the cascaded type under both shaded and unshaded conditions [9]. This reduces the system's overall losses. Hitherto, the work on the integrated converter topology has not included a thorough analysis, either on the operating principles, or a suitable set of control system designs, which can become more complicated and distinctive when additional converters are embedded within the PV modules. However, the work described in [9] involves linking the integrated converter directly to a grid-connected inverter. Such a topology complicates the system's overall dynamics [31] and may cause a higher voltage fluctuation, requiring the use of a larger capacitor to be connected across the PV modules. In addition, the operating

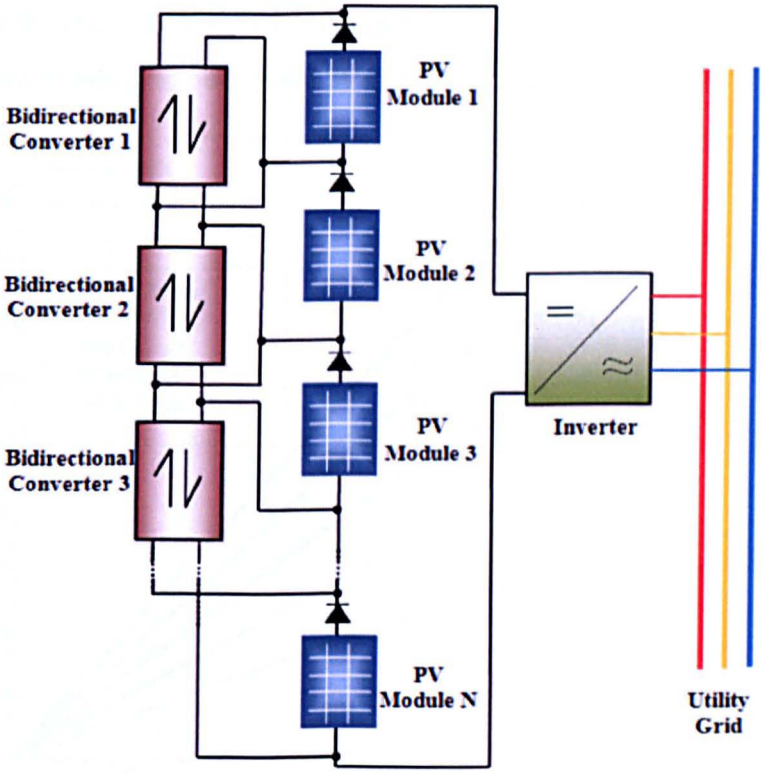

Figure 1.9 Integrated converter configuration for serially connected PV modules

voltage across all the serially connected PV modules may still be significantly lower than the inverter rated input voltage [10]. Potentially, these issues can be solved if the terminal of all the PV-integrated converters is connected with another step-up converter that has its output connected to a DC bus. The development of this improved scheme with its associated control strategies constitutes a challenging task which can lead to novel outcomes.

1.4 Energy Management and Control for PV Systems

1.4.1. Unshaded PV Systems

The major challenge in a PV energy system is to harness as much power as possible under continuously changing weather conditions, including the cell temperature and the light intensity. When no panel is shaded from the sunlight, the performance of a PV system depends closely on the environmental factors. Figure 1.10 illustrates the output power-voltage (P-V) characteristics of a module and its dependency on the cell temperature and insolation level. It can also be observed that the maximum output power levels vary with environmental conditions. Maximum power can then be obtained by adjusting the voltage across the PV module according to that corresponding to peak point as indicated by MPPs in Figure 1.10. The voltage

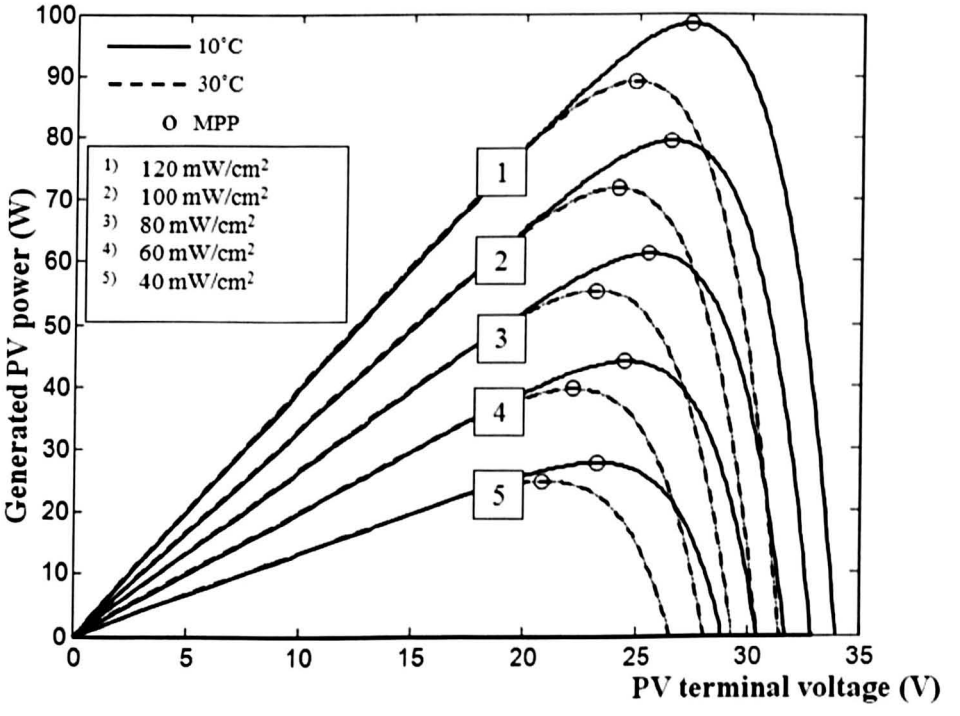

Figure 1.10 Power-voltage characteristics for a PV panel with 52 cells connected in series

regulation can be achieved by using power electronic voltage converters [32, 33]. Hence over the years, many researchers have employed various maximum power points (MPPs) tracking schemes to design the control system; these have provided energy gains of at least 25% compared to an uncontrolled system [32]. Recently, Salas has reviewed these MPP tracking algorithms comprehensively, and classified them into three main categories [33]:

1) Indirect control for MPP tracking
2) Direct control for MPP tracking and
3) Artificial intelligence methods

The indirect control method involves the use of pre-determined parameters and data which are obtained from a prior evaluation of the PV module. In particular, the work contributed by researchers in references [34, 35] has focused on the mathematical modelling of a PV module using a numerical approximation method. The model receives weather measurements including the solar insolation and cell temperature as inputs and generates the PV voltage corresponding to the MPP as the output. Through this approach, an *n*-th order polynomial curve-fitting technique has been employed to largely model the P-V curve of a module [33, 35]. One of these polynomials is given as

$$P_{PV} = \theta_o + \theta_1 V_{PV} + \theta_2 V_{PV}^{\ 2} + \theta_3 V_{PV}^{\ 3} + ... + \theta_n V_{PV}^{\ n} \qquad (1.1)$$

where P_{PV} is the PV power output, V_{PV} is the PV terminal voltage, and θ_is are the pre-determined model parameters that are changing with weather conditions. The Newton-Raphson method is then used to compute the MPP voltage. One of the major disadvantages for this method is that the model requires a large amount of memory to store the values for the model's parameters [33].

On the other hand, the direct control technique is based on the online measurement of voltage and/or current. For this technique, two approaches are widely used in PV power systems, namely, the perturbation and observation method (P&O) [36, 37], and the incremental conductance method (IncCond) [38]. The key concept for these approaches is that the regulation of the PV voltage is performed until a zero value is obtained for the ratio between the PV power and voltage variations, which is given as

$$\Delta_{PV} = \frac{P_{PV}(kT_s) - P_{PV}((1-k)T_s)}{V_{PV}(kT_s) - V_{PV}((1-k)T_s)} \tag{1.2}$$

where $P_{PV}(kT_s)$ and $V_{PV}(kT_s)$ are the measured values for the PV power and voltage after the k-th sampling period T_s. However, P&O has the problem of continuous oscillation around the optimal operating point [35] while there is a higher complexity in the circuit for IncCond controller [33].

To avoid the drawbacks of the above approaches, model-based control techniques have recently received an increased attention for the implementation of an MPP tracking scheme [33]. Using this method, an Artificial Intelligence (AI) model is employed to estimate the PV current value for each weather condition and a PV voltage value. As illustrated by the flowchart in Figure 1.11, this process is repeated until the whole range of voltage-current pairs has been obtained. The voltage-current pair which gives the maximum power value is then selected as the reference for the PV operating voltage.

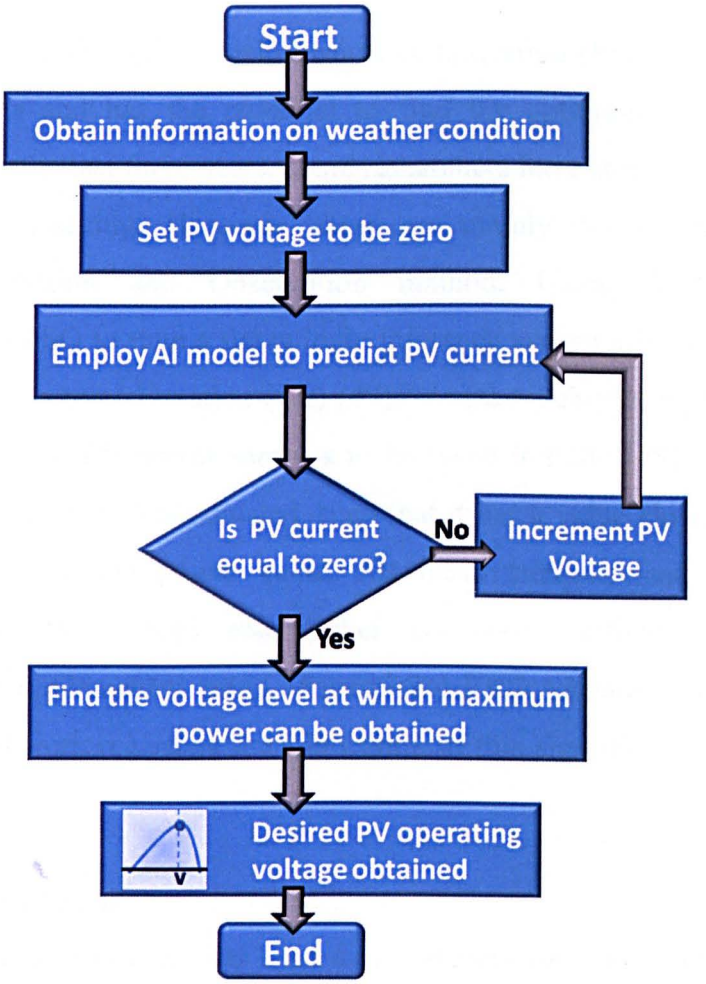

Figure 1.11 Flowchart for tracking the maximum power point tracking of PV using modelling-based approach

Various AI models have been developed to realise the control for tracking the MPP of the PV. One of them, by Melit *et al.*, is through the Adaptive Neuro-Fuzzy Inference System (ANFIS), which requires a gradient descent method and least square algorithm to design the model parameters [39, 40]. The key advantage of the developed model is that it can be re-tuned online. However, the tuning algorithm may lead to a sub-optimal model and hence other better solutions have not been explored adequately [41]. Therefore, researchers have recently focused on other efficient tuning algorithms. For example, using genetic algorithm and radial function neural network, an AI model for the PV can be more accurately generated by evaluating a number of possible solutions and selecting the one which satisfies most of the design requirements [42, 43]. Based on the natural evolution process, this searching mechanism is iteratively performed by using a group of solutions which offer high performances to form a new group of possible solutions. However, the model tuning method requires a prolonged period of time and high computation effort to process [44].

Another algorithm through Particle Swarm Optimization (PSO) involves only arithmetic operations and has the potential to find the optimum solution more quickly [45, 46]. For the last three years, some researchers have started to apply this algorithm for MPP tracking. However, these are mainly developed from the conventional Perturbation and Observation method. Using this approach, Khaehintung applied PSO to tune a fuzzy logic inference system which is aimed at minimizing the magnitude of Equation (1.2) [47]. Another scheme, by Chen *et al.* requires a number of the PV power samples to be taken initially [48]. Using PSO algorithm, the PV voltage is then adjusted, such that it has a value closer to that of the sample with the highest power value. All these methods lead to smaller fluctuations in the PV voltage and higher conversion efficiencies; hence, outperforming those implemented using conventional P&O schemes. Nevertheless, there is no published work regarding the application of this algorithm to the model-based control for PV.

1.4.2. Shaded PV Systems

Over the last five years there has been more research on control strategies for maximising power extraction under partial shading conditions. These have been

implemented mainly on PV systems protected by bypass diodes. Unlike uniform irradiation where only one peak power point is present for a whole panel for each weather state, there are multiple peak power points as shown in the Power-Voltage curve of Figure 1.12. It is difficult to quickly and accurately locate the maximum power point on the P-V curve for the specific panel in real time. Two main approaches have been reported so far. The first is still based on the traditional Perturb & Observe method (P&O) [38, 49] which has been applied widely to commercial PV power generators, while the other is based on using mathematical or numerical models of the PV plant [36, 50]. The P&O method, though simple to understand and implement, requires changing the terminal voltage repeatedly to locate the peak power points. It is slow, introducing noise into the system and may fall into a local maximum under non-uniform irradiation conditions.

To avoid these defects, various intelligent searching schemes have been tried and tested [51 – 56]. One peak point searching scheme, proposed by Miyatake *et al.* [51] uses the Fibonacci sequence numbers to iteratively define and shift the search range. This method can also widen the search range for sudden changes of weather conditions and has been shown to be both efficient and flexible. Another technique by Kobayashi *et al.* begins the search with the unshaded operating point which is determined by the open-circuit voltage and short-circuit current measurements [52]. Patel *et al.* proposed a searching scheme which locates the local optimal points with

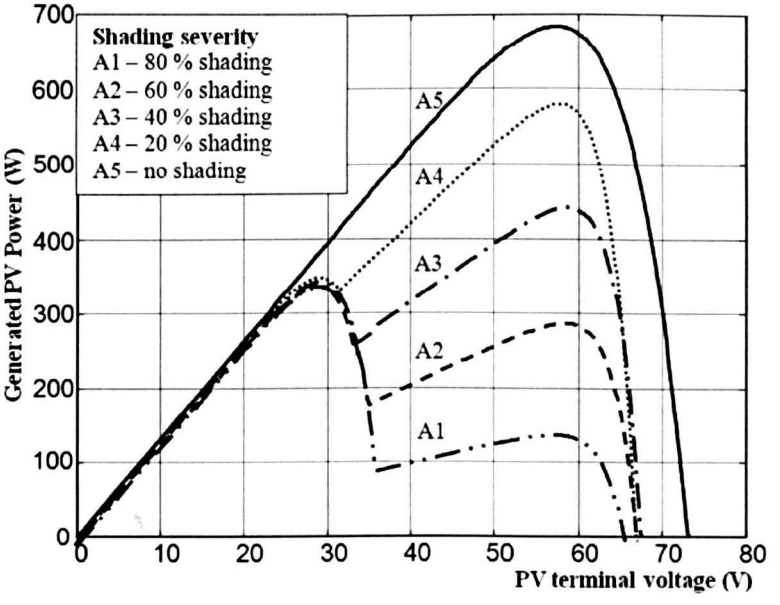

Figure 1.12 Power-Voltage characteristics for a system with two serially linked PV modules

the number of points being known a priori from the configuration of the panels [53].

It then identifies the global maximum by comparing the local peak values. Numerical models for PV panels under non uniform illumination conditions, such as the one based on using the Lambert W-function [56], have been proposed. However, their application in MPP tracking is as yet, to be developed. Nevertheless, all of the above approaches can only lead to sub-optimal operation.

For the systems using cascaded or integrated converters, MPP tracking of each PV module can be performed independently [9]. Hence the schemes similar to those for unshaded systems can be applied.

1.5 Review of Neuro-Fuzzy Model and Particle Swarm Optimisation Training Method

1.5.1 Artificial Neural Network

By the mid 20th century, the emergence of computer technology simplified the design of artificial neurons. The earliest breakthrough was achieved by McCulloch and Pitts who focused on the mathematical modelling of the nervous activity in a human brain [57]. Their work then led to the development of a fundamental structure for a neuron; an example with two inputs and one output is shown in Figure 1.13. The neuron multiplies each input by a weight factor first, and then aggregates the weighted inputs before computing the output using an activation function, which can be sigmoid, binary or linear [58].

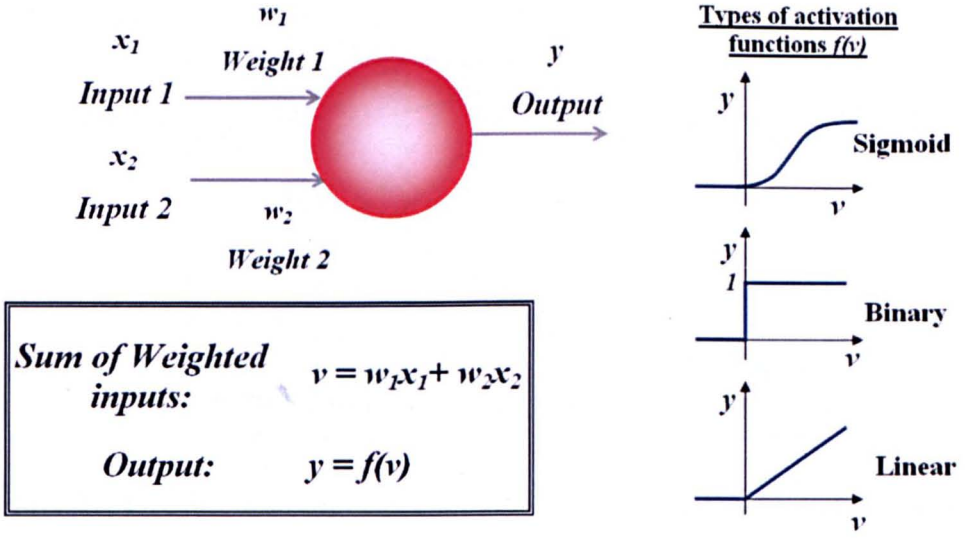

Figure 1.13 Fundamental structure of an artificial neuron

Networks of neurons are interconnected in order to achieve the functions of the biological neural system. When this structure is applied to a modelling technique, an artificial neural network (ANN) is formed and the interconnecting neurons become the processing elements which are working together simultaneously to represent the relationship between the inputs and outputs [59]. An example of a multiple-input-and-single-output (MISO) network with one input layer, one hidden layer and one output layer is shown in Figure 1.14. The activation function used for this example is a sigmoid. It can be observed that N_I sampled inputs signals are scaled first by the weighting factors, w. They are then used to compute the signals of the hidden layer using the activation function given by

$$f_h(net_h) = \frac{1}{1+e^{(-net_h)}} \tag{1.3}$$

where $net_h = \sum_{i=1}^{I} \left(w_{ih}^{\alpha} \cdot x_i \right)$

with x_i being the i-$^{\text{th}}$ input and $w_{ih}{}^{\alpha}$ the weight linking i-th input to h-th hidden layer nodes. The resulting signals from the hidden layer are then propagated through another set of weighted connections to the output layer where the corresponding output is computed using the function given by

$$Output = f_o\left(\sum_{h=1}^{N_H} w_h^{\beta} \cdot f_h(net_h) \right) \tag{1.4}$$

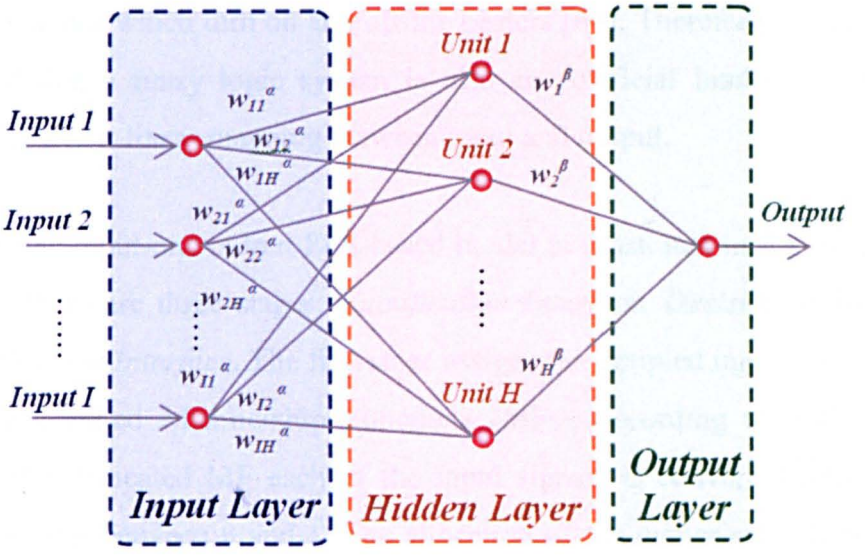

Figure 1.14 A multiple-input-and-single-output (MISO) artificial neural network

N_H is the number of nodes in the hidden layer, w_h^{β} is the weight linking the h-th hidden layer unit to the output and $f_o(\ )$ is another sigmoid function similar to Equation (1.3).

To apply this network for modelling a process, the weight values have to be adjusted accordingly. This can be done through a model training process based on the collection of sufficient input-output data. The drawback of the final model is that the information on its characteristics is solely represented by the weight matrices from which a detailed interpretation of the model is difficult to obtain [60]. Moreover, there is no standard set of rules for a designer to choose the number of hidden layers which will lead to a highly optimum model.

1.5.2 Fuzzy Logic System

Since its introduction by Zadeh [61], the fuzzy logic system (FLS) has been successfully employed to control various applications including those in the power engineering [62], medicine [63], household appliances [64], computer systems [65] and transport systems [66]. This is because most of these systems are non-linear. An example for this can be found in the heating system used by modern rice cookers, toasters and irons [64]. A fuzzy logic control can be used first to acquire continuously varying signals, including the measured temperature and its desired value as the imprecise inputs. These signals are evaluated using a set of fuzzy rules and then a definite set of PWM output signals are generated to control the operation of the switches which turn on and off the heaters [64]. Therefore, it has been widely accepted that a fuzzy logic system is also an Artificial Intelligence type model, providing a non-linear mapping between input and output.

A one-input-one-output FLS-based model is illustrated in Figure 1.15. As can be seen there are three stages; *Fuzzification Interface, Decision-making Unit and Defuzzification Interface*. The first stage assigns the sampled input signals to specific categories, called Membership Functions (MFs), according to their magnitudes. Within the dedicated MF each of the input signals is converted into a numerical value ranging between 0 and 1. The allocation of the numerical values, also called fuzzy values, can be performed through evaluation of one of several functions, such as triangular function, Gaussian distribution, sigmoidal and polynomial as shown in

Figure 1.16[67]. In the example shown in Figure 1.15, input, x is located in the 'HIGH' MF which is denoted by FX_1 and is then assigned a fuzzy value λ_1. Stage one operation also considers ambiguous cases where an input signal may be within the intersecting region of two or more MFs representing different linguistic labels as FX_1, FX_2, ..., FX_i. Subsequently a single input value may have a set of fuzzy logic values, λ_1, λ_2, ..., λ_i.

In the second stage, the *Decision-Making Unit*, the assigned fuzzy logic values are assessed by a number of fuzzy rules, named R_1, R_2, ... R_i, which lead to output

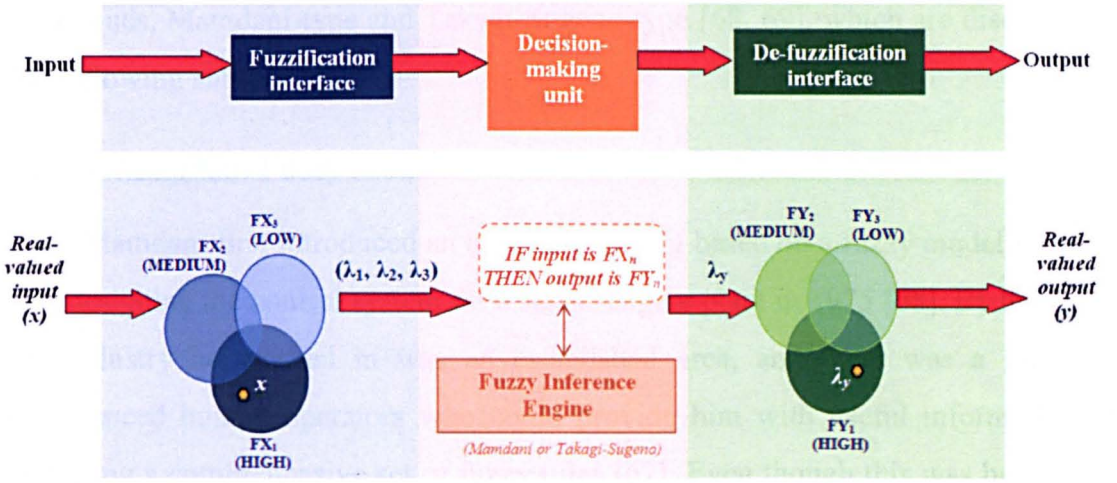

Figure 1.15 A one-input-one-output FLS-based model

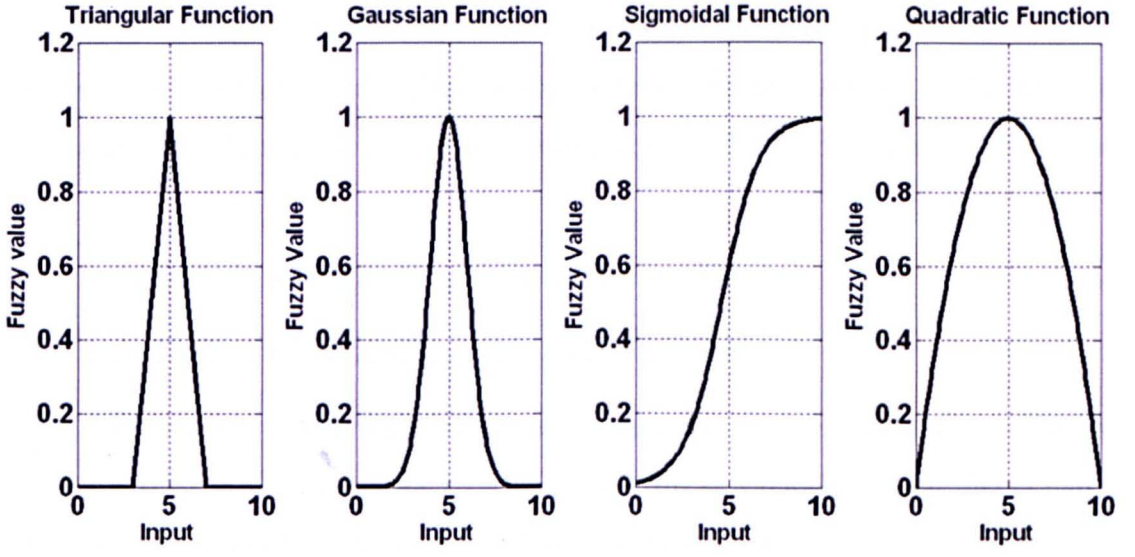

Figure 1.16 Various functions for performing the allocation of the fuzzy values

decisions. One of the rules may be, as shown in Figure 1.15, written as

IF *input* is FX_n THEN *output* is FY_n. (1.5)

The rule consists of two components; the premise 'IF' part which sets the condition for the rule and the consequent 'THEN' part which determines its outcome. For the latter, FY_n, it is represented by a linguistic label which will then be used by the *Fuzzy Inference Engine* to generate its corresponding fuzzy value. The fuzzified output, λ_y is then converted back to its real-valued form, y, by the *Defuzzification Interface*.

All of the above can be achieved through one of the two widely used techniques, Mamdani-type and Takagi-Sugeno-type [68, 69], which are discussed in the following sub-sections.

1.5.2.1 Mamdani Fuzzy Model

Mamdani first introduced an inference system based on a fuzzy model when he was designing the control system for a steam-engine plant in 1975 [68]. By that time, the industry he worked in was an established area, and there was a group of experienced human operators who could provide him with useful information on designing a comprehensive set of fuzzy rules [67]. Even though this was based on a heuristic tuning method, an automatic control without human intervention has been implemented successfully for the plant.

An example of the Mamdani fuzzy model with two inputs and one output is illustrated in Figure 1.17. The stage 1 *Fuzzification* layer performs the fuzzy conversion for input values using triangular functions as described in the previous sub-section. In the second part of this example, two of the fuzzy rules are expressed as

Rule 1: IF x_a is FA_1 AND x_b is FB_1 THEN y is FY_1. (1.6)

Rule 2: IF x_a is FA_2 AND x_b is FB_2 THEN y is FY_2. (1.7)

The premise part for each rule now depends on a pair of MFs, $FA_1 - FB_1$ for Rule 1 and $FA_2 - FB_2$ for Rule 2. The smaller fuzzy value from each fuzzy pair is taken as the weight for the corresponding rule. For this example, λ_{B1} is taken as w_1 for Rule 1 and λ_{A2} as w_2 for Rule 2, as shown in Figure 1.17. The rule weights are

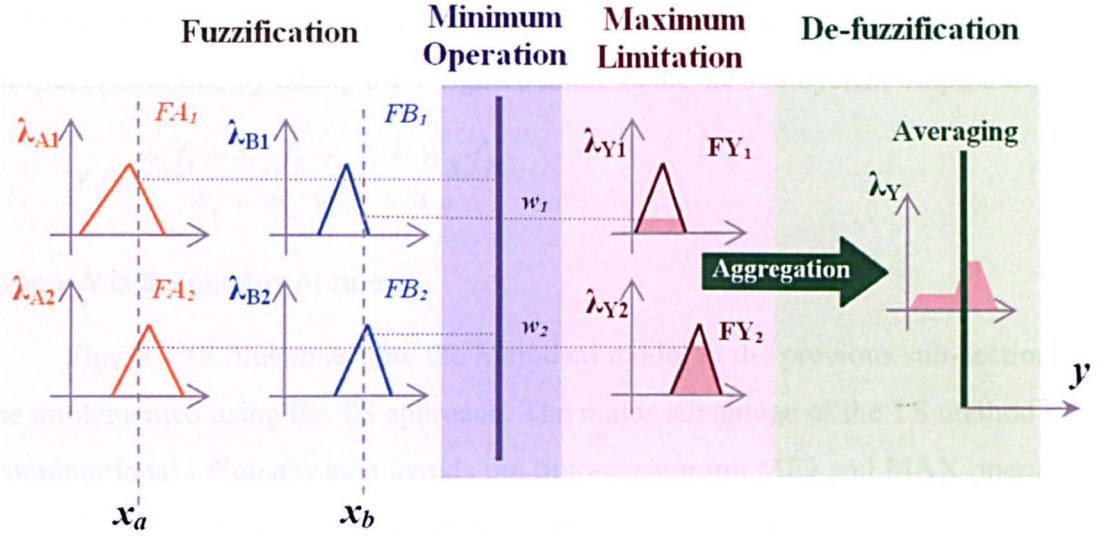

Figure 1.17 A two-input-one-output Mamdani fuzzy model

used to set as the maximum limit for the corresponding FY as shown in the figure. The MF for the overall output is then obtained by integrating all the limited MFs of FY and their average is taken as the actual output value, i.e. aggregation. Since w_2 has a higher value for this example the linguistic label, FY_2 has a dominant feature in the overall output compared to that of FY_1.

1.5.2.2 Takagi-Sugeno Model

A more systematic method for designing an optimum fuzzy model structure was proposed in 1985, named as the Takagi-Sugeno (TS) inference system [69]. Compared with Mamdani fuzzy model the main feature of this model lies in expressing the non-linear relationship between input and output using a set of linear equations. This is performed at stage 2, the *Decision-Making Unit*, thus instead of defining a set of fuzzy rules, a set of linear equations, also called sub-systems, expressed as

$$f_k = c_k^0 + c_k^1 x_1 + c_k^2 x_2 + ... + c_k^m x_m \tag{1.8}$$

are used leading to a set of the outputs, f_k. Note c_k^i in the equation are the linear coefficients for k-th sub-system while x_i is the i-th input to the model and m is the total number of inputs.

The dominance of these sub-systems within the overall model is evaluated by the rule weight which is the product of the associated fuzzy logic values from the

fuzzification interface stage, namely the weighting factors w_i. The overall model output is obtained by taking the weighted mean of all the sub-system outputs as

$$y = \frac{w_1 f_1 + w_2 f_2 + ... + w_N f_N}{w_1 + w_2 + ... + w_N} \tag{1.9}$$

where N is the number of rules.

Figure 1.18 illustrates how the Mamdani model in the previous sub-section can be implemented using the TS approach. The major advantage of the TS method is its computational efficiency as it avoids the time-consuming MIN and MAX operations of the Mamdani-type [67]. Only multiplications and additions are required, and this makes the structure even more desirable for the arithmetic function based tuning methods like particle swarm optimization. Moreover since the TS approach works with multiple linear models, it is suitable to be used for a wide range of applications based on linear systems [70]. Nevertheless for the TS model, the computations of the sub-system outputs and the rule weights are performed simultaneously within a sample period. Designing a TS model can also be challenging as it does not support the formation of fuzzy rules from human knowledge [71]. Hence, accurate tuning of parameters becomes the key factor in producing a highly optimum model.

1.5.3 Neuro-Fuzzy Models

To design a fuzzy model, the optimum number of rules and the details of the membership functions have to be determined a priori. While all this may be done heuristically, it remains a challenging task for most designers [68]. Hence from the

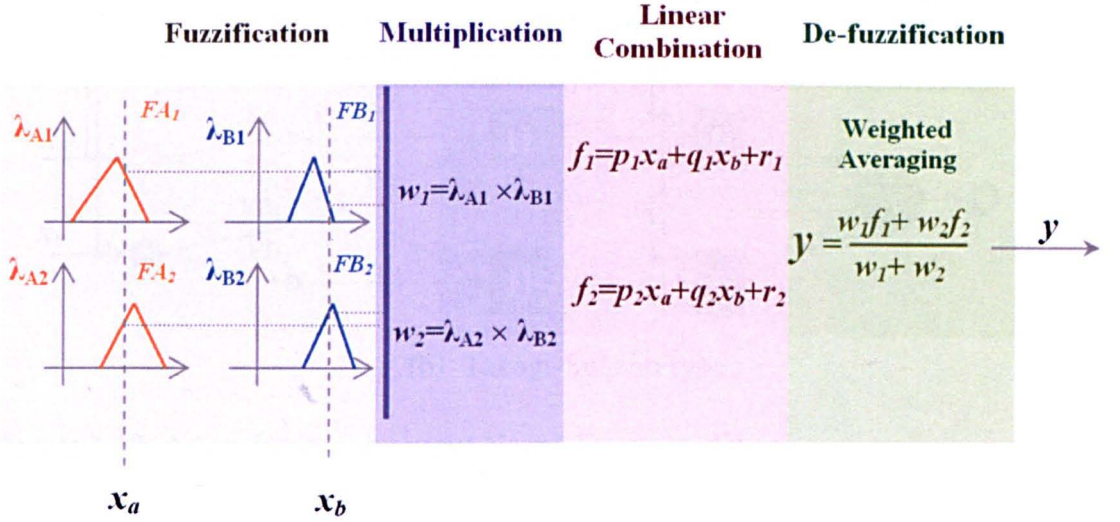

Figure 1.18 A two-input-one-output Takagi-Sugeno fuzzy model

1990s, researchers began to integrate fuzzy logic schemes into neural network technology [60, 72]. In this approach, a model can be in standard neural network structure while its internal parameters and weighting factor are defined according to rules of fuzzy models.

Figures 1.19(a) and (b) show two Neuro-Fuzzy models. The input layer, consisting of two nodes, performs similar function to that of the fuzzification interface, i.e. to convert the input data to fuzzy values, λs. In the hidden layer, the neurons are formed by using different fuzzy models; the one in Figure 1.19(a) adopts logic MIN-MAX operation hence is a Mamdani-type, and the other in Figure 1.19(b) employs multiplication operations according to Takagi-Sugeno scheme. In addition, at the output layer in Figure 1.19(a) the model output value is derived using an integration function, while that in Figure 1.19(b) is obtained by using weighted averaging. Note all the outputs of f_k in Figures Figure 1.19(b) are those of a set of linear sub-systems as described in the previous sub-section.

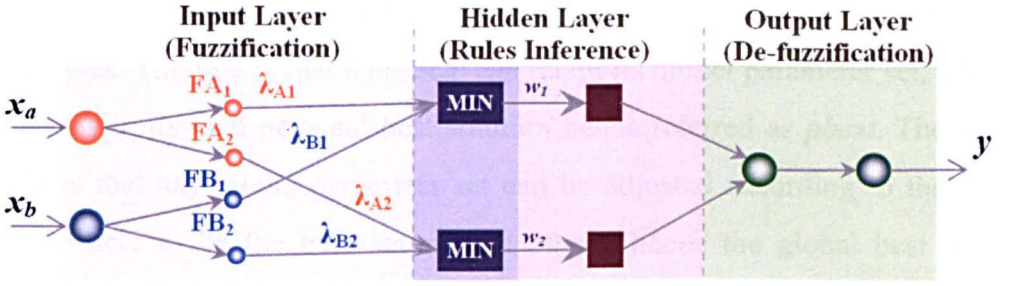

(a) Mamdani type

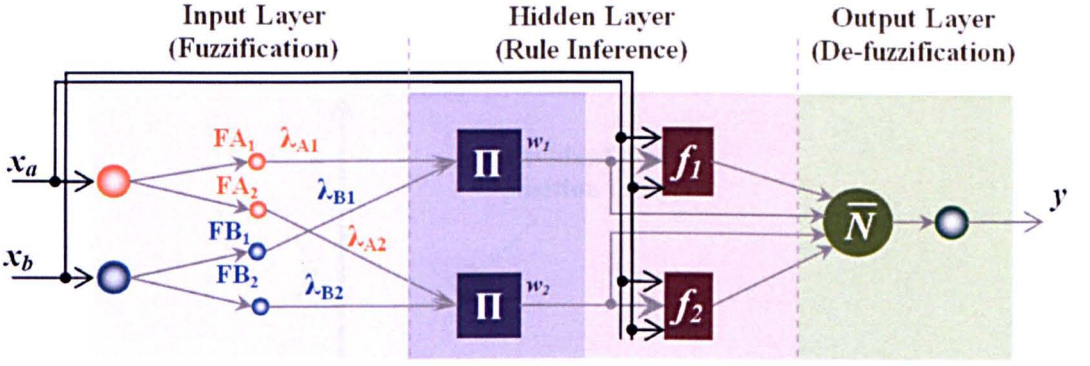

(b) Takagi-Sugeno type

Figure 1.19 A two-input-one-output Neuro-Fuzzy model

1.5.4 Particle Swarm Optimization Method and its Applications to Model Training

A PSO is a type of evolutionary computational technique introduced by Kennedy and Eberhart in 1995 [73]. Their work originated from other researchers who were aiming at simulating the social behaviour of a flock of birds, or a shoal of fish, which is referred to as the particle swarm [74]. To put this in the context of the modelling technique, each individual in the swarm is a particle which represents a solution for a model and its position in a multi-dimensional space is defined by the model parameters. An example in Figure 1.20 shows a particle for a model which has two parameters representing the particle's co-ordinates (x_p, y_p).

PSO can be conceptualized through the flocking of birds, for instance, towards a location where an ample supply of food can be found. One factor influencing the flock dynamics is the cognitive feature through which every individual in the flock remembers their location through its past experience. The other factor is the social behaviour through which every individual can exploit the neighbours' knowledge on the location. Hence, the search for an optimal model using a PSO is based on two key principles. The first is that a particle can retain its model parameter set, which is associated with its own personal best solution hence referred as ***pbest***. The second principle is that any model parameter set can be adjusted according to that which leads a particle to be the best among the others, hence the global best solution referred as ***gbest.*** The model training process can then be summarized as follows [74, 75]:

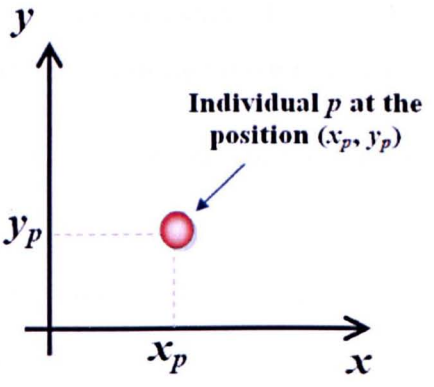

Figure 1.20 Position of particle p which potentially is the solution for a model having two parameters

1) Set p particles with random values initially; each particle has N_d parameters for the model. As described above, all the values for N_d parameters indicate the positions of p particles in a N_d-dimensional space.

2) For each p particle, predict the output value, $\hat{y}_p$, using the desired input data and corresponding model parameter set, then evaluate its difference from the desired value, y_p*, using an objective cost function $E_p = \left|\hat{y}_p - y_p *\right|$,

3) Compare calculated E_p above, to that achieved previously for the same particle and setting the one with lower E_p value as the current position, namely, the current personal best, ***pbest***. This is performed for all the p particles.

4) Compare E_p of one particle with that of another and set the one giving the lowest value as the current overall best. If this E_p value is even lower than that of the previous overall best, its current position is used to update ***gbest.***

5) Update the position of each particle using the following formula

$$\Phi_p[k+1] = \Phi_p[k] + \Delta_p[k] \tag{1.10}$$

where $\Delta_p[k]$ is given as

$$\Delta_p[k] = rand_1(pbest - \Phi_p[k]) + rand_2(gbest - \Phi_p[k]) \tag{1.11}$$

where $rand_1$ and $rand_2$ are two stochastic variables allocated with a value ranging between 0 and 1. They are used to prevent the search from being trapped within the sub-optimal region, and hence widen the scope of exploration for an optimal model [74]. The first term, $rand_1(pbest - \Phi_p[k])$ in Equation 1.11 features the *cognitive* feature of a particle, while the *social* behaviour can be exhibited through the term, $rand_2(gbest - \Phi_p[k])$.

6) Return to Step 2 until either the maximum number of iterations is reached or E_p reaches the minimum set value.

Using a two-parameter model as an example, the PSO tuning algorithm can be illustrated further as depicted in Figures 1.21(a) — 1.21(c). Note that each figure represents a particular particle position for each possible scenario.

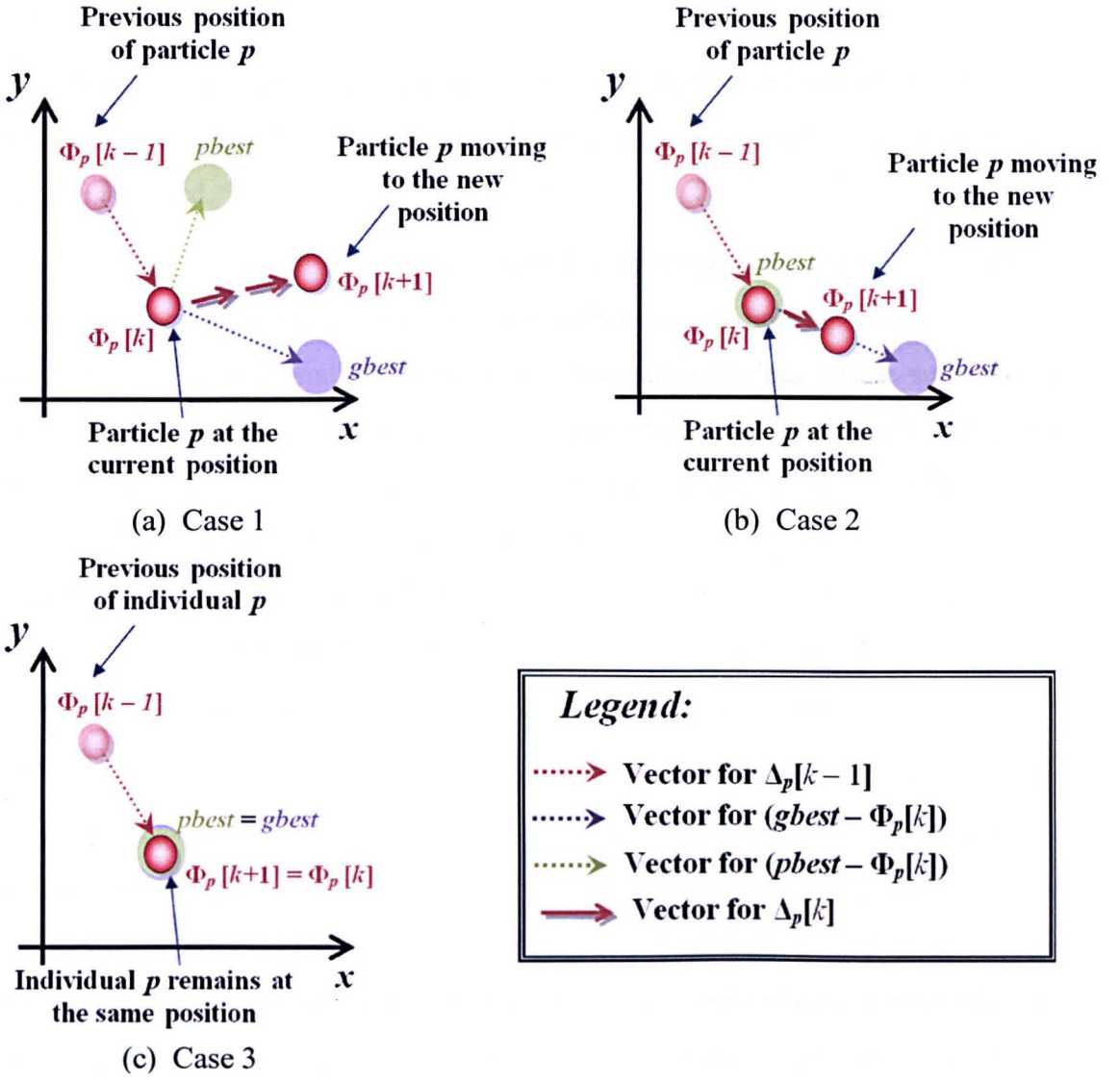

Figure 1.21 Illustrative examples for three possible cases of particle movements

Case 1: Figure 1.21(a)

Particle p is currently located at a position different from those of ***pbest*** and ***gbest***. The model parameters should be adjusted such that p is located in between them.

Case 2: Figure 1.21(b)

The model defined by the current location is the most optimum so far for particle p and hence, its ***pbest*** is located at this position. However, this is still not the ***gbest***. Therefore, the particle is moved towards the position of overall best particle.

Case 3: Figure 1.21(c)

The current location of particle p leads to the best model that all particles have achieved so far, and hence it remains in this position, to which other particles will also be attracted.

The above described algorithm is based on the original PSO process, which has some shortcomings [76]. These include either the iteration process stops pre-maturely at a sub-optimal solution, or becoming unstable due to the sudden large changes of parameters. One way to solve these problems was through multiplying the stochastic variables in Equation (1.11) by a factor of 2 [73]. The effect of this change is that each of them will then have a mean of 1, increasing the probability for a particle to "fly" past a local optimum point, while keeping the searching process in control. Nevertheless by 1998, Shi and Eberhart discovered that the two terms in Equation (1.11) are not sufficient to improve the performance of PSO [76].

Thus another "momentum" term is added into Equation (1.11) to pull the particles away from the local search area [76], and this has been successful for most PSO applications [47, 48, 77, 78]. However, this approach has two major drawbacks including the unnecessary fluctuation in the searching process and more iteration required for finding an acceptable model [76]. Hence, a time varying inertia factor is introduced into the "momentum" term such that the algorithm has the chance to explore the solution space widely during the initial searching process, and towards the end, it will explore the search area within which the best solutions of all particles can be found. Therefore, the update of a particle position is determined using an improved formula given as

$$\Delta_p[k] = 2rand_1(pbest - \Phi_p[k]) + 2rand_2(gbest - \Phi_p[k]) + \Omega[k]\Delta_p[k-1] \qquad (1.12)$$

where the third term represents the "momentum" effect comprising the previous position update Δ_p[k-1] and its inertia factor, Ω. Throughout the optimization process, Ω decreases linearly within its optimum range proposed by Shi and Eberhart, i.e. between 1.2 and 0.5 [74].

As can be seen, PSO becomes a desirable choice as it only needs arithmetic operations, and this can shorten the time for model tuning. Nevertheless, since the above-described design parameters were determined through some empirical studies,

the ranges of their values can only be estimated roughly [76, 79]. Therefore, when the optimization method is applied to a PV system, the design parameters still have to be finely tuned according to the specified design requirements.

1.6 Gap in Literature and Thesis Contributions

It has been well recognized that bypass diodes have been used to protect PV modules from thermal destruction under partial shading effects. However, this cannot prevent the significant reduction in power output. To address these issues conclusively, an integrated converter configuration has been proposed by previous researchers for serially connecting multiple PV modules [8, 9]. The work contributed, however, has only focused on the circuit design while the control technique has been largely ignored. The latter is essential in leading all the PV modules to MPP generation and becomes more complicated when there are more PV modules.

Another challenge in getting a PV-integrated converter accepted as a suitable solution to partial shading effect is to minimize the system losses due to the converter while maintaining its high steady-state and transient performances. Thus, Ćuk converters which have low input and output current ripples become an attractive choice. However, researchers working on these converters mainly aimed at designing a feedback controller, which gives high converter performances, but this requires complex control algorithms and additional circuitry. All of these may not be necessary if the converter has an acceptable open-loop response. To achieve this, adequate selection of these parameters is needed, but it can be an intricate task as the transient response may be improved at the expense of the steady-state ripple. In addition all the work contributed has not considered the analysis on the discontinuous-conduction-mode (DCM). This is necessary as it will facilitate the converter design and its operating limits can also be identified.

The control system based on this modelling approach has the potential to lead all the interconnected PV modules to maximum power generation. To achieve this, artificial-intelligence based models are employed for predicting the MPPs of a PV generator under specific weather conditions. This can be done accurately by using the modelling techniques proposed by the researchers in [42, 43], although these are time-consuming to implement, and may require an expensive processor for designing the

model practically. Therefore, a computationally efficient algorithm such as the Particle Swarm Optimization can be applied for PV modelling. By incorporating the structure optimization scheme into the training algorithm, a PV model can be made more compact and hence, can potentially be implemented in a single-chip digital-signal-processor (DSP)-based microcontroller. This also helps to reduce the hardware size and the cost for a PV energy system.

Therefore to narrow the gap in the literature, this thesis has the following contributions:

- Developing a co-ordinated control scheme for the PV-integrated converter configuration which leads to maximum power generation;
- Developing an optimal design scheme for selecting the components of a step-down and step-up Ćuk converters;
- Developing an artificial intelligence based PV model which is accurate, compact, and can be generated using minimal computation effort.

1.7 Aim and Objectives

The aim of this research is to develop a converter system which is capable of maximising PV power output under any partial shading conditions. To achieve this successfully, high-performance converters with robust MPP control algorithms are employed. Therefore, the work in this thesis is based on three main objectives. They are

- To analyse and develop an effective control scheme for a PV-converter integrated configuration that can maximise energy extraction from PV panels under varying weather conditions.
- To investigate, design and apply the cost-efficient DC-DC converters to the PV system. The desirable converters are those that can maintain stable system dynamics and a high steady-state performance.
- To study and derive accurately an optimum PV model which is used for the system design and control. It is required to employ a computationally efficient technique to generate the model.

1.7.1 Scope of Thesis

The scope of this research covers a review of existing research, the novel control technique for the PV-integrated converter, the novel scheme for selecting the converter components, the new modelling technique for PV and the experiments carried out to demonstrate the validity of the proposed schemes. All these are detailed in the chapters as follows:

Chapter 2:

The existing knowledge of PV characteristics which leads to the issue of partial shading is reviewed in detail in this chapter. A complete equivalent circuit model for a PV cell under any illumination conditions is introduced and the effect due to partial shading is thoroughly described. A preliminary simulation study has demonstrated that the bypass diodes incorporated into PV energy systems fail to conclusively solve the issue of reduced output power resulting from the partial shading effects.

Chapter 3:

This chapter presents a detailed analysis of a step-down Ćuk converter leading to four transfer functions of the converter in two different operating modes, namely, variable input – constant output voltages suitable for controlling a solar photovoltaic (PV) power generation system; and variable output – constant input voltage applicable to a variable speed motor drive. A novel converter design procedure, which is based on the optimal performances in both transient and steady-states, is also described in this chapter. This method has been verified through simulation and the results obtained are discussed in detail.

Chapter 4:

In this chapter, a similar analysis as that performed in Chapter 3 is extended to the Ćuk step-up converter operating in continuous-conduction-mode. A further set of generalized transfer function models are developed to describe the variations in input voltage due to both the small perturbation of output voltage, and duty cycle. Based on these models, a negative-feedback control system can be implemented by employing Nyquist stability criterion and the Bode plots. The design is simulated in

MATLAB-SIMULINK and the advantages of the control system are demonstrated through its robustness to varying operating conditions.

Chapter 5:

An in-depth analysis is presented on the operating principles of the integrated photovoltaic module and DC-DC converter configuration for obtaining maximum power generation under non-uniform solar illumination conditions. A novel coordinated control scheme, using the above proposed model-based MPP prediction, is developed to adjust the duty ratios of all converters according to changing weather conditions. A complete simulation system having three photovoltaic modules has been developed to validate the proposed scheme. The design methods for all these and the simulation results are discussed in detail in this chapter. The application of the Perturbation and Observation (P&O) algorithm to the MPP control for the integrated converters has also been investigated.

Chapter 6:

This chapter presents a modelling technique using the concept of Particle-Swarm-Optimization (PSO), plus a Neuro-Fuzzy network technique for representing the electrical characteristics of a PV generator. The developed PV model is compact, interpretable and can be used to accurately predict the MPPs of a PV module in real time. The newly developed set of procedures for generating the model is fully described in this chapter. This technique has been successfully applied through the re-construction of the current-voltage of a practical PV module.

Chapter 7:

This chapter firstly validates experimentally the proposed design scheme in Chapter 3 through both the development of practical Ćuk step-down and Ćuk step-up converters. These converters have also been used successfully to regulate the voltage across a 20-Watt PV generator according to its desired operating points. This has been achieved using the proposed PV model which has been implemented on a fast but cost-effective dsPIC-based microcontroller.

Chapter 8:

This chapter concludes the research with a summary of the achievements and contributions of this thesis, and a presentation of recommendations for future work.

Chapter 2
Modelling of PV Cells under Partial Shading Conditions

2.1 Introduction

A solar PV cell is a power supply with a strongly non-linear current – voltage (I-V) relationship that is highly dependent on the cell temperature and the incident solar irradiance. One well-applied technique for describing the I-V characteristics with respect to weather conditions is to represent the physics of the PV cell using an equivalent circuit model [80 – 83]. Various proposed models have been used for many simulation studies, though mainly assuming uniform solar illumination [20, 68, 69]. When a group of cells is not illuminated uniformly, a more complete model is required which includes the reverse-bias characteristics [5, 86, 87, 72]. The improved model can also be used to analyze and develop optimum control strategies for the complete system.

In this chapter, descriptions of PV cells in both forward-biased and reverse-biased operations are presented. The effects of non-uniform shading are then explained, based on the complete equivalent circuit model. A PV simulation program developed for this research is also described. Finally, using the derived I-V characteristics for a PV cell, the benefits and drawbacks of protection diodes for the performance are explored.

2.2 Fundamentals of PV Energy Conversion

2.2.1 Operation Principle of a PV Cell

A crystalline silicon PV cell is mainly fabricated by doping one side of a silicon crystal ingot with donor atoms and the other with acceptor atoms [81], producing layers known respectively as the n-layer and the p-layer. This process firstly causes majority electrons to diffuse from the n-layer and recombine with the majority holes in the p-layer. This leaves behind strips of immobile ions within the depletion region, forming the p-n junction. The resulting electric field then attracts minority electrons from the adjoining region of p-layer to drift towards the junction

and recombination also occurs around the adjoining region of n-layer. A thermal equilibrium state is only achieved when the total number of charge carriers engaging in diffusion is equal to that for the drift process. This is illustrated in Figure 2.1 which shows the formation of the p-n junction and its corresponding energy band diagram for a non-illuminated PV cell.

When solar rays are incident on the cell, some of the photons are absorbed by the semiconductor while others may penetrate through the material or reflect from the surface. If the absorbed photon has energy greater than that of the band-gap, the electrons are excited into the conduction band leaving behind holes in the valence band. This occurs both in the n-side and p-side of the depletion region, as illustrated in Figure 2.2.

Through the drift process, the generated electrons in the p-side of the depletion region momentarily move across the junction and recombine with the generated holes in the n-side. Likewise through diffusion, some of the generated electrons in the n-side of the depletion region cross into the p-n junction while others flow to the load before recombining with the generated holes in the p-side. The charge carriers flowing through the load also produce a forward-bias across the junction.

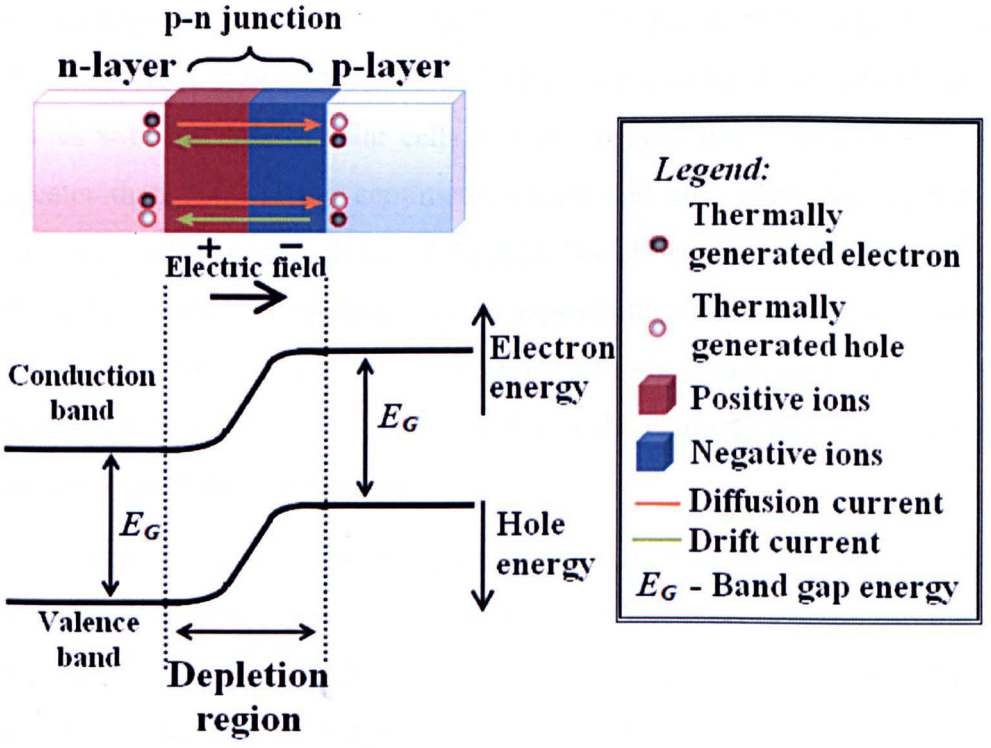

Figure 2.1 Formation of p-n junction and its energy band diagram for a non-illuminated PV cell

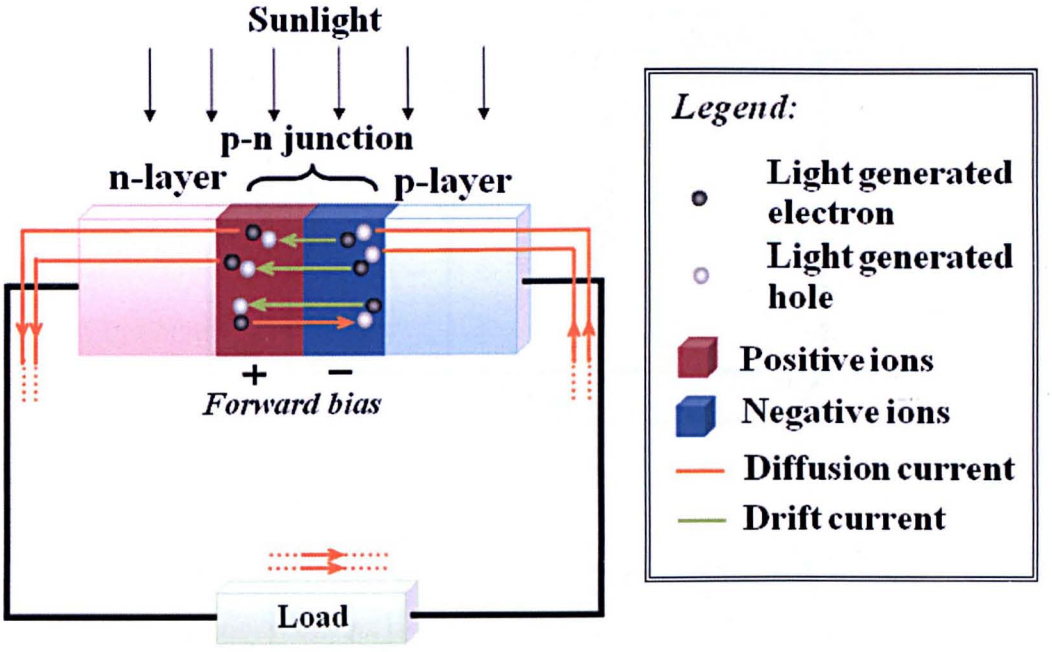

Figure 2.2 Generation of electron-hole pairs when a PV cell is illuminated and their flow through the load

During the energy conversion process, internal losses occur which can be mainly represented as series and shunt ohmic resistances R_s and R_{sh}. They respectively characterise the bulk resistance of the semiconductor material and the leakage current flowing through the lattice defects in the depletion region [81]. To obtain high conversion efficiency, low R_s is highly desirable and in a conventional PV module, it is usually less than 5 Ω per centimetre square of cell area [81]. R_{sh} varies with the type of solar cells. For monocrystalline silicon cells, it has a value greater than 1000 Ω per centimetre square cell area while for the polycrystalline type, this value is as small as 100 Ω [81]. The above described characteristics for the PV cell can then be modelled by an equivalent circuit model as shown in Figure 2.3(a). The current source, I_{ph}, represents the light generated current. I_D, the current flowing through the diode, D_{ph}, collectively characterizes the overall diffusion process across the p-n junction.

A more accurate two-diode model has also been developed [81], as shown in Figure 2.3(b). This model considers the recombinations occurring in the n-type and p-type layers beyond the depletion region. These are characterized by the diode, D_{P1}, through which diode current I_{d1} is flowing. On the other hand, D_{P2} represents the recombination process involving the light-excited holes and electrons within the depletion region. Since both recombinations can be dominant for a real solar cell,

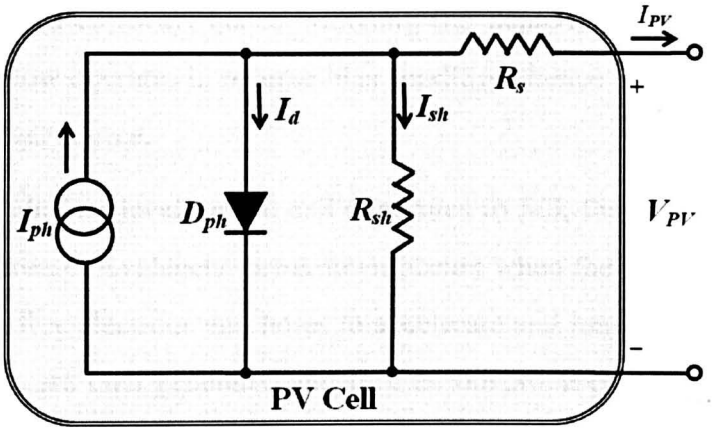

(a) Single-diode model

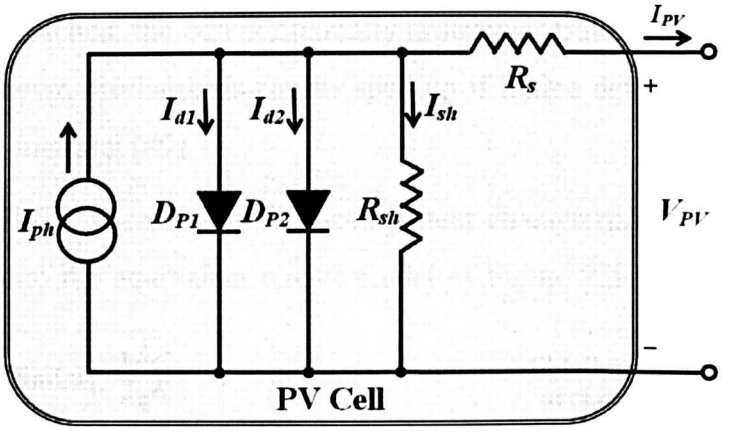

(b) Two-diode model

Figure 2.3 Equivalent circuit models for a PV cell

this model is more suitable for the analysis of a practical PV generator [81]. However, the disadvantage is having to rely on more parameters and increasing the complexity of the modelling technique. The simulation study in this work, therefore, uses the single-diode model shown in Figure 2.3(a).

2.2.2 PV Cell Under Non-Uniform Illumination

No PV cells have identical I-V characteristics even though they may be manufactured through the same process. Characteristic mismatching is also caused by operating under non-uniform illumination conditions and/or temperatures. The latter is considered in this work.

An electrical mismatch occurs when a PV cell is connected in series to another which is illuminated with a different level of solar irradiation, as shown in Figure 2.4. Under this condition, a surplus of charge carriers is generated in the cell experiencing the higher level of irradiation. This causes the majority carriers in the

other cell to be pulled away, hence widening the depletion region. The cell with lower radiation now operates in reverse-bias condition, hence acts as an internal load rather than a power source.

As the irradiation level on the cell continues to fall, the internal electric field strength will increase. Avalanche breakdown occurs when the electric field is strong enough to cause free electrons and holes to accelerate and ionize other lattice atoms. New free carriers are then generated and further ionization continues to occur. This process effectively raises the cell temperature more rapidly compared to the dissipation of heat to the surroundings [89]. When the cell maximum operating temperature is reached, the cell is thermally destroyed. Both of these avalanche and thermal breakdown mechanisms can be sped up if lattice defects are present in the semiconductor material [89].

To model this phenomenon, the component characterising the reverse current is introduced into the equivalent circuit model of Figure 2.3 [5, 7, 90]. One earlier

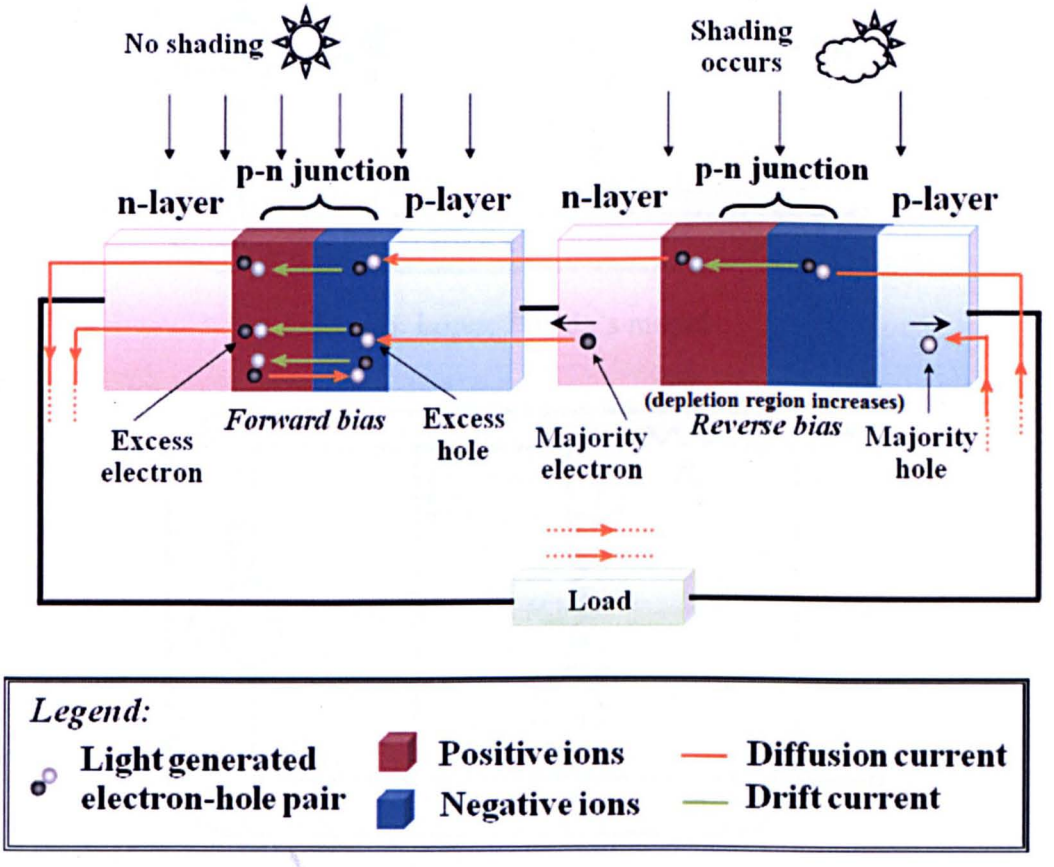

Figure 2.4 Generation of electron-hole pairs when two PV cells are non-uniformly illuminated and their flow through the load

version includes a current source, M_{ph}, in the branch between the diode D_{ph} and shunt resistor R_{sh}, and is expressed as $M_{ph} = K_{ph}(I_{ph} - I_d)$ with $0 < K_{ph} \leq 1$ as shown in Figure 2.5(a) [88]. In a later work, the model has been reconfigured as shown in Figure 2.5(b) [91]. Instead of using an additional current source as above, a voltage source, E_{PV}, is incorporated in the shunt resistance R_{sh} branch. This model recognizes that the avalanche breakdown due to partial shading has an effect on the leakage current and has been used widely for simulation studies [91]. There are other numerical methods to model the reverse characteristics of a PV cell but it can be tedious and can only be simplified when the empirical data measurements about the cell characteristics are available [91, 92].

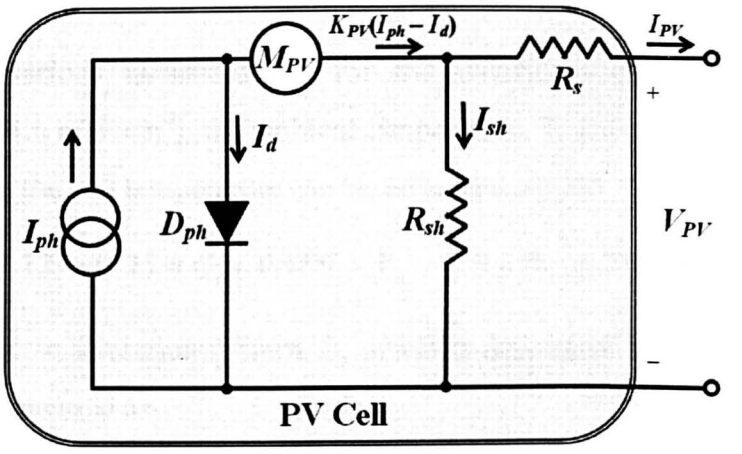

(a) Lopez-Pineda's model

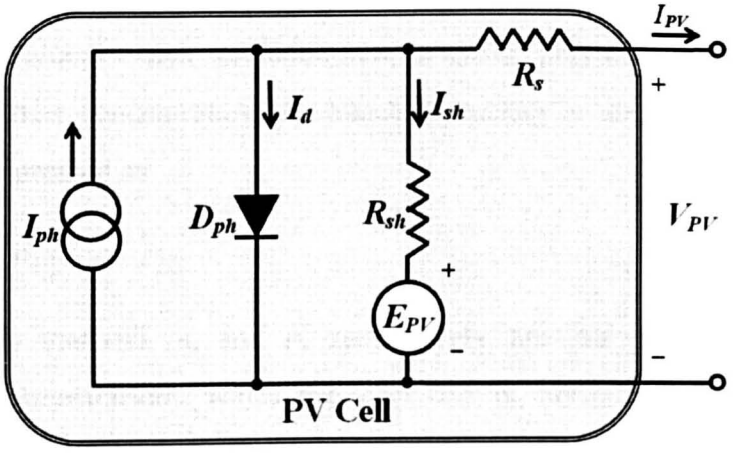

(b) Bishop's model

Figure 2.5 PV model incorporated with cell reverse-bias characteristics

2.2.3 Equations for Parameters in the Equivalent Circuit Model

Using the complete PV model as shown in Figure 2.5(b), the expression representing the output current from a PV cell is written as

$$I_{PV} = I_{ph} - I_d - I_{sh} \tag{2.1}$$

The diode current I_d is characterized by the equation given by [38]

$$I_d = I_o\left(\exp\left[\frac{q(V_{PV} + I_{PV} R_s)}{AK_t T_c}\right] - 1\right) \tag{2.2}$$

where V_{PV} is the voltage across PV output, q is the electronic charge, T_c is the solar cell temperature in Kelvin, K_t is the Boltzmann constant and the term A defines the cell deviation from the ideal p-n characteristics [38]. For a real crystalline silicon solar cell, it has a value between 1.5 and 2 [83].

Using various measurements for the weather conditions including solar insolation, G (in mW/cm^2), the ambient temperature, T_a (in °C), and the wind speed, W_s (in m/sec), the cell temperature can be estimated as [84]

$$T_c = 3.12 + 0.25 \times G + 0.899 \times T_a - 1.3 \times W_s + 273 \tag{2.3}$$

The reverse saturation current, I_o, which is dependent linearly on the solar cell area can be expressed as

$$I_o = J_o \times Cell\ \ Area \tag{2.4}$$

where the reverse saturation current density is J_o. At a particular cell temperature, it has a specific value for each semiconductor material. This is determined by its level of intrinsic carrier concentration, n_i, which according to the Law of Mass Action [93], can be expressed as

$$n_o p_o = n_i^2 \tag{2.5}$$

In n-type material, n_o and p_o respectively are the majority and minority equilibrium concentrations while the opposite is defined for p-type material. Therefore with a higher level of intrinsic carrier concentration, the probability for the recombination of electrons with the holes increases, causing a rise in J_o [93]. This reduces the power delivered from the PV cell to the load.

Furthermore, the value of I_o for a specific cell area will still vary with the cell temperature and this can be evaluated using the formula given as [38]

$$I_o = I_{or}\left(\frac{T_c}{T_r}\right)^3 \exp\left(\frac{qE_G}{AK_t}\left[\frac{1}{T_r} - \frac{1}{T_c}\right]\right) \tag{2.6}$$

where I_{or} is the reverse saturation current measured at reference temperature, T_r, and the energy band gap for silicon, E_G, is set at 1.1 eV. The simulation work in this thesis is based on the solar cell model in [84] and hence, the value for I_{or} = 19.9693 $\times 10^{-6}$ A was taken based on the surface area of the cell at T_r = 301.18 K.

The light generated current I_{ph} is also dependent on the cell area as

$$I_{ph} = J_{ph} \times Cell\ \ Area \tag{2.7}$$

where J_{ph} is the light generated current density. At higher levels of solar insolation and cell temperature, more electron-hole pairs are excited. The variation of I_{ph} with the environmental factors is described by [38]

$$I_{ph} = (I_{scr} + k_i[T_c - T_r])\frac{G}{100} \tag{2.8}$$

where I_{scr} which is set as 2.52 A represents the cell short-circuit current based on the surface area of the cell studied by the researcher in [84] and it was measured at a cell temperature of T_r as well as solar insolation of G = 100 mW/cm^2. Since I_{ph} varies proportionally with the number of light-generated hole-electron pairs and hence solar insolation with a linear coefficient of 100 is included in Equation (2.8). *ki* is the temperature coefficient and has a value of 0.0017 A/K.

As shown in Figure 2.5(b), both R_{sh} and E_{pv} determine the leakage current, I_{sh}, which is written as [5]

$$I_{sh} = \left(\frac{V_{PV} + I_{PV}R_s}{R_{sh}}\right) + \frac{E_{PV}}{R_{sh}} \tag{2.9}$$

and $$E_{PV} = a(V_{PV} + I_{PV}R_s)\left(1 - \frac{V_{PV} + I_{PV}R_s}{V_{BR}}\right)^{-n} \tag{2.10}$$

where a is the fraction of ohmic current involved in the avalanche breakdown [5] and V_{BR} is the cell breakdown voltage. n is the avalanche breakdown exponent

ranging from 3 to 6, depending on the material and the technology used to fabricate the junction [92, 93].

Assuming uniform illumination, a PV module having n_p strings of n_s cells connected in series can be treated as a single-cell generator. Therefore, the lumped parameter modelling technique can be applied and the PV output current is given by [84]

$$I_{PV} = n_p I_{ph} - n_p I_o \left(\exp\left[\frac{qV_{jo}}{AK_t T} \right] - 1 \right) - \left(\frac{V_{jo}}{R_{shT}} \right) \left(1 + a \left[1 - \frac{V_{oj}}{V_{BR}} \right]^{-n} \right) \qquad (2.11)$$

where $V_{jo} = (V_{PV} + I_{PV} R_{sT})$ and the total ohmic resistances now become

$$R_{sT} = \frac{n_s}{n_p} R_s \text{ and } R_{shT} = \frac{n_s}{n_p} R_{sh}. \qquad (2.12)$$

The output power for the PV module can then be calculated as

$$P_{PV} = I_{PV} V_{PV} \qquad (2.13)$$

It should be noted that both the relationship of PV voltage with the current and that of the power with the environmental conditions are non-linear.

2.3 Simulation Studies for a PV Module under Uniform Illumination

2.3.1 Numerical Procedures

Using the described model above, the current-voltage (I-V) characteristics can be derived for a PV module under uniform illumination. This involves numerically solving the implicit function in Equation (2.11) which can be implemented using the generally applied three-stage procedure, as illustrated by the flowchart in Figure 2.6 [42, 83].

1) Parameter Initialization

The constants relating to the ohmic resistances, energy band gaps, cell breakdown voltage, cell short-circuit and saturation currents at the reference

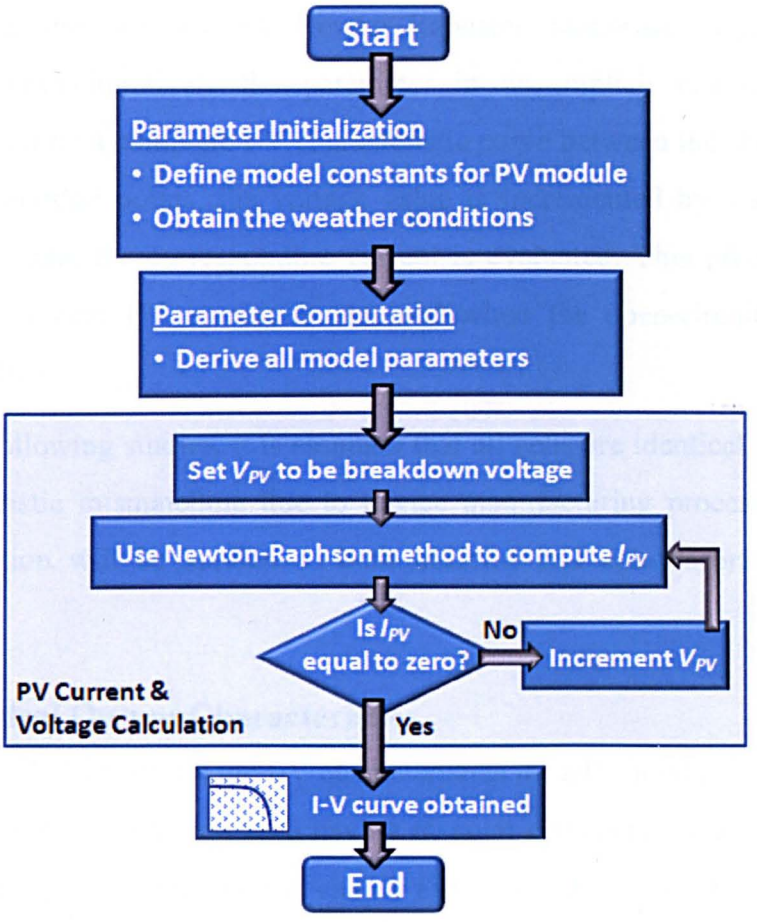

Figure 2.6 Flowchart for constructing I-V curves of a PV panel

temperature are initialised with the values based on the specifications for silicon solar cells used in the literature [5, 38, 42, 81, 84]. In addition, the information about the weather conditions and the number of cells for the module can be provided at this stage.

2) Parameter Computation

The parameters such as the cell temperature, leakage current and light generated current are calculated with respect to the weather conditions using formulae given in the previous subsection. The total ohmic resistances, on the other hand, depend on the solar cell arrangement and have to be obtained from the manufacturer.

3) PV Current and Voltage Calculation

This is needed to obtain the I-V characteristics of a PV generator. To do this, V_{PV} is initially set to any value within the voltage variation range of the panel being modelled, though it is usually set to cell breakdown voltage, V_{BR}. Corresponding to each voltage value the current, I_{PV}, is then computed

using the well-known Newton-Raphson numerical algorithm which estimates iteratively the parameter in an implicit equation [94]. For generating a complete I-V characteristic curve between the short circuit and open-circuit points, the voltage value is incremented by a small amount, ΔV_{PV}, and the corresponding current is evaluated. This process continues until a zero PV current is obtained when the open-circuit condition is reached.

In the following studies, it is assumed that all cells are identical, i.e. any slight cell characteristic mismatching due to device manufacturing process are ignored. This assumption will be applied to both uniform and non-uniform illumination conditions.

2.3.2 Electrical Output Characteristics

Figure 2.7(a) illustrates the I-V characteristics for a PV module, consisting of 4 parallel-connected strings with each having 60 solar cells connected in series, under 3 different array cell temperature values (10, 20, 30°C) and 4 levels of solar insolation (10, 40, 70, 100 mW/cm^2). The corresponding power-voltage (P-V) relationships are shown in Figure 2.7(b). Under uniform illumination, all the generating units are operating in forward-bias condition and hence, the PV characteristics mainly focus on the positive voltage region. The maximum power points (MPPs) which are noted by black dots can be found mainly within the 'knee' region of the I-V characteristics. In addition, it can be observed that the power increases with the insolation level and decreases with the cell temperature. However, the variation in the former is far more significant than that in the latter. Equation (2.3) shows that the cell temperature is closely dependent on the solar insolation level. Hence, a small drop of power due to the rising temperature can be overcome by the higher power increment introduced by the increase in solar irradiation [83].

Figure 2.7(c) shows the variation of voltage for MPPs under different weather conditions in a three-dimensional plot. From the graph, the magnitude of the MPP voltage is directly proportional to the solar insolation while it has an inverse relationship with the cell temperature. This may still require a model which could track the MPPs based on the measured weather conditions. The detail for this will be discussed in Chapter 6.

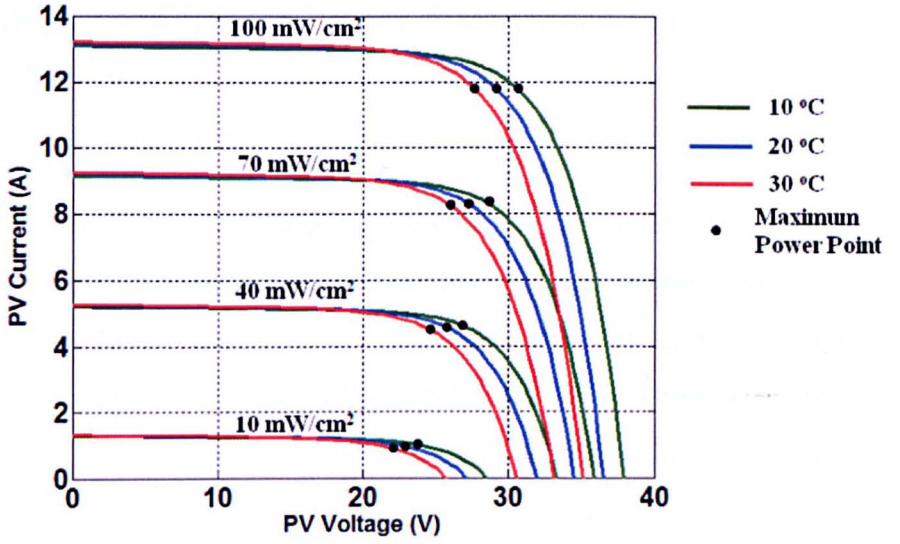

(a) Current-voltage characteristics

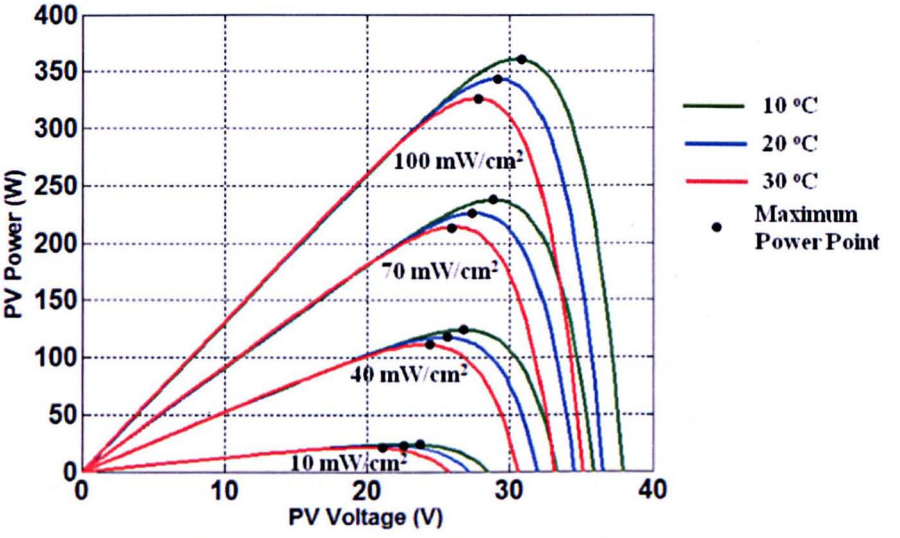

(b) Power-voltage characteristics

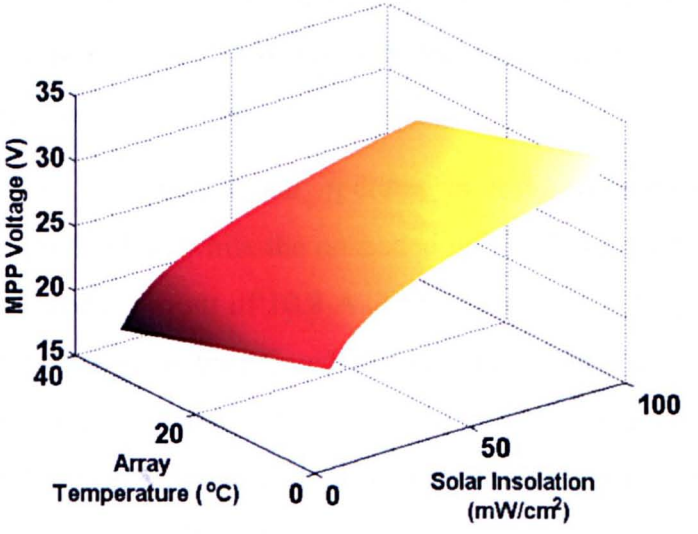

(c) MPP voltage levels

Figure 2.7 Electrical characteristics of a PV module under different weather

2.4 Simulation Studies for PV modules Under Non-Uniform Illumination

2.4.1 Serially-Connected PV Modules

When multiple PV modules are connected in series, the current flowing through all units is equal, while the terminal voltage is the sum of voltages of individual units. In this analysis, an example system as shown in Figure 2.8 is considered. This consists of two PV modules linked in series without using any bypass diodes and R represents an adjustable external load. The modules are irradiated with unequal insolation levels of 100 and 75 mW/cm^2 respectively. Following the process illustrated by the flowchart in Figure 2.9, the overall system characteristics can be obtained first by producing the I-V curves for both modules separately. To calculate the total voltage for a given current value, the individual voltages of the two modules are summed together to obtain the total PV voltage. As depicted by the I-V curves of PV_1 and PV_2 in Figures 2.10(a) and (b), this process starts from the open-circuit condition to the avalanche breakdown region. Figure 2.10(c) shows the resulting I-V characteristics for the whole PV system.

It can be observed that at point A, the voltages across PV_1 and PV_2 are respectively 36 and 34.2 V with a current of 1.9 A flowing through them. Hence, the power from both units can be delivered to R.

At point B, a current of 9.1 A is flowing through both PV modules. As the current increases from this point, the voltage across the shaded module begins to decrease more rapidly than that of the unshaded one. Nevertheless, both modules are still supplying power to the load.

At point C, the shaded cell operates in the reverse-biased region with a terminal voltage of -31 V, while the unshaded unit still generates power at a voltage of around 30 V and a current of 10.8 A. The total output voltage is nearly zero and hence no output power is transferred to the load R because the shaded PV_2 now becomes a load to PV_1. This leads to localized hot-spot heating which can damage cell encapsulation materials and permanently reduce the system power output [89]. It is also important to note that PV system only operates at point C if the controller allows to have zero voltage to be applied across both the PV modules.

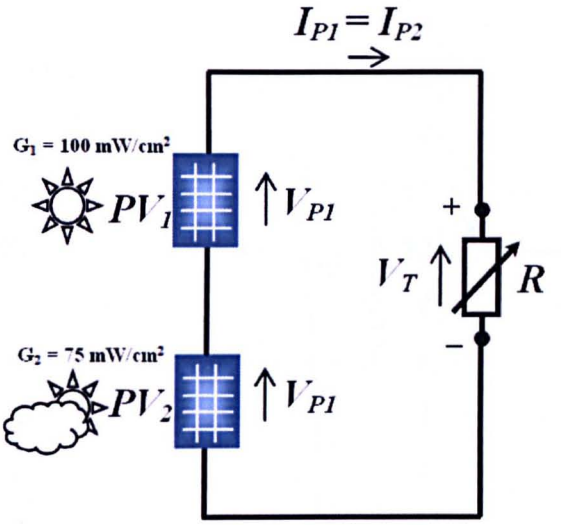

Figure 2.8 Unprotected PV system having two serially linked modules under non-uniform illumination

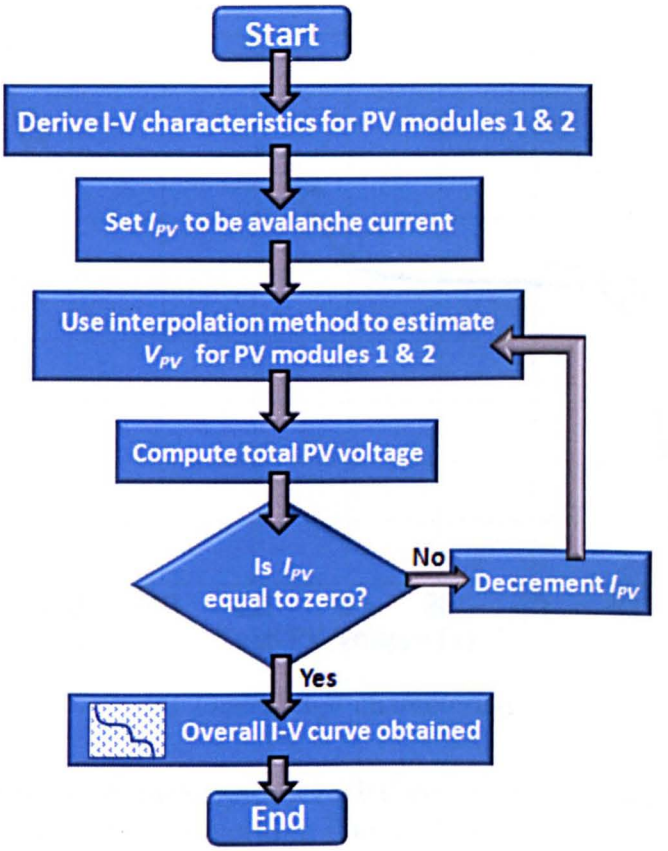

Figure 2.9 Flowchart for construction of current-voltage characteristics for a PV system consisting of two serially linked modules under non-uniform illumination

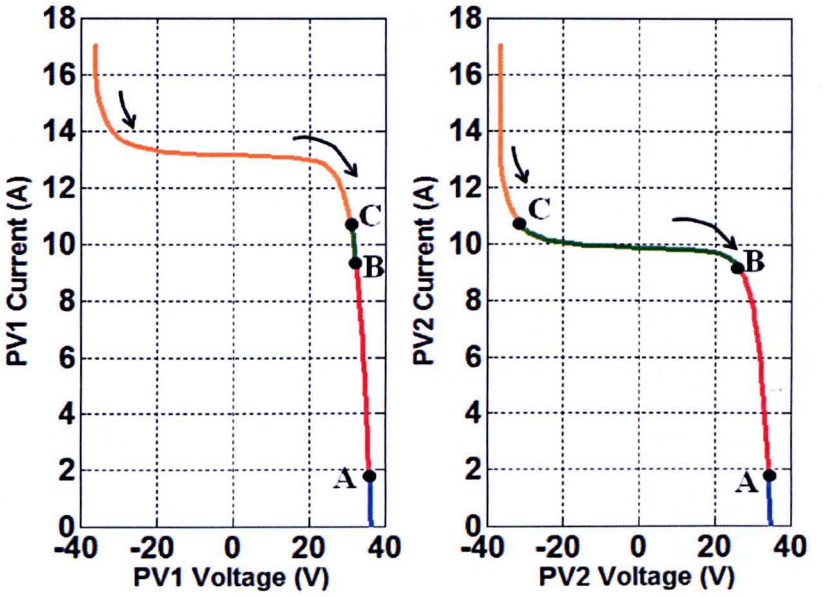

(a) I-V characteristics for PV_1 (b) I-V characteristics for PV_2

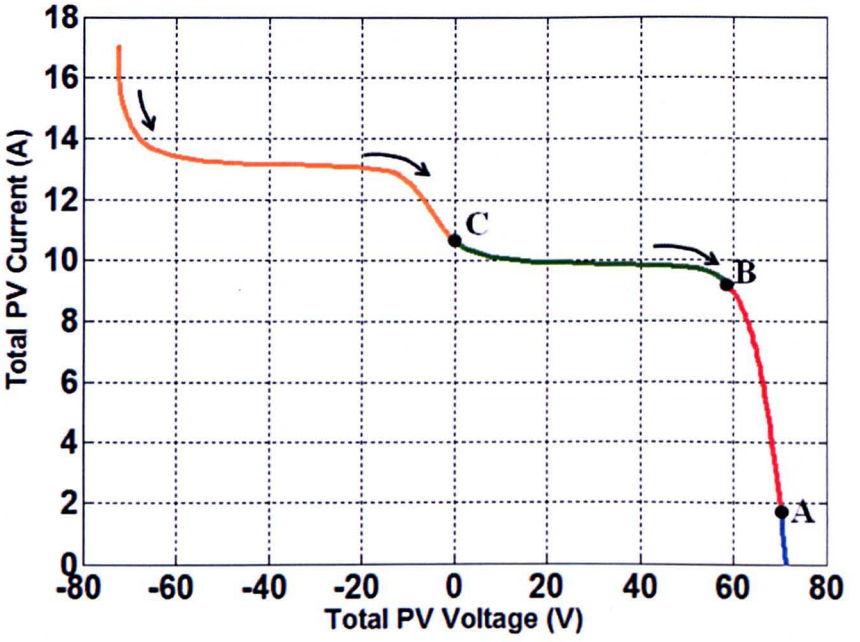

(c) Overall I-V characteristics

Figure 2.10 Electrical characteristics for a PV system consisting of two serially-linked modules under non-uniform illumination

2.4.2 Parallel-Connected PV Modules

A PV system having two modules connected in parallel is shown in Figure 2.11 and they are illuminated respectively with solar insolations of 100 and 75 mW/cm^2. Simulation of this system is similar to that for the above series chain of modules except that at a given PV voltage value, the total output current is computed by summing together the individual PV currents. Figures 2.12(a) – 2.12(c) illustrate the I-V characteristics for individual PV modules and that of the overall system.

As can be observed in Figure 2.12(c), at point X, the total output current of the PV system to the load is nearly zero. This is because the power generated by the unshaded module PV_1, is consumed by the shaded PV_2, and hence beomes a load to the former. Similar to the previous case in the serial connection, linking PV modules in parallel may also cause cell thermal destruction under partial shading conditions. Some protection schemes have been applied to most conventional PV modules and these are discussed in the next section.

2.5 Simulation Studies for PV Modules Protected by Diodes

A PV module can be protected by using both bypass and blocking diodes as discussed below.

2.5.1 Bypass Diode

Ideally, a bypass diode is connected across each PV cell so that it can be protected from being destroyed thermally. However, such a scheme requires additional space to house the diodes for a PV module which may consist of a number of cells to build up the desired terminal voltage level [95]. A compromise, instead, is

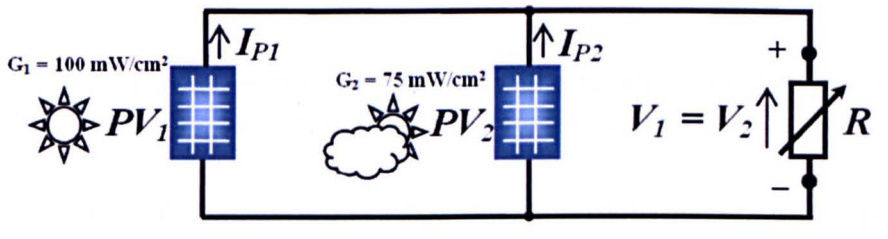

Figure 2.11 Unprotected PV system having two parallel-connected modules under non-uniform illumination

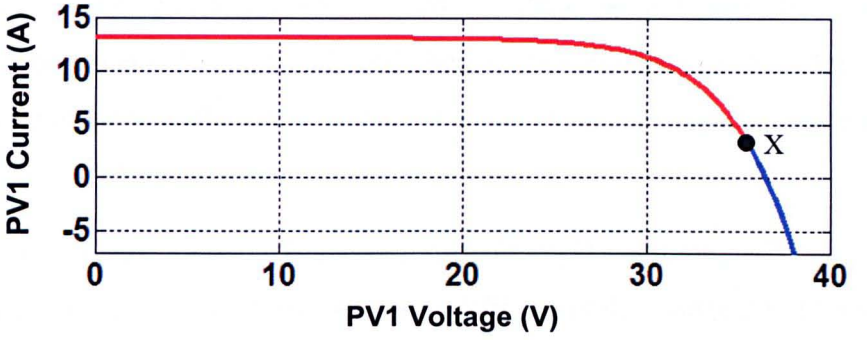

(a) I-V characteristics for PV_1

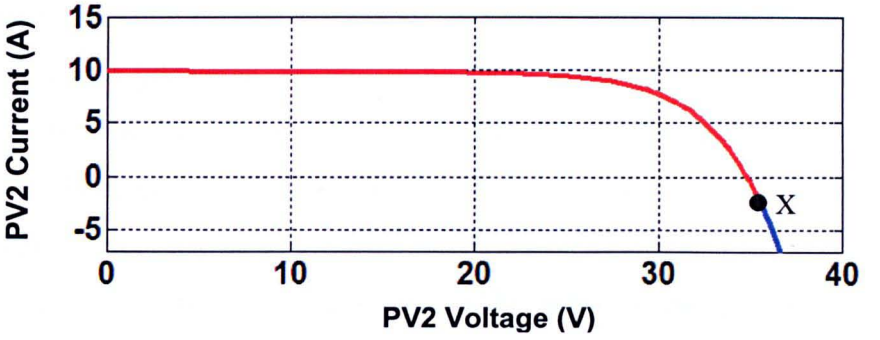

(c) I-V characteristics for PV_2

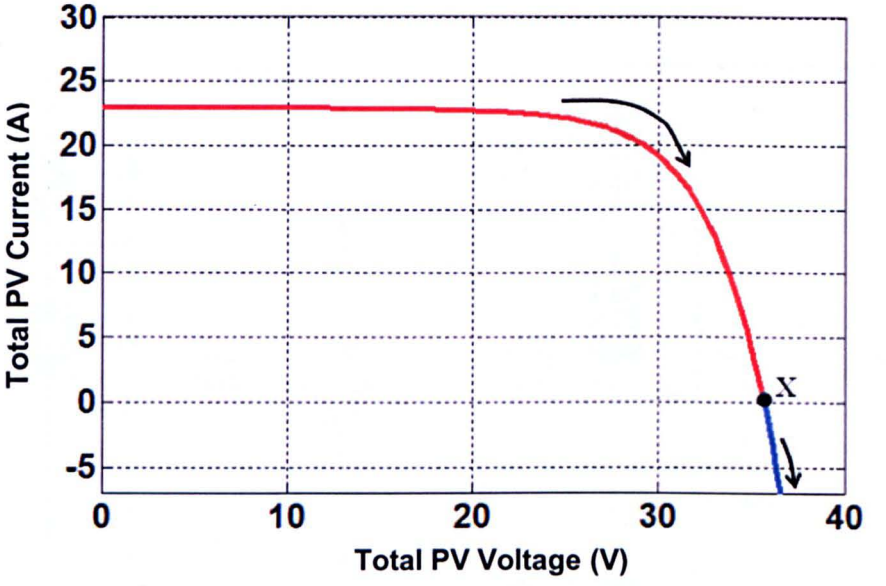

(d) Overall I-V characteristics

Figure 2.12 Electrical characteristics for a PV system consisting two parallel-connected modules under non-uniform illumination

made between the protection scheme and its costs by having one bypass diode for a string of cells connected in series. The number of cells in one string depends on the maximum reverse-bias voltage a cell can withstand before significant damage is caused. The maximum reverse voltage for a polycrystalline silicon cell, for instance, is approximately 13-volt and the maximum number of cells per diode is between 18

and 24 [5, 6, 12]. The rationale for such a connection is based on the worst case scenario when one cell is shaded, and the power generated by the other unshaded cells does not exceed the defined limit for the maximum power dissipated in the shaded cell.

The advantages of using bypass diodes are explained using a PV system shown in Figure 2.13(a). This considers a string of PV modules connected in series where one bypass diode is connected in parallel with opposite polarity to each module. When partial shading occurs, the bypass diode provides a parallel path for a part of the total current generated by the unshaded modules to flow through, hence the current through the shaded module can be as low as that determined by the light intensity. This diversion of current flow is as depicted in Figure 2.13(b). In practice, a silicon diode can only be forward-biased at a voltage above 0.5 – 0.7 volt [96] and hence, a negligibly small reverse voltage will appear across the shaded unit while cell thermal breakdowns can be significantly reduced.

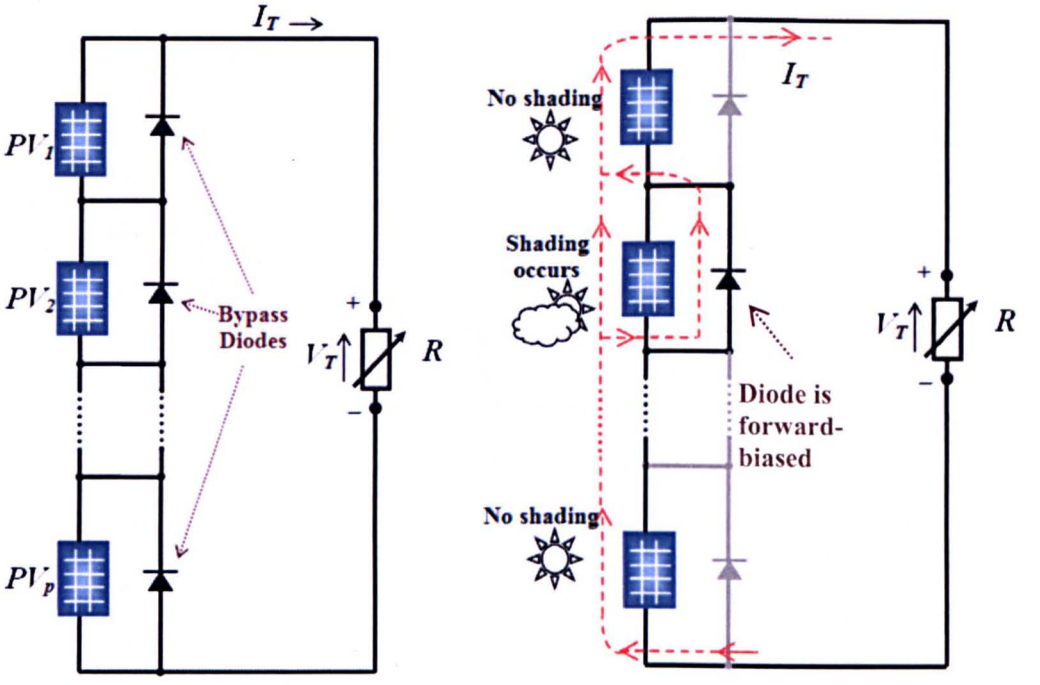

(a) Bypass diode for each PV module

(b) Flow of current when one module is shaded

Figure 2.13 PV system integrated with bypass diodes

The effect on the power performance for the system above can be complicated as there are many different shading patterns. The analysis given below is for the simplest case of a PV system having only two modules connected in series as described in Section 2.4.1, but with bypass diodes connected across each. The I-V and P-V characteristics for the two modules are respectively illustrated in Figures 2.14 and 2.15.

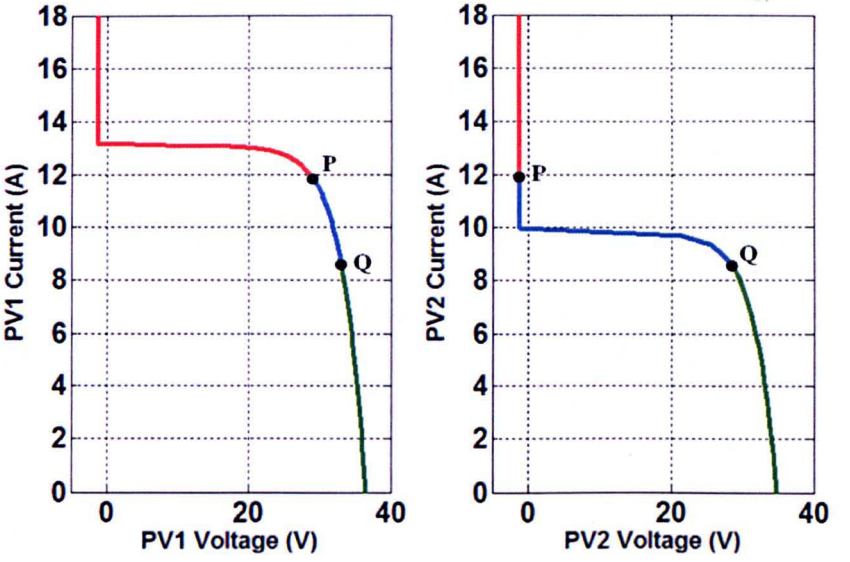

(a) I-V characteristics for PV_1 (a) I-V characteristics for PV_2

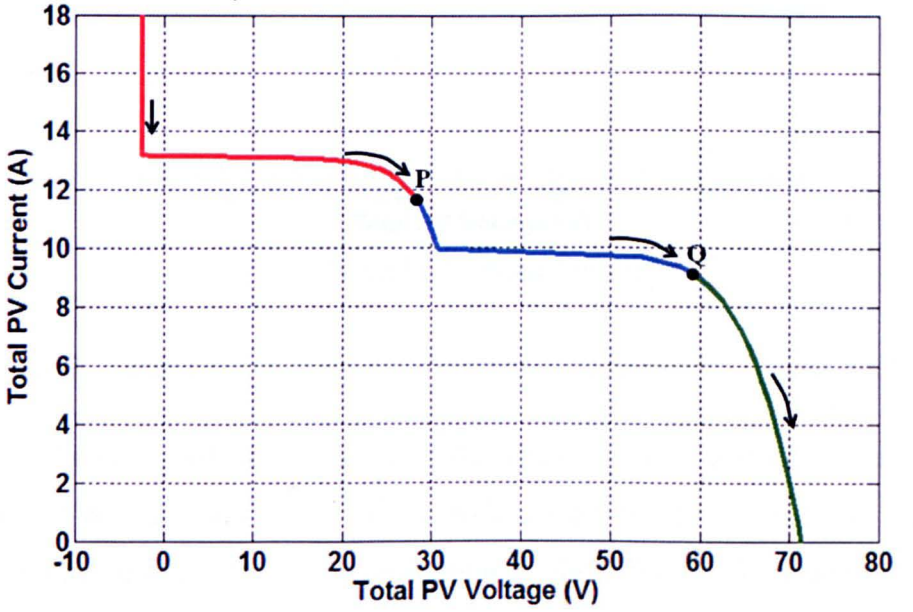

(c) Overall I-V characteristics

Figure 2.14 I-V characteristics for a PV system integrated with bypass diodes

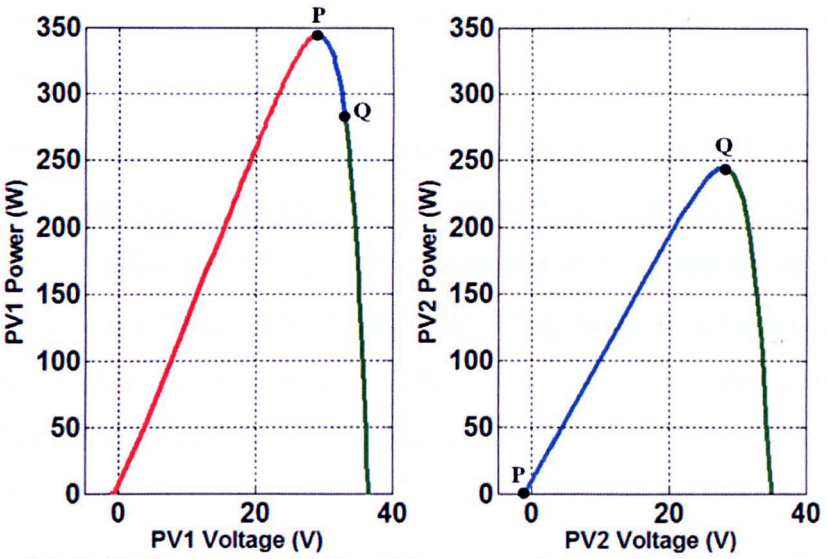

(b) P-V characteristics for PV_1

(b) P-V characteristics for PV_2

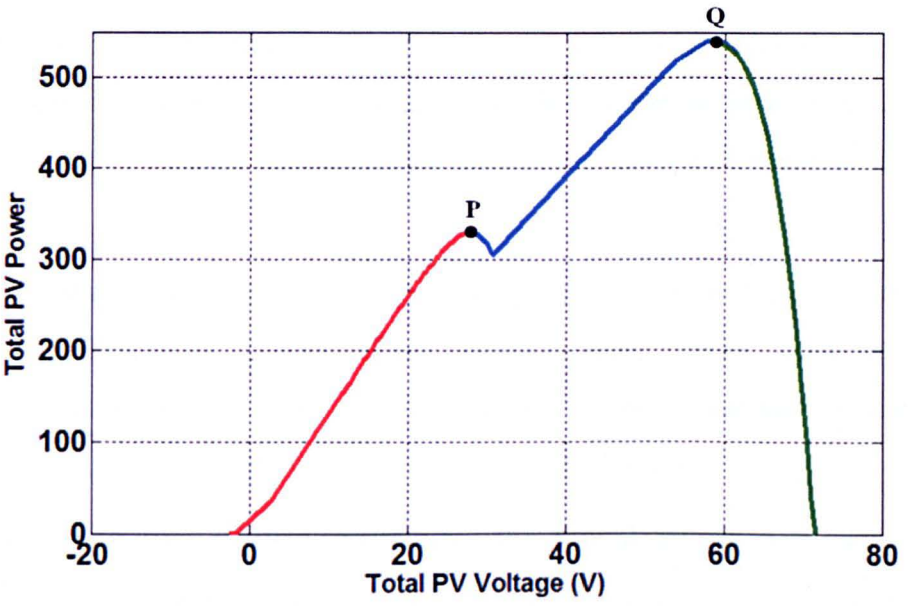

(c) Overall I-V characteristics

Figure 2.15 P-V characteristics for a PV system integrated with bypass diodes

It can be observed that at point P, the unshaded unit generates a maximum power of 348 W at 29.84 V. The bypass diode across the shaded unit now becomes forward-biased, limiting its power dissipation to about 9.6 W. Therefore, 97.2% of the maximum power from the unshaded unit can still be transferred to the load while the shaded unit is protected by the activated bypass diode.

At point Q, the voltages across the unshaded and shaded units respectively are 31.2 and 28.4 V. All bypass diodes are de-activated and hence both units are

generating a total power of 523 W which is higher than that at point P. Nevertheless, this may not be always the case when the shaded unit is illuminated with different insolation levels.

Figures 2.16(a), (b) and (c) respectively show the individual power-voltage characteristics and that of the overall for a two-PV module system protected by the bypass diodes. In this analysis, PV_1 is illuminated with a constant light level while PV_2 with 5 different levels. For all cases, the PV generators are under constant cell temperature. Figures 2.16(c) shows that there exists two power peaks located within Regions LO and HI which are in the ranges 22 – 30 V and 52 – 68 V respectively. The higher power peak is the global peak which represents the total maximum power that can be extracted from the PV generators equipped with bypass diodes. It can be observed that when the insolation level on the shaded unit is lower than 50 mW/cm^2, the peak power points are located within Region LO under which the bypass diode of the shaded unit becomes forward-biased. When the reverse occurs, the peak power points are located within Region HI under which all bypass diodes are de-activated.

By assuming the two PV modules separately supply energy to two different loads, the individual power-voltage characteristics under different shading conditions are similar to those shown in Figure 2.16(a). The sum of their power peaks represents the total power extractable from both units.

Under the five shading conditions, the global power peak and the total available peak power that can be extracted from both units with their corresponding PV voltage values are listed in Table 2.1. The value of global peak power is always lower than that of the corresponding extractable peak power. One can observe that the voltage level for the global peak depends on the shading severity of PV_2.

A factor is defined to represent the seriousness of unequal illumination between two identical PV modules as

$$\alpha = \frac{\text{Insolation level of the shaded PV}}{\text{Insolation level of the unshaded PV}} = \frac{G_{shaded}}{G_{unshaded}} \tag{2.14}$$

A full blackout on the shaded module corresponds to $\alpha = 0$ while $\alpha = 1$ indicates homogeneous illumination between the two modules. The power loss for a complete range of uneven lighting conditions can be illustrated in Figure 2.17.

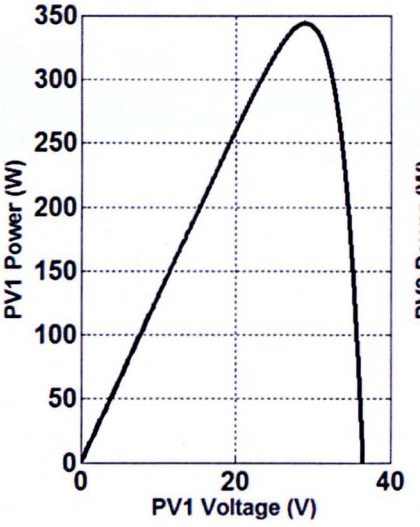

(b) P-V characteristics for PV_1

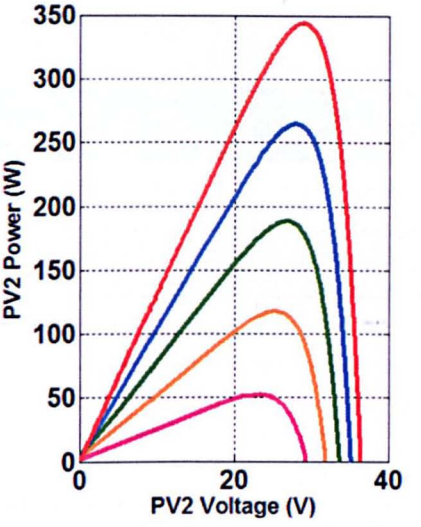

(c) P-V characteristics for PV_2

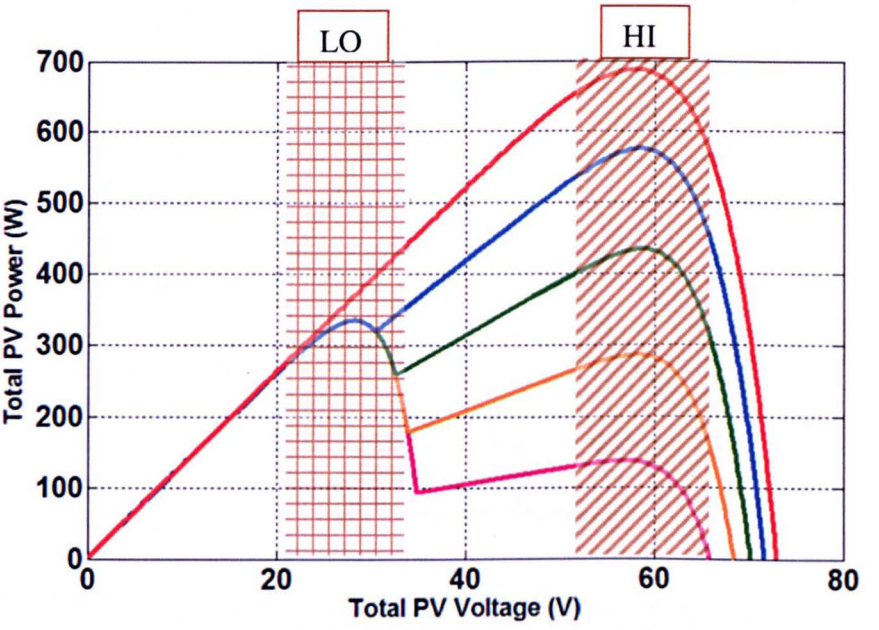

(a) Overall P-V characteristics

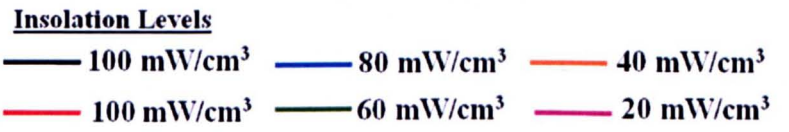

Figure 2.16 P-V characteristics under different shading conditions for a PV system integrated with bypass diodes

Table 2.1 Power variation for PV system integrated with bypass diodes under different shading conditions but constant cell temperature

Insolation (mW/cm^3)	PV_1 (unshaded)	100				
	PV_2 (shaded)	20	40	60	80	100
Shading level, α		0.2	0.4	0.6	0.8	1.0
Cell Temperature (°C)		20				
Global Peak Power (W)		355.9	355.9	441.8	579.7	687.2
Voltage at Global Peak (V)		29.86	29.86	58.52	57.68	54.64
Extractable Peak Power (W)		396.01	461.3	532.2	607.7	687.2

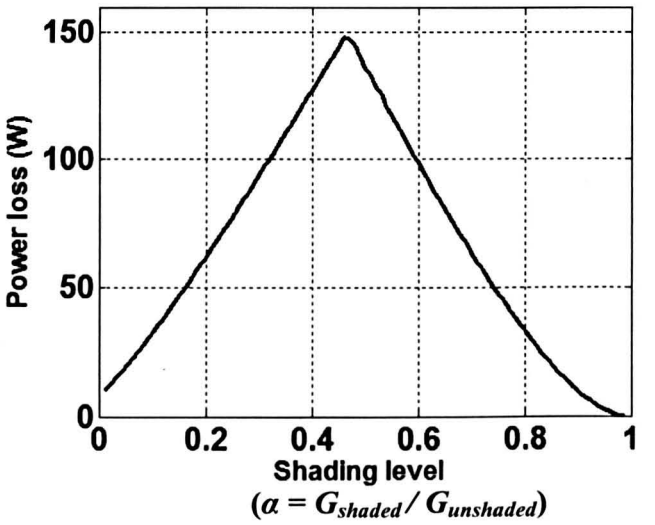

Figure 2.17 Effect of shading level on the power loss for bypass diode scheme

When α = 0, the shaded unit does not generate any power. Its bypass diode is activated under the global peak power operating point, causing a small voltage drop across the shaded unit. Hence, there is still a power loss which is as low as 10.27 W comparing to the available power that can be extracted from both units when they operate alone.

When α is between 0 and 0.48, the global peaks are within the low voltage range of LO and under these operating points, the bypass diode of the shaded unit is activated. This prevents the shaded unit from generating power regardless of the fact that as α increases, its illumination level rises and more power could in principle be extracted from it. Hence the power loss increases with α within this range and when

α is close to 0.48, there is as much as 148 W of power loss. Nevertheless within this α range, the global peak power level is almost equal to the maximum power level of the unshaded unit.

When α is between 0.48 and 1, the global peaks are within the high voltage range of HI and all bypass diodes are de-activated. However under these operation conditions, the current flowing through both modules is limited by the degree of shading, inhibiting maximum power generation by the unshaded unit. Hence, the maximum power level for the output is only equal to the sum of peak power of the shaded unit and that of the limited operating point for the unshaded unit. Nevertheless as α increases towards unity, higher current can flow and more power can be extracted from both modules while the power loss becomes less severe.

When $\alpha = 1$, all bypass diodes are still de-activated and both PV modules can operate at their MPP points allowing all extractable power of 687.2 W to be supplied to the load. Therefore there is no power loss under this condition.

With a total number of 120 cells, the above analysis effectively assumes that half of them are illuminated with a lower solar insolation than the other half. Figure 2.18 shows the variation in power loss for different proportions of shaded cells ranging from 5 to 90 cells using a 3-D plot in Figure 2.18(a) and its corresponding plane view in Figure 2.18(b). Within the complete range of the shading proportions, the maximum power losses vary between 35.7 and 148.9 W. These occur at the shading levels ranging from $\alpha = 0.15$ to $\alpha = 0.8$. In particular when the number of shaded cells is low, the peak points for the power loss occur within the higher end of shading range (i.e. $\alpha > 0.5$). The reverse occurs when there are more cells being shaded.

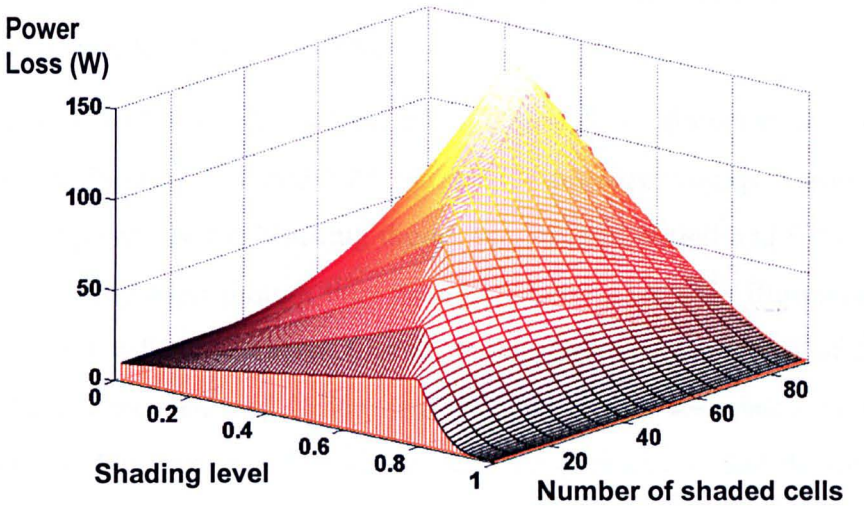

(b) 3-D plot

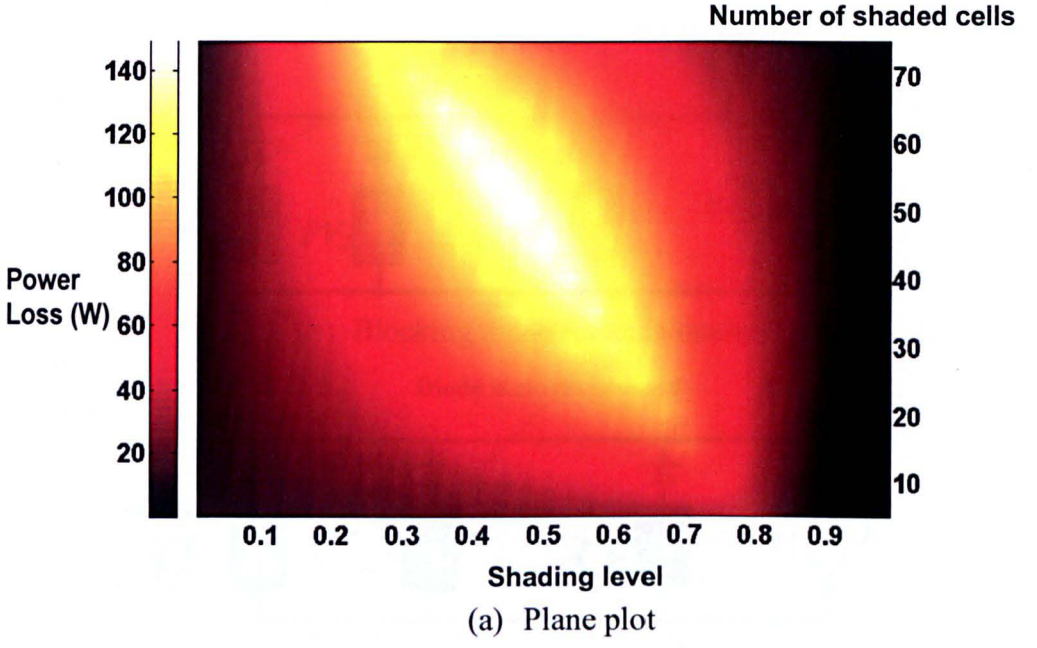

(a) Plane plot

Shading level = $G_{shaded} / G_{unshaded}$

Figure 2.18 Effect of shading level and shading area on the power loss for bypass diode scheme

2.5.2 Blocking Diode

A blocking diode, on the other hand, is connected in series with each PV module as shown in Figure 2.19(a). When there is no partial shading, the diode is forward-biased allowing the current from the corresponding PV module to flow to the output. When the light levels are different, the operating voltage of unshaded

modules may surpass the open-circuit voltages of the shaded ones. The blocking diode for the latter becomes reverse-biased preventing external current flowing into its branch, as shown in Figure 2.19(b).

For a two-PV-module system, the I-V and P-V characteristics are shown respectively in Figures 2.20 and 2.21. As the PV terminal voltage varies from 0 to 35.5 V (i.e. at point M), the blocking diodes are forward-biased and PV modules are operating normally even though they may be inhomogeneously illuminated. When the PV terminal voltage increases further, the open-circuited voltage of the shaded unit has been exceeded and hence, the blocking diode associated to it will be reverse- biased. No current is flowing out from the shaded unit and the power to the load now is only supplied by the other unshaded unit.

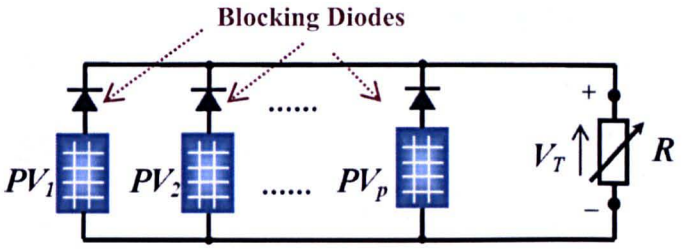

(b) Blocking diode for each module

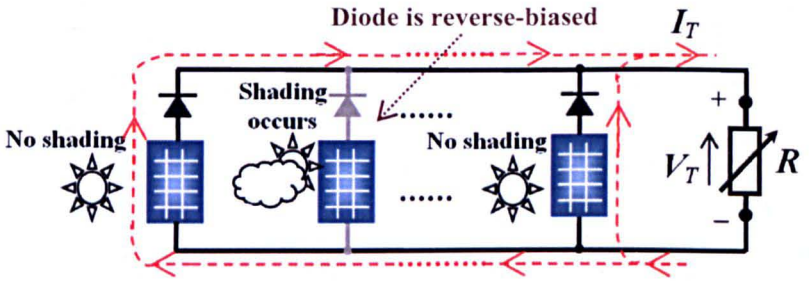

(a) Flow of current when one module is being shaded

Figure 2.19 PV system integrated with blocking diodes

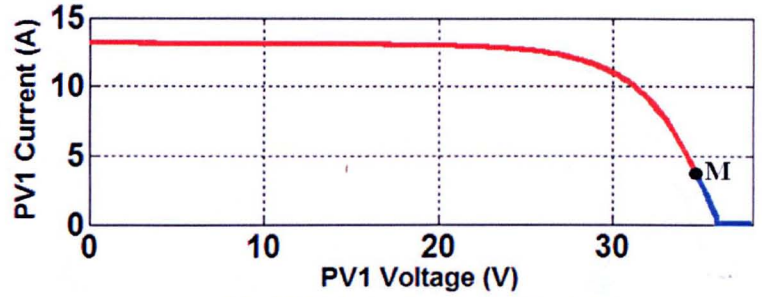

(a) I-V characteristics for PV_1

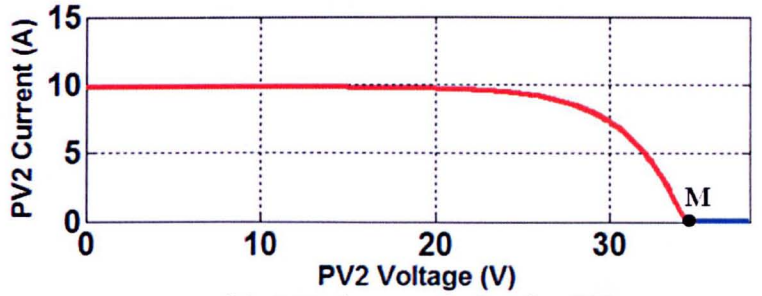

(b) I-V characteristics for PV_2

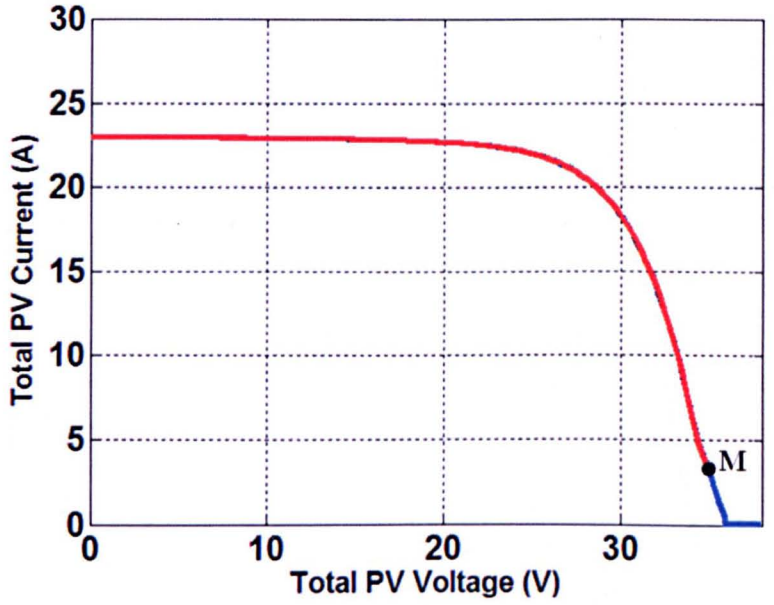

(c) Overall I-V characteristics

Figure 2.20 Current-voltage characteristics for a PV system integrated with blocking diodes

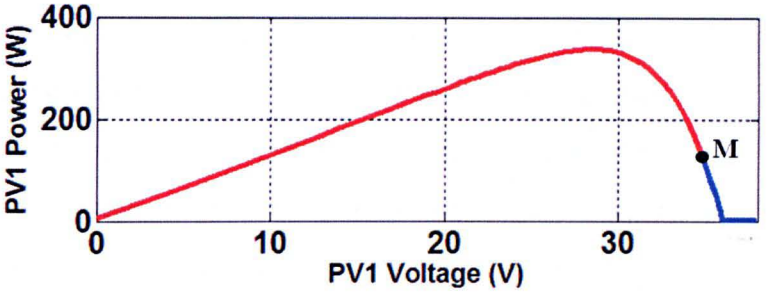

(a) P-V characteristics for PV_1

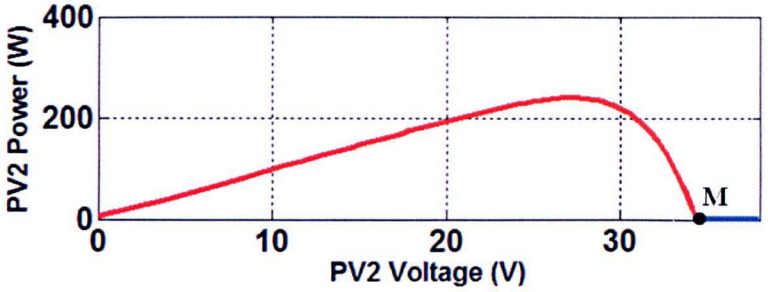

(b) P-V characteristics for PV_2

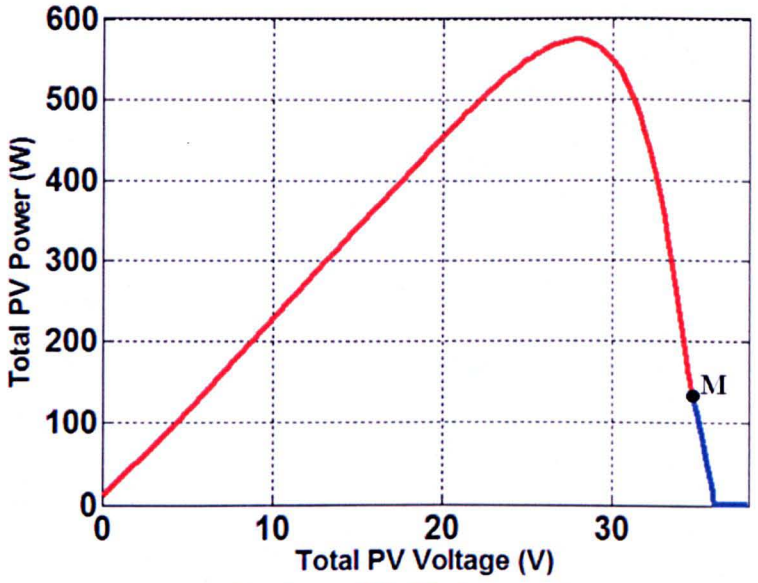

(c) Overall P-V characteristics

Figure 2.21 Power-voltage characteristics for a PV system integrated with blocking diodes

Under different shading conditions, the P-V characteristics are illustrated by Figure 2.22 and the maximum power points are all located between 25 and 30-volt range. Table 2.2 lists out the available solar power and the maximum power that can be extracted from the PV generators when they are integrated with blocking diodes. Though the difference is less significant comparing to the bypass diode case, the extractable power is still lower than the maximum available power. The power loss for a complete range of uneven lighting conditions is shown in Figure 2.23. The definition for α is the same as that for the bypass diode case.

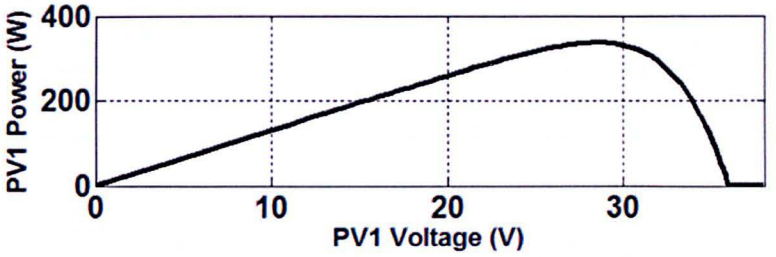

(a) P-V characteristics for PV_1

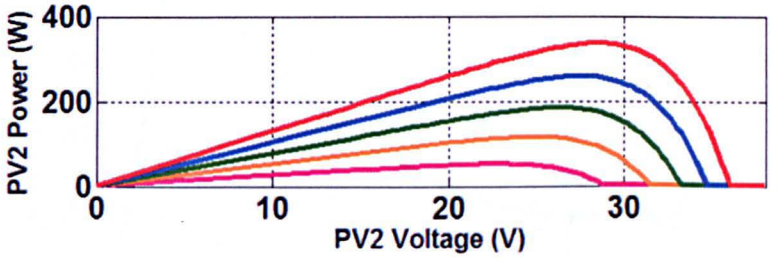

(b) P-V characteristics for PV_2

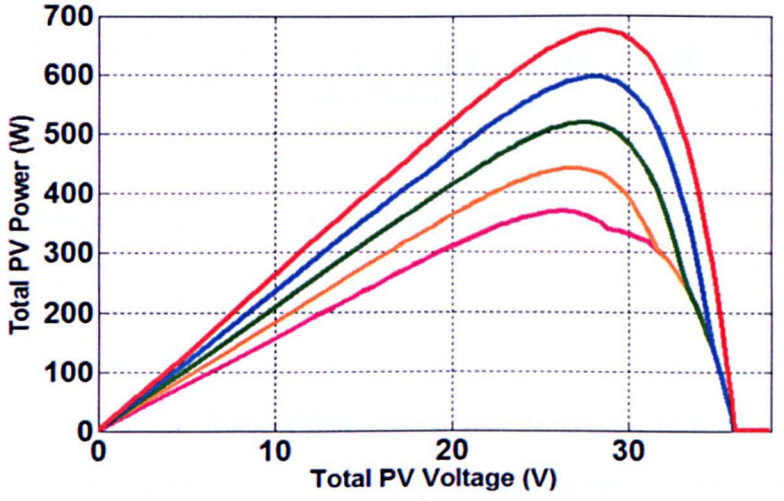

(c) Overall P-V characteristics

Figure 2.22 Power-voltage characteristics under different shading conditions for a PV system integrated with blocking diodes

Table 2.2 Power variation for PV system integrated with blocking diodes under different shading conditions but constant cell temperature

Insolation (PV_1 (unshaded) / (mW/cm^3) PV_2 (shaded))	100				
	20	40	60	80	100
Shading level, α	0.2	0.4	0.6	0.8	1.0
Cell Temperature (°C)	20				
Maximum Power (W)	367.4	440.6	516.1	593.6	687.2
Voltage at P_{max} (V)	26.21	26.77	27.61	27.89	28.45
Extractable Peak Power (W)	396.01	461.3	532.2	607.7	687.2

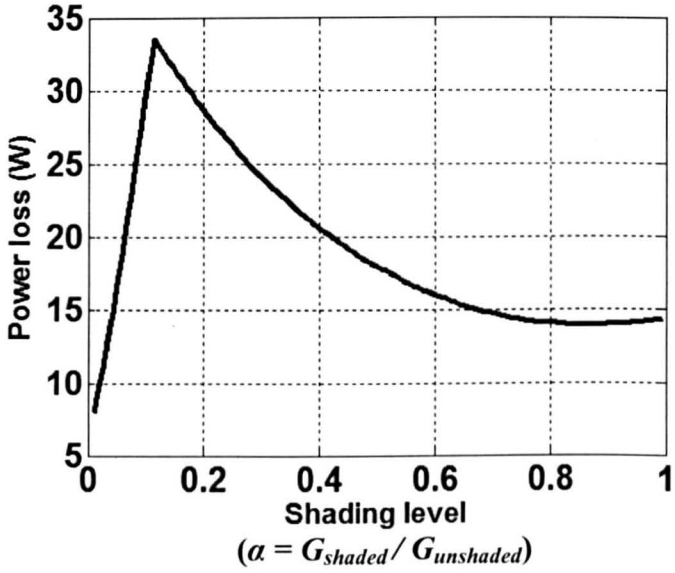

Figure 2.23 Effect of shading level on the power loss for blocking diode scheme

When α = 0, a full blackout occurs on shaded module which is now isolated from the system by its reverse-biased blocking diode while the other unit is operating normally. Nevertheless, there is still a small power loss of 7.97 W which is due to the voltage drop resulting from the forward-biasing of blocking diode for the unshaded unit.

When α is between 0 and 0.11, the open circuit voltage of the shaded unit is lower than the operating voltage of the global MPP. As α increases from 0 to 0.11, the shaded unit potentially can generate more power but its blocking diode is still reverse-biased preventing it from delivering power to the load. Hence, the power

loss increases to 33.5 W at $\alpha = 0.11$. Nevertheless, the overall maximum power is still almost equal to that of the unshaded unit.

When α is between 0.11 and 1, the open circuit voltage of the shaded unit becomes higher than the operating voltage of the global MPP. Therefore, all the blocking diodes are activated and both modules are allowed to generate power, albeit the generating capability of the unshaded unit being limited by the shading severity of the shaded one. As α increases towards unity, the operating voltage of the global MPP is closer to that of the MPP for the unshaded unit. Hence, more power can be extracted to the load reducing the system loss.

When $\alpha = 1$, there is some power loss of 14.33 W which is caused by the voltage drop across the activated blocking diodes for both modules.

2.6 Summary

This chapter presents the operating principles and the modelling of a PV solar system operating under homogeneous and inhomogeneous distributions of irradiation. The analysis assumes that each module connected to the system is evenly shaded/unshaded. Through incorporating the reverse cell characteristics into the single-diode model for a PV module, the development of a complete equivalent circuit has been analysed. This has led to the derivation of equations which are used to describe the current flowing from an illuminated PV module and the electrical power generated by it. The relationship of power with the environmental conditions is non-linear. A Newton-Raphson iterative method was used to produce the current-voltage and power-voltage characteristics of a PV module. The PV voltage at which maximum power that can be extracted increases with illumination while decreases with cell temperature. The simulation model has also been used to study the effects of partial shading. When multiple PV modules are linked together without bypass or blocking diodes, it has been demonstrated that a shaded unit may operate as a load consuming the power generated by other units.

To prevent the power dissipation in the shaded cell, a bypass diode is connected across each of the PV modules linked in series. The analysis of the overall current-voltage characteristics showed that the power dissipation in a shaded module can be limited by forward-biasing the corresponding bypass diode. The major

drawback for this scheme is the existence of multiple power peaks which are scattered within a wide range of operating voltage. Another disadvantage of the bypass diode is that not all the available solar power can be extracted. To analyze this, an example PV system with two modules has been used. It has been found that as much as 148 W or 30% of power can still be extracted from the system. An investigation has also been done for PV systems with more generating units and has revealed that the power loss increases with the number of shaded units.

An analysis has also been done for blocking diode which is linked in series with each of the parallel-connected PV modules. It has been demonstrated that in the event of an inhomogeneous illumination between two PV modules, the shaded unit can be protected from being destroyed thermally by reverse-biasing the blocking diode. However under most shading levels, this only occurs beyond the MPP region of the shaded unit. An application example has also shown that the maximum power loss due to blocking diode is lower than that in the bypass diode case.

Chapter 3
Analysis, Modelling and Design of a Ćuk Step-Down Converter

3.1 Introduction

A Ćuk step-down converter has at least two modes of operation, namely constant input voltage - variable output voltage; and constant output voltage – variable input voltage, which might be used as a DC motor drive or a PV power system, respectively as shown in Figures 3.1(a) and 3.1(b). A thorough and accurate analysis of the steady-state and transient behaviours of the converter in both operating modes is important for the design of the converter and its associated control system. The responses of the circuit depend on the values of the four components L_1 and L_2, as well as C_n and C_o in the circuit, and they also vary according to the circuit operation points. For a PV plant application, for example the operating condition changes frequently as the terminal voltage of the PV panel, i.e. the converter input voltage, varies with the changes of weather conditions while the converter output voltage must be held constant according to the load requirement. It is not obvious that any chosen set of the four circuit components would lead to satisfactory performance for all possible PV operating conditions. Adequate selection of these parameters can be intricate as the transient response may be improved at the expense of the steady-state ripple [97]. Furthermore, a proper preliminary converter design may obviate the need for costly advanced control schemes.

This chapter presents a detailed analysis and design scheme for a Ćuk step-down converter. The operating principle in continuous-conduction-mode at the steady state is reviewed in Section 3.2. The derivations of the four transfer functions for the two different operating conditions are detailed in Section 3.3. Based on these models, a novel Ćuk converter design method is developed to select the four circuit parameters; this is presented in Section 3.4. In Section 3.5, the designed circuit has been analysed and validated through simulation for both operation modes. Finally, in Section 3.6, an analysis is presented for the converter operating in the discontinuous-conduction-mode for both constant input voltage and constant output voltage cases.

The designed circuit has been validated through experimental tests and this will be presented in Chapter 7.

3.2 Operating Principles in Continuous Conduction Mode

The Ćuk step-down converter, shown in Figure 3.1, is a unidirectional circuit and can operate in one of the two modes, namely, the left-hand side voltage V_i is adjustable while the right-hand side voltage V_o is constant and vice versa. The analysis below is applicable to both modes and assumes an ideal circuit, i.e. the internal resistance of the circuit components can be neglected; and the diode D and switch S are turned on/off instantaneously and their on/off state losses are ignored. The key element in the circuit is capacitor C_n, which transfers energy from input to output. If the capacitors C_i, C_o and C_n are sufficiently large, fluctuations of V_i, V_o and V_{cn} around their average levels will be small. Also with high enough switching frequency, i_1 and i_2, which are the currents flowing through inductors L_1 and L_2 respectively, can be considered varying linearly over time during a switching period.

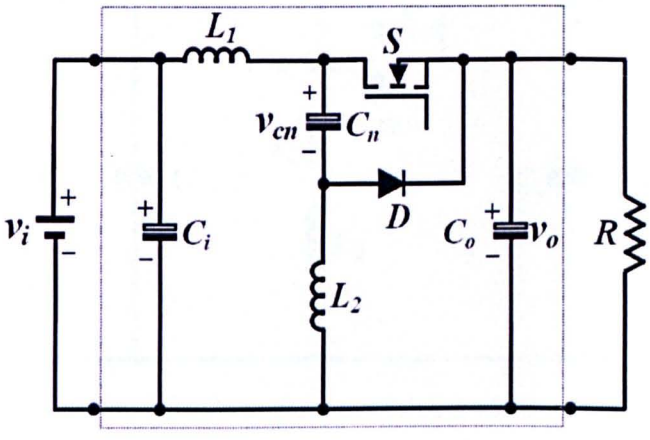

(a) Constant input voltage – variable output voltage

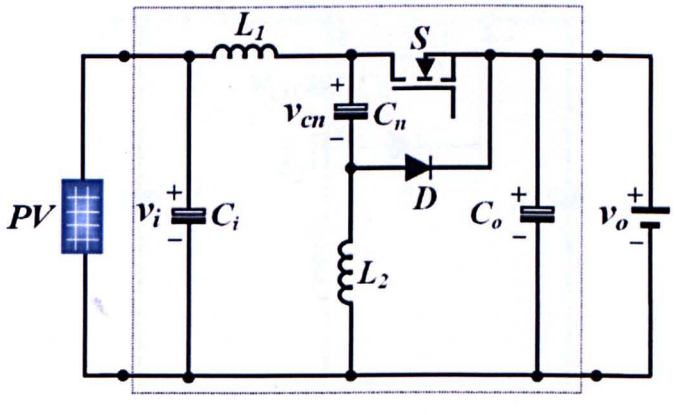

(b) Constant output voltage – variable input voltage

Figure 3.1 Ćuk step-down converter for two different operation modes

The following analysis uses 'smoothed' voltages and currents defined as the instantaneous values averaged over one switching period. Then in the steady state the inductor voltages, V_{L1} and V_{L2} are zero and so one obtains

$$V_{cn} = V_i \tag{3.1}$$

In this analysis, continuous-conduction-mode (CCM) at steady state is considered. When switch S is turned on for a time t_{on}, the circuit state is as shown in Figure 3.2(a). The voltage across L_1 is $(V_i - V_o)$ and positive resulting in the inductor L_1 being charged with energy so current i_1 is increasing linearly. The diode D is now reverse-biased, so C_n discharges through switch S to load impedance R and L_2, causing i_2 also increasing linearly. As shown in Figure 3.2(b), when S is turned off, D becomes forward-biased and energy to R is supplied by the source and that stored in L_2. C_n is now charged through D by energy from both the source and L_1. Therefore, both the currents i_1 and i_2 are decreasing during the turn-off time t_{off}. The

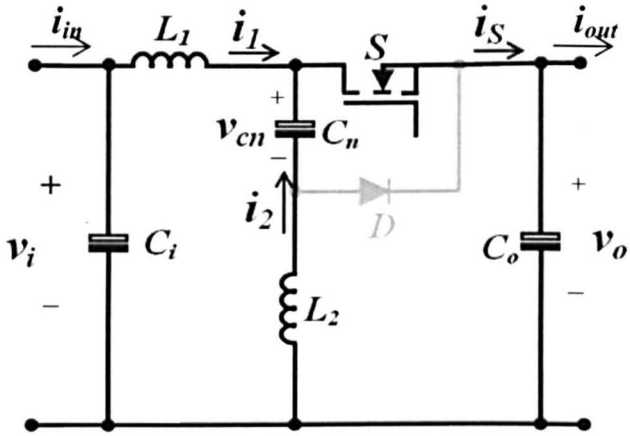

(a) Converter switch-on state

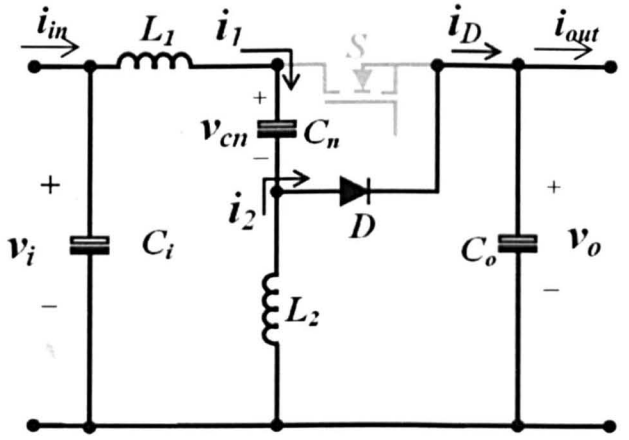

(b) Converter switch-off state

Figure 3.2 Converter circuit states for continuous-conduction-mode

corresponding voltage and current waveforms are shown in Figure 3.3. The switching period is defined as $T_s = t_{on} + t_{off}$ and the duty ratio as $K = t_{on} / T_s$. For steady-state operation, the net change in the inductor current is zero and hence the voltage-time balance equations for L_1 and L_2 are given respectively by

$$(V_i - V_o)K + (V_i - V_{cn} - V_o)(1 - K) = 0$$

and

$$(V_{cn} - V_o)K - V_o(1 - K) = 0 \tag{3.2}$$

Eliminating V_{cn} gives the relationship between V_i and V_o as

$$K = \frac{V_o}{V_i} \tag{3.3}$$

For a lossless circuit, the converter input power, P_{in} equals to the output power, P_{out}. Hence

$$V_o I_{out} = V_i I_{in} \tag{3.4}$$

where

$$V_o(I_1 + I_2) = V_i I_{in}$$

and I_{out} is the converter output current while I_{in} is the converter input current.

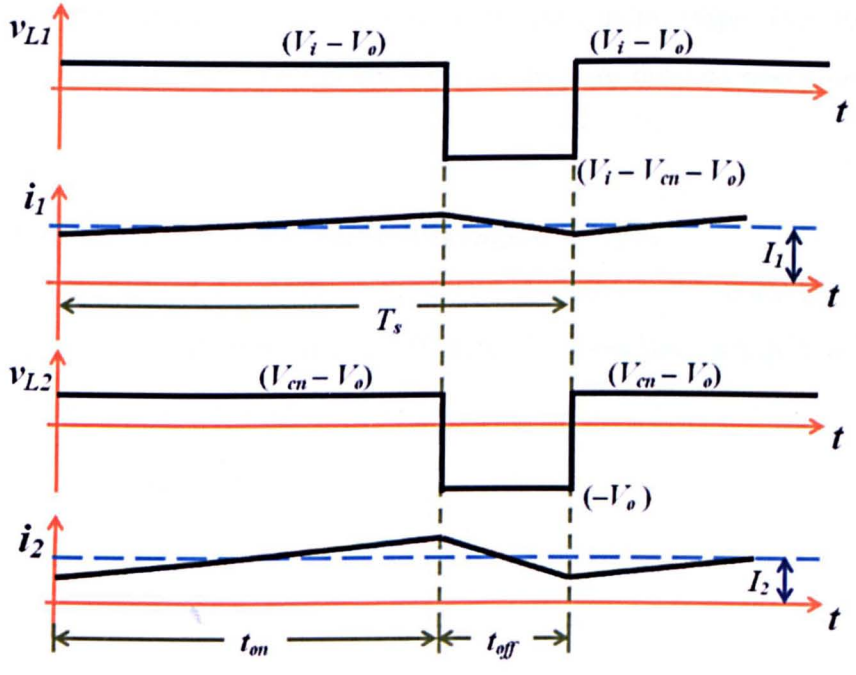

Figure 3.3 Voltage and current waveforms for the converter

Substituting Equation (3.3) into (3.4), one yields the relationship between the currents flowing through L_1 and L_2 as

$$\frac{I_1}{I_2} = \frac{K}{1-K} \tag{3.5}$$

This conforms to the discussion in [21] that the relationship between input and output voltages is analogous to the one in a Buck converter and the total current flowing to the load is $I_{out} = I_1 + I_2$. The input-output current ratio therefore is $K = I_{in}/I_{out}$.

3.3 Transfer Function Model

This is necessary for the design of the Ćuk converter and analyzing its dynamic characteristics when different component values are used. A state-space averaging model can be derived by first including the input and output voltages of the converter within the state variables, since they change with the values of the input and output currents as well as the capacitors respectively. The only independent variable in this model, in terms of not being affected by any internal circuit elements, is the duty cycle, k while the supply current, i_{in} is assumed independent. Transfer functions for the conditions of the constant output voltage – variable input voltage, and vice versa, are derived yielding two different relationships. Two further transfer functions with k as the independent variable are also derived based on perturbation analysis.

3.3.1 A General State-Variable Averaging Model

This is derived by writing equations describing the converter operation in CCM for both switch turn-on and off states. Thus when switch S is on, the state equation can be described by

$$\dot{\mathbf{x}} = \mathbf{A}_1\mathbf{x} + \mathbf{B}i_{in} \tag{3.6}$$

where

$$\mathbf{x} = \begin{bmatrix} x_1 \\ x_2 \\ x_3 \\ x_4 \\ x_5 \end{bmatrix} = \begin{bmatrix} v_i \\ i_1 \\ i_2 \\ v_{cn} \\ v_o \end{bmatrix},$$

$$\mathbf{A}_1 = \begin{bmatrix} 0 & -1/C_i & 0 & 0 & 0 \\ 1/L_1 & 0 & 0 & 0 & -1/L_1 \\ 0 & 0 & 0 & 1/L_2 & -1/L_2 \\ 0 & 0 & -1/C_n & 0 & 0 \\ 0 & 1/C_o & 1/C_o & 0 & -1/C_oR \end{bmatrix} \text{ and } \mathbf{B} = \begin{bmatrix} 1/C_i \\ 0 \\ 0 \\ 0 \\ 0 \end{bmatrix}$$

For each switching period the time instant when switch S is turned on is denoted as τ_1, and that when it is turned off as τ', hence the turn-on duration $t_{on} = \tau' - \tau_1$. Assuming switching frequency, $f_s = 1/T_s$, is high, (i.e. $T_s \ll$ time constant of inductors L_1 and L_2), one yields

$$\dot{\mathbf{x}} \approx \frac{\mathbf{x}(\tau') - \mathbf{x}(\tau_1)}{t_{on}} \tag{3.7}$$

So, at the end of switching on time one obtains

$$\mathbf{x}(\tau') = (\mathbf{I} + \mathbf{A}_1 t_{on})\mathbf{x}(\tau_1) + \mathbf{B} t_{on} i_{in} \tag{3.8}$$

Similarly the circuit state when S is turned off can be described by

$$\dot{\mathbf{x}} = \mathbf{A}_2 \mathbf{x} + \mathbf{B} i_{in} \tag{3.9}$$

where

$$\mathbf{A}_2 = \begin{bmatrix} 0 & -1/C_i & 0 & 0 & 0 \\ 1/L_1 & 0 & 0 & -1/L_1 & -1/L_1 \\ 0 & 0 & 0 & 0 & -1/L_2 \\ 0 & 1/C_n & 0 & 0 & 0 \\ 0 & 1/C_o & 1/C_o & 0 & -1/C_oR \end{bmatrix}$$

Setting τ_2 as the time instant when the turn-off interval ends, hence $t_{off} = \tau_2 - \tau'$, and

$$\dot{\mathbf{x}} \approx \frac{\mathbf{x}(\tau_2) - \mathbf{x}(\tau')}{t_{off}} \tag{3.10}$$

Subsequently Equation (3.10) can be expressed as

$$\mathbf{x}(\tau_2) = (\mathbf{I} + \mathbf{A}_2 t_{off})\mathbf{x}(\tau') + \mathbf{B} t_{off} i_{in} \tag{3.11}$$

Substituting $\mathbf{x}(\tau')$ in (3.11) by (3.8), one obtains

$$\mathbf{x}(\tau_2) = (\mathbf{I} + \mathbf{A}_2 t_{off})(\mathbf{I} + \mathbf{A}_1 t_{on})\mathbf{x}(\tau_1) + [(\mathbf{I} + \mathbf{A}_2 t_{off})t_{on} + t_{off}]\mathbf{B} i_{in} \tag{3.12}$$

With ($t_{on} \times t_{off}$) the term is significantly smaller than the product of any inductor or capacitor values hence negligible, and replacing t_{on} by kT_s and t_{off} by $(1 - k)T_s$, the averaged state-variable model over one switching period is given as

$$\begin{bmatrix} \dot{x}_1 \\ \dot{x}_2 \\ \dot{x}_3 \\ \dot{x}_4 \\ \dot{x}_5 \end{bmatrix} = \begin{bmatrix} 0 & -\frac{1}{C_i} & 0 & 0 & 0 \\ \frac{1}{L_1} & 0 & 0 & \frac{-(1-k)}{L_1} & -\frac{1}{L_1} \\ 0 & 0 & 0 & \frac{k}{L_2} & -\frac{1}{L_2} \\ 0 & \frac{(1-k)}{C_n} & \frac{-k}{C_n} & 0 & 0 \\ 0 & \frac{1}{C_o} & \frac{1}{C_o} & 0 & -\frac{1}{C_o R} \end{bmatrix} \begin{bmatrix} x_1 \\ x_2 \\ x_3 \\ x_4 \\ x_5 \end{bmatrix} + \begin{bmatrix} \frac{1}{C_i} \\ 0 \\ 0 \\ 0 \\ 0 \end{bmatrix} i_{in} \tag{3.13}$$

The above equations denote a nonlinear averaged model for Ćuk step-down converter. They are linear with respect to the state variables provided the load R is constant and the system remains in continuous-conduction-mode. Since k may vary with time, the state equation consists of time varying coefficients. In this case, a transfer function with respect to k is derived by analysis of small perturbations.

3.3.2 Derivation of Transfer Functions by Small Perturbations

3.3.2.1 Small Signal State-Variable Model

This involves representing all state variables including k and i_{in} in Equation (3.13) as the sum of their corresponding DC components and AC perturbations, these are

$$\begin{aligned} \mathbf{x} &= \mathbf{X} + \hat{\mathbf{x}} \\ i_{in} &= I_{in} + \hat{i}_{in} \\ k &= K + \hat{k} \end{aligned} \tag{3.14}$$

Subsequently, the matrix in Equation (3.13) is expanded as

$$
\begin{aligned}
C_i \frac{dV_i}{dt} + C_i \frac{d\hat{v}_i}{dt} &= (I_{in} - I_1) + (\hat{i}_{in} - \hat{i}_1) \\
L_1 \frac{dI_1}{dt} + L_1 \frac{d\hat{i}_1}{dt} &= (V_i - K'V_{cn} - V_o) + (\hat{v}_1 - K'\hat{v}_{cn} - \hat{v}_o + V_i\hat{k}) + \hat{k}\hat{v}_{cn} \\
L_2 \frac{dI_2}{dt} + L_2 \frac{d\hat{i}_2}{dt} &= (KV_i - V_o) + (K\hat{v}_{cn} - \hat{v}_o + V_i\hat{k}) + \hat{k}\hat{v}_{cn} \\
C_n \frac{dV_{cn}}{dt} + C_n \frac{d\hat{v}_{cn}}{dt} &= (K'I_1 - KI_2) + (K'\hat{i}_1 - K\hat{i}_2 - I_o\hat{k}) - \hat{i}_o\hat{k} \\
C_o \frac{dV_o}{dt} + C_o \frac{d\hat{v}_o}{dt} &= \left(I_1 + I_2 - \frac{V_o}{R}\right) + \left(\hat{i}_1 + \hat{i}_2 - \frac{\hat{v}_o}{R}\right)
\end{aligned}
\tag{3.15}
$$

where $K' = 1 - K$.

By assuming the AC perturbations are negligibly small compared to their corresponding steady-state DC values, hence higher-order nonlinear terms can be eliminated. In addition, the derivatives of all state variable DC terms equal to zero, thus Equation (3.13) becomes a linearized state-variable equation as

$$
\begin{bmatrix} \dot{\hat{v}}_i \\ \dot{\hat{i}}_1 \\ \dot{\hat{i}}_2 \\ \dot{\hat{v}}_{cn} \\ \dot{\hat{v}}_o \end{bmatrix} = \begin{bmatrix} 0 & -\frac{1}{C_i} & 0 & 0 & 0 \\ \frac{1}{L_1} & 0 & 0 & \frac{-K'}{L_1} & -\frac{1}{L_1} \\ 0 & 0 & 0 & \frac{K}{L_2} & -\frac{1}{L_2} \\ 0 & \frac{K'}{C_n} & \frac{-K}{C_n} & 0 & 0 \\ 0 & \frac{1}{C_o} & \frac{1}{C_o} & 0 & -\frac{1}{C_oR} \end{bmatrix} \begin{bmatrix} \hat{v}_i \\ \hat{i}_1 \\ \hat{i}_2 \\ \hat{v}_{cn} \\ \hat{v}_o \end{bmatrix} + \begin{bmatrix} 0 \\ \frac{R}{L_1K^2} \\ \frac{R}{L_2K^2} \\ -\frac{1}{C_nK} \\ 0 \end{bmatrix} I_{in}\hat{k} + \begin{bmatrix} \frac{1}{C_i} \\ 0 \\ 0 \\ 0 \\ 0 \end{bmatrix} \hat{i}_{in}
\tag{3.16}
$$

3.3.2.2 Transfer Functions for Constant V_i and Variable V_o

In an application such as controlling a DC motor speed, output voltage V_o is a variable while input voltage V_i remains essentially constant, hence input side capacitor C_i in Equation (3.16) can be considered infinitely large. The 5 × 5 matrix in Equation (3.16) is reduced to a 4 × 4 matrix and the last term in right-hand side of this equation is eliminated, hence it becomes

$$
\dot{\hat{\mathbf{x}}}_i = \mathbf{M}_i\hat{\mathbf{x}}_i + \mathbf{P}_i\hat{v}_i + \mathbf{N}_i I_{in}\hat{k}
\tag{3.17}
$$

where

$$\hat{\mathbf{x}}_i = \begin{bmatrix} \hat{i}_1 \\ \hat{i}_2 \\ \hat{v}_{cn} \\ \hat{v}_o \end{bmatrix}, \mathbf{M}_i = \begin{bmatrix} 0 & 0 & \frac{-K'}{L_1} & -\frac{1}{L_1} \\ 0 & 0 & \frac{K}{L_2} & -\frac{1}{L_2} \\ \frac{K'}{C_n} & \frac{-K}{C_n} & 0 & 0 \\ \frac{1}{C_o} & \frac{1}{C_o} & 0 & -\frac{1}{C_o R} \end{bmatrix}, \mathbf{P}_i = \begin{bmatrix} \frac{1}{L_1} \\ 0 \\ 0 \\ 0 \end{bmatrix}, \mathbf{N}_i = \begin{bmatrix} \frac{R}{L_1 K^2} \\ \frac{R}{L_2 K^2} \\ -\frac{1}{C_n K} \\ 0 \end{bmatrix}$$

The small-signal equation for output voltage is given as

$$\hat{v}_o = \mathbf{Z}_o \hat{\mathbf{x}}_i \tag{3.18}$$

where $\mathbf{Z}_o = [0 \quad 0 \quad 0 \quad 1]$.

As $\hat{v}_i = 0$, the duty ratio can be taken as the control variable and the output voltage as the controlled variable. Hence, the transfer function between them is

$$\begin{aligned} G_{ok}(s) &= \left.\frac{\hat{v}_o(s)}{\hat{k}(s)}\right|_{\hat{v}_i=0} \\ &= \mathbf{Z}_o(s\cdot\mathbf{I}-\mathbf{M}_i)^{-1}\mathbf{N}_i = \frac{(L_1+L_2)C_nRs^2-(KL_1-K'L_2)Ks+R}{\alpha_4 s^4+\alpha_3 s^3+\alpha_2 s^2+\alpha_1 s+1}\frac{I_{in}}{K^2} \end{aligned} \tag{3.19}$$

The transfer function for output-to-input voltages can be derived as

$$\begin{aligned} G_{oi}(s) &= \left.\frac{\hat{v}_o(s)}{\hat{v}_i(s)}\right|_{\hat{k}=0} \\ &= \mathbf{Z}_o(s\cdot\mathbf{I}-\mathbf{M}_i)^{-1}\mathbf{P}_i = \frac{L_2C_ns^2+K}{\alpha_4 s^4+\alpha_3 s^3+\alpha_2 s^2+\alpha_1 s+1} \end{aligned} \tag{3.20}$$

where

$$\begin{aligned} \alpha_4 &= L_1L_2C_nC_o \\ \alpha_3 &= \frac{L_1L_2C_n}{R} \\ \alpha_2 &= \left(C_n[L_1+L_2]+C_o[K^2L_1+K'^2L_2]\right) \\ \alpha_1 &= \frac{1}{R}\left(K^2L_1+K'^2L_2\right) \end{aligned}$$

It is noted that Equation (3.20) can be directly derived from the averaged state-variable model of Equation (3.13) when the same assumption as above is applied.

As shown respectively in Equations (3.19) and (3.20), both transfer functions are varying with K and have four poles and two zeros though the latter is linear and time invariant when K is a constant. The zeros in $G_{ok}(s)$ (Equation (3.19)) may appear in the right-half s-plane, also known as the non-minimum phase characteristic, depending on the load resistance R and values of filter inductances L_1 and L_2 multiplying respectively the steady-state duty ratio K and K'. The non-minimum phase effect results in that when $\hat{k}$ is increased instantaneously the output voltage will instead initially decrease which is the opposite of what eventually takes place. On the other hand, as K decreases the middle term in the numerator of transfer function $G_{ok}(s)$ (Equation (3.19)) becomes positive, hence, the right-half-plane zeros no longer exist. However, the reduction of K yields $G_{ok}(s)$ less damped and hence the responses to step change of k become more oscillatory as shown in Figure 3.4. These undesirable features of the Ćuk step-down circuit can be reduced by properly selecting the values of the circuit components, hence highlighting the importance of having an optimal design scheme as presented in Section 3.4.

3.3.2.3 Transfer Functions for Constant V_o and Variable V_i

On the other hand when the converter is used to control a PV system, the input is connected to a PV generator as shown in Figure 3.1(b) and under a specific condition, its current varies according to the I-V characteristics of the PV and its

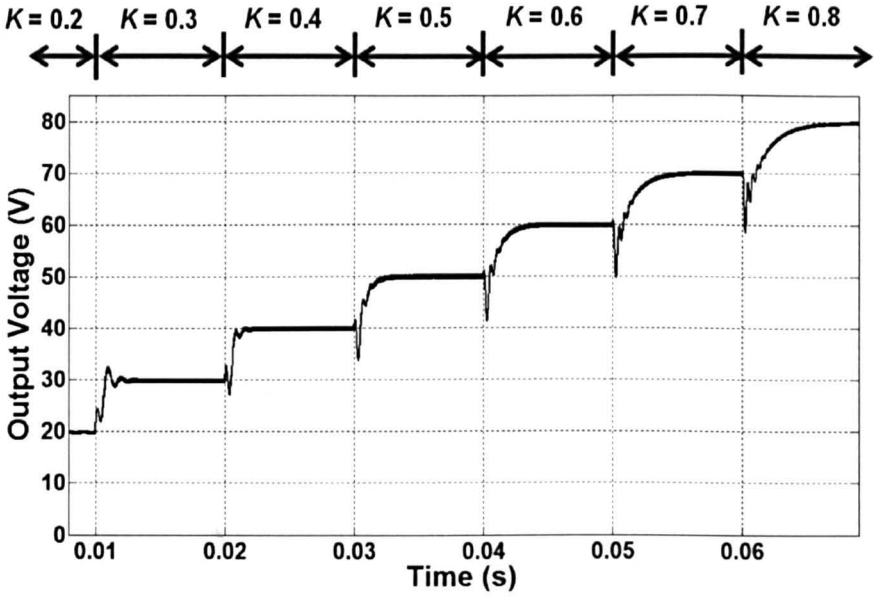

Figure 3.4 Step responses of $G_{ok}(s)$ at different K values

normal operating range, thus the source current is now

$$\hat{i}_{in} = \frac{\hat{v}_i}{-R_{PV}} \tag{3.21}$$

where R_{PV} is the slope of I-V characteristic at its steady-state point and is always varying.

Assuming output voltage is maintained by a constant DC source, hence, C_o can be considered infinitely large and the model defined by Equation (3.13) can be re-written as

$$\dot{\hat{\mathbf{x}}}_o = \mathbf{M}_o \hat{\mathbf{x}}_o + \mathbf{P}_o \hat{v}_o + \mathbf{N}_o V_o \hat{k} \tag{3.22}$$

where

$$\hat{\mathbf{x}}_o = \begin{bmatrix} \hat{v}_i \\ \hat{i}_1 \\ \hat{i}_2 \\ \hat{v}_{cn} \end{bmatrix}, \mathbf{M}_o = \begin{bmatrix} -\frac{1}{C_i R_{PV}} & -\frac{1}{C_i} & 0 & 0 \\ \frac{1}{L_1} & 0 & 0 & \frac{-K'}{L_1} \\ 0 & 0 & 0 & \frac{K}{L_2} \\ 0 & \frac{K'}{C_n} & \frac{-K}{C_n} & 0 \end{bmatrix},$$

$$\mathbf{P}_o = \begin{bmatrix} 0 \\ -\frac{1}{L_1} \\ -\frac{1}{L_2} \\ 0 \end{bmatrix} \text{ and } \mathbf{N}_o = \begin{bmatrix} 0 \\ \frac{1}{L_1 K} \\ \frac{1}{L_2 K} \\ -\frac{1}{C_n R_{PV} K^2} \end{bmatrix}$$

The small-signal equation for the input voltage is given as

$$\hat{v}_i = \mathbf{Z}_i \hat{\mathbf{x}}_o \tag{3.23}$$

where $\mathbf{Z}_i = \begin{bmatrix} 1 & 0 & 0 & 0 \end{bmatrix}$

By assuming $\hat{v}_o = 0$, the transfer function model for $\hat{v}_i / \hat{k}$ can be expressed as

$$G_{ik}(s)=\left.\frac{\hat{v}_i(s)}{\hat{k}(s)}\right|_{\hat{v}_o=0}$$
$$=\mathbf{Z}_i\cdot(s\cdot\mathbf{I}-\mathbf{M}_o)^{-1}\mathbf{N}_o=-\frac{C_nL_2Ks^2+\frac{K'L_2}{R_{PV}}s+K^2}{\beta_4s^4+\beta_3s^3+\beta_2s^2+\beta_1s+\beta_0}\frac{V_o}{K^2} \tag{3.24}$$

and transfer function model for $\hat{v}_i/\hat{v}_o$ is

$$G_{io}(s)=\left.\frac{\hat{v}_i(s)}{\hat{v}_o(s)}\right|_{\hat{k}=0}$$
$$=\mathbf{Z}_i\cdot(s\cdot\mathbf{I}-\mathbf{M}_o)^{-1}\mathbf{P}_o=\frac{C_nL_2s^2+K}{\beta_4s^4+\beta_3s^3+\beta_2s^2+\beta_1s+\beta_0} \tag{3.25}$$

where

$$\beta_4=L_1L_2C_iC_n$$
$$\beta_3=\frac{L_1L_2C_n}{R_{PV}}$$
$$\beta_2=\left(C_nL_2+C_i\left[K^2L_1+K'^2L_2\right]\right)$$
$$\beta_1=\frac{1}{R_{PV}}\left(K^2L_1+K'^2L_2\right)$$
$$\beta_0=K^2$$

Again Equation (3.25) can be derived directly from the DC averaged model in Equation (3.13) based on the same assumption and when R_{PV} is a constant. The non-linear characteristics of G_{ik}(s) in Equation (3.24) are shown clearly as pole and zero positions would vary with the change of input variable k, though unlike previous case of $G_{ok}(s)$ when output voltage is constant G_{ik}(s) shows no non-minimum phase feature.

3.4 Converter Design Principles

The converter design involves selecting proper values for inductors, L_1 and L_2, as well as capacitors, C_n and C_o. The design presented below is based on the operation mode of constant V_i and variable output V_o. It should also satisfy the particular application of constant V_o output and variable V_i of the same specifications when a PV panel is connected.

The criteria for selection are

1) to eliminate as much input current and output voltage ripples as possible at the steady states, and
2) to obtain high performance voltage responses during transient intervals.

3.4.1 Selecting L_1 and C_o

For selecting L_1 the maximum ripple value for i_1 is required. At the steady state, the peak-to-peak change of i_1 during on-state of the switch is expressed as

$$\Delta i_1 = \frac{K}{L_1 f_s}(V_i - V_o) \tag{3.26}$$

The voltage applied across L_1 during either turn-on or turn-off periods, and device switching frequency f_s are known according to the application. Thus for a given operating condition L_1 can be determined based on the desired maximum value for Δi_1.

The charges accumulated across C_o during switch turn-on time and those released during turn-off time lead to the fluctuation in v_o as shown in Figure 3.5. Hence for selecting C_o, the magnitude of the output voltage ripple is expressed as

$$\Delta v_o = \frac{\Delta q_o}{C_o} = \frac{\Delta i_o}{8 C_o f_s} \tag{3.27}$$

where Δi_o in the Equation (3.27) equals to $\Delta i_1 + \Delta i_2$ and Δi_2 is determined by the expression:

$$\Delta i_2 = \frac{K}{L_2 f_s}(V_{cn} - V_o) \tag{3.28}$$

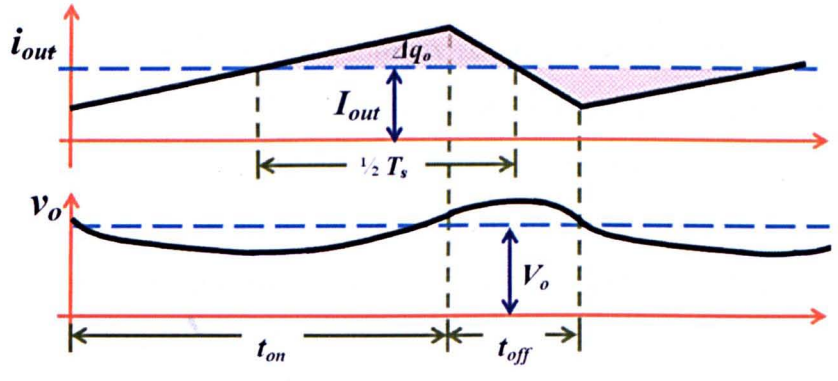

Figure 3.5 Output current and voltage waveforms for Ćuk step-down converter

Substituting Δi_o in Equation (3.27) by the sum of Δi_1 (Equation (3.26)) and Δi_2 (Equation (3.28)), one obtains

$$\Delta v_o = (\Delta i_1 + \Delta i_2)\left[\frac{1}{8C_o f_s}\right] \tag{3.29}$$

Designing C_o according to Equation (3.29) is difficult since it requires both Δi_1 and Δi_2. However, C_o can be pre-evaluated using Equation (3.27) according to the required Δv_o, load R and switching frequency f_s. The calculated value may not be satisfactory as Δv_o is also affected by L_2 which is designed according to the transient response below.

3.4.2 Selecting C_n and L_2

This is aimed at obtaining a step response with minimal overshoot and oscillations, as well as short settling time. As shown in Equation (3.19) the circuit may present non-minimum phase feature. The optimal solution for C_n and L_2 is obtained by predicting the output voltage responses for different C_n and L_2 pairs, and selecting the one giving the minimum variance between the samples of the voltage response and its desired value following a step change in k. To prevent the transient performance from being affected by the inherent non-minimum phase feature, a weighted cost function is defined as

$$E = \sum_{n=1}^{n=m} \left(V_o^* - w v_o[nT_n]\right)^2 \tag{3.30}$$

where V_o^* is the ideal output voltage value, $v_o[nT_n]$ is the n-th sample of the voltage response due to the change of duty ratio, and m is the total number of samples taken. The values for the weighting factor w are carefully set in this case as $w = 1$ for $v_o[nT_n] > v_o[0]$ and $w = 0.985$ otherwise. These values are selected so that the variance introduced by the non-minimum phase feature is less significant than that due to the output voltage transient response. Calculations of E can then be carried out for a range of C_n and L_2 combinations while using the same pair of L_1 and C_o values selected in the previous sub-section. The optimal C_n and L_2 pair should be the one giving the minimum E value.

Having selected L_2 it is necessary to re-tune C_o by using Equation (3.29) since both L_1 and L_2 for Δi_1 and Δi_2 in this equation are defined. The C_o thus updated can

be used again to re-tune L_2 using the optimal procedure described above. This process can be repeated until Δv_o and the transient cost function E (Equation 3.30) are below the defined limits. A flowchart shown in Figure 3.6 summarizes the above described design procedure for selecting L_1, L_2, C_o and C_n.

3.5 Simulation Results

3.5.1 Design Specifications

The above proposed procedure has been applied to design a 500W converter with the specifications listed in Table 3.1.

To select the other components, L_1 is set to 12.5 mH and C_o to 10.0 μF for K = 0.5. For selecting L_2 and C_n, a set of cost function values is evaluated as described in the previous section. Figures 3.7(a) and (b) show the E value variations for C_n

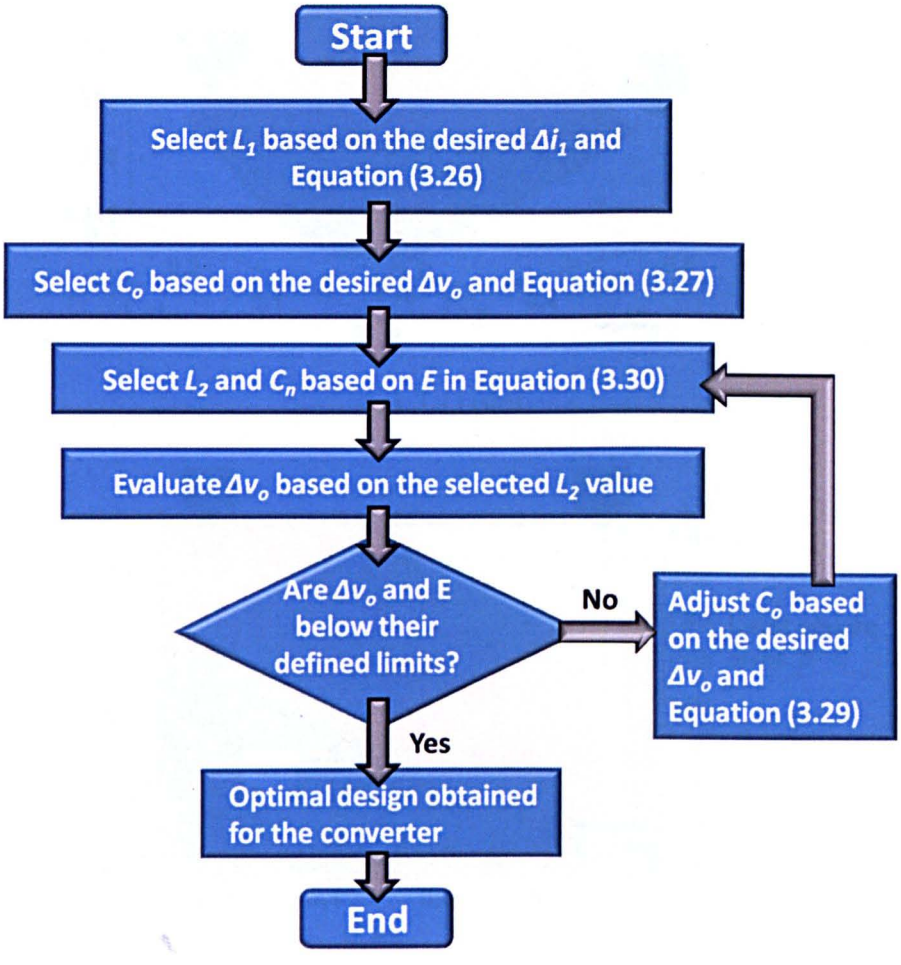

Figure 3.6 Flowchart for selecting the converter components, L_1, L_2, C_o and C_n

Table 3.1 Design specifications for a 500W Ćuk Step-down Converter

Parameters	Symbols	Values
Input voltage	V_i	100 V
Output voltage	V_o	30 - 70 V
Load resistance	R	5 Ω
Switching frequency	f_s	20 kHz
Maximum output voltage ripple (%)	Δv_o	2 percent of V_o
Maximum input current ripple (%)	Δi_l	2 percent of I_l

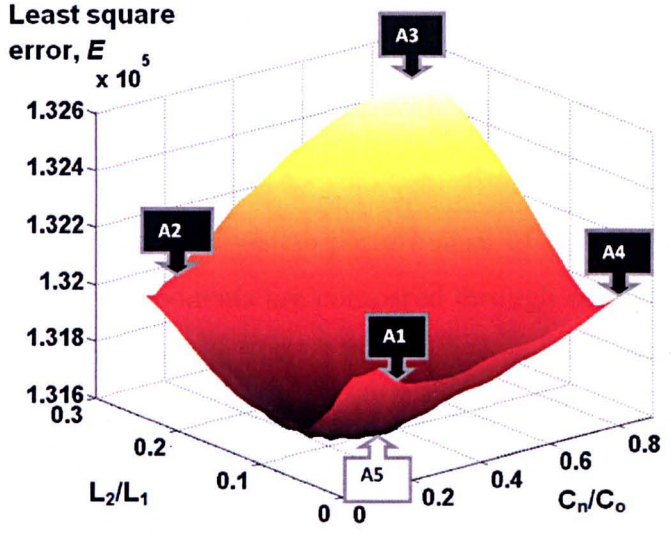

(a) 3-D plot

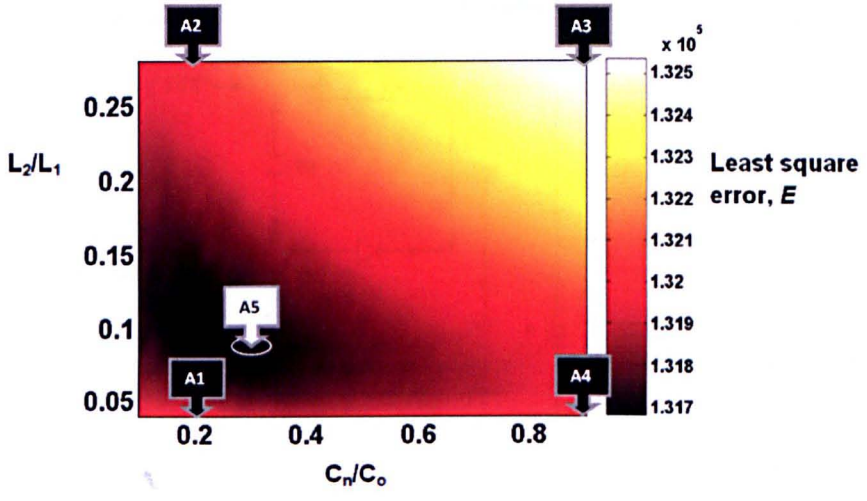

(b) Plane plot

Figure 3.7 Performance evaluation for the converter

changing from 1.0 to 9.0 μF and L_2 from 0.5 to 3.5 mH, using a 3-D plot and its corresponding plane view. In both diagrams, E values are plotted against the ratios, C_n/C_o and L_2/L_1.

As can be observed, E decreases with the reduction of both L_2 and C_n. In particular, the trough is at where C_n/C_o lies between 0.2 to 0.4, i.e., C_n ranging from 2.0 to 4.0 μF, and L_2/L_1 between 0.06 to 0.1, i.e., L_2 ranging from 0.75 mH to 1.25 mH. The lowest E value in this case is given at the point notated as A_5 with $L_2 = 0.9$ mH and $C_n = 3.0$ μF.

3.5.2 Result Discussions

To verify the proposed design scheme described above, a number of parameter sets are selected for performance comparison as shown in Figure 3.7; these are A_1 to A_5. Their respective E values together with the L_2 and C_n pairs are given in the diagram.

The transient and steady-state performance of the converter corresponding to the above selected components are compared through computer simulations using a computer model built using SIMULINK as shown in Figure 3.8. Output voltage responses for five different cases due to the same pattern of duty ratio change (i.e. from $K = 0.4$ to $K = 0.5$) are shown in Figures 3.9(a) – 3.9(e). Their performance factors are listed in Table 3.2 for comparison.

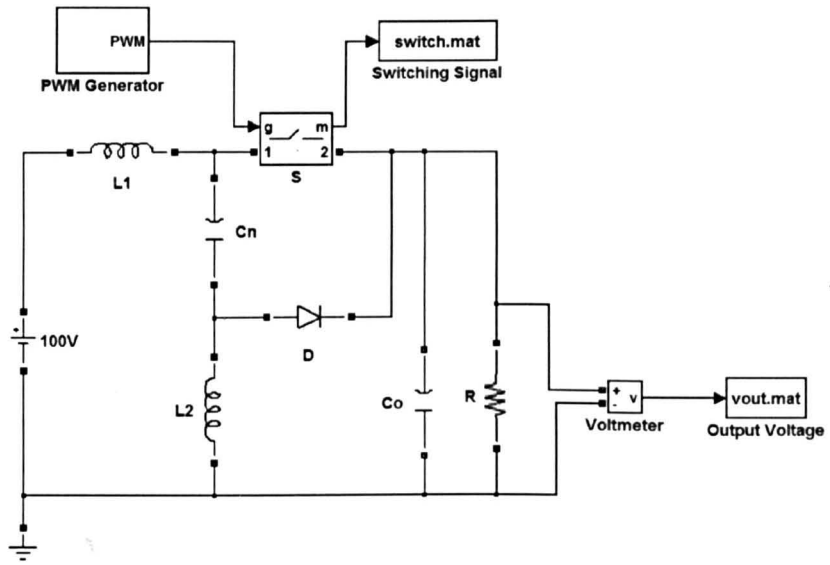

Figure 3.8 Computer model used for converter simulations

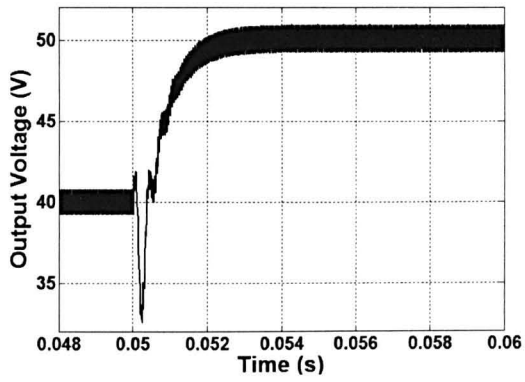

(a) Case A_1: L_2 = 0.5 mH & C_n = 2.0 μF

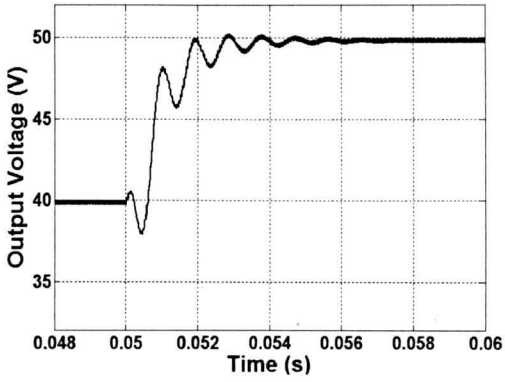

(b) Case A_2: L_2 = 3.5 mH & C_n = 2.0 μF

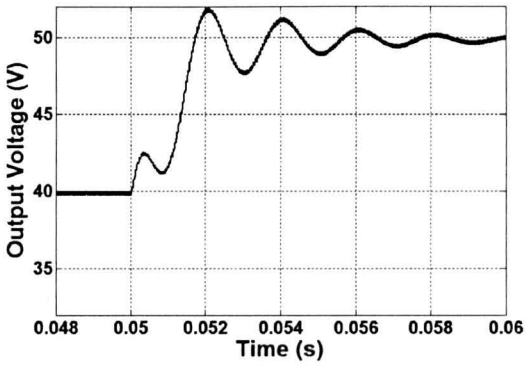

(c) Case A_3: L_2 = 3.5 mH & C_n = 9.0 μF

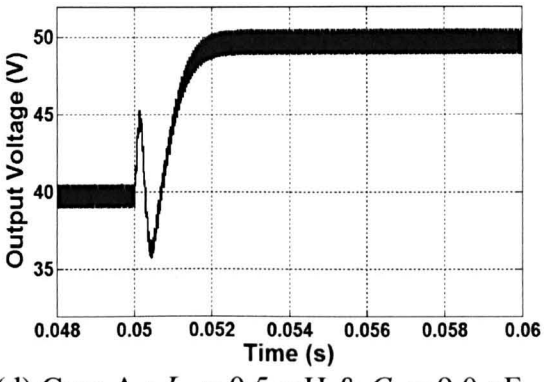

(d) Case A_4: L_2 = 0.5 mH & C_n = 9.0 μF

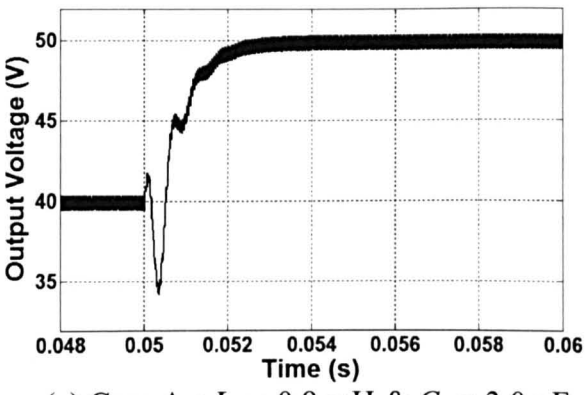

(e) Case A_5: L_2 = 0.9 mH & C_n = 3.0 μF

Figure 3.9 Transient response of the output voltage due to duty ratio variation for various pairs of L_2 and C_n values

Table 3.2 Transient and steady-state performance for the Ćuk step-down converter

Points	C_n (μF)	L_2 (mH)	V_o ripple (%)	Undershoot (%)	Settling time (ms)	E (10^5 V^2)
A_1	2.0	0.5	3.4	20.0	2.5	1.3190
A_2	2.0	3.5	0.5	5.0	7.0	1.3195
A_3	9.0	3.5	0.5	0	14.0	1.3250
A_4	9.0	0.5	3.2	10.7	2.1	1.3190
A_5	3.0	0.9	1.9	15.0	2.4	1.3160

For case A_1, L_2 = 0.5 mH and C_n = 2.0 μF. The transient response shows a large undershoot of 20 percent due to non-minimum phase effect, though it takes a relatively short time of about 2.5 ms to settle into a steady state. However, the steady-state ripple magnitude is higher than the desired 2-percent.

Case A_2 has a small undershoot of 5 percent and the steady-state ripple percentage is below 2-percent limit. However, the step response is oscillatory and takes 7 ms to settle down.

Case A_3 has no initial undershoot which is desirable. However, the transient response is subject to high levels of oscillation and takes a long time to settle down. In addition, the E value is the highest among all the cases.

Case A_4 has the best transient response comparing to the previous cases apart from the initial spikes. However, its steady-state ripple percentage is still undesirably high.

Case A_5 gives the minimum E value with an undershoot of 15 percent, the transient response time of about 2.4 ms, and the steady-state ripple of within 2 percent. This has the best performance with C_n = 3.0 μF, about one third of C_o and L_2 = 0.9 mH, less than one tenth of L_1.

The Bode plots of the above five cases are given in Figure 3.10. For all cases the gains at low frequencies and the transient characteristics are functions of the input voltage V_i, hence the circuit operating point. The resonant frequency, determined approximately as $\sqrt{1/L_pC_o} = \sqrt{(L_1+L_2)/L_1L_2C_o}$, varies around $2\times10^3 \rightarrow 3\times10^4$

rad/sec for different combinations of C_n and L_2. The phase angle reduces to -180° around the range of resonant frequency for all five cases, which is due to the two right-hand-plane zeros having breakpoint frequencies near to the same frequency range.

It can be observed that Case A_5 offers the best performance in terms of its damping while giving fast response in comparison to the other four cases. The Bode plot of this case shows that it has the highest resonant frequency. In addition, the input current ripple for case A_5 remains within the 2% limit as shown in Figure 3.11.

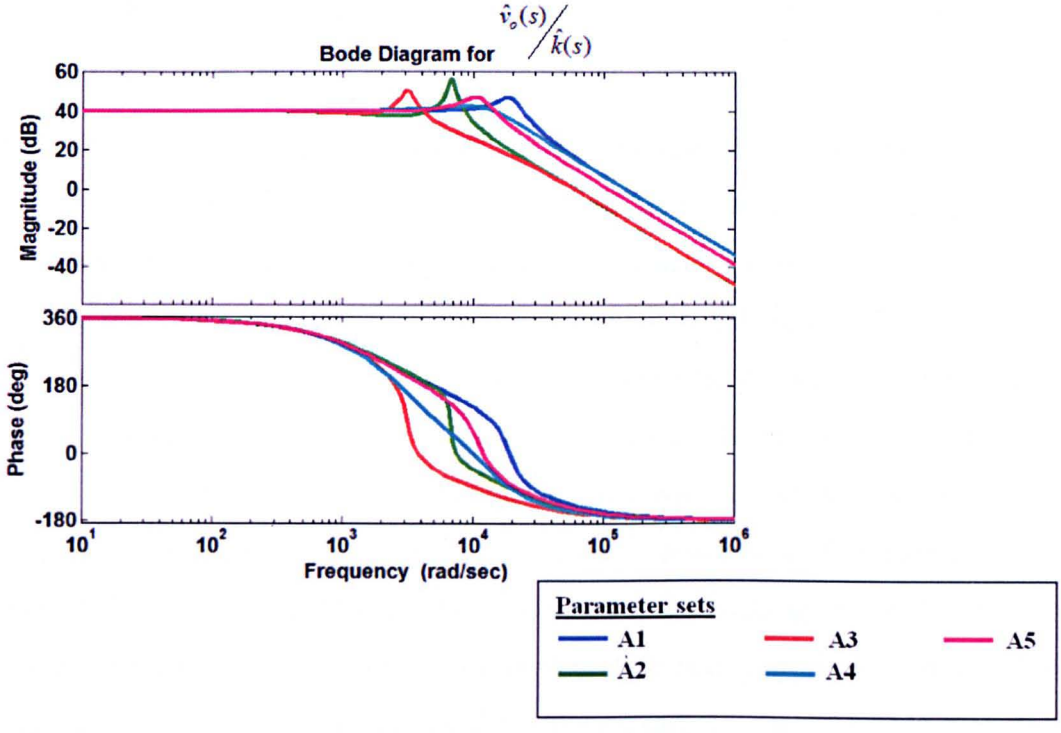

Figure 3.10 Frequency response for various sets of L_2 and C_n pairs

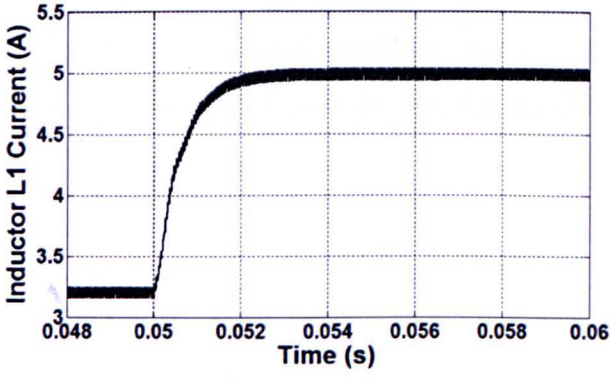

Figure 3.11 Simulated response for the current flowing through inductor L_1

The converter designed above was also used to test a simulated PV system with variable input voltage and constant output voltage. The simulated PV module has a string of 220 series cells, hence giving the same power rating as that of the previous case shown in Figures 3.9 at 100 V. This corresponds to an insolation of 85 mW/cm^2 and a cell temperature of 20°C. The output voltage is now maintained by a constant source of 50 V. The step responses for four different designs are shown in Figures 3.12(a) – 3.12(d). Duty ratio k is now changed from 0.55 to 0.5 and hence, PV voltage changes from 90.9 V to 100 V. The percentage of change (which is about 10% of the steady-state voltage operating point) is the typical value used by other authors in MPP tracking algorithm [42, 83]. Again, case A_5 offers the best transient result amongst five in terms of fast response and no transient oscillation.

The PV terminal voltage responses for case A_5 when K changes from 0.4 to 0.8 are shown in Figure 3.13. It can be observed that for larger K values (greater than 0.5), the response becomes highly oscillatory; conversely it is heavily damped for K changes at the lower end (less than 0.5). This shows that there is a desired narrow region on the I-V characteristic curves of a PV panel where variations of K lead to faster and non-oscillatory terminal voltage variations as shown in Figure 3.14. It is important to know this range when using the converter to perform the maximum power point tracking, as too large a K value leads to unnecessary fluctuation around the peak power point while too small K slows down the tracking speed. To obtain a PV voltage response with overshoot of less than 20% and settling time of less than 30 ms, the desired operating range, for the current example, should be between 83.3 V and 113.6 V, corresponding to $K = 0.6$ and $K = 0.44$, respectively as denoted by the unshaded region in Figure 3.14. It is also important to note that at the start-up stage before the PWM signal is sent to the converter, the desired voltage value and hence the duty cycle of the PWM signal could be firstly set according to the MPP prediction model of the PV module. This is to prevent the converter from operating within the shaded region in Figure 3.14.

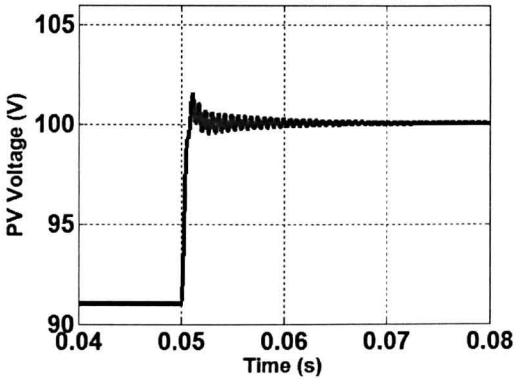

(a) Case A_1: L_2 = 0.5 mH & C_n = 2.0 μF

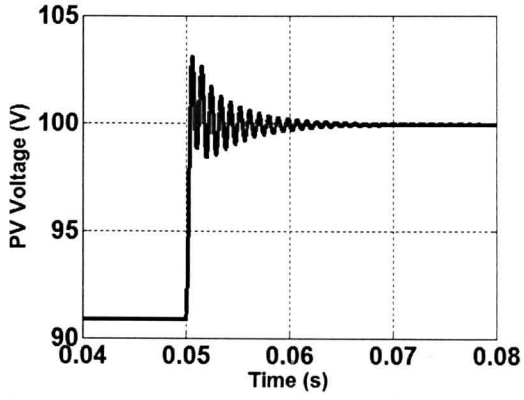

(b) Case A_2: L_2 = 3.5 mH & C_n = 2.0 μF

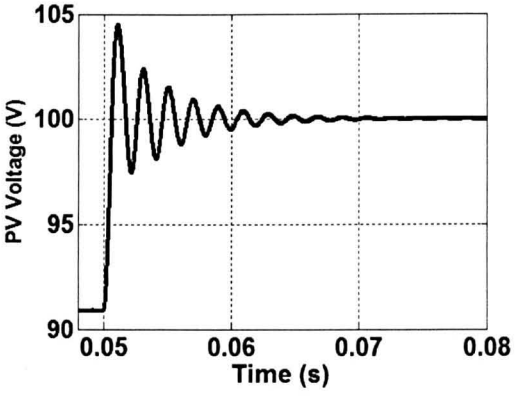

(c) Case A_3: L_2 = 3.5 mH & C_n = 9.0 μF

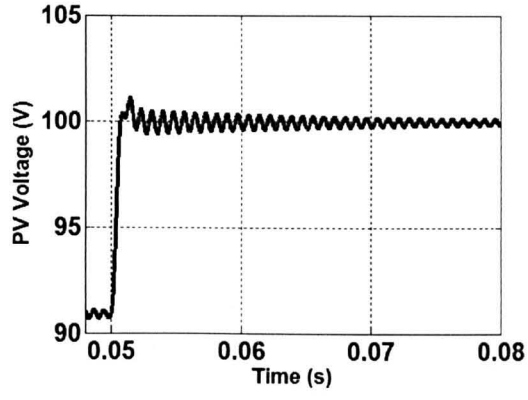

(d) Case A_4: L_2 = 0.5 mH & C_n = 9.0 μF

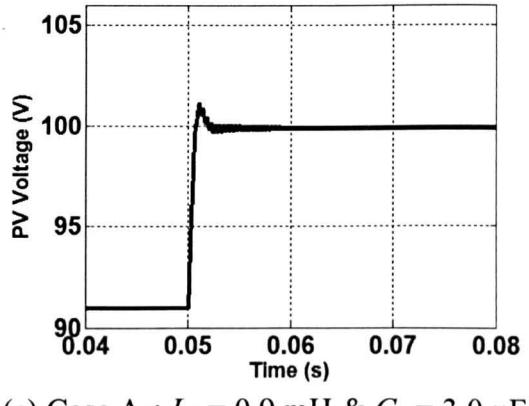

(e) Case A_5: L_2 = 0.9 mH & C_n = 3.0 μF

Figure 3.12 Transient responses of PV voltages with different L_2 and C_n values

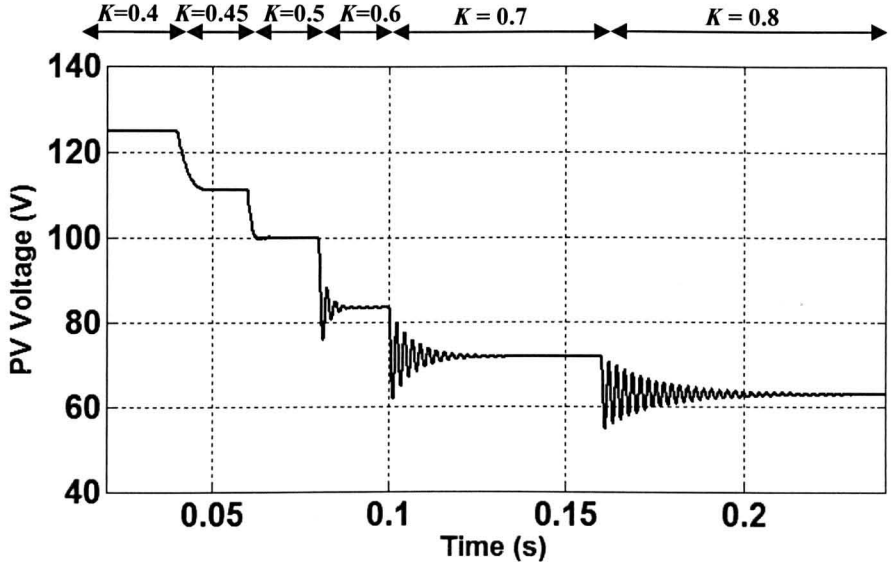

Figure 3.13 Step responses of PV terminal voltage for different K values

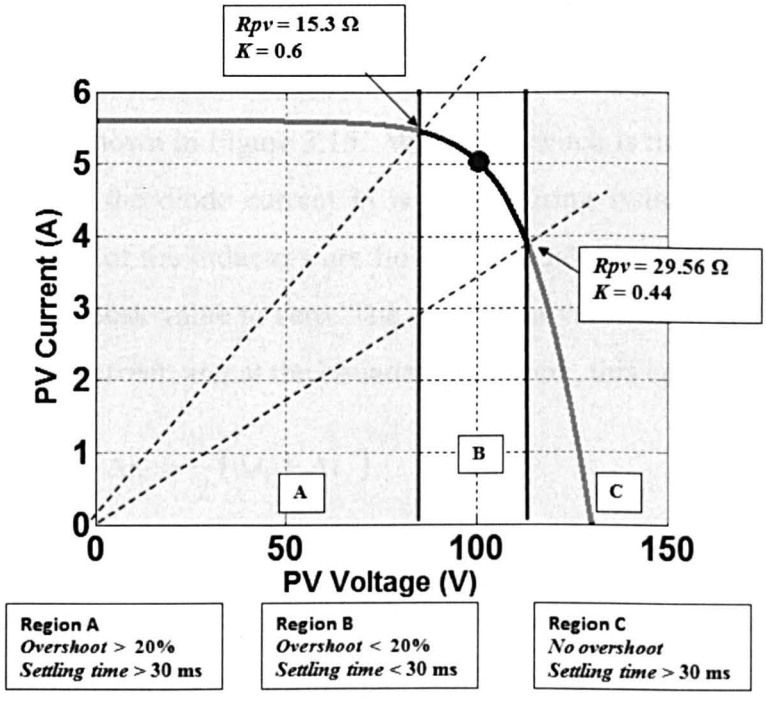

Figure 3.14 Variation range of K for a PV panel under a specific weather condition

3.6 Converter Operation in Discontinuous Conduction Mode

In the previous analysis, the converter components were selected based on the continuous-conduction-mode of operation (CCM). However, they may lead to the non-linear operation when the following conditions occur:

- Diode current becomes zero during the switch turn-off time
- Voltage across C_n becomes zero during the switch turn-on time.

The former occurs when the output current is lower than the total peak-to-peak current ripples in inductor L_1 and L_2. For the latter, the load is drawing a sufficiently large current that the voltage on C_n discharges to zero during the switch on time. Under each of these conditions, the effects on the converter operation and its design scheme are explored in the following sections.

3.6.1 Discontinuous Diode Current Mode (DDCM)

Assuming C_n is sufficiently large and hence fluctuation in v_{cn} around its average level is negligible, the analysis is performed firstly with the converter operating at the boundary between DDCM and CCM. The currents flowing through L_1, L_2, D and S are shown in Figure 3.15. When the switch is turned on, the diode is reversed-biased and the diode current i_D is zero. During switch turn-off time, the discharging currents of the inductors are flowing through the diode, and hence i_D is decreasing from its peak value to zero. The total mean value for i_1 and i_2 is equal to the average output current, and at the boundary condition, this can be expressed as

$$I_{OB\,(DDCM\,)} = \frac{1}{2}\Delta i_o = \frac{1}{2}\left(\Delta i_1 + \Delta i_2\right) \tag{3.31}$$

If the output current drawn by the load is lower than that in Equation (3.31), the converter will operate in diode-current-discontinuous-conduction mode. Under this condition, the analysis is performed based on the two different operating conditions; constant input voltage – variable output voltage, and vice versa.

3.6.1.1 Constant V_i and Variable V_o

When the converter operates as a DC drive, output voltage is variable while V_i is taken as constant. To express Equation (3.31) in terms of V_i, T_s, L_p and K, V_o can be eliminated by substituting Equations (3.26) and (3.28) (i.e. the ripple equations

from the Section 3.4.1.) into Equation (3.31). Thus, the converter will operate in DDCM if the output current is lower than the following current limit:

$$I_{OB\,(DDCM\,)} = \frac{V_i T_s (L_1 + L_2)}{2 L_1 L_2} K(1-K) = \frac{V_i T_s}{2 L_p} K(1-K) \tag{3.32}$$

Using the designed converter in Section 3.5, $I_{OB(DDCM)}$ varies for a different duty ratio, K as shown in Figure 3.16. At $K = 0.5$, the peak-to-peak inductor currents

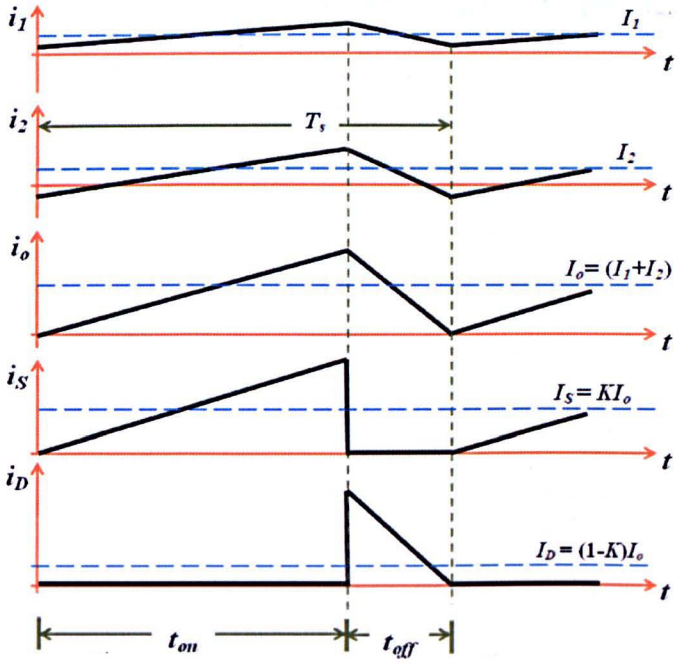

Figure 3.15 Current waveforms for the converter operating at the boundary between DDCM and CCM

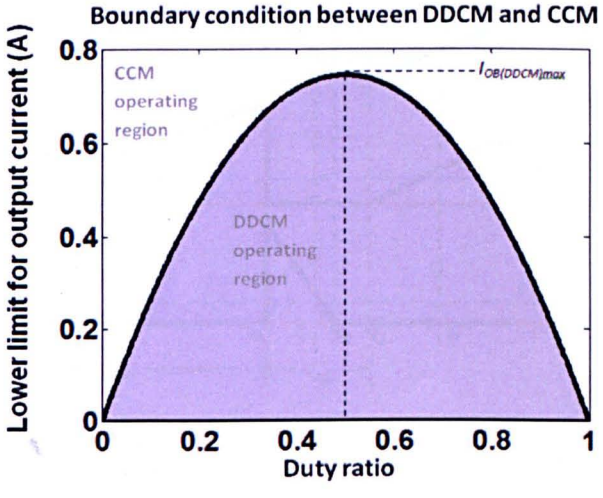

Figure 3.16 Boundary output current between CCM and DDCM with constant input voltage source

are the highest and, hence, $I_{OB(DDCM)}$ has a maximum value of 0.744 A which is evaluated from

$$I_{OB\,(DDCM\ ),\max} = \frac{V_i T_s}{8 L_p} \tag{3.33}$$

As K is changing from 0.5 to 0 and from 0.5 to 1, $I_{OB(DDCM)}$ decreases from the peak value. Under DDCM operating condition, the resulting current waveforms are shown in Figure 3.17. Based on the converter design in the previous section, L_1 is at least 10 times higher than L_2; hence, $\Delta i_2 > \Delta i_1$. The circuit operation in one switching cycle can be divided into 5 stages. Operation in each stage is explained as follows:

Stage 1: From t_a to t_b, S is turned on and D is reverse-biased. During this period, the circuit operation is similar to the switch turn-on state of continuous-conduction-mode as shown in Figure 3.18(a).

Stage 2: From t_b to t_c, S is open. i_D is decreasing but has a positive instantaneous value and hence D is forward-biased. The circuit state during this period is similar to the switch turn-off period of the continuous-conduction-mode as shown in Figure 3.18(b).

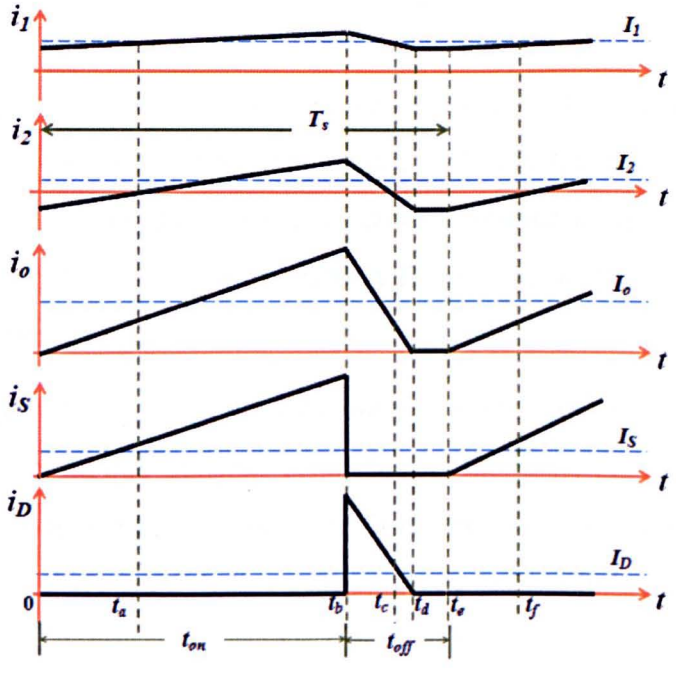

Figure 3.17 Current waveforms when the converter is operating in DDCM

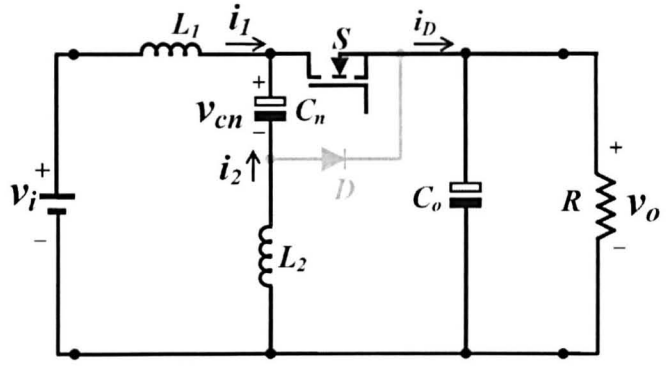

(a) Converter circuit states from t_a to t_b

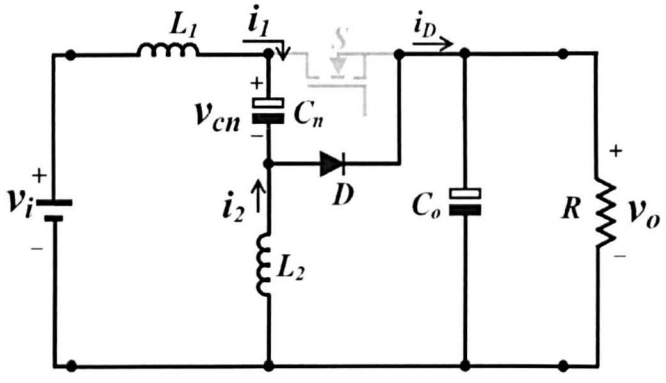

(b) Converter circuit states from t_b to t_c

Figure 3.18 Converter circuit states from t_a to t_c

Stage 3: At t_c, S is still open and L_2 is fully discharged. From this point to t_d, L_2 is being charged by L_1 through V_i and C_n. Hence, i_2 is increasing in the opposite direction to those in the previous states while i_1 is decreasing. The magnitude of i_1 is greater than i_2 and there is some current flowing through the forward-biased D as shown in Figure 3.19(a).

Stage 4: At t_d, S is still open but the magnitude of i_1 is equal to that of i_2 resulting in zero diode current. From this point to t_e, D becomes reverse-biased isolating the load from the converter. Since the steady-state value for the voltage across C_n is V_i, there is no further current decay in both inductors within this period. The circuit state within this period is shown in Figure 3.19(b).

Stage 5: From t_e to t_f, S is turned on again and the circuit state, as shown in Figure 3.19(c), is similar to that in Stage 1 except that now the inductor L_2 is discharging its energy to L_1 through C_n and V_i. This continues until, t_f is reached. At

this time, L_2 is fully discharged and i_2 starts to be charged in the same direction as that in Stage 1, hence a full cycle of DDCM is achieved.

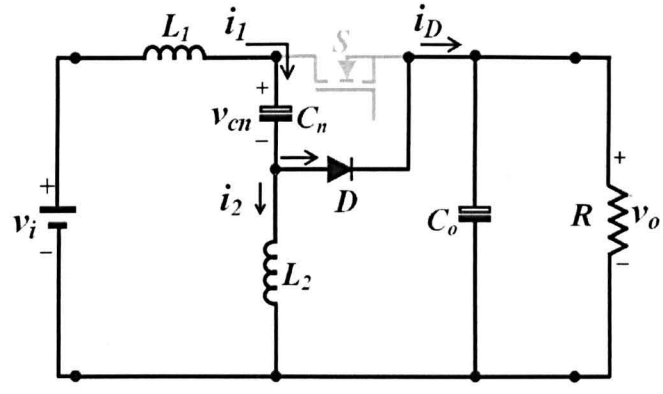

(a) Converter circuit states from t_c to t_d

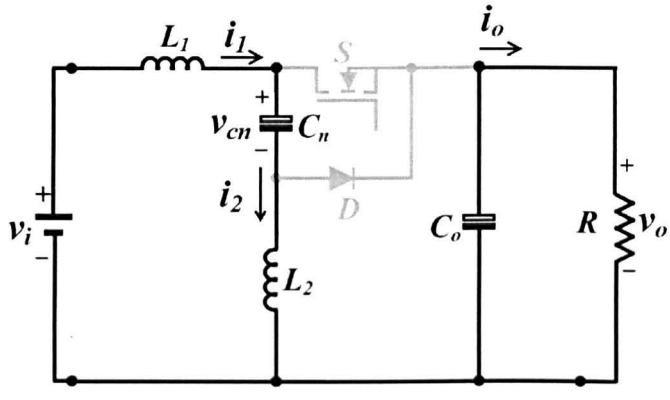

(b) Converter circuit states from t_d to t_e

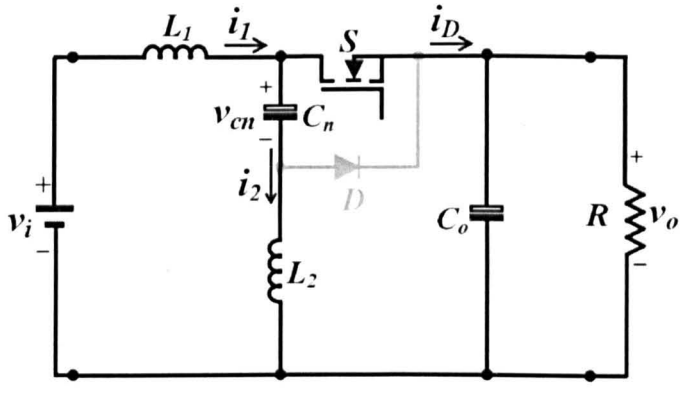

(c) Converter circuit states from t_e to t_f

Figure 3.19 Converter circuit states from t_c to t_f

At steady state, the net changes in i_1 and i_2 are zero and hence voltage-time balance equations for L_1 and L_2 are given respectively by

$$(V_i - V_o)KT_s + (V_i - V_{cn} - V_o)\Delta_D T_s = 0$$

and $$(V_{cn} - V_o)KT_s + (-V_o)\Delta_D T_s = 0 \tag{3.34}$$

where $\Delta_D T_s = t_d - t_b$ denotes the time period during which the switch is turned off and the diode current has a non-zero value, while Δ_D represents the fraction of the switching time when the diode is active.

Eliminating V_{cn} gives the relationship between output and input voltages which is given by

$$\frac{V_o}{V_i} = \frac{K}{K + \Delta_D} \tag{3.35}$$

Based on the steady-state waveform for i_{out}, the average output current can be expressed as

$$I_{out} = (\Delta i_1 + \Delta i_2)\left(\frac{K + \Delta_D}{2}\right) \tag{3.36}$$

where $\Delta i_1 = \frac{V_o}{L_1}\Delta_D T_s$ and $\Delta i_2 = \frac{V_o}{L_2}\Delta_D T_s$

Thus, Δ_D can be defined as

$$\Delta_D = \frac{2L_p I_{out}}{KV_i T_s} \tag{3.37}$$

Eliminating Δ_D by substituting (3.37) into (3.35) gives the equivalent DDCM voltage conversion ratio as

$$\frac{V_o}{V_i} = \frac{K^2}{K^2 + \frac{1}{4}\left(I_{out} / I_{OB(DDCM),\max}\right)} \tag{3.38}$$

When the converter operates in DDCM, the input-output voltage relationship becomes non-linear, as depicted by Equation (3.38). Using the converter design in Section 3.5, the voltage relationship is shown in Figures 3.20 and it has been plotted against the normalized output current, $I_{out} / I_{OB(DDCM),\max}$. The current value

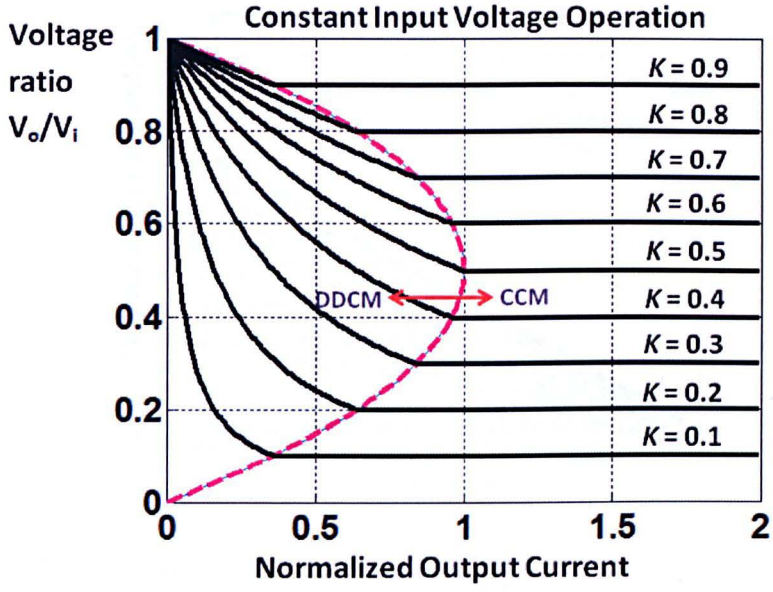

Figure 3.20 Input-output voltage relationship for the converter keeping V_i constant at the boundary condition is denoted by the dashed line. As $I_{out}/I_{OB\,(DDCM\,),\max}$ decreases from the boundary current limit to zero for any duty cycle value, the converter output-input voltage ratio approaches unity.

3.6.1.2 Constant V_o and Variable V_i

Conversely when the converter is applied to an MPP tracker for a PV array, V_i may fluctuate, while V_o is taken as a constant. Thus, the lower limit for the output current is written as

$$I_{OB\,(DDCM\,)} = \frac{V_o T_s}{2L_p}(1-K) \tag{3.39}$$

Based on the converter specifications in Section 3.5, Figure 3.21 shows the plot of $I_{OB(DDCM)}$ as a function of duty ratio K. At $K = 0$, the peak-to-peak inductor currents are the highest and hence $I_{OB(DDCM)}$ has a maximum value of 1.5 A which is given by

$$I_{OB\,(DDCM\,),\max} = \frac{V_o T_s}{2L_p} \tag{3.40}$$

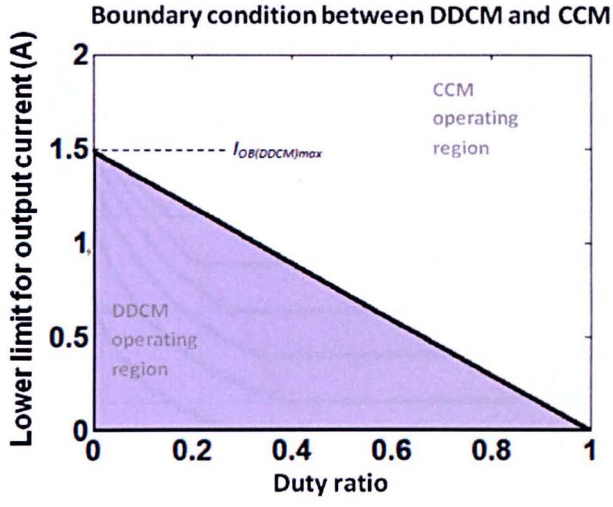

Figure 3.21 Boundary output current between CCM and DDCM with constant output voltage

$I_{OB(DDCM)}$ decreases as K increases and it has a value of 0 when $K = 1$. The operating principles for this operating condition are the same as that for constant V_i and variable V_o but Δ_D now can be expressed as

$$\Delta_D = \frac{2L_p I_{out}}{V_o T_s} \tag{3.41}$$

Subsequently, the equivalent DDCM voltage conversion ratio is expressed as

$$\frac{V_o}{V_i} = \frac{K}{K + \left(I_{out} \Big/ I_{OB(DDCM),\max} \right)} \tag{3.42}$$

The output-input voltage relationship becomes non-linear, as depicted by Figures 3.22 when the normalized output current, $I_{out} / I_{OB(DDCM),\max}$ is below the $I_{OB(DDCM)}$ boundary denoted by the dashed line. As $I_{out} / I_{OB(DDCM),\max}$ decreases from the boundary current limit to zero for any duty cycle value, the V_o/V_i ratio also becomes unity.

From the above analysis, it can be observed that the linear operating region for constant V_i and variable V_o conditions is wider both at low and high K values while for constant V_o and variable V_i, the region is only wider when K is large.

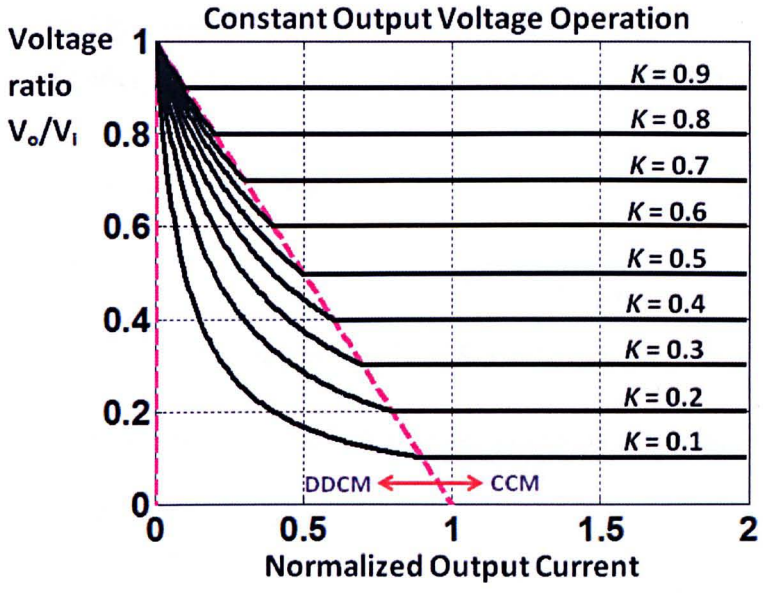

Figure 3.22 Input-output voltage relationship for the converter, keeping V_o constant

3.6.2 Discontinuous Capacitor Voltage Mode (DCVM)

Assuming L_1 and L_2 are sufficiently large, fluctuations of i_1 and i_2 around their average levels are negligible. Analysis firstly considers the converter when it is operating at the boundary between DCVM and CCM. The voltages across V_{cn} and D are shown in Figure 3.23. During switch turn-off time, C_n is charged by the inductor current i_1 and the voltage across it, v_{cn} is increasing. The diode remains forward biased and hence there is a negligibly small voltage drop across it. During switch turn-on time, C_n discharges its energy to L_2 and hence v_{cn} is decreasing from its peak value, which is Δv_{cn} to zero. On the other hand, the diode is reverse-biased and the voltage across it is the reverse of v_{cn}.

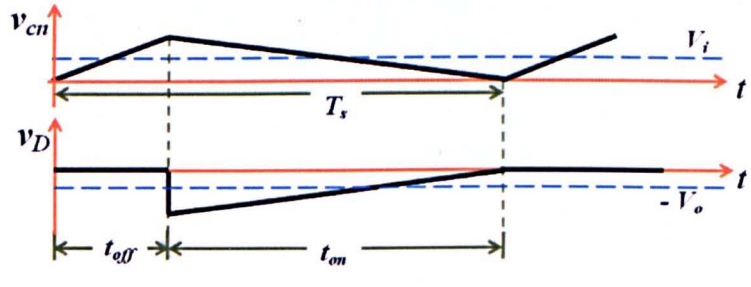

Figure 3.23 Voltage waveforms when the Ćuk step-down converter is operating at the boundary between CCM and DCVM

The average value of v_{cn} over a switching period is equal to that of the input voltage and under this boundary condition, it can be expressed as

$$V_{cn} = V_i = \frac{1}{2}\Delta v_{cn} = \frac{KT_s}{2C_n} I_2 \tag{3.43}$$

where

$$I_2 = (I_1 + I_2)(1 - K) = I_{out}(1 - K) \tag{3.44}$$

Meanwhile, the average value for the diode voltage is given by

$$V_D = -\frac{K}{2}\Delta v_{cn} = -KV_i = -V_o \tag{3.45}$$

3.6.2.1 Constant V_i and Variable V_o

When the converter is applied to a DC motor for speed control, the input voltage is constant while the output voltage can be regulated by adjusting the switching duty ratio. To express Equation (3.43) in terms of I_{out}, C_n, T_s and K, the I_2 term can be substituted by Equation (3.44). Thus, the converter operates in the DCVM if the output current has a value greater than the following current limit:

$$I_{OB(DCVM)} = \frac{2V_i C_n}{T_s K(1 - K)} \tag{3.46}$$

Using the converter design in Section 3.5, Figure 3.24 shows the plot of $I_{OB(DCVM)}$ as a function of duty ratio K. At K = 0.5, the value of $I_{OB(DCVM)}$ has a

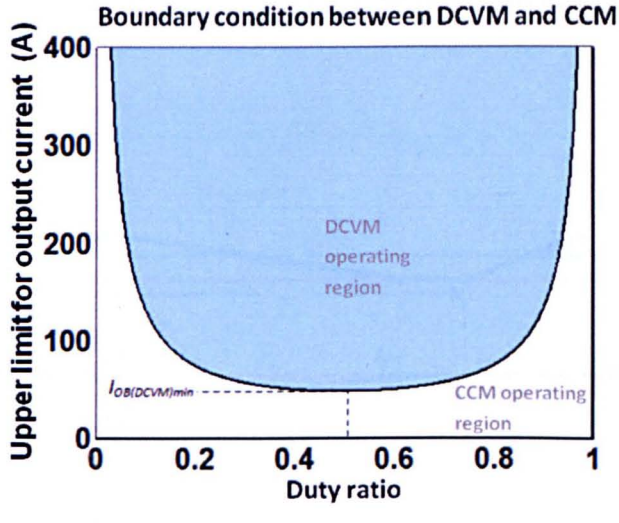

Figure 3.24 Boundary output current for the converter between CCM and DCVM with constant input voltage source

minimum value of 48 A which can be computed from

$$I_{OB\,(DCVM\ ),\min} = \frac{8V_i C_n}{T_s} \tag{3.47}$$

The voltage waveforms for when the converter operates in DCVM, are shown in Figure 3.25. The operation of the circuit can be explained in three stages as follow:

Stage 1: From 0 to t_x, S is turned off and D is forward-biased. During this period, the circuit operation which is similar to switch turn-off state of the CCM as shown in Figure 3.26(a).

Stage 2: From t_x to t_y, S is turned on and D is now reverse-biased. Energy is transferred from C_n to L_2 and R through S causing a decay in v_{cn}. This continues until v_{cn} reaches zero value at t_y. The circuit state from t_x to t_y is illustrated by Figure 3.26(b).

Stage 3: From t_y to t_z, S is still turned on but D becomes forward-biased as C_n has been fully discharged. Energy is now supplied to R by the source and L_2 while L_1 is still charged by V_i through S and V_o. The circuit state within this period is shown in Figure 3.26(c). A cycle of DCVM is achieved when S is turned off again at t_z.

At steady state, the net change in v_{cn} is zero and hence the current-time balance equation for C_n is given by

$$(-I_2)\Delta_C T_s + I_1(1-K)T_s = 0 \tag{3.48}$$

and $\Delta_C T_s = t_y - t_x$. Hence, we have the relationship between I_1 and I_2 given as

$$\frac{I_1}{I_2} = \frac{\Delta_C}{(1-K)} \tag{3.49}$$

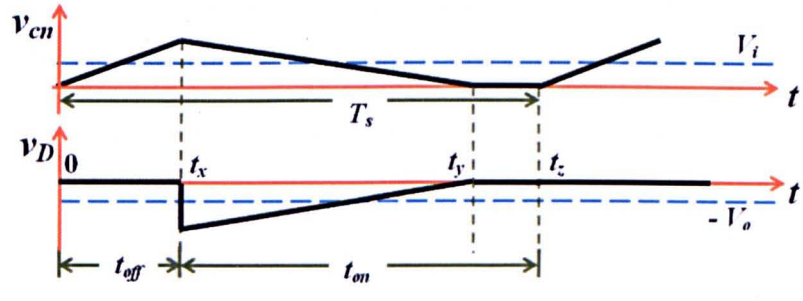

Figure 3.25 Voltage waveforms when the converter operating in DCVM

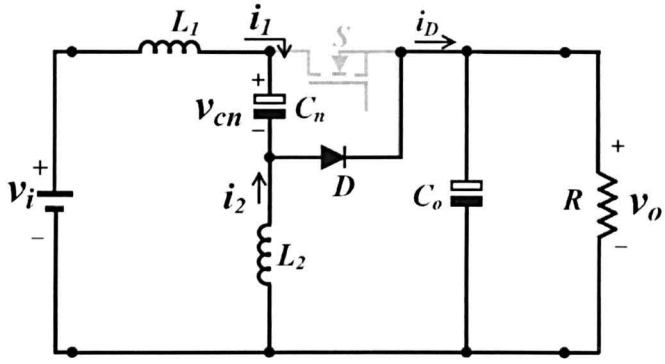

(a) Converter circuit states from 0 to t_x

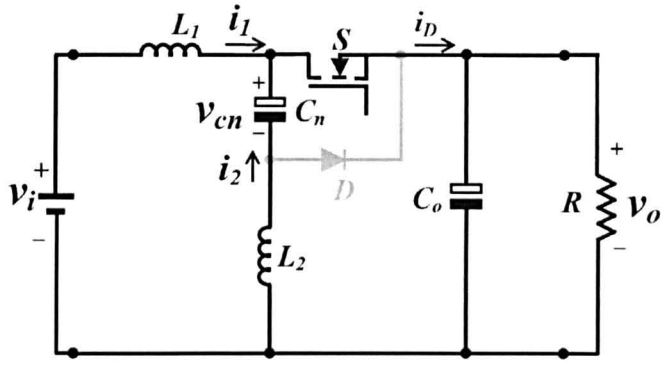

(b) Converter circuit states from t_x to t_y

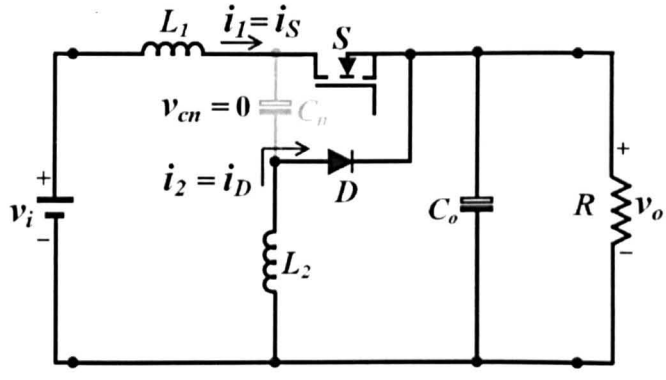

(c) Converter circuit states from t_y to t_z

Figure 3.26 Circuit states when the Ćuk step-down converter is operating in DCVM

The average voltage across C_n which is V_i can be written as

$$V_i = V_{cn} = \frac{I_1 T_s}{2C_n}(1 - K)(1 - K + \Delta_C) \tag{3.50}$$

The average voltage across D, V_D which is $-V_o$ can be written as

$$V_o = -V_D = \frac{I_2 \Delta_C T_s}{C_n}\left(\frac{\Delta_C}{2}\right) = \frac{I_1 T_s}{2C_n}(1-K)\Delta_C \tag{3.51}$$

Subsequently by taking the ratio between Equations (3.51) and (3.50), the relationship between output and input voltages is obtained as

$$\frac{V_o}{V_i} = \frac{\Delta_C}{1-K+\Delta_C} \tag{3.52}$$

Assuming a lossless converter, the relationship between input and output currents is given by

$$\frac{I_{in}}{I_{out}} = \frac{I_1}{I_1+I_2} = \frac{V_o}{V_i} = \frac{\Delta_C}{1-K+\Delta_C} \tag{3.53}$$

Eliminating I_{in} by substituting Equation (3.53) into (3.50) gives

$$V_i = \frac{I_{out} T_s}{2C_n}(1-K)\Delta_C \tag{3.54}$$

Thus, Δ_C can be expressed as

$$\Delta_C = \frac{2V_i C_n}{I_{out} T_S (1-K)} = \frac{I_{OB(DCVM)\min}}{4(1-K)I_{out}} \tag{3.55}$$

Eliminating Δ_C by substituting (3.55) into (3.52) gives the equivalent DCVM conversion ratio as

$$\frac{V_o}{V_i} = \frac{1}{4(1-K)^2\left(I_{out}/I_{OB(DCVM),\min}\right)+1} \tag{3.56}$$

For a wide range of K values, the output-input voltage ratio is plotted against the normalized output current, $\left(I_{out}/I_{OB(DCVM),\min}\right)$ as shown in Figure 3.27. As can be observed, the ratio can become non-linear when the output current drawn by the load is greater than $I_{OB(DCVM)}$ which is denoted by the dashed line. As $\left(I_{out}/I_{OB(DCVM),\min}\right)$ increases further from the line, the voltage ratio gradually decreases towards zero.

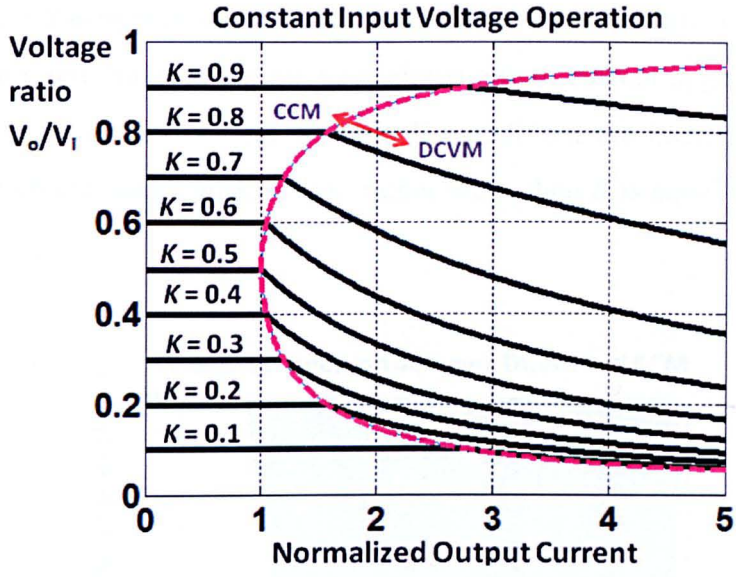

Figure 3.27 Input-output voltage relationship for the converter, keeping V_i constant

3.6.2.2 Constant V_o and Variable V_i

On the other hand, when the converter is applied to an MPP tracker for a PV array, V_i is variable and V_o is taken as a constant. Thus, the upper limit for the output current is written as

$$I_{OB\,(DCVM\,)} = \frac{2V_oC_n}{T_sK^2(1-K)} \tag{3.57}$$

Using the designed converter in Section 3.5, Figure 3.28 shows the plot of $I_{OB(DCVM)}$ as a function of K. At $K = 2/3$, $I_{OB(DCVM)}$ has a minimum value of 40.5 A which is given by

$$I_{OB\,(DCVM\,),\min} = \frac{13.5V_oC_n}{T_s} \tag{3.58}$$

In addition, Δ_C for this case can be written as

$$\Delta_C = \frac{2V_oC_n}{I_{out}T_SK(1-K)} = \frac{I_{OB\,(DCVM\,)\min}}{6.75K(1-K)I_{out}} \tag{3.59}$$

Subsequently, the equivalent DCVM voltage conversion ratio is expressed as

$$\frac{V_o}{V_i} = \frac{1}{6.75K(1-K)^2\left(I_{out}/I_{OB\,(DCVM\,),\min}\right)+1} \tag{3.60}$$

Under this operating condition, the voltage ratio, as shown in Figure 3.29 may also become non-linear when the normalized output current is greater than $I_{OB(DCVM)}$. Similar to the constant V_i and variable V_o condition, the linear operating region is wider at both low and high K values, rather than when K is equal to 0.5.

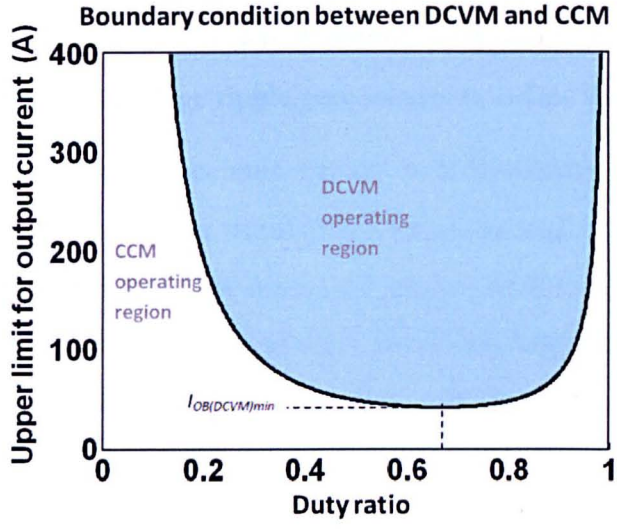

Figure 3.28 Boundary output current for the converter between CCM and DCVM with constant output voltage

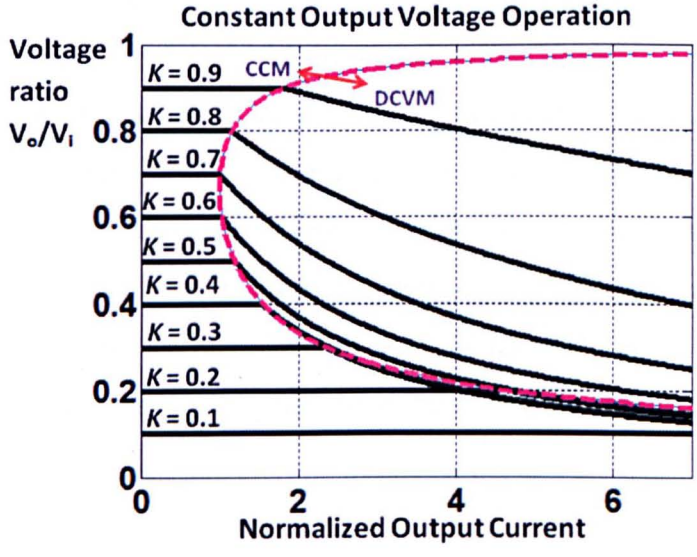

Figure 3.29 Input-output voltage relationship for the converter keeping V_o constant

3.7 Summary

This chapter presented a detailed study of the Ćuk step-down converter through deriving generalised transfer function models for two different operating modes, namely, constant input voltage - variable output voltage, and constant output voltage - variable input voltage. A novel method for selecting the energy storage components in the circuit has been developed. This is based on minimising the sum of squared errors between the desired and actual output voltages as well as suppressing the steady-state current and voltage ripple percentages to below the desired levels.

Simulation results for specimen circuits with five different parameter sets were presented and compared. These simulations, using the real circuit and including the effects of chopping, validated the analytical design method. The designed converter also works well for both operating modes. However, when controlling the terminal voltage of a PV panel, to achieve fast and well-damped maximum power point searching the duty ratio of the converter can only vary within a narrow range determined by the I-V characteristics of the PV module under the specific weather conditions.

The converter has also two other modes of operation which differ from the continuous-conduction-mode. The first is the discontinuous-diode-conduction-mode under which the diode current falls to zero over part of the switch turn-off period. This mode results from the final load current being less than a certain value. In the other mode, the voltage across the intermediate capacitor, C_n falls to zero during part of the switch turn-on period. This results from large values of the load current. Both modes were fully analysed for both constant input voltage, and constant output voltage cases. Onset of each mode is marked by the appearance of a non-linear relationship between the relevant voltage and the duty cycle K. The boundaries between modes were shown graphically in the $V_o - K$ or $V_i - K$ plane.

Chapter 4
Modelling and Control of a Ćuk Step-up Converter

4.1 Introduction

As reviewed in Chapter 1, the conventional Ćuk converter can also be modified to obtain a Ćuk step-up converter with its output voltage always higher than the input. This converter is particularly useful as an interface between a low-voltage DC power supply like a PV module and a high-voltage load or a high-voltage DC bus. Like the Ćuk step-down type, a Ćuk step-up converter also has at least two modes of operation, namely constant input voltage – variable output voltage, and constant output voltage – variable input voltage, which might be used for either a DC motor drive, or a PV power system as shown in Figures 4.1(a) and 4.1(b). A thorough and accurate analysis of the steady-state and transient behaviours of the converter in both operating modes is important for the design of the control system. In particular, when the converter is applied to a PV system, its dynamics will change as the input varies with the weather conditions, while the output is maintained constant so that the maximum power point tracking for the PV can be achieved efficiently. Moreover, with the linearized transfer function models, the regulation of converter duty cycle can be implemented using classical control technique which is cheaper and more straightforward to implement than more advanced control systems.

In this chapter, an analysis is performed on a Ćuk step-up converter operating in continuous-conduction-mode. Using a state-space averaging method and small signal analysis as proposed in Chapter 3, the first set of transfer function models is derived to describe the variations in the output voltage due to both small perturbations of input voltage and duty cycle. Another set of transfer function models is also developed to describe the variations in input voltage due to both small perturbation of output voltage and duty cycle. Based on these models, a negative-feedback control system can be implemented by employing Nyquist stability criterion and the Bode plots. Using this method, a controller based on lead-lag compensation technique is implemented to regulate the voltage for a PV module.

The design is simulated in MATLAB-SIMULINK and the advantages of the control system are demonstrated through its robustness to varying operating conditions. This converter has also been applied to the PV-integrated converter configuration which will be discussed in Chapter 5 of this thesis.

4.2 Converter Operation in Continuous Conduction Mode

Similar to the Ćuk step-down converter discussed in Chapter 3, the Ćuk step-up converter is also a unidirectional circuit that can operate in one of the two modes, namely, the left-hand side voltage V_i adjustable while right-hand side voltage V_o constant and vice versa. Under these operating modes, the schematic circuits for the converter are shown in Figures 4.1(a) and 4.1(b). The analysis below is applicable to both modes and assumes an ideal circuit, i.e. the internal resistance of the circuit

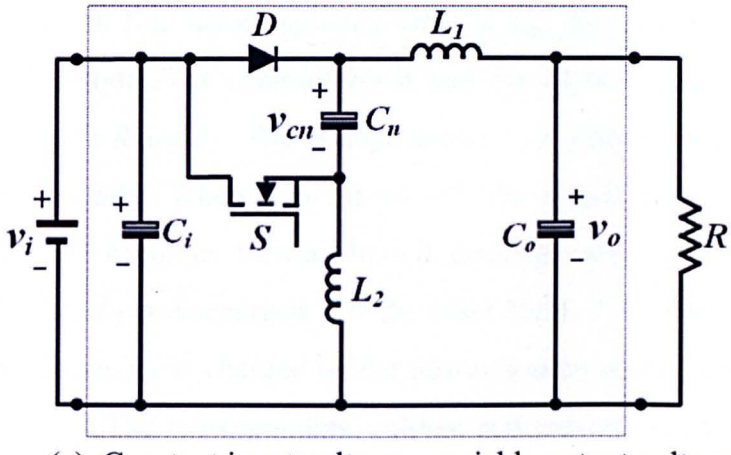

(a) Constant input voltage – variable output voltage

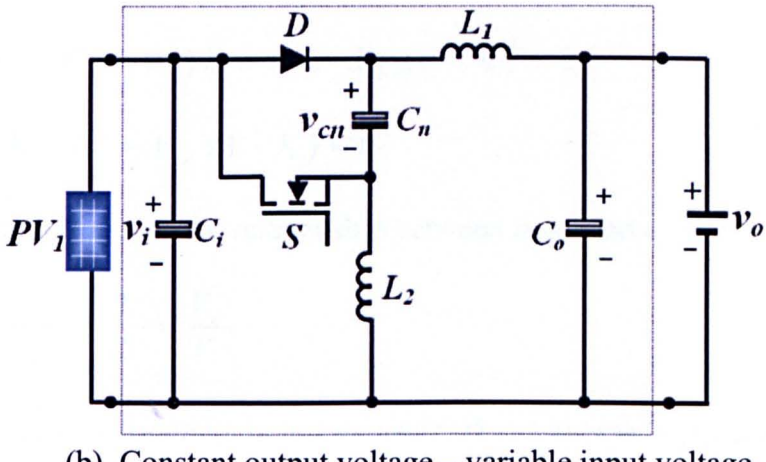

(b) Constant output voltage – variable input voltage

Figure 4.1 Ćuk step-up converter for two different operation modes

components can be neglected; and the diode D and switch S are turned on/off instantaneously and their on/off state losses are ignored. The key element in the circuit is still the capacitor C_n, which transfers energy from input to output. If the capacitors C_i, C_o and C_n are sufficiently large, fluctuations of V_i, V_o and V_{cn} around their average levels will be small. Also with high enough switching frequency, i_1 and i_2 can be considered varying linearly over time during a switching period. The following analysis uses smoothed voltages and currents defined as the instantaneous values averaged over one switching period. In this analysis also, continuous-conduction-mode (CCM) at steady state is considered. However unlike the Ćuk step-down converter, the averaged value for the voltage across C_n is now given as

$$V_{cn} = V_o \tag{4.1}$$

4.2.1 Operating Principles

When switch S is turned on for a time of t_{on}, the circuit state is as shown in Figure 4.2(a). Diode D is reverse-biased and the input voltage, together with C_n, supplies energy to R and L_1. The voltage across L_2 is now V_i resulting in the current i_2 increasing linearly. When S is turned off, the circuit structure is illustrated in Figure 4.2(b). D becomes forward-biased causing only the input voltage supply energy to R; thus L_1 is discharged. On the other hand, V_i is connected across C_n and L_2 in series. Hence, C_n is charged by the power source while L_2 is being discharged through V_i to C_n. The corresponding voltage and current waveforms are shown in Figure 4.3. For steady-state operation, the net change in the inductor current is zero and thus the voltage-time balance equations for L_1 and L_2 are given by

$$(V_i + V_{cn} - V_o)K + (V_i - V_o)(1 - K) = 0$$

and $$V_i K + (V_i - V_{cn})(1 - K) = 0 \tag{4.2}$$

Eliminating V_{cn} gives the relationship between input and output voltages as

$$\frac{1}{1-K} = \frac{1}{K'} = \frac{V_o}{V_i} \tag{4.3}$$

For the case of lossless circuit elements, the converter input power P_{in} equals the output power, P_{out}, hence, we have

$$V_i I_{in} = V_o I_{out} = V_o I_1 \quad \text{and} \quad V_i I_{in} = V_i (I_1 + I_2) \tag{4.4}$$

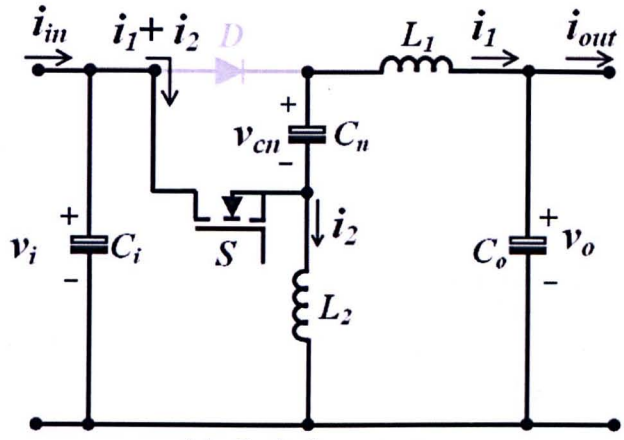

(a) Switch-on state

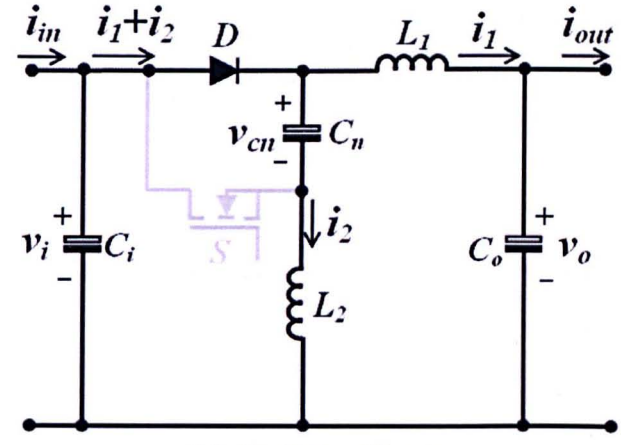

(b) Switch-off state

Figure 4.2 Ćuk step-up converter circuit states for continuous conduction modes

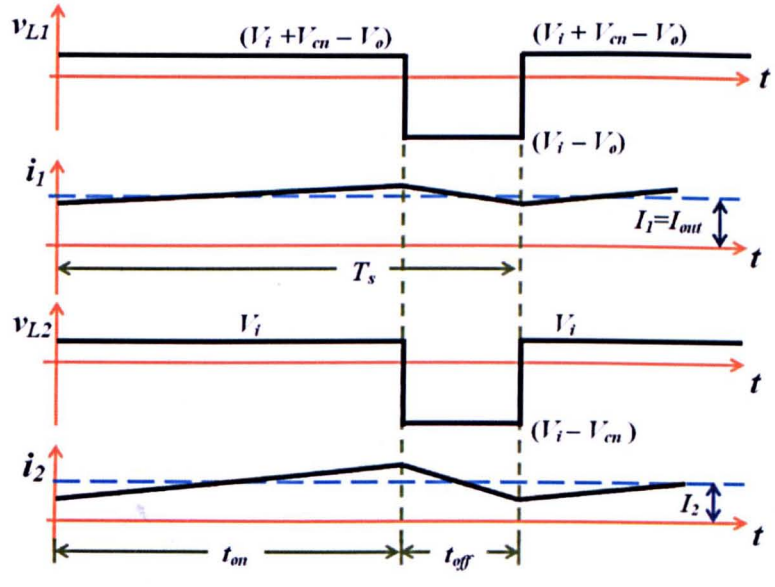

Figure 4.3 Voltage and current waveforms for the converter

where I_{in} is the converter input current and the input-output current relationship is now given by

$$\frac{I_{out}}{I_{in}} = \frac{I_1}{I_{in}} = 1 - K \tag{4.5}$$

Substituting (4.3) into (4.4), we yield the relationship between the currents flowing through L_1 and L_2 as

$$\frac{I_2}{I_1} = \frac{K}{1-K} \tag{4.6}$$

This also conforms to the discussion in [22] that the relationship between input and output voltages is analogous to the one in a Boost converter and the total current flowing from the source is $I_{in} = I_1 + I_2$.

4.2.2 Transfer Function Model

Using the similar derivation procedure for the step-down case, the generalised state-space averaging model for a Ćuk step-up converter can be derived as

$$\begin{bmatrix} \dot{x}_1 \\ \dot{x}_2 \\ \dot{x}_3 \\ \dot{x}_4 \\ \dot{x}_5 \end{bmatrix} = \begin{bmatrix} 0 & -\frac{1}{C_i} & -\frac{1}{C_i} & 0 & 0 \\ \frac{1}{L_1} & 0 & 0 & \frac{k}{L_1} & -\frac{1}{L_1} \\ \frac{1}{L_2} & 0 & 0 & -\frac{(1-k)}{L_2} & 0 \\ 0 & -\frac{k}{C_n} & \frac{(1-k)}{C_n} & 0 & 0 \\ 0 & \frac{1}{C_o} & 0 & 0 & -\frac{1}{C_o R} \end{bmatrix} \begin{bmatrix} x_1 \\ x_2 \\ x_3 \\ x_4 \\ x_5 \end{bmatrix} + \begin{bmatrix} \frac{1}{C_i} \\ 0 \\ 0 \\ 0 \\ 0 \end{bmatrix} i_{in} \tag{4.7}$$

where

$$\mathbf{x} = \begin{bmatrix} x_1 \\ x_2 \\ x_3 \\ x_4 \\ x_5 \end{bmatrix} = \begin{bmatrix} v_i \\ i_1 \\ i_2 \\ v_{cn} \\ v_o \end{bmatrix}$$

Equation (4.7) denotes a nonlinear averaged model for a Ćuk step-up converter which is linear with respect to the state variables, provided the load R is constant and the system remains in continuous conduction mode. Since k may vary with time, the

state equation consists of time varying coefficients. In this case a transfer function with respect to k is derived by analysis of small perturbations.

In the application such as controlling a DC motor speed, output voltage V_o is a variable while the input voltage V_i effectively remains constant, thus input side capacitor C_i can be considered infinitely large. The method described in Section 3.2.2 can then be used for the derivation of transfer functions by small perturbations. Therefore, the control-to-output voltage transfer function for a Ćuk step-up converter can be given by

$$G_{ok}(s) = \left.\frac{\hat{v}_o(s)}{\hat{k}(s)}\right|_{\hat{v}_i(s)=0} = \frac{L_2 C_n R K'^2 s^2 - K L_2 s + R K'^2}{\vartheta_4 s^4 + \vartheta_3 s^3 + \vartheta_2 s^2 + \vartheta_1 s + K'^2} I_{in} \tag{4.8}$$

where

$$\vartheta_4 = L_1 L_2 C_n C_o$$
$$\vartheta_3 = \frac{L_1 L_2 C_n}{R}$$
$$\vartheta_2 = \left(C_n L_2 + C_o \left[K'^2 L_1 + K^2 L_2\right]\right)$$
$$\vartheta_1 = \frac{1}{R}\left(K'^2 L_1 + K^2 L_2\right)$$

The input-to-output voltage transfer function is expressed as

$$G_{vi}(s) = \left.\frac{\hat{v}_o(s)}{\hat{v}_i(s)}\right|_{\hat{k}(s)=0} = \frac{C_n L_2 s^2 + K'}{\vartheta_4 s^4 + \vartheta_3 s^3 + \vartheta_2 s^2 + \vartheta_1 s + K'^2} \tag{4.9}$$

Similar to those in the step-down case, both $G_{ok}(s)$ and $G_{vi}(s)$ for Ćuk step-up converter are varying with K and have four stable poles and two zeros; most crucially the former system which may posses right-hand plane zeros and thus presenting non-minimum phase characteristics. The dynamic features of this converter are also found to be closely dependent on the values of the circuit components including the circuit operating point, i.e., the values of steady-state duty ratio K and K'.

On the other hand when the converter is used to control a PV system, the input is connected to a PV generator as shown in Figure 4.1(b) and under a specific weather condition, its current varies according to the PV I-V characteristics and its normal operating range, thus the source current is now

$$\hat{i}_{in} = \frac{\hat{v}_i}{-R_{PV}} \tag{4.10}$$

where R_{PV} is the slope of I-V characteristic at its steady-state point and is always varying. Assuming output voltage, V_o is a constant DC source, hence, C_o can be considered infinitely large. Using the derivation method in Section 3.2.2, the transfer function model for $\hat{v}_i / \hat{k}$ can be expressed as

$$G_{ik}(s) = \frac{\hat{v}_i}{\hat{k}} = -\frac{C_n(L_1 + L_2)s^2 + \frac{K'}{R_{PV}}\left[L_1(K')^2 - L_2(K)^2\right]s + 1}{\rho_4 s^4 + \rho_3 s^3 + p_2 s^2 + \rho_1 s^1 + 1} V_o \tag{4.11}$$

and transfer function model for $\hat{v}_i / \hat{v}_o$ is

$$G_{io}(s) = \left.\frac{\hat{v}_i(s)}{\hat{v}_o(s)}\right|_{\hat{k}=0} = \frac{C_n L_2 s^2 + K}{\rho_4 s^4 + \rho_3 s^3 + \rho_2 s^2 + \rho_1 s + 1} \tag{4.12}$$

where

$$\rho_4 = C_i C_n L_1 L_2$$
$$\rho_3 = \frac{C_n L_1 L_2}{R_{PV}}$$
$$p_2 = C_i\left[L_1(K')^2 + L_2(K)^2\right] + C_n(L_1 + L_2)$$
$$\rho_1 = \frac{1}{R_{PV}}\left[L_1(K')^2 + L_2(K)^2\right]$$

Again Equation (4.12) can be derived directly from the DC averaged model Equation (4.7) based on the same assumption, when R_{pv} is a constant. The non-linear characteristics of G_{ik}(s) in Equation (4.11) are shown clearly as pole and zero positions would vary with the change of input variable k, though unlike the previous case of $G_{ok}(s)$ when output voltage is constant, G_{ik}(s) shows no non-minimum phase feature.

4.3 Controller Design Principles

The controller design presented in this section is applied as an MPP tracker for a PV system and hence is based on the converter operation mode of a variable V_i and constant V_o. The regulation of the converter duty cycle can be performed using a feedback control system as shown in Figure 4.4. $H(s)$ is the controller transfer function, G_{ik}(s) is the plant for the control system, and V_i^*(s) is the reference value

for the controlled variable, which is the voltage across the PV module. The latter is compared with its measured value, V_i(s) and the difference between these two values is taken as the error signal $E(s)$. It is then multiplied with $H(s)$ to obtain the converter duty cycle, $K(s)$ which is used to regulate V_i(s) accordingly.

When V_i(s) has stabilised, the measured E value is the system steady-state error and according to the Final Value Theorem it can be written as [98]

$$E(0) = \lim_{s\to 0} s\frac{1}{1+H(s)G(s)}V_i(s) = \frac{1}{1+H(0)G(0)}\lim_{s\to 0} sV_i(s) \tag{4.13}$$

where $H(0)$ and $G(0)$ are the DC gains for $H(s)$ and $G(s)$. The objective for the control system is to have a small $E(0)$ and to achieve this, a scalar controller having a large DC gain, which is the simplest, can be used for $H(s)$. However, this may result in poor stability, or instability for the V_i response.

Therefore, a dynamic controller using compensation technique [99] can be designed for $H(s)$ based on the transfer function $G_{ik}(s)$. Note that the negative sign in $G_{ik}(s)$ (Equation (4.11)) signifies that a positive change in duty ratio leads to a negative change in the input voltage and to regulate the duty cycle in the right direction, $H(s)$ is also a negative transfer function. However, both transfer functions are along the forward loop of the block diagram in Figure 4.4. A cascade of H(s) and G_{ik}(s) results in the cancellation of their negative signs and therefore, it is also similar to a cascade of two positive transfer functions which can be defined as

$$G_{ik}'(s) = -G_{ik}(s)$$

and $$H'(s) = -H(s) \tag{4.14}$$

For ease of explanation, the transfer functions in Equation (4.14) will be used for the following design procedure.

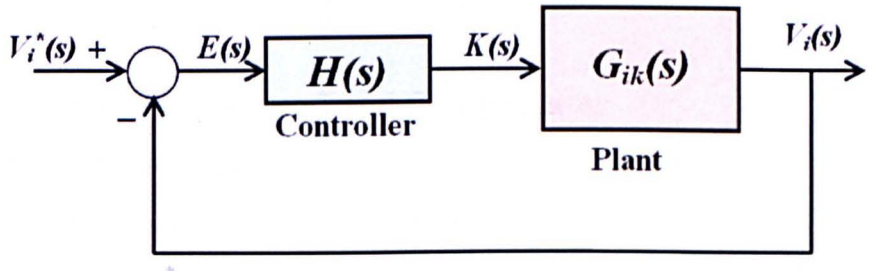

Figure 4.4 Control block diagram for converter duty cycle regulation

4.3.1 Evaluating the Frequency Response for $|G_{ik}(s)|$

The transfer function $G_{ik}'(s)$ is firstly evaluated for a given set of components (i.e. C_i, C_n, L_1 and L_2) and the desired operating points for the converter (i.e. V_i, V_o, K and R_{PV}). The design of the dynamic controller then starts by evaluating the frequency response of $G_{ik}'(s)$ from which the information about its crossover frequency, ω_c (in rad/sec) and phase margin, PM (in degree) can be extracted. The former is the frequency at which the system magnitude is equal to 0 dB while the latter is the amount of phase lag that be added before the closed-loop system becomes unstable. Note that the PM is computed by adding 180° to the phase measured at ω_c.

The second step of the design is to identify the desired speed of the response and the stability of the closed-loop system. The forth-order system can be approximated as a second-order system if the two of the system poles have less dominant effects than the other two poles on the transient response [99]. The value for ω_c and the PM can then be given as [99]

$$\omega_c = \frac{1.8}{t_r}$$

and $$\text{PM} = 100\zeta \tag{4.15}$$

where t_r is the response rise time, and ζ is the damping level of the transient response. Using the design equation in (4.15), the desired ω_c and the PM can be evaluated based on the defined values for t_r and ζ. Using the transfer function model derived in Section 4.2, a dynamic controller using compensation technique can be designed based on the frequency response of $G_{ik}(s)$. A lead compensator is used to improve the response speed while minimizing the response overshoot when a step input is applied. A lag compensator is also employed to minimize the steady state error.

4.3.2 Designing the Phase Lead Compensator

If an amount of phase lead is required to be added and/or a higher crossover frequency is needed, a phase lead compensator with a scalar gain of N_{lead} is used and its transfer function can be designed as [98]

$$H_{lead}(s) = N_{lead}\frac{(1+s\alpha_d\tau_d)}{(1+s\tau_d)} \tag{4.16}$$

The maximum phase lead introduced is set to be equal to the additional amount of phase lead required and therefore is expressed as

$$\varphi_{\max(lead)} = \sin^{-1}\frac{\alpha_d - 1}{\alpha_d + 1} \tag{4.17}$$

The frequency at which $\varphi_{max(lead)}$ is introduced is set to be equal to the required ω_c and hence, can be written as

$$\omega_{\max(lead)} \frac{1}{\tau_d \sqrt{\alpha_d}} \tag{4.18}$$

In addition, at $\omega_{max(lead)}$ the gain introduced is expressed as

$$H(j\omega_{\max(lead)}) = N_{lead}\sqrt{\alpha}_d \tag{4.19}$$

Hence, N_{lead} can be evaluated based on the amount of gain that has to be added by the compensator to achieve the required ω_c.

4.3.3 Designing the Phase Lag Compensator

If only a lead compensator is used as the controller, the DC gain of $H_{lead(s)}$ in Equation (4.16) may not be large enough to obtain a satisfactory amount of $E(0)$. To eliminate $E(0)$, a proportional-plus integral (P+I) controller which is a type of phase lag compensator is connected in cascade with the phase lead compensator and its transfer function is given as [98]

$$H_{lag}(s) = \frac{(s + \omega_L)}{s} \tag{4.20}$$

Hence, a pure integrator term ($1/s$) is introduced in the forward loop and a zero steady-state error, for instance, can be obtained for a step in V_i(s). However to reduce its effects on the phase lead compensator, the amount of phase lag and gain introduced should be negligible around ω_c. This is achieved by setting its breakpoint frequency ω_L to be at least 10 times less than ω_c.

The dynamic controller for the converter, therefore, can be obtained as

$$H(s) = -H'(s) = -H_{lead}(s)H_{lag}(s) \tag{4.21}$$

The term R_{pv} in $G_{ik(s)}$ is time variant and closely dependent on V_i while the controller is designed based on a constant R_{pv}. Thus, the performance of the controlled converter may not be satisfactory and re-tuning is needed for the

compensator transfer functions in Equations (4.16) and (4.20). This process is repeated until satisfactory transient performance is obtained.

4.4 Controller Design Example

4.4.1 Design Specifications

The above principles are used to design a controller for the Ćuk step-up converter in a PV system as shown in Figure 4.1(b). The simulated PV module at the converter input has 4 parallel strings of 120 serially-connected cells, giving 690 W at V_i = 58 V at insolation of 100 mW/cm^2 and a cell temperature of 20°C. The DC power supply at the converter output is a constant voltage source with V_o = 100 V. The latter can be either supplied by battery or a capacitor across which the voltage is maintained by a grid-connected converter. Applying the design principles proposed in Chapter 3, the converter components can be determined as L_1 = 12.5 mH, L_2 = 0.9 mH, C_n = 2 μF and C_i = 16 μF, assuming a converter switching frequency of 20 kHz. Substituting these values into Equation (4.11), the Bode plots representing the frequency response G_{ik}'(s), when K = 0.42, are displayed in Figure 4.5.

4.4.2 Frequency Response Analysis

Equation (4.11) shows the DC gain for G_{ik}(s) can be determined by the value of V_o and thus it is 40 dB. An over-damped pole and a real zero respectively have a breakpoint frequency at around 1.29 × 10^3 rad/sec, hence no gain and phase shift are introduced at the low frequency end. Another over-damped pole has a breakpoint frequency 9.3 × 10^3 rad/sec where the gain starts to decrease at -20 dB/decade and the phase tends towards 90°. Two other poles are complex conjugates with breakpoint frequencies of 15 × 10^3 rad/sec. Due to their low damping ratio, they cause a resonant peak in the gain, but after this, the gain decreases at -60 dB/decade while the phase tends towards -270°. This continues until the breakpoint frequency of the other real zero at 29 × 10^3 rad/sec. Therefore within the high frequency range, the gain falls at -40 dB/decade, while the phase tends towards −180°.

On the other hand, the gain reaches unity at 92 × 10^3 rad/sec which corresponds to ω_c for G_{ik}'(s). In addition, the phase margin is found to be -10.6° and

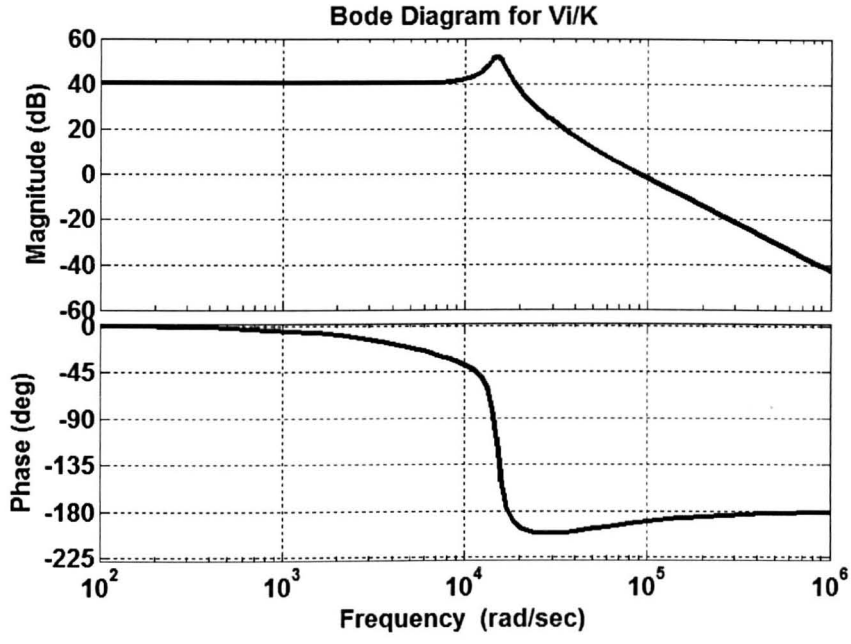

Figure 4.5 Frequency response for V_i due to small perturbations of K

the gain margin, which is measured when the phase is -180°, is approximately -44.6 dB.This indicates that the G_{ik}'(s) locus encircles the -1 + j0 point in the Nyquist plot and hence the Nyquist stability criterion is not satisfied [99]. Therefore for instance, if a scalar controller with a gain of about 0.005 and above is used in the feedback control system, V_i will become unstable.

4.4.3 Controller Transfer Function

The desirable value for ω_c is 2.81 × 10^4 rad/sec which is about five times less than the switching frequency, ω_s (in rad/sec) This ω_c value is chosen so that all the high frequency noise in the measured input voltage can be attenuated and unnecessary oscillation in the control output, i.e. the PWM signal, can be prevented. The design criteria for a second order system are set as reference, and therefore the desired phase margin is set as 60° so that the closed-loop response for V_i with an overshoot of no more than 10 % can be obtained.

At the frequency of 2.81 × 10^4 rad/sec, the gain is 25 dB and the phase is -200°. To achieve the desirable PM and ω_c, a phase lead compensator is required to provide an additional positive phase of 90° and a gain of –25 dB. For the former, an extra 10° of phase lead has been included to make up for any phase lag contributed by the second compensator. If the phase lead compensation is performed in a single stage, α_d according to Equation (4.16) will be so large that no practical resistor and capacitor can be used to implement the compensator circuit [98]. Therefore, the

phase lead compensation is performed in two stages, with each contributing a gain of -12.5 dB and a phase of 45 ° at the frequency of 28.1×10^3 rad/sec.

For the phase lag compensator, ω_L is chosen to be 0.5×10^3 which is low enough so that at a frequency of around 28.1×10^3 rad/sec, it only introduces 0.002 dB gain and a phase lag of 1.15°. The Bode plots for the above the lead and lag compensators are respectively displayed in Figures 4.6(a) and 4.6(b).

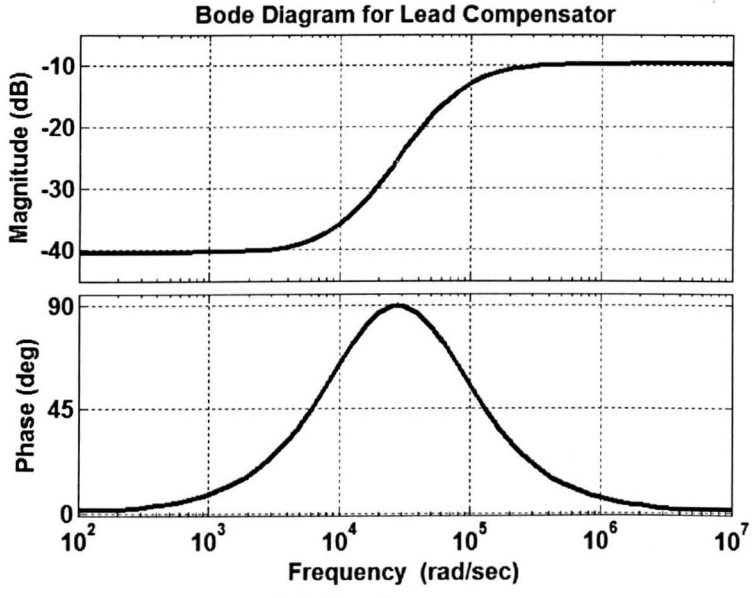

(a) Lead compensator

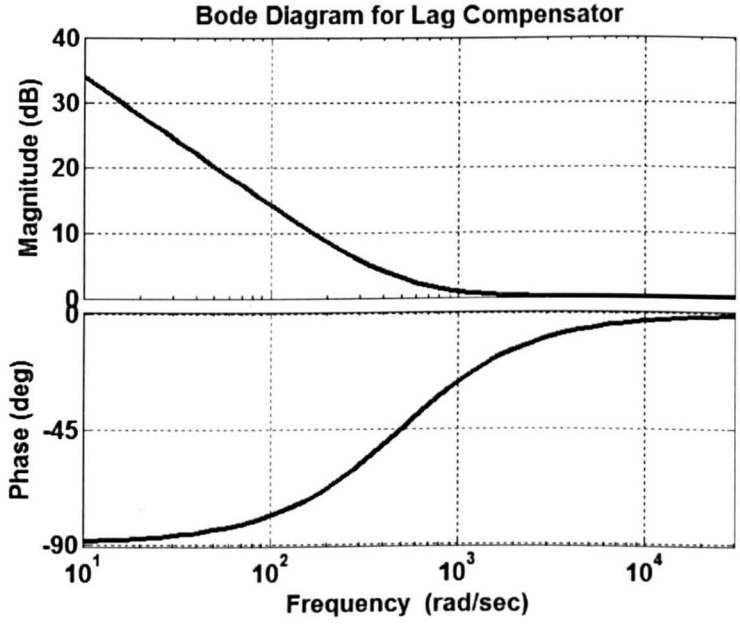

(b) Lag compeansator

Figure 4.6 Frequency response for the compensators

With the above information, the design equations in (4.16), (4.20) and (4.21) are used to derive the overall controller transfer function which can be written as

$$H(s) = -4.77\frac{(85.93\times10^{-6}s+1)^2(2\times10^{-3}s+1)}{s(14.74\times10^{-6}s+1)^2} \tag{4.22}$$

Therefore, the Bode plots for the new open-loop transfer function $H(s)G_{ik}(s)$ are shown in Figure 4.7. As can be observed, the phase margin now becomes 67° and the crossover frequency is at 28.1 × 10^3 rad/sec. The phase tends towards -180° at a high frequency and hence, the gain margin is large. By examining the Nyquist plot displayed in Figure 4.8, the locus of $H(s)G_{ik}(s)$ does not cross or encircle the -1 +j0 point and hence, the closed loop system will have a stable response [99].

4.4.4 Simulation Results

Prior to the evaluation of the PV-converter system with the above described controller design; a computer model is built in the MATLAB-SIMULINK software environment. The power circuit including the converter is built using SimPowerSystem Toolbox, while the controller is implemented using the Control Toolbox. A set of MATLAB algorithm written for the PV panel is simulated and integrated into model through an S-function. The output of the control system (i.e. the duty ratio value) is kept within the allowable range of between 0 and 1.

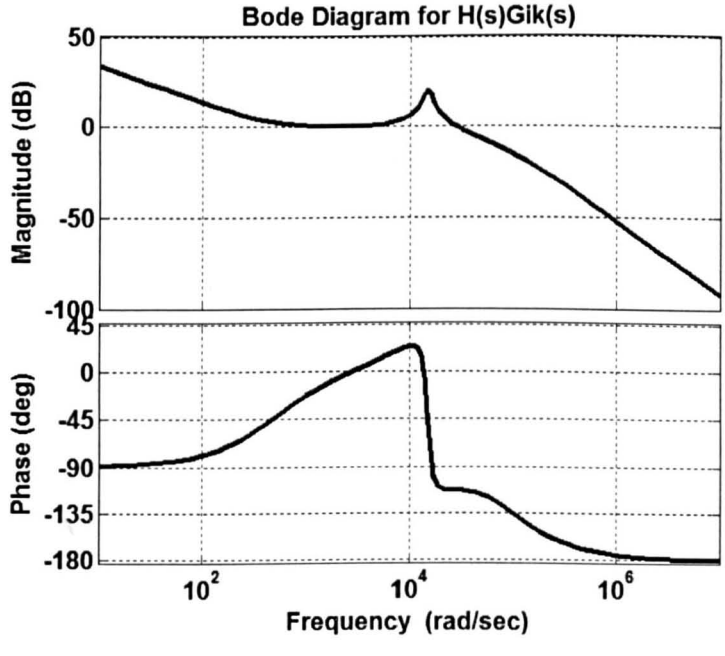

Figure 4.7 Frequency response for the forward loop transfer function $H(s)G_{ik}(s)$

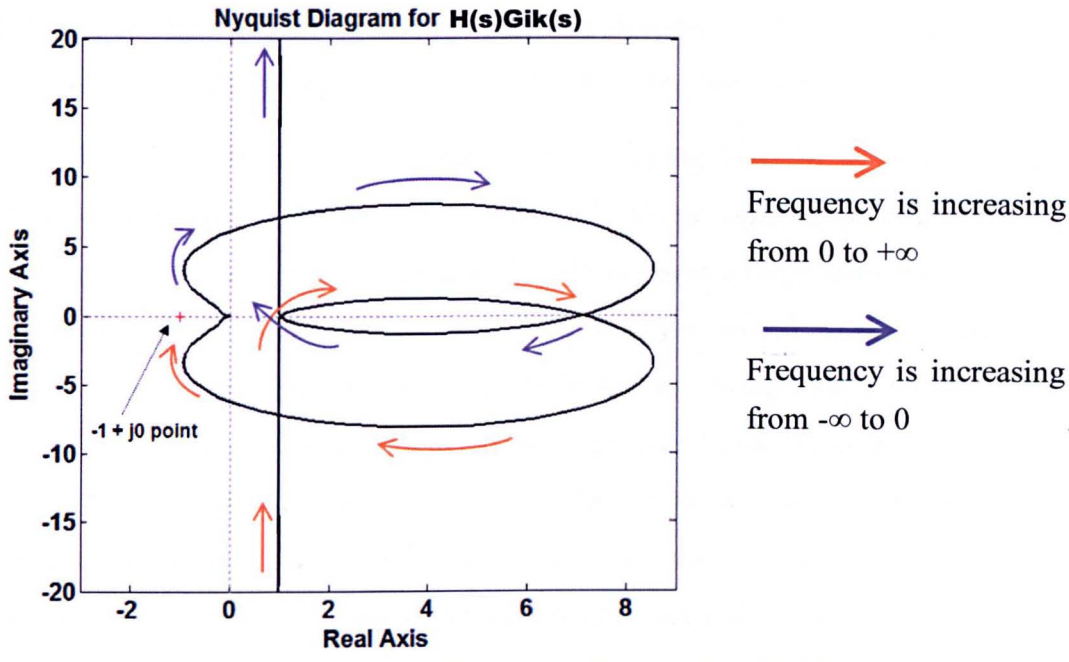

Figure 4.8 Nyquist plot for the forward loop transfer function $H(s)G_{ik}(s)$

The insolation on the PV module may drop requiring the desired PV voltage to be decreased according to the specified MPP operating point. Hence, the converter performance is initially evaluated with a step change in V_i^* from 70 to 58 V while the controller is used to regulate the converter duty cycle. The PV voltage response is displayed in Figure 4.9(a). As can be observed, the simulated response follows closely with its reference value. They are denoted by black solid and red dashed lines respectively. When the step is introduced, a small overshoot of about 1 V which is 8 % out of the total amount of voltage change is obtained. It also takes about 4 ms before it settles to the steady-state value.

The performance of the closed-loop system can then be compared to that of the open-loop where the converter duty cycle is directly changed from $K = 0.3$ to $K = 0.42$, respectively corresponding to the reference voltages used in the previous test. The response for the PV voltage is displayed in Figure 4.9(b); a black solid line represents the simulated response and the red dashed line represents the PV voltage calculated from the reference K value. Even though the open-loop response has no overshoot, it takes 8 ms to settle to a steady state. In addition, the steady-state error is about 0.05 V under the operating point of $K = 0.42$. The faster response obtained in the closed-loop system can be explained by the fact that during the transition stage from one steady-state point to another, a higher duty ratio (comparing to the new

steady-state point) is initially applied to the converter (as can be observed from t = 0.05 to 0.052 in Figure 4.9(a)). The duty ratio then decreases to the new steady-state point when the PV voltage begins to follow with the reference value.

The above evaluations can be done for V_i^* changing from 70 to 68 V for the closed-loop system, and K changing from 0.3 to 0.32 for the open-loop system. Their responses are shown in Figures 4.10(a) and 4.10(b) respectively. With the closed-loop controller, the PV voltage response can be sped up around 10 times. On the other hand when V_i^* is changed from 30 to 28 V for the closed-loop system and K from 0.3 to 0.32 for the open-loop system, the respective V_i responses are shown in Figures 4.11(a) and 4.11(b). When the closed-loop controller is used, V_i response is still stable and only takes about 3 ms to stabilise. Conversely, when the controller is not used, the V_i response has a higher voltage oscillation and takes about 34 ms to stabilise.

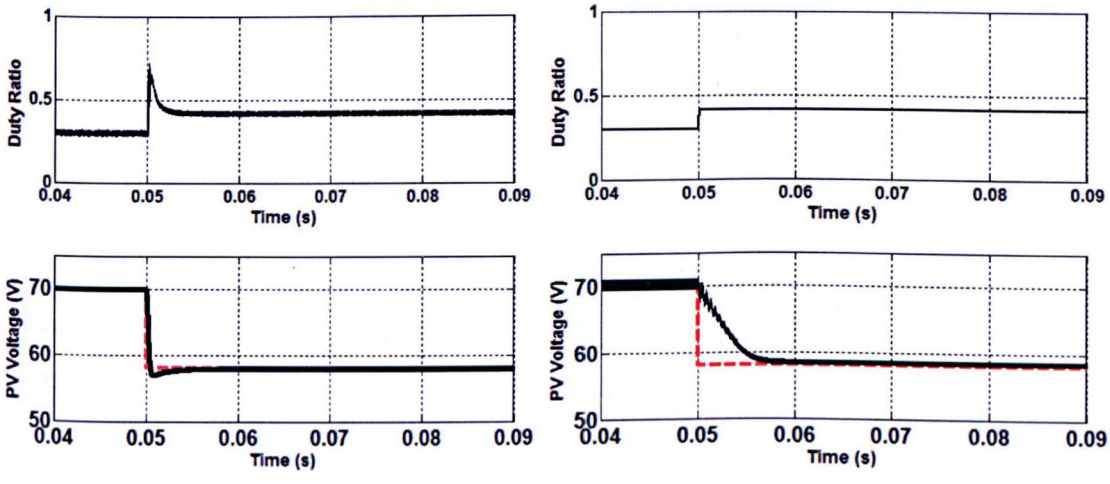

Figure 4.9 Simulated V_i response when the operating point changes from 70 to 58 V for the PV voltage or from K = 0.3 to K = 0.42 for the duty cycle

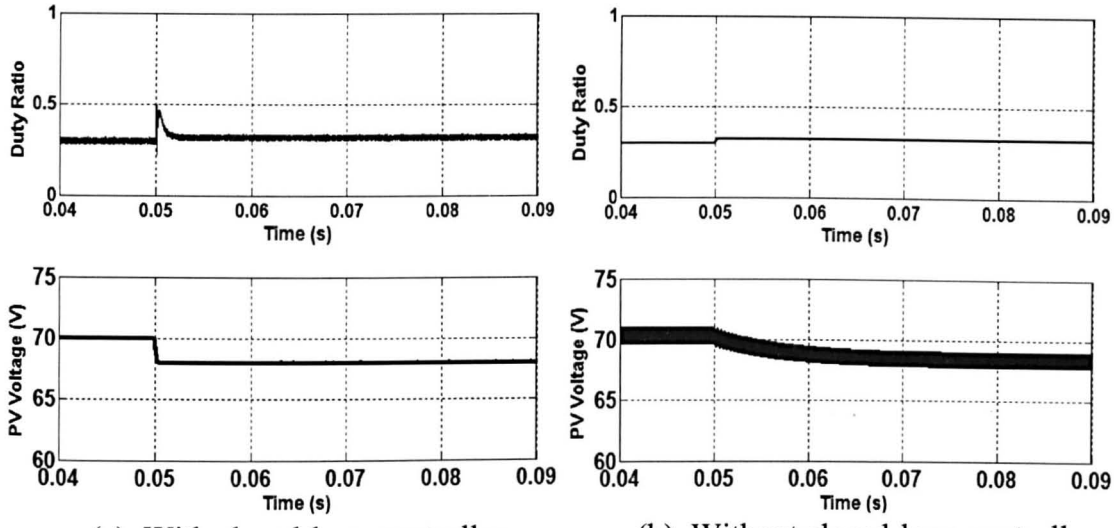

(a) With closed-loop controller (b) Without closed-loop controller

Figure 4.10 Simulated V_i response when the operating point changes from 70 to 68 V for the PV voltage or from $K = 0.3$ to $K = 0.32$ for the duty cycle

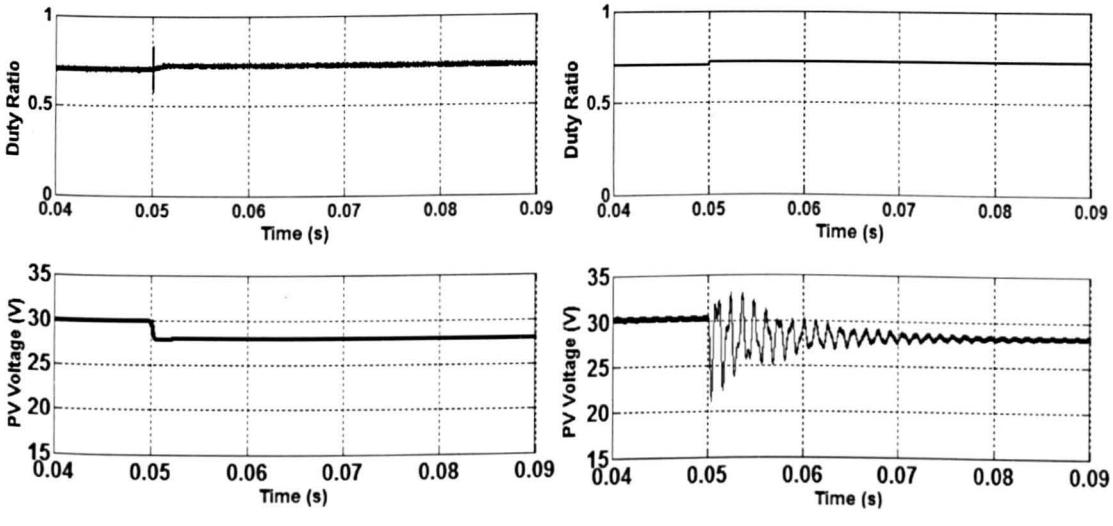

(a) With closed-loop controller (b) Without closed-loop controller

Figure 4.11 Simulated V_i response when the operating point changes from its desired voltage is changed from 30 to 28 V or from $K = 0.7$ to $K = 0.72$

Another evaluation can also be performed for V_i responses to a variation in the weather condition and hence, the operating point of I_{pv} changes. For this set of simulations, the solar insolation level changes from 100 to 50 mW/cm^2 at $t = 0.05$ second. The simulation is firstly performed for the open-loop system and K is fixed at 0.42. Figures 4.12(a) and 4.12(b) show the variation in solar insolation and the simulated V_i response respectively. When the solar insolation drops, V_i plunges to as

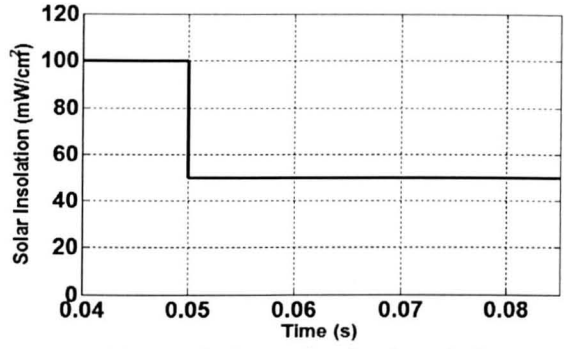

(a) Variation of solar insolation

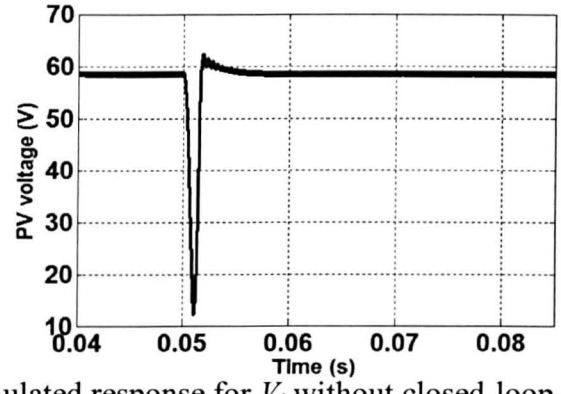

(b) Simulated response for V_i without closed-loop controller

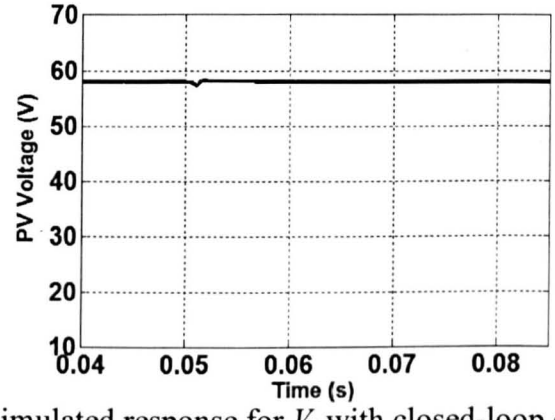

(c) Simulated response for V_i with closed-loop controller

Figure 4.12 Evaluation performed for changing solar insolation

low as 12 V and takes about 7 ms to stabilise again at its desired value of 58V. The same simulation is performed for the closed-loop system but now V_i^* is fixed at 58 V and the voltage response is shown in Figure 4.12(c). When the solar insolation drops, V_i has a small voltage overshoot which is about 0.8 V and it takes only 2 ms for the controller to restore V_i to its reference value.

It can be observed that the controller has been successfully designed to provide fast but stable transient response for different operating conditions. In addition, the steady-state performance of V_i can also be improved as the steady-state ripple for the open loop system is larger than that for the closed-loop system. This is due to the fact that the PV current is not constant, but varies with V_i. Its fluctuation is then

considered as the disturbance to V_i which can be attenuated by having a feedback controller.

4.5 Summary

A new approach for controlling a PV system is introduced through using a Ćuk step-up converter which has continuous input and output current ripples.

This chapter has presented a detailed analysis of a Ćuk step-up converter leading to four transfer function models for the converter in two different operating modes, namely, variable input – constant output voltages suitable for controlling a solar photovoltaic (PV) power generation system and variable output – constant input voltage applicable to a variable speed motor drive. While the latter is shown to exhibit a response with a non-minimum phase feature to switch duty ratio variation, the former has only minimum phase feature.

To improve the performance of the voltage response across a PV system, a feedback control system has been applied for regulating the duty cycle for the converter. With the developed transfer function model, a lead-lag compensator can be designed based on the frequency response and desired closed-loop performance. By using the closed-loop controller, the speed of the V_i response for the K value (i.e. equal to 0.42) specified for the converter design in this chapter has been increased by at least double. It also improves the V_i response for other operating conditions. For instance, the response can be sped up by at least 10 times at $K = 0.3$, and for $K = 0.7$, the fluctuation in V_i can be eliminated. Moreover, the disturbances due to the continuously changing of the PV current with the voltage can be suppressed by having a feedback controller. Such fast and stable response leads to the converter being a plausible choice for controlling the voltage of a PV system operating under rapidly changing weather conditions.

Chapter 5
Analysis and Control of PV-Integrated Converter

5.1 Introduction

As discussed in Chapter 2, bypass diodes provide protection to a PV generator under partial shading conditions, but the power output that can be extracted is still significantly reduced.

The main aim of Chapter 5 is to present a different approach. Instead of using bypass diodes, the proposed method embeds bidirectional Ćuk converters in the series PV strings to avoid complete current bypassing of the shaded string. This chapter also describes the novel scheme used for controlling the converter operation. Through this scheme, the generated power can be significantly increased as well as protecting shaded cells from thermal breakdown.

In this section, the basic configuration of the PV-integrated converter scheme and its operating principle are described first. An example system consisting of three serially connected panels and three DC-DC Ćuk converters will be discussed. The control schemes and simulation results for MPP tracking will then be presented and compared with the conventional system using bypass diodes.

5.2 General System Configuration

The PV system configuration under study is shown in Figure 5.1, where bidirectional Ćuk DC-DC converters are integrated with the PV modules which are connected in series; a single Ćuk step-up converter, as described in Chapter 4, is also connected at the main terminals, functioning as the power conditioner.

The basic idea of this scheme is to use these internal bidirectional converters to provide a variable impedance bypass for the power flow. Under uniform illumination the generated power from all modules are ideally the same, therefore no bypass is required, the converters are idle giving infinitely high impedance. However, when light intensities are different, the module currents at optimum power are different and the converters provide a bypass current path which allows this

condition to exist, even though the currents at the two outermost terminals must be equal. With coordinated control of these converters the scheme should enable all the modules in the chain to operate at their optimum power point.

The key devices for achieving the enhanced performance are the internal converters as represented by the pink blocks at the left-hand side of Figure 5.1. They must enable current to flow in both directions and, for each converter, the polarities of input and output voltages must be reversed. Both bidirectional Ćuk [100] (shown in Figure 5.2) and buck-boost [19] converters satisfy these conditions. However the former is chosen for this structure as it provides ripple-free current at both input and output terminals. The power ratings of converter components are selected considering the worst scenario when one PV module is totally shaded while the others are unshaded.

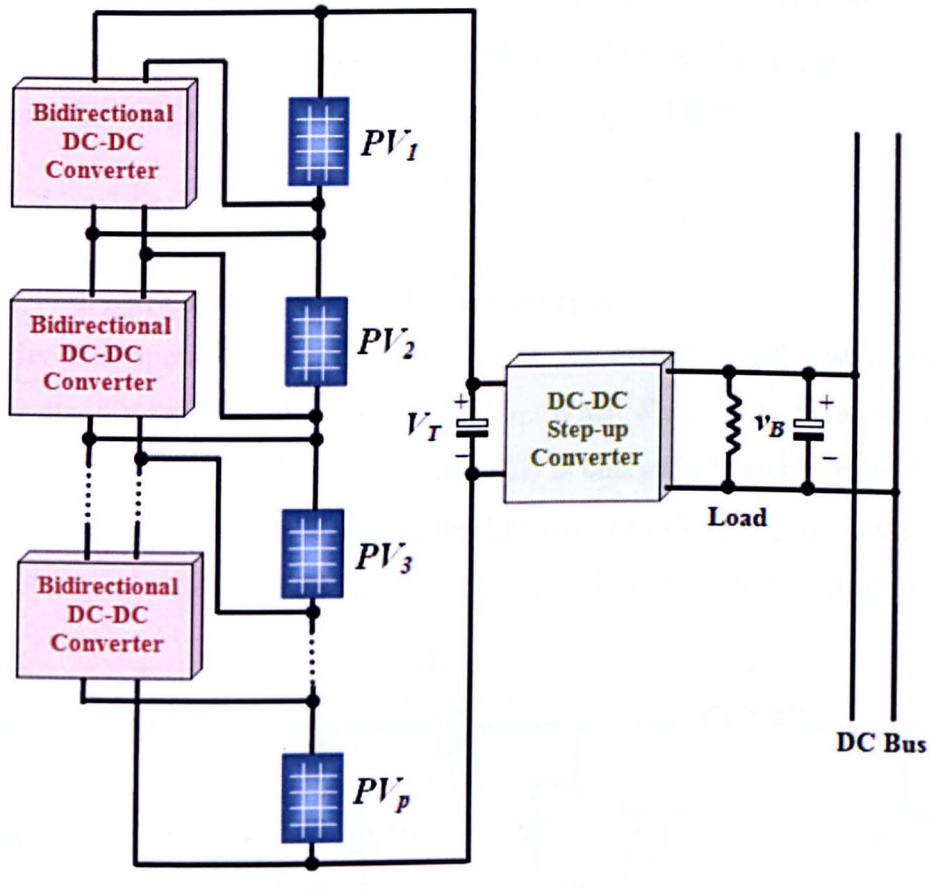

Figure 5.1 Configuration of a PV-integrated converter

5.2.1 Bidirectional Ćuk DC-DC Converter

As shown in Figure 5.2, the converter has two pairs of switching devices, switch S_{11} – diode D_{21} and switch S_{21} – diode D_{11}. Only one device pair can be active for a fixed operating condition. Two inductors L_{11} and L_{21} are at the V_{P1} and V_{P2} sides respectively. A capacitor C_{n1} is used to transfer energy from V_{P1} to V_{P2} or vice versa depending on which side acts as the input terminals. For example if the input voltage is V_{P1}, the energy transfer is from V_{P1} to V_{P2}, $S_{11} - D_{21}$ are active and the switching duty ratio is K_{11}.

Assuming capacitors C_1, C_{n1} and C_2 are sufficiently large, steady-state fluctuations of V_{P1}, V_{cn1} and V_{P2} around their average levels will be small. Also with high enough switching frequency, i_{L11} and i_{L21}, the inductor currents flowing through L_{11} and L_{21} respectively, can be considered to vary linearly with time during a switching period. The following analysis uses smoothed voltages and currents defined as the instantaneous values averaged over one switching period. Then in steady state, the voltages across both inductors are zero and hence,

$$V_{cn1} = V_{P1} + V_{P2} \tag{5.1}$$

5.2.1.1 $S_{11} - D_{21}$ are active and $S_{21} - D_{11}$ are inactive

Under this operating condition, $S_{11} - D_{21}$ are turned on/off instantaneously within the fixed time interval according to K_{11}. When S_{11} is turned on, the circuit state is shown in Figure 5.3(a). The inductor L_{11} is charged by energy from V_{P1} and hence the inductor current i_{L11} is increasing linearly. The diode D_{21} is now reverse-biased by V_{cn1} and C_{n1} discharges energy to L_{21} and V_{P2} through S_{11}, causing i_{L21} to

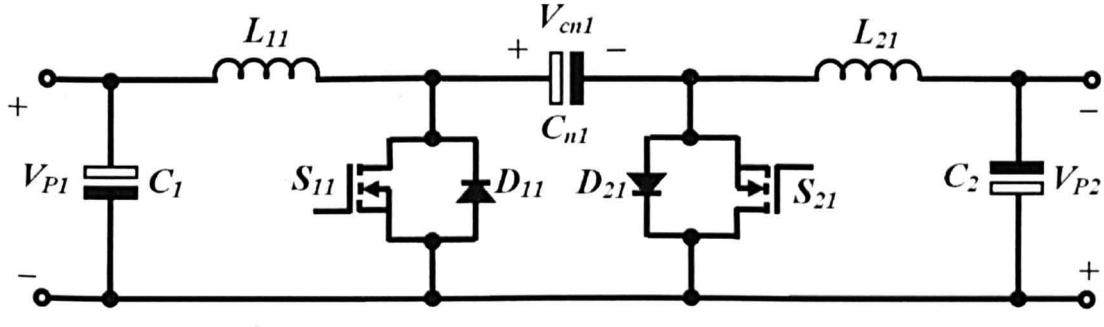

Figure 5.2 Schematic circuit of a bidirectional Ćuk converter

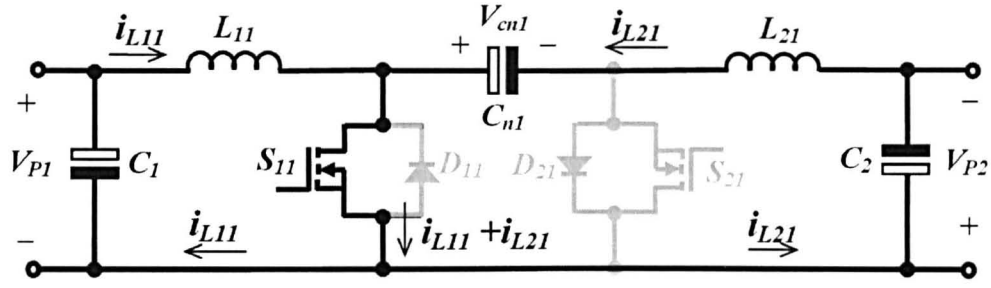

(a) Converter circuit state when S_{11} is turned on

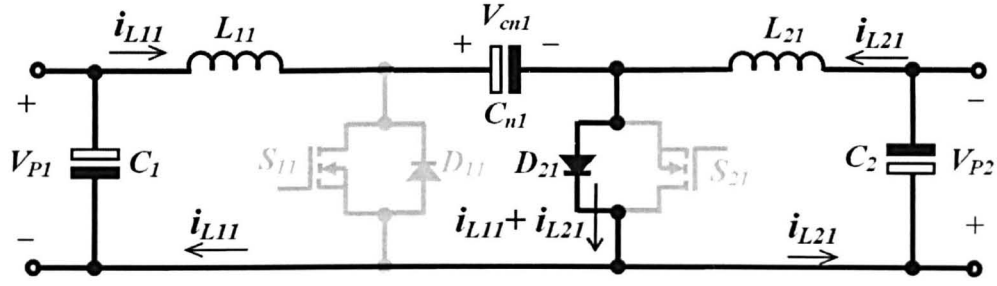

(b) Converter circuit state when S_{11} is turned off

Figure 5.3 Circuit states of a bidirectional Ćuk converter with S_{11} - D_{21} being active

increase linearly. When S_{11} is turned off, D_{21} becomes forward-biased as shown in Figure 5.3(b). The energy to C_{n1} is supplied by L_{11} while that to V_{P2} is by L_{21}, causing both i_{L11} and i_{L21} to decrease linearly. With t_{on} and t_{off} as the switching turn-on and off times, a switching period is represented by $T_s = t_{on} + t_{off}$. The net change in the inductor current is zero, and hence the voltage-time balance equations for L_{11} and L_{21} are given respectively by

$$V_{P1}K_{11} + (V_{P1} - V_{cn1})(1 - K_{11}) = 0$$

and $$(V_{cn} - V_{P2})K_{11} - V_{P2}(1 - K_{11}) = 0 \tag{5.2}$$

Eliminating V_{cn1} gives the relationship between V_{P1} and V_{P2} as

$$\left|\frac{V_{P2}}{V_{P1}}\right| = \frac{K_{11}}{1 - K_{11}} \tag{5.3}$$

For a lossless network, the current relationships can be expressed as [19]

$$\left|\frac{I_{L21}}{I_{L11}}\right| = \frac{1 - K_{11}}{K_{11}} \tag{5.4}$$

5.2.1.2 $S_{21} - D_{11}$ are active and $S_{11} - D_{21}$ are inactive

Conversely when V_{P2} is the input voltage, V_{P1} the output, $S_{21} - D_{11}$ becomes active with switching duty ratio K_{21}. When S_{21} is turned on and the circuit state is shown in Figure 5.4(a), the diode D_{11}, is reverse-biased causing C_{n1} to discharge its energy to L_{11} and V_{P1}. The inductor currents i_{L11} and i_{L21} are increasing linearly and are now flowing through S_{21}. When S_{21} is turned off, D_{11} becomes forward-biased as shown in Figure 5.4(b). The energy to C_{n1} is supplied by L_{21} while that to V_{P1} is by L_{11}, causing both i_{L11} and i_{L21} to decrease linearly. It is worth noting that i_{L11} and i_{L21} now have the opposite directions to those in the previous case, since the energy transfer is from V_{P2} to V_{P1}. In addition, the voltage-time balance equations for L_{11} and L_{21} can be expressed as

$$V_{P2}K_{21} + (V_{P2} - V_{cn1})(1 - K_{21}) = 0$$

and $$(V_{cn1} - V_{P1})K_{21} - V_{P1}(1 - K_{21}) = 0 \qquad (5.5)$$

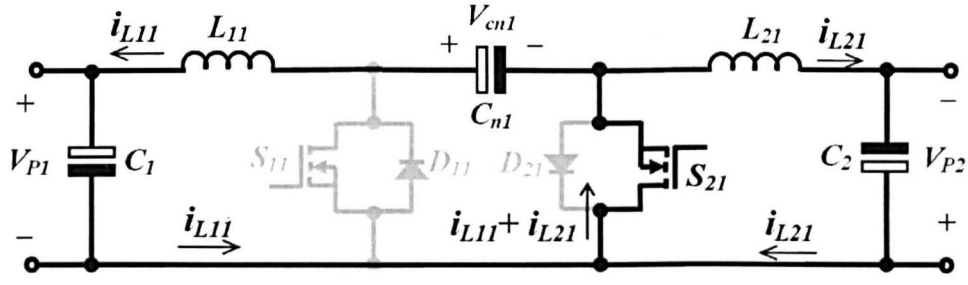

(a) Converter circuit state when S_{12} is turned on

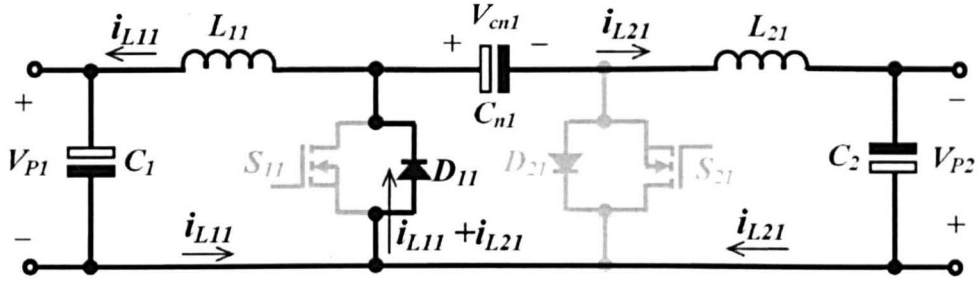

(b) Converter circuit state when S_{12} is turned off

Figure 5.4 Circuit states of a bidirectional Ćuk converter with $S_{21} - D_{11}$ being active

Hence, the voltage and current relationships are respectively re-written as

$$\left|\frac{V_{P1}}{V_{P2}}\right| = \frac{K_{21}}{1-K_{21}}$$

and $$\left|\frac{I_{L11}}{I_{L21}}\right| = \frac{1-K_{21}}{K_{21}} \tag{5.6}$$

5.2.2 Bidirectional Ćuk DC-DC Converter with Two PV Modules

Using the above converter for a two PV module system as shown in Figure 5.5, Module 1 (PV_1) is connected to one end of the Ćuk converter and Module 2 (PV_2) to the other. The load is connected between the positive end of PV_1 and the negative end of PV_2. When both modules are uniformly illuminated, the Ćuk converter is idle and the current is flowing through PV_2 and PV_1 to load terminals.

However if PV_2 is shaded, the power generated by PV_1 will be higher. Hence, the latter is regarded as the input end of the converter, and S_{11} - D_{21} are made active. Following the operation as described in Section 5.2.1, S_{11} is turned on and off at constant frequency within the fixed time interval according to K_{11}. Neglecting losses at the steady state, the total power generated by both panels can be given as

$$P_T = V_T I_T = (V_{P1} + V_{P2}) I_T = V_{P1} I_T + V_{P2} I_T \tag{5.7}$$

where I_T is the output current from the PV system and may be expressed as either

$$I_T = I_{P1} - I_{L11} \text{ or} \tag{5.8}$$

$$I_T = I_{P2} + I_{L21} \tag{5.9}$$

Both two PV module terminal voltages have the relationship as defined by Equation (5.3), while the converter current relationship is by Equation (5.4). Substituting I_{L21} in Equation (5.9) by Equation (5.4) one obtains

$$I_{L11} = (I_T - I_{P2})\left(\frac{K_{11}}{1-K_{11}}\right) \tag{5.10}$$

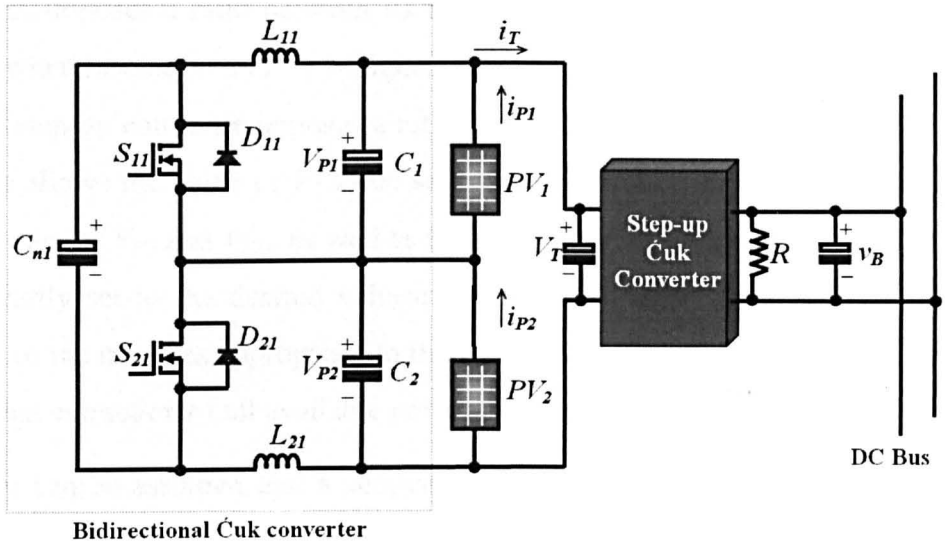

Figure 5.5 Integrated converter configuration for a two PV module system

Replacing I_{L11} by Equation (5.10), Equation (5.8) becomes

$$\begin{aligned} I_T &= I_{P1} - (I_T - I_{P2})\left(\frac{K_{11}}{1-K_{11}}\right) \\ &= I_{P1}(1-K_{11}) + I_{P2}K_{11} \end{aligned} \tag{5.11}$$

Thus substituting I_T in (5.7) by (5.11) and also using Equation (5.3), the output power is given as

$$\begin{aligned} P_T = V_T I_T &= \left(V_{P1} + V_{P1}\left(\frac{K_{11}}{1-K_{11}}\right)\right)\left(I_{P1}(1-K_{11}) + I_{P2}K_{11}\right) \\ &= V_{P1}I_{P1} + V_{P1}\left(\frac{K_{11}}{1-K_{11}}\right)I_{P2} \end{aligned} \tag{5.12}$$

The above analysis shows that by varying the duty ratio K_{11} in Equation (5.12), the power produced by the shaded panel, can be varied. In the limit when $K_{11} = 0$, the system output power is $P_T = V_{P1}I_{P1}$, hence the shaded panel does not produce power. This resembles the situation when a bypass diode is switched on, and a zero voltage is applied across PV_2. However when $0 < K_{11} < 1$, the output power of the shaded PV_2 is no longer zero, subsequently the total generated power can be increased.

Referring again to Figure 5.5, the system's operation can be summarized as: the duty ratio of the internal bidirectional Ćuk converter, which can be set by the

controller, imposes a ratio between its input and output voltages, i.e. between V_{P1} and V_{P2} when insolation on PV_1 is higher than that on PV_2. Now the duty ratio of the terminal step-up converter imposes a ratio between V_T and the DC bus voltage, and therefore allows the value of V_T to be set by the controller. Since $V_T = V_{P1} + V_{P2}$, both the sum of V_{P1} and V_{P2}, as well as their ratio can be set freely. Hence, both can be arbitrarily set to the desired values; these can be made equal to the optimum voltages of the modules appropriate to their individual irradiation levels. This shows clearly that extraction of all available power is possible.

If it can be assumed that a successful controller is in operation, placing both modules at their maximum power points, a stronger statement can be made. Photovoltaic modules have the property that the current (and voltage) at the maximum power point is an increasing function of the light level. (This might not be true of all conceivable generators with non-linear I-V characteristics and variable output capability.)

The total power output is also the sum of the individual powers from the modules, giving:

$$P_T = V_T I_T = (V_{P1} + V_{P2}) I_T = V_{P1} I_{P1} + V_{P2} I_{P2} - P_{loss} \tag{5.13}$$

where P_{loss} is any power absorbed in the bypass converter.

This can be rewritten as

$$P_T = V_T I_T = (V_{P1} + V_{P2}) I_T = (V_{P1} + V_{P2}) I_{P1} + V_{P2}(I_{P2} - I_{P1}) - P_{loss} \tag{5.14}$$

Supposing for example that PV_1 has the greater insolation, under optimum settings one obtains $I_{P1} > I_{P2}$ and Equation (5.14) now shows that $I_{P1} > I_T$. It follows that the current flow into L_{11} is positive (in Equation (5.8), $I_{L11} > 0$) and that power flow in the inner converter is from top to bottom in Figure 5.5. Hence the direction of power flow in the converter, and thus its operating mode, are determined simply by observing that bypassed power flows away from the module with the highest light level. This is not self-evident, but would apply if the PV modules were replaced with any type of generator whose optimum current increases with the available power level. It would not necessarily hold under non-optimum conditions, as might exist during transient conditions while the controller is settling. The following analysis and control scheme of the integrated converters is mainly for partial shading

conditions when it can be assumed that the integrated converters operate in continuous conduction mode. This condition may not necessarily hold when all the PV modules are uniformly irradiated or when they are irradiated with slightly different solar intensities.

5.3 Operating Principles of Multiple Module System

When there are more than two modules, the system structure and control principle become more complex. In the first part of this section, a three-module system is presented as shown in Figure 5.6 and its operation modes are explained in detail. When this scheme is applied to systems having more than three modules, a different switching scheme which is based on desired operating points of the PV panels can be used. Such a scheme is also discussed in this section.

5.3.1 Three-PV module System

Figure 5.6 shows an integrated PV-converter system consisting of three PV modules and two bidirectional Ćuk converters, forming two generating units. While converter 1 connects PV modules 1 and 2 in the same manner as that shown in Figure 5.5, converter 2 links PV modules 2 and 3. Clearly two converters overlap at

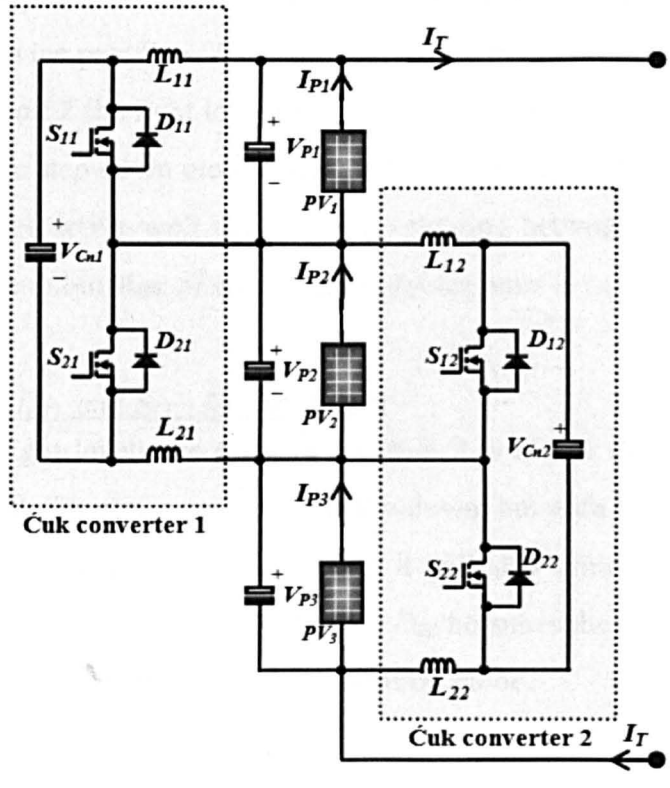

Figure 5.6 Integrated converter configuration for a three PV module system

PV_2 terminals. There are four device pairs in this system. The second subscript for the device symbols denotes the converter it is associated to, so $S_{11} - D_{21}$ and $S_{21} - D_{11}$ are device pairs for converter 1 while $S_{12} - D_{22}$ and $S_{22} - D_{12}$ for converter 2.

It can first be noted that the same argument as in Section 5.2.2 shows how the operating points can be set, and maximum power can be extracted. The sum of the three cell voltages ($V_{P1} + V_{P2} + V_{P3}$) is set by the duty ratio of the final Ćuk step-up converter, while its partitioning is determined by the two ratios, $V_{P1} : V_{P2}$ and $V_{P2} : V_{P3}$ which can be set by the duty ratios of the two bypass converters.

5.3.1.1 Two valid operating modes

The operating modes of the above two converters are determined by the conditions of irradiance on the individual power generation units as analysed in section 5.2.2. For uniform irradiation, both converters are again idle with all switches inactive. Different switching schemes apply when there is inhomogeneous light incidence, and two example cases are described in the following:

Case 1: $S_{11} - D_{21}$ and $S_{22} - D_{12}$ are active

If in unit 1 the light level on PV_1 is higher than that of PV_2, converter 1 may operate in step-down mode having PV_1 as its input source and PV_2 at its output terminals. Device pair $S_{11} - D_{21}$ is now active with duty ratio varying from 0.5 to 1. Likewise in unit 2 the light level on PV_3 is higher than that on PV_2, converter 2 may also operate in step-down mode having PV_3 as input and PV_2 output. Device pair $S_{22} - D_{12}$ becomes active with the duty ratio ranging between 0.5 and 1. The current flow for this combination of the activated device pairs is as shown in Figure 5.7(a).

Case 2: $S_{21} - D_{11}$ and $S_{12} - D_{22}$ are active

If the light levels are such on PV_2 that it is higher than on PV_1 and PV_3, the operation mode for converter 1 is still step-down, but with $S_{21} - D_{11}$ active, PV_2 side as input and PV_1 output. For converter 2, it will also work in step down mode with PV_2 side as input and PV_3 as output. $S_{12} - D_{22}$ becomes the active device pair. Figure 5.7(b) shows the current flow in this operation mode.

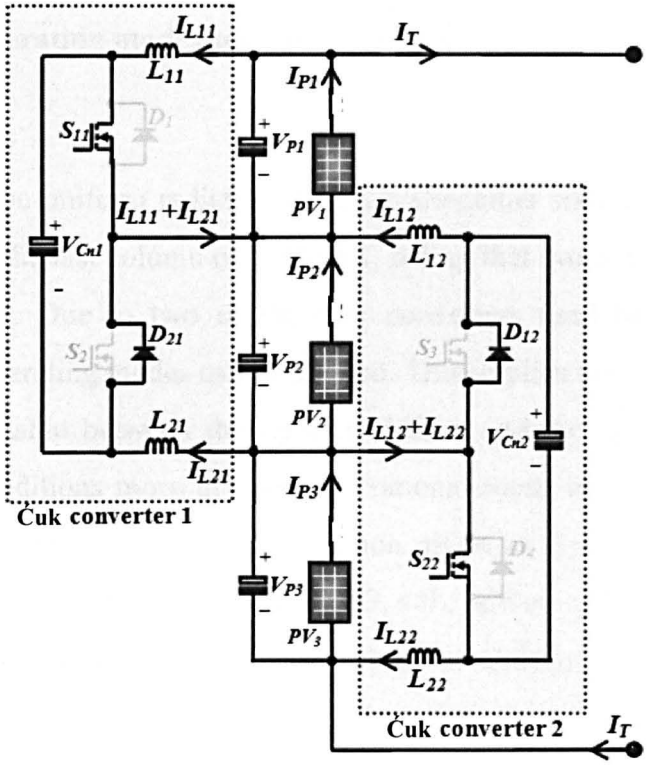

(a) Converter circuit states when $S_{11} - D_{21}$ and $S_{22} - D_{12}$ are active

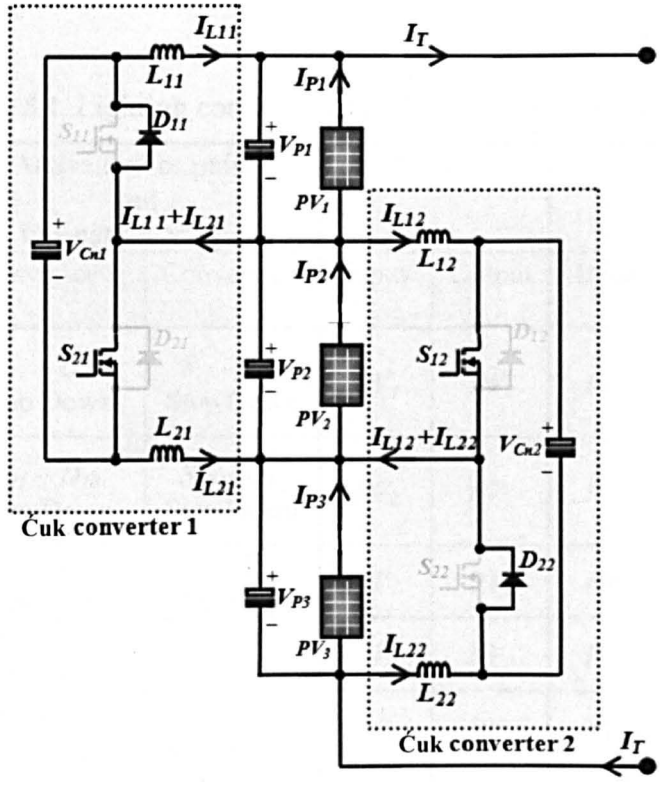

(b) Converter circuit states when $S_{21} - D_{11}$ and $S_{12} - D_{22}$ are active

Figure 5.7 Circuit states for the integrated converter operating under different modes

5.3.1.2 Operating modes selection schemes

Scheme 1

For non-uniform radiation there are altogether six different lighting conditions as listed in the last column of Table 5.1, noting that symbol G denotes solar intensity in mW/cm^2. Due to two of the Ćuk converters used being bi-directional, eight different operating modes can be applied. This implies that there is no simple one-to-one relationship between the light conditions and the operating modes. For some lighting conditions more than one operational mode is plausible as listed in Table 5.1. For example for the light condition given as $G_2<G_3\leq G_1$, modes 1 and 3 are applicable, while for condition $G_2<G_1<G_3$, either modes 1 or 6 may be used. Selection of operating modes under these conditions can be problematic and the preferred ones are therefore those which enable the maximum power output from all three PV modules. Two examples are given below for a system having three modules with the same characteristics as those given in Chapter 2.

Table 5.1 Lighting conditions and their corresponding operation modes

Mode	Active device pairs and Operation Modes		Unit 1		Unit 2		Light Conditions
	Converter 1	Converter 2	Input	Output	Input	Output	
1	$S_{11}-D_{21}$ Step Down	$S_{22}-D_{12}$ Step Down	PV_1	PV_2	PV_3	PV_2	$G_2<G_3\leq G_1$ OR $G_2<G_1<G_3$
2	$S_{21}-D_{11}$ Step Down	$S_{12}-D_{22}$ Step Down	PV_2	PV_1	PV_2	PV_3	$G_3\leq G_1<G_2$ OR $G_1<G_3<G_2$
3	$S_{11}-D_{21}$ Step Down	$S_{12}-D_{22}$ Step Up	PV_1	PV_2	PV_2	PV_3	$G_2\leq G_3<G_1$
4	$S_{11}-D_{21}$ Step Down	$S_{12}-D_{22}$ Step Down	PV_1	PV_2	PV_2	PV_3	$G_3\leq G_2\leq G_1$
5	$S_{11}-D_{21}$ Step Up	$S_{12}-D_{22}$ Step Down	PV_1	PV_2	PV_2	PV_3	$G_3<G_1\leq G_2$
6	$S_{21}-D_{11}$ Step Up	$S_{22}-D_{12}$ Step Down	PV_2	PV_1	PV_3	PV_2	$G_2\leq G_1<G_3$
7	$S_{21}-D_{11}$ Step Down	$S_{22}-D_{12}$ Step Down	PV_2	PV_1	PV_3	PV_2	$G_1\leq G_2\leq G_3$
8	$S_{21}-D_{11}$ Step Down	$S_{22}-D_{12}$ Step Up	PV_2	PV_1	PV_3	PV_2	$G_1<G_3\leq G_2$

Case 1: G_1 = 80 mW/cm^2, G_2 = 100 mW/cm^2 and G_3 = 40 mW/cm^2

For MPP operation, the desirable operating voltages and currents of all modules are listed along Case 1 row in Table 5.2. Hence the desired values for I_T and V_T can be estimated by evaluating the total power equation expressed as

$$P_T = V_T I_T = V_{P1} I_{P1} + V_{P2} I_{P2} + V_{P3} I_{P3} \tag{5.15}$$

In this case, the desired value for I_{P1} is 9.5 A, but the required output terminal current I_T is 8.9 A. The remaining 0.6 A of current can be supplied to the Ćuk converter unit 1 as I_{L11} and thus, the $S_{11} - D_{21}$ pair should be active. On the other hand, the desired value for I_T is greater than I_{P3} which is 4.8 A, requiring the excess current from the terminal to flow into the converter 2 as I_{L22}, hence, $S_{12} - D_{22}$ is activated. Therefore according to Table 5.1, Mode 5 is applicable for this condition.

Case 2: G_1 = 50 mW/cm^2, G_2 = 100 mW/cm^2 and G_3 = 40 mW/cm^2

For this case, G_1 decreases to 50 mW/cm^2 and the light condition is still given as $G_3 < G_1 \leq G_2$ the same as the previous case. However, Mode 2 is applicable for this operating condition following the consideration of its MPP operating voltages and currents listed in Table 5.2. This is due to the fact that unlike the previous case, the desired value for I_{P1} is now less than that for I_T. Thus, the device pair $S_{21} - D_{11}$ for converter 1 should be activated, instead.

Table 5.2 MPP Operations for Case 1 and Case 2

	Desired operating points for PV Modules							
	V_{P1} (V)	V_{P2} (V)	V_{P3} (V)	I_{P1} (A)	I_{P2} (A)	I_{P3} (A)	V_T (V)	I_T (A)
Case 1: G_1: 80 mW/cm^2 G_2: 100 mW/cm^2 G_3: 40 mW/cm^2	28.0	29.5	25.4	9.5	11.9	4.8	82.9	8.9
Case 2: G_1: 50 mW/cm^2 G_2: 100 mW/cm^2 G_3: 40 mW/cm^2	26.3	29.5	25.4	5.9	11.9	4.8	81.2	7.7

Scheme 2

As can be seen from above, just based on Table 5.1 it is not clear which combination of active device pairs should be used for some given sets of insolation levels. Thus another practical scheme for selecting operating modes is derived.

Instead of using a particular light condition to find its corresponding operating mode by referring to Table 5.1, this method groups all modes giving the same combination of active device pairs and derives a unique corresponding light level relationship. For example Modes 3, 4 and 5, can be unified since they all have S_{11} – D_{21} and S_{12} – D_{22} device pairs active. The unique light condition for these modes can be derived as follows. When S_{11} – D_{21} device pair is active, I_{L1} flows into Ćuk converter 1 and hence

$$I_{P1} - I_T > 0 \tag{5.16}$$

Expressing Equation (5.16) in terms of power and voltage, one obtains

$$\frac{P_{P1}}{V_{P1}} - \frac{P_1 + P_2 + P_3}{V_{P1} + V_{P2} + V_{P3}} > 0 \tag{5.17}$$

Equation (5.17) can be re-arranged such that the voltage terms are placed on the left and the power terms on the right side of the inequality sign, and thus, becomes

$$\frac{V_{P1} + V_{P2} + V_{P3}}{V_{P1}} > \frac{P_1 + P_2 + P_3}{P_1} \tag{5.18}$$

As the analysis focuses mainly on MPP region and the variation of the PV voltage due to the light changes is less significant comparing to that of the PV power. Assuming a constant average value of 3 is taken for the voltage ratio, Equation (5.18) is expressed as

$$P_1 + P_2 + P_3 < 3P_1 \tag{5.19}$$

As discussed in Chapter 2, the maximum power varies almost linearly with the solar insolation. Hence P_1, P_2 and P_3 in Equation (5.19) can be respectively substituted by G_1, G_2 and G_3, hence yields

$$G_1 + G_2 + G_3 < 3G_1 \tag{5.20}$$

which can be written as

$$\frac{G_2 + G_3}{2} < G_1 \tag{5.21}$$

Thus for a specific set of the insolation levels if they give a relationship as above the operation mode for the Ćuk converter 1 can be determined. The assumption made for the above analysis can be justified according to the example PV module given in Section 2.2.2. In this case, the power ratio on the right-hand-side of Equation (5.18) varies from 1.13 to 30.58 as the voltage ratio on the left-hand-side changes from 2.2 to 3.95. This is measured on a wide range of solar insolation of between 10 mW/cm^2 and 100 mW/cm^2 and that of cell temperature between 0 and 30°C.

To verify this scheme, Case 1 in Table 5.1 is taken as an example; the light relationship is now $\frac{G_2 + G_3}{2} < G_1$ hence, S_{11} – D_{21} device pair should be active. However for Case 2, since the light equation is $\frac{G_2 + G_3}{2} > G_1$ so we have the S_{21} – D_{11} device pair activated. This corresponds to the condition when I_{L11} flows out of the converter and thus,

$$I_{P1} - I_T < 0 \tag{5.22}$$

Similar analysis can be applied to determine active device pairs for converter 2 but now it is based on the current direction of I_{L22}. Therefore S_{12} – D_{22} are to be activated if the light condition is given as $\frac{G_1 + G_2}{2} > G_3$, while the condition for $S_{22} - D_{12}$ to be active is when $\frac{G_1 + G_2}{2} < G_3$. Combining these two inequalities with the ones for converter 1, there are four light condition combinations as listed in Table 5.3, and each corresponds to a combination of two active device pairs. As can be seen, this scheme leads to a simpler method for choosing converter operating modes compared with the first scheme; hence it is used for the simulated system below.

Table 5.3 Unified light conditions for the same combination of device pairs

Mode	Active device pairs and Operation Modes		Unit 1		Unit 2		Light Conditions
	Converter 1	Converter 2	Input	Output	Input	Output	
1	$S_{11} - D_{21}$	$S_{22} - D_{12}$	PV_1	PV_2	PV_3	PV_2	$\frac{(G_2 + G_3)}{2} < G_1$ AND $\frac{(G_1 + G_2)}{2} < G_3$
2	$S_{21} - D_{11}$	$S_{12} - D_{22}$	PV_2	PV_1	PV_2	PV_3	$\frac{(G_2 + G_3)}{2} > G_1$ AND $\frac{(G_1 + G_2)}{2} > G_3$
3, 4, 5	$S_{11} - D_{21}$	$S_{12} - D_{22}$	PV_1	PV_2	PV_2	PV_3	$\frac{(G_2 + G_3)}{2} < G_1$ AND $\frac{(G_1 + G_2)}{2} > G_3$
6, 7, 8	$S_{21} - D_{11}$	$S_{22} - D_{12}$	PV_2	PV_1	PV_3	PV_2	$\frac{(G_2 + G_3)}{2} > G_1$ AND $\frac{(G_1 + G_2)}{2} < G_3$

5.3.2 Switching Scheme for More Than Three PV Modules

For the system shown in Figure 5.8 (when they are more than three PV modules) it can be difficult to determine the appropriate switching modes for the Ćuk converters based solely on light conditions as described in Section 5.3.1.2.

The system shown in Figure 5.8 has m PV modules and $(m - 1)$ bidirectional Ćuk converters. For ease of readability, only the inner Ćuk converters are drawn while V_T refers to the input voltage to the outer Ćuk step-up converter. As is known, the power generated from each module depends on the levels of insolation and cell temperature, the knowledge of the corresponding voltage and current values under optimal operation is needed for determining the operating modes. This is obtained through using a mathematical model of the PV module and the development of such a model will be discussed in Chapter 6.

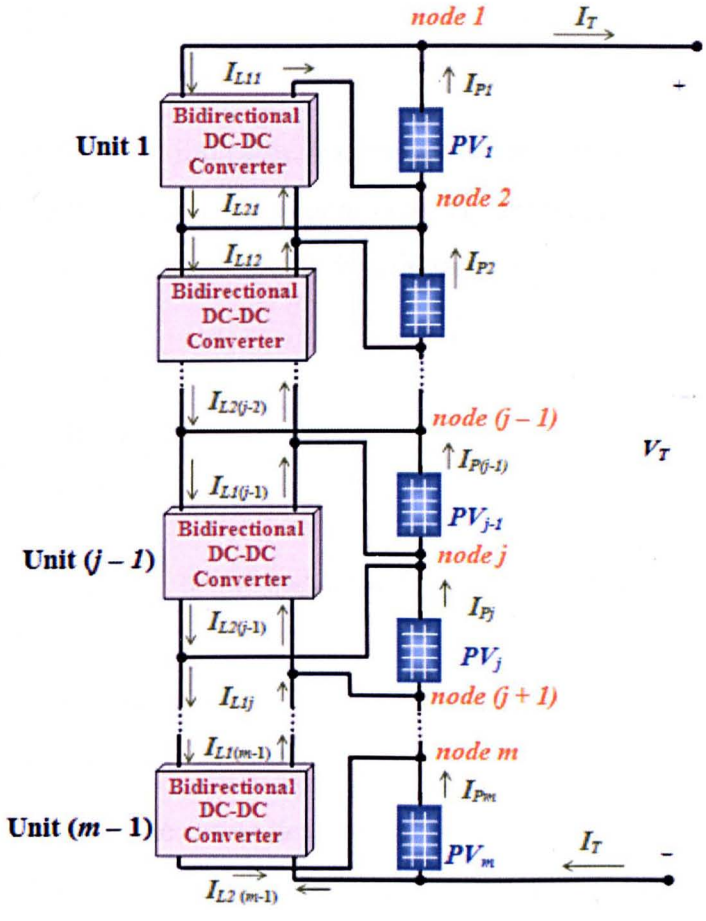

Figure 5.8 Flows of currents around PV-integrated converters for m-PV-module system

The switching scheme in this section follows the analysis given at the end of Section 5.2.2, whereby the selection for the operation mode of each inner converter is based on the bypassed power flowing through it. This is achieved by observing the desired direction for the inductor currents, given a specific set of the model-predicted optimal PV operating points. The operation mode selection is performed in the order starting from the first bidirectional Ćuk converter 1 at the top left of the system in Figure 5.8, to the converter $(m - 1)$ at the bottom.

Assuming all PV modules in the chain of the system in Figure 5.8 are identical and a model of them is available, to determine the switching modes and duty ratios of the converters, the model is then used to predict the optimal voltage and current values for each module. The information, thus, obtained can be applied to calculate the optimal system terminal current as

$$I_T^* = \frac{V_{P1}^* I_{P1}^* + V_{P2}^* I_{P2}^* + ... + V_{Pm}^* I_{Pm}^*}{V_{P1}^* + V_{P2}^* + ... + V_{Pm}^*} \tag{5.23}$$

where the superscript * indicates that the associated parameter is the value at the optimal power point predicted by the models. By applying Kirchhoff's current law at node 1, the desired inductor currents for converter 1 can then be obtained as

$$I_{L11}^* = I_{P1}^* - I_T^* \tag{5.24}$$

$$\text{and } I_{L21}^* = I_{L11}^* \frac{(1 - K_{11}^*)}{K_{11}^*} \tag{5.25}$$

where $K_{11}^* = \left| \frac{V_{P2}^*}{V_{P1}^* + V_{P2}^*} \right|$ is the desired duty cycle for converter 1.

Clearly, when I_{L11}^* and I_{L21}^* from Equations (5.24) and (5.25) are positive $S_{11} - D_{21}$ are active; conversely, $S_{21} - D_{11}$ are active.

For converter 2, the active device pair can be determined according to I_{L11}^* and I_{L21}^* calculated previously from Equations (5.24) and (5.25) and the model-predicted I_{P1}^* and I_{P2}^*. By applying Kirchhoff's current law at node 2 as indicated in Figure 5.8, one can observe that I_{L12}^* for converter 2 has a positive value if the $S_{12} - D_{22}$ pair is active and hence,

$$\left(I_{P2}^* - I_{P1}^*\right) + \left(I_{L11}^* + I_{L21}^*\right) > 0 \tag{5.26}$$

Conversely, the $S_{22} - D_{12}$ pair is active if

$$\left(I_{P2}^* - I_{P1}^*\right) + \left(I_{L11}^* + I_{L21}^*\right) < 0 \tag{5.27}$$

In addition, the inductor currents for converter 2 can be evaluated as

$$I_{L12}^* = \left(I_{P2}^* - I_{P1}^*\right) + \left(I_{L11}^* + I_{L21}^*\right) \tag{5.28}$$

$$\text{and } I_{L22}^* = I_{L12}^* \frac{(1 - K_{22}^*)}{K_{22}^*} \tag{5.29}$$

where $K_{12}^* = \left| \frac{V_{P3}^*}{V_{P3}^* + V_{P2}^*} \right|$ is the desired duty cycle for converter 2.

For the subsequent converters, an additional term is needed and for example, at node j in Figure 5.8, $I_{L2(j-2)}$ should be added to the Kirchhoff's current law equation. Hence, the $S_{1j} - D_{2j}$ pair for j-th converter is active if

$$\left(I_{Pj}^{*} - I_{P(j-1)}^{*}\right) + \left(I_{L1(j-1)}^{*} + I_{L2(j-1)}^{*}\right) - \left(I_{L2(j-2)}^{*}\right) > 0 \tag{5.30}$$

Conversely, the $S_{2j} - D_{1j}$ pair becomes active if

$$\left(I_{Pj}^{*} - I_{P(j-1)}^{*}\right) + \left(I_{L1(j-1)}^{*} + I_{L2(j-1)}^{*}\right) - \left(I_{L2(j-2)}^{*}\right) < 0 \tag{5.31}$$

Note that all the terms to the left of the inequality signs in Equations (5.30) and (5.31) are known since I_{Pj}^{*} and $I_{P(j-1)}^{*}$ are obtained from the model and $I_{L1(j-1)}^{*}$, $I_{L2(j-1)}^{*}$, and $I_{L2(j-2)}^{*}$ are the evaluated inductor currents for the preceding converters. The inductor currents for j-th converter can then be written as

$$I_{L1j}^{*} = \left(I_{Pj}^{*} - I_{P(j-1)}^{*}\right) + \left(I_{L1(j-1)}^{*} + I_{L2(j-1)}^{*}\right) - \left(I_{L2(j-2)}^{*}\right) \tag{5.32}$$

and $$I_{L2j}^{*} = I_{L1j}^{*} \cdot \frac{\left(1 - K_{2j}^{*}\right)}{K_{2j}^{*}} \tag{5.33}$$

where $K_{1j}^{*} = \left| \dfrac{V_{P(j+1)}^{*}}{V_{Pj}^{*} + V_{P(j+1)}^{*}} \right|$ is the desired duty cycle for converter j.

A similar procedure through the evaluation of Equations (5.30) and (5.31) is also applied to determine the active device pair for the subsequent converter. Thereafter, Equations (5.32) and (5.33) are used to evaluate its inductor currents. When there is a change in weather conditions, PV models will generate a new set of PV operating points and Equations (5.24) – (5.33) have to be re-evaluated to update the switching scheme for the converters. In the same manner as above, this is done in the order starting from the bidirectional Ćuk converter 1 at the top left of system in Figure 5.8, to the converter (m – 1) at the bottom. A flowchart shown in Figure 5.9, summarizes the above described procedure in determining the switching scheme based on pre-determined PV models.

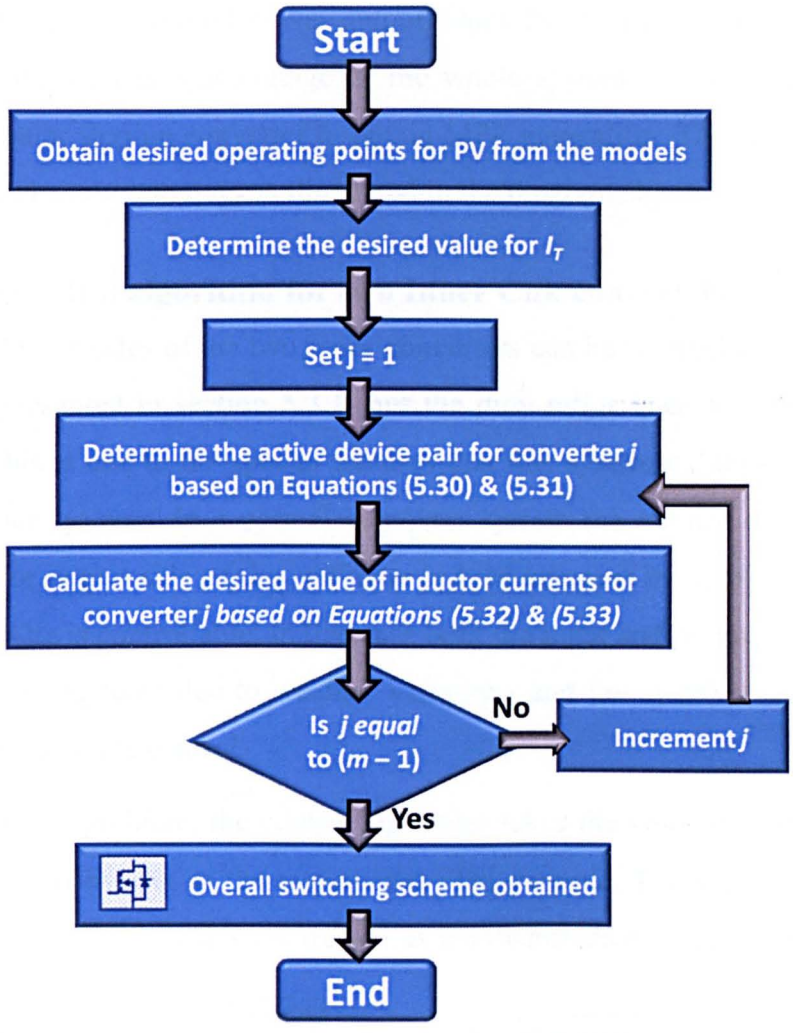

Figure 5.9 Flowchart for determining the switching modes of the inner Ćuk converters for an *m*-PV-module system

5.4 Model-based Control for MPP Tracking

The objective of a desired control scheme for the above system is to enable all PV modules in the chain to operate at their peak power points during any weather conditions. The following discussion focuses on the three-PV module system described in section 5.3.1. The system consists of three converters: two inner bidirectional Ćuk converters; and one terminal step-up Ćuk converter. Hence the coordinated control of these converters is essential for achieving the optimal performance. The rationale and procedure of the control scheme described is as follows: according to the measured levels of sun light and shading conditions within each unit, the switching modes for the two inner converters can be selected following the scheme described in Section 5.3.1. Subsequently their duty ratios can be set in order to lead the terminal voltage for each of the three PV modules

corresponding to their maximum power output. Once the operating modes of inner converters are set, the terminal voltage of the whole system can be regulated by controlling the outer step-up converter to obtain MPP generation. The configuration for the system and control strategy is illustrated in the diagram shown in Figure 5.10.

5.4.1 Voltage control algorithm for two Inner Ćuk converters

The switching modes of the two inner converters can be determined according to the scheme presented in section 5.3.1, but the duty ratios need to be regulated continuously. This is due to the special features that this system exhibits compared to other converter systems. In a normal converter system the voltage on one side, either the input or output side of the converter is held constant by a voltage source; hence the other side is controllable. In this case both the input and output voltages of the converter may fluctuate due to weather variations and the system may become unstable without adequate control.

To address this problem, the control algorithm takes the voltage on the output end of a particular converter as the major controlled variable. The variations of the input voltage from its ideal levels are treated as the disturbance to the output, hence

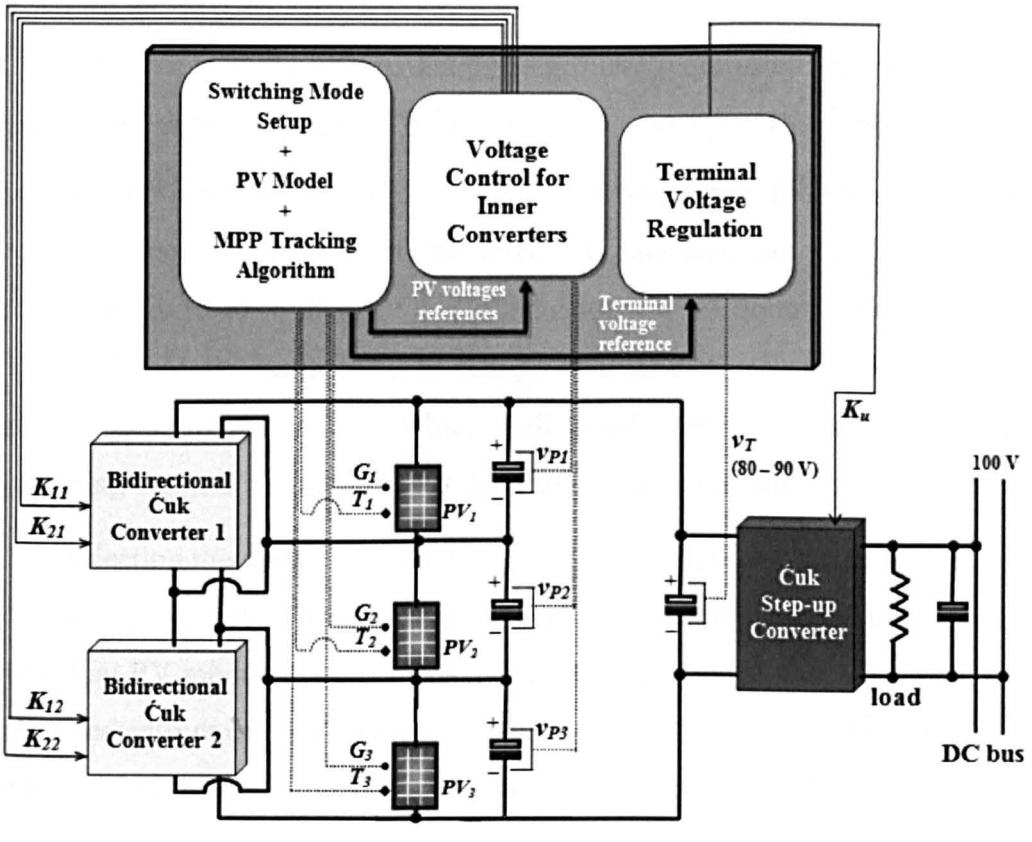

Figure 5.10 Configuration of the overall system control

they have to be eliminated or, at least, minimized. Thus, in the P+I control formulae, the errors of the input voltage must be subtracted from both proportional and integration terms. For any particular operation mode, the duty ratios for the two converter switches are evaluated following the P+I controller algorithm as

$$K_{11} = N_{p1}\left[\left(V_{P2}^{*} - V_{P2}\right) - \left(V_{P1}^{*} - V_{P1}\right)\right] + N_{i1}\int\left[\left(V_{P2}^{*} - V_{P2}\right) - \left(V_{P1}^{*} - V_{P1}\right)\right]dt \tag{5.34}$$

$$K_{21} = 1 - K_{11} \tag{5.35}$$

$$K_{22} = N_{p2}\left[\left(V_{P2}^{*} - V_{P2}\right) - \left(V_{P3}^{*} - V_{P3}\right)\right] + N_{i2}\int\left[\left(V_{P2}^{*} - V_{P2}\right) - \left(V_{P3}^{*} - V_{P3}\right)\right]dt \tag{5.36}$$

$$K_{12} = 1 - K_{22} \tag{5.37}$$

where V_{P1}, V_{P2}, and V_{P3} are measured, PV panel voltages and V_{P1}^{*}, V_{P2}^{*}, V_{P3}^{*} are their corresponding optimal values. K_{11}, K_{21}, K_{12} and K_{22} are the duty cycles for S_{11}, S_{21}, S_{12} and S_{22} respectively. N_{p1} and N_{i1} are the proportional and integral gain values, respectively, for controller in Ćuk converter 1, while N_{p2} and N_{i2} are for Ćuk converter 2.

It is clear from the above, that this algorithm requires the information about the desired PV voltages prior to setting V_{P1}^{*}, V_{P2}^{*} and V_{P3}^{*}. This can be obtained by applying a model-based approach. In this work, three PSO-based Neuro-Fuzzy models, respective to each of the three PV modules, are established using the technique described in Chapter 6 and embedded in the control system as shown in Figure 5.10. Upon every detected change of illumination conditions, these models estimate the voltage values which will yield the corresponding PV modules generating the peak power and feed them to the corresponding control loop.

Selecting the control variables N_{p1}, N_{p2}, N_{i1} and N_{i2} are based on the principles of achieving a fast dynamic response, and eliminating steady-state errors in the individual PV module's output voltage. This inner control loop effectively removes the poles introduced by capacitors across each PV panel; hence it reduces the complications posed to the terminal step-up converter controller as discussed in the next section.

5.4.2 Terminal Voltage Regulation for the Ćuk step-up converter

The circuit diagram of the Ćuk step-up converter on the output of the PV system is shown in Figure 5.11. The input voltage of this converter is determined by the PV system terminal capacitor, while its output voltage is kept constant by a voltage source such as a battery, or a DC power supply. The objective of the converter control is to adjust its input voltage properly, i.e. the PV system terminal voltage, such that the system output power is always at the maximum power level. Hence, the reference voltage for the input of this converter is set as the sum of reference voltages for three PV modules used in the previous section.

The reference value can be applied directly to adjust the duty cycle for the converter based on the voltage value of the DC power supply. This approach is suitable for a PV system with a limited operating range as discussed in Chapter 3. However as the system has three PV modules, the operating ranges of the input voltage and the duty cycle of the Ćuk step-up converter are wider comparing to a single PV panel system. Therefore, the high transient performance of the PV voltage may not be achieved under certain operating conditions. This is demonstrated through the transfer function between the switch duty ratio and PV side voltage for this converter which can be expressed as

$$G_{ik}(s) = -\frac{V_B C_u (L_B + L_G)s^2 + I_T (L_B(1-K_u) - L_G(K_u))s + V_B}{q_4 s^4 + q_3 s^3 + q_2 s^2 + q_1 s + 1} \tag{5.38}$$

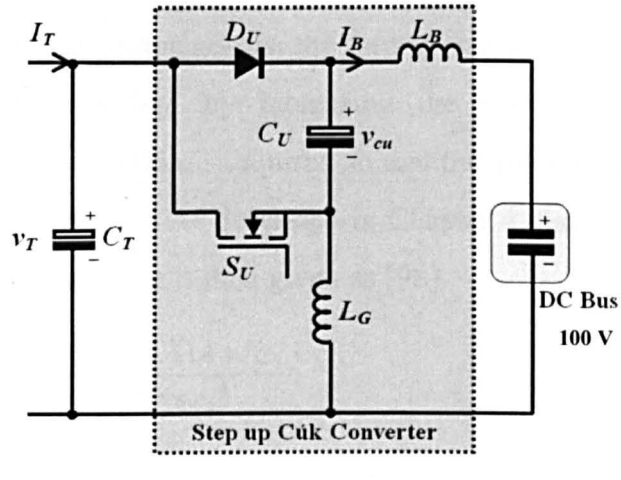

Figure 5.11 Schematic circuit for the terminal Ćuk step-up converter

where

$$q_1 = \frac{1}{R_{PV}}\left(L_G K_u^{\,2} + L_B(1-K_u)^2\right)$$

$$q_2 = \left(C_u(L_G + L_B) + C_T\left(L_G K_u^{\,2} + L_B(1-K_u)^2\right)\right)$$

$$q_3 = \frac{C_u L_1 L_2}{R_{PV}}$$

$$q_3 = C_T C_u L_1 L_2$$

k_u = duty cycle for S_u

and R_{PV} is the slope of $I-V$ characteristic at its steady-state point.

Note that the negative sign in $G_{ik}(s)$ indicates that the terminal voltage is varying inversely with the duty ratio. As discussed in Chapter 4, the transfer function is a system having four poles and two zeros, and hence at high frequencies, its phase tends towards -180°, while its magnitude falls at -40 dB/decade. As can be observed from the Equation (5.38), the bandwidth and the phase margin of this system are closely dependent on the switch duty cycle of the converter and for a chosen set of converter components; they may not satisfy the design criteria for the transient performances.

A closed-loop feedback control using compensation technique, as discussed in Chapter 4, can be used to obtain the overall desired performance for the converter. This involves lead and lag compensators; the former speeds up the voltage response while maintaining its stability, by increasing the system phase margin and bandwidth. The lag compensation is required so that the voltage regulation becomes less susceptible to disturbances. As described in Chapter 4, the transfer function for the overall lead-lag compensator is then given as [98]

$$G_{comp}(s) = -K_{comp}\frac{(1+s\alpha_d\tau_d)(1+s/\omega_L)}{s(1+s\tau_d)} \tag{5.39}$$

where the maximum phase lead of $\sin^{-1}\dfrac{\alpha_d - 1}{\alpha_d + 1}$ occurs at the frequency of $\dfrac{1}{\tau\sqrt{\alpha_d}}$ rad/sec while the ω_L is the breakpoint frequency of the lag compensator.

To avoid counter-action of this controller with the previously described P + I converters, the duty cycle regulation for this converter is only performed when PV voltage responses due to the latter, have stabilized within a specified range of fluctuation. The flowchart shown in Figure 5.12 summarizes the implementation of the above-described control for the PV-integrated converter using a modelling-based approach.

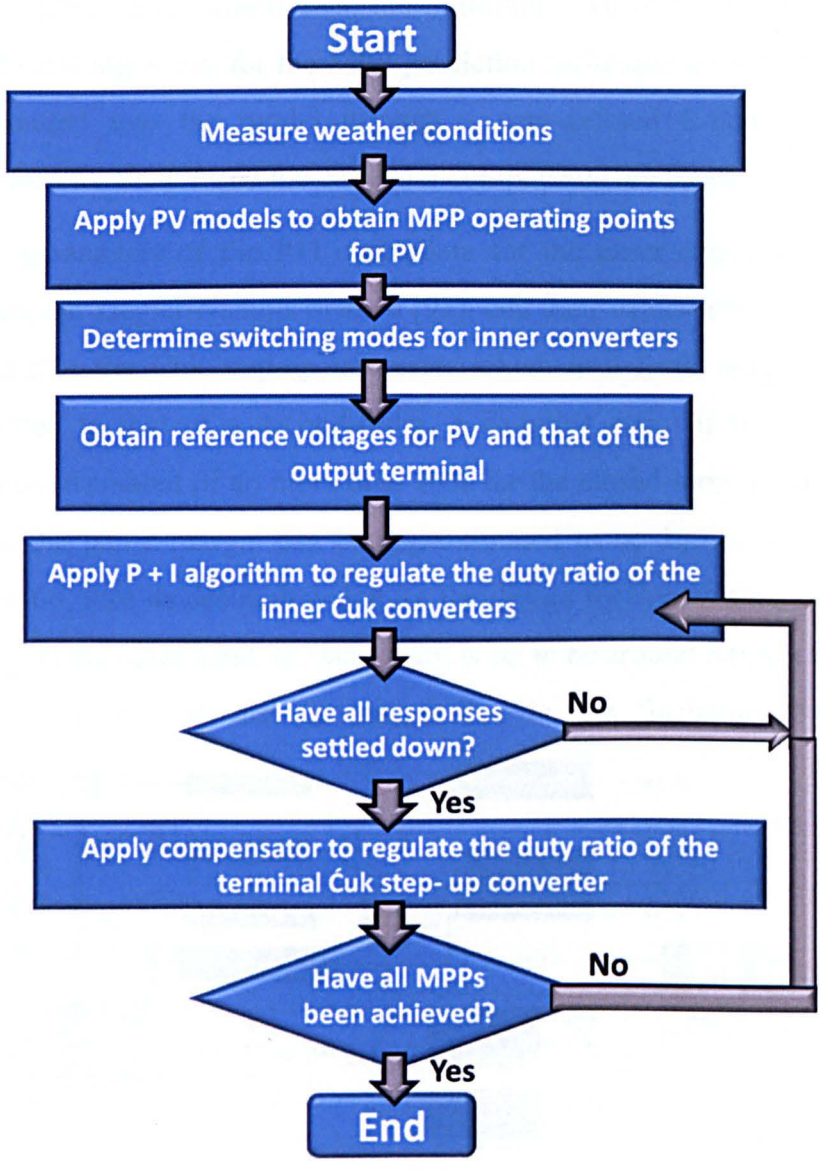

Figure 5.12 Flowchart for the control of a PV-integrated converter using model-based approach

5.4.3 Simulation and Discussion

Prior to the performance evaluation of the PV-integrated converter and MPP tracking control scheme presented in the previous sections, a computer model for a three PV module system has been developed using the MATLAB-SIMULINK software package as shown in Figure 5.13. The model employs a Power System toolbox which contains circuit blocks for power components for the converter. The model also applies the switching scheme based on the light conditions in Table 5.3.

To implement the controllers, the Simulink Control System toolbox is used. The MATLAB algorithm for the MPP prediction technique described in Chapter 4, is incorporated into the model through a user-defined S-Function block. The specifications for the PV and the converter components are listed in Table 5.4.

The parameters of the P+I controllers for the inner converters are carefully tuned using the Ziegler-Nichols method [98], and their values are listed in Table 5.4. Assuming that the Ćuk step-up converter which is a forth order system can be approximated to that of a second-order, a damping ratio of 0.6 is desirable for obtaining an overshoot of no more than 10% for the closed-loop response for V_T. As is known, the phase margin can be approximated to be 100 times more than the damping ratio, thus its desirable value for the design for the terminal compensator is set to 60°. On the other hand, its bandwidth is set to be around 5 times lower than the switching frequency so that all noises due to the fluctuation in V_T can be

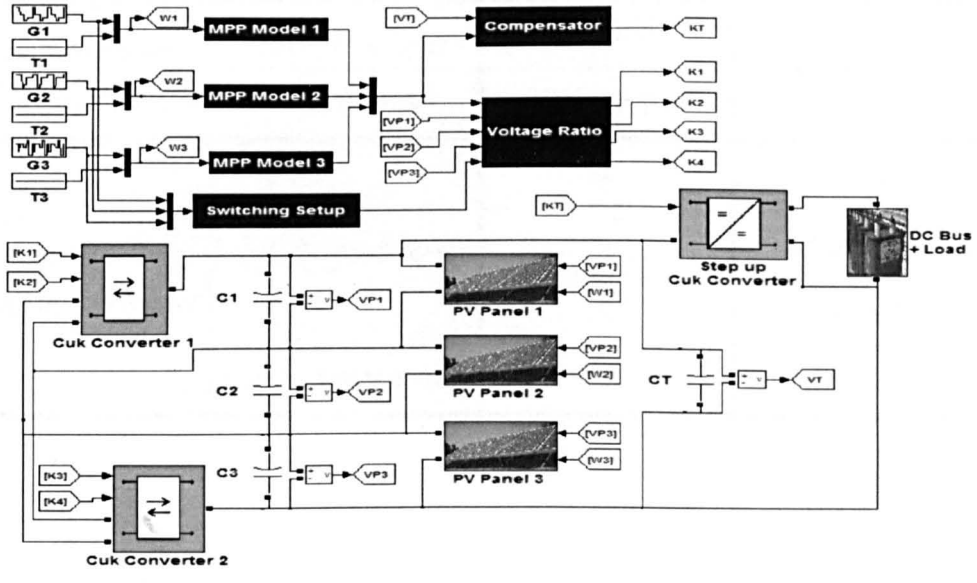

Figure 5.13 Computer model of a PV-integrated converter system consisting of three PV module

Table 5.4 Design specifications for 1044 W three-PV-module system

Parameters		Symbols	Values
PV Module	No. series cells	n_s	60
	No. parallel cells	n_p	4
	Maximum power at T = 20° C and G = 100 mW/cm^2	P_{mpp}	348 W
	MPP voltage at T = 20° C and G = 100 mW/cm^2	V_{mpp}	29.12 V
Rated bus voltage		V_{bus}	100 V
Switching frequency		f_s	20 kHz
Inductors		L_{11}, L_{21}, L_{12} and L_{22}	8 mH
		L_B	12.5 mH
		L_G	0.9 mH
Capacitors		C_{n1} and C_{n2}	10 μF
		C_U	2 μF
		C_1, C_2 and C_3	50 μF
P+I controllers for inner converters 1 & 2	Proportional gains	N_{p1} and N_{p2}	0.036
	Integral gains	N_{i1} and N_{i2}	0.9393
Compensator for Ćuk step-up converter	Lead Compensation	α_d	7.969
		τ_d	12.30×10^{-6}
		K	1.33×10^3
	Lag Compensation	ω_L	1.257×10^3

attenuated and the oscillation in the control output, i.e. the PWM signal can be prevented. Hence the crossover frequency is set at $\omega = 30 \times 10^3$ rad/sec. A two-stage lead and one-stage lag compensator is developed with the former contributing an additional 19 dB gain and 102° phase lead. The parameters for the compensator are also listed in Table 5.4.

The simulation was performed under different weather conditions to validate the proposed control scheme. Figure 5.14 displays the simulated responses for the three PV modules with uniform insolation and also 3 different partial shading conditions. Figures 5.14(a), (b) and (c) respectively show the variation in solar insolation levels, the PV voltage responses and power obtained from the individual PV modules. The model predicted voltage values (obtained from the PSO neuro-fuzzy modelling in Chapter 6) are denoted by the red dotted lines and the black solid lines represent the simulated responses. All PV modules are operating under the same cell temperature of 20°C and initially, they are uniformly irradiated with $G_1 = G_2 = G_3 = 60$ mW/cm^2.

At t = 0.6 second, PV_2 receives more solar insolation. Consequently, the switching devices are activated/de-activated accordingly, and the MPP model starts to compute the new PV_2 voltage reference. At first this causes the PV voltages to be regulated appropriately by adjusting the duty cycles for inner Ćuk converters. When the responses begin to stabilize, the operating point of the Ćuk step-up is subsequently updated. After 0.07 second, all the PV voltages follow closely to their reference values.

At t = 0.7 second, insolation levels on PV_1 and PV_3 change simultaneously. The control system can still quickly restore the optimal PV operation.

At t = 0.8 second, the insolation level on PV_3 starts to drop significantly and in particular, this leads to a small voltage overshoot of 0.6 V for PV_1. Even though thereafter, there is a small fluctuation, the voltage responses are adequately dampened by the controllers.

Table 5.5 lists the maximum power that can be drawn from the PV modules and the total power extracted using the PV-integrated converter under the 3 shading conditions. The latter is lower than the former by no more than 6 W due to the fact that all the PV voltages follow closely with their MPP reference values.

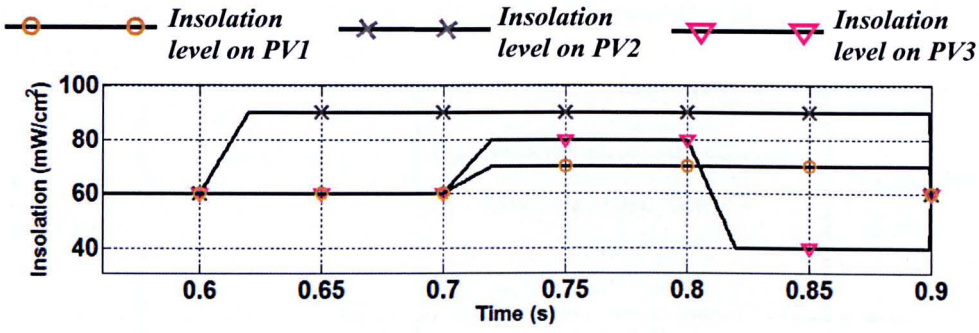

(a) Variation in solar insolation levels

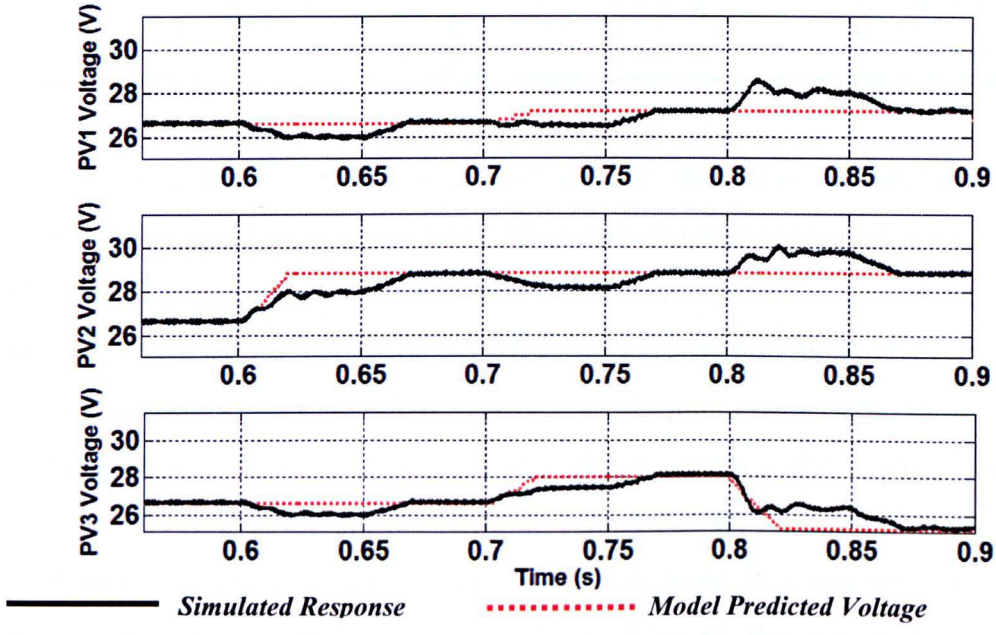

(b) Comparison between simulated voltage response and that predicted by model

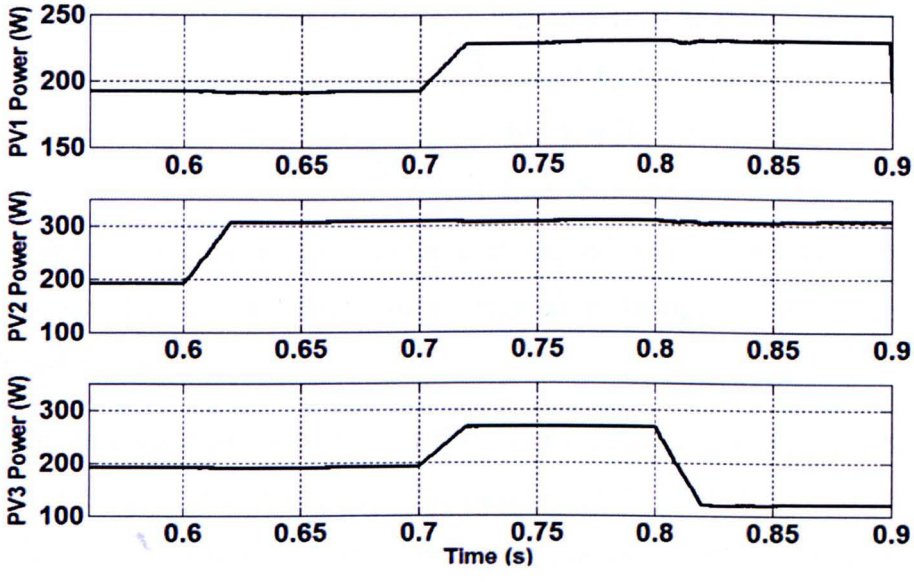

(c) Power obtained from individual PV modules

Figure 5.14 Simulated responses for the modelling-based approach using P + I controller and a feedback compensator for duty ratio regulation

Table 5.5 Maximum power available from the PV modules and the power extracted using PV-integrated converter

Cell Temperature	Solar Insolations (mw/cm^2)			Optimal power that can be drawn from the PV modules	Total Power Extracted
	G_1	G_2	G_3		
20° C	60	60	60	578.2 W	573.8 W
	60	90	60	692.1 W	687.1 W
	70	90	80	805.2 W	803.6 W
	70	90	40	658.0 W	655.9 W

The advantage of the P+I controllers for the inner converters can be highlighted through the comparison of their performance to that of an open-loop feedforward system where the duty cycles of inner converters are computed by directly applying the model predicted MPP voltages to Equations (5.3) and (5.6). The feedforward system simulation with the similar weather variation is then performed. Figures 5.15(a), (b) and (c) respectively displays the weather variation, the PV voltage responses, and the obtained output power. As can be observed, the PV voltages are subject to large overshoots when there is a change in insolation level. In particular at $t = 0.8$ second, V_{P3} falls 2.4 V below the predicted value while V_{P1} has an overshoot of around 1.3 V. This also causes a dip of about 27 W in the total power at $t = 0.821$ second as shown in Figure 5.16. The power output obtained from the open-loop feedforward system is depicted by the blue dotted line and that using the closed-loop P+I controller is by the black solid line. They are compared to the ideal power value by the red dashed line. Nevertheless, when the voltage responses stabilize (i.e. 0.08 second after a change in weather conditions), there is a small difference between the total power obtained in the open-loop system and that in the closed-loop system.

It can be concluded that while MPPs can still be achieved when the inner converters are regulated using feedforward control, the above proposed P+I controllers are still important for limiting the amount of PV voltage overshoots which may occur when there is a significant change in weather conditions.

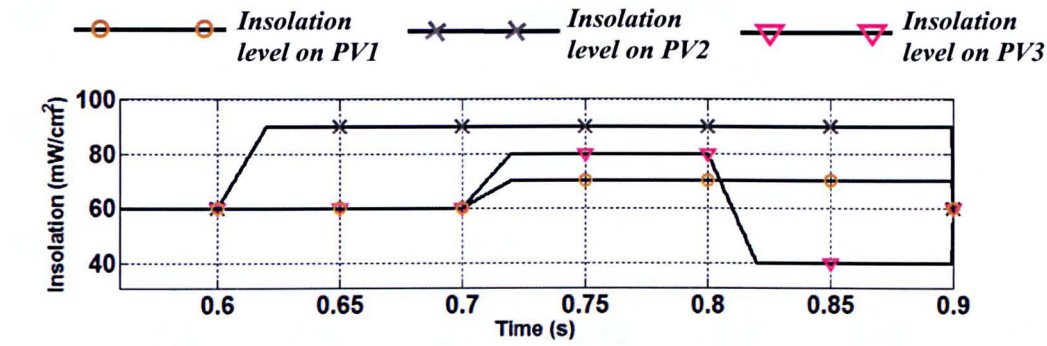

(a) Variation in solar insolation levels

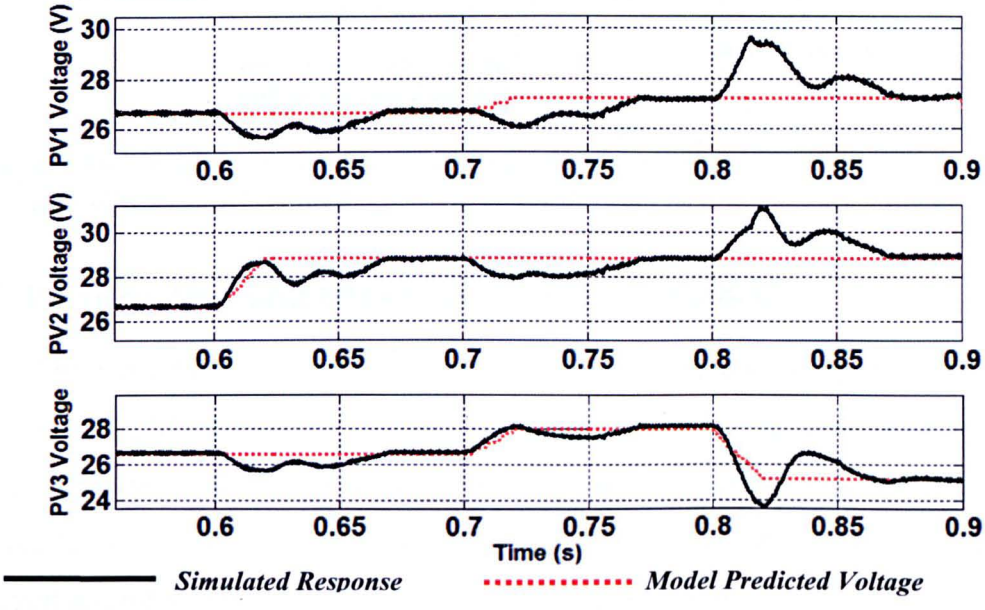

(b) Comparison between simulated voltage response and that predicted by model

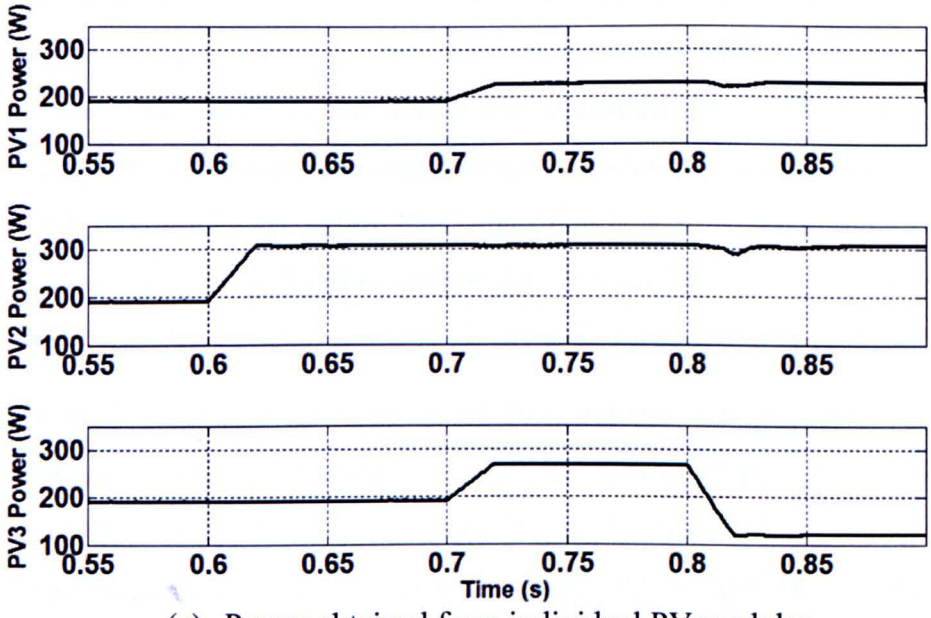

(c) Power obtained from individual PV modules

Figure 5.15 Simulated responses for modelling-based approach using feedforward control for duty ratio regulation

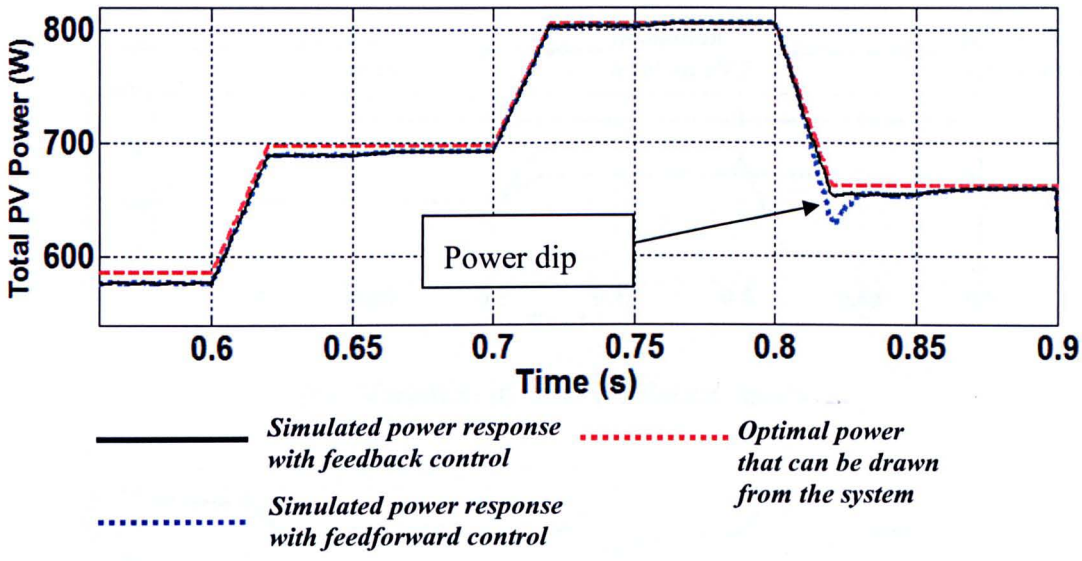

Figure 5.16 Power output responses for the three PV module system with modelling-based control

5.5 Perturbation and Observation (P&O) Method

Alternatively, it is possible to use the well-known Perturbation and Observation (P&O) method [38, 49] in searching for the optimal voltage values. Upon every detected change of illumination conditions, the optimal voltages for the PV modules are obtained by a set of P&O algorithm and the converter duty ratios are updated accordingly.

Using this method, another computer model is implemented with all the design specifications being the same as those for model-based type except that now the control system is based on the MATLAB algorithm for P&O tracking and is incorporated into the model through another user-defined S-Function block. It is noted that at the initial stage before P&O algorithm is applied, the optimal values for PV voltages are set as equal and hence the duty cycles of the inner converters are set as 0.5.

Figures 5.17(b) and (c) respectively demonstrates the simulated voltage and power responses under the shading conditions as shown in Figure 5.17(a) which are the same as those in Section 5.4.3. Comparing to the model-based control scheme, the voltage responses are more oscillatory as the P&O algorithm is continuously finding the best duty ratio values for achieving MPPs. The PV voltages also have large overshoots again at t = 0.8 second, when the solar insolation on PV_3 changes more significantly. This is due to the fact that like the feedforward control technique

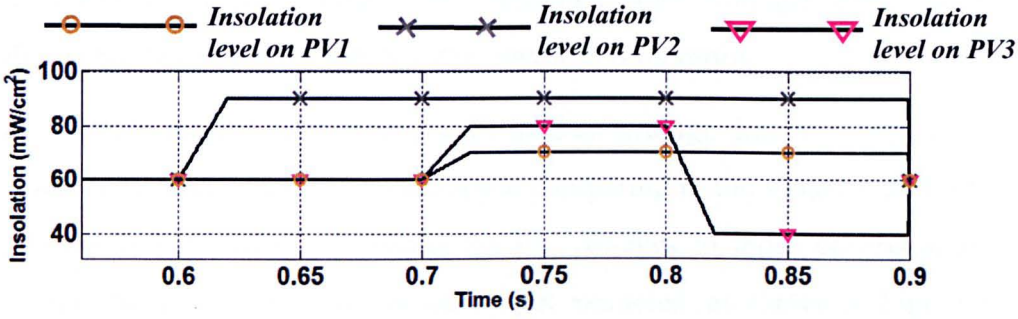

(a) Variation in solar insolation levels

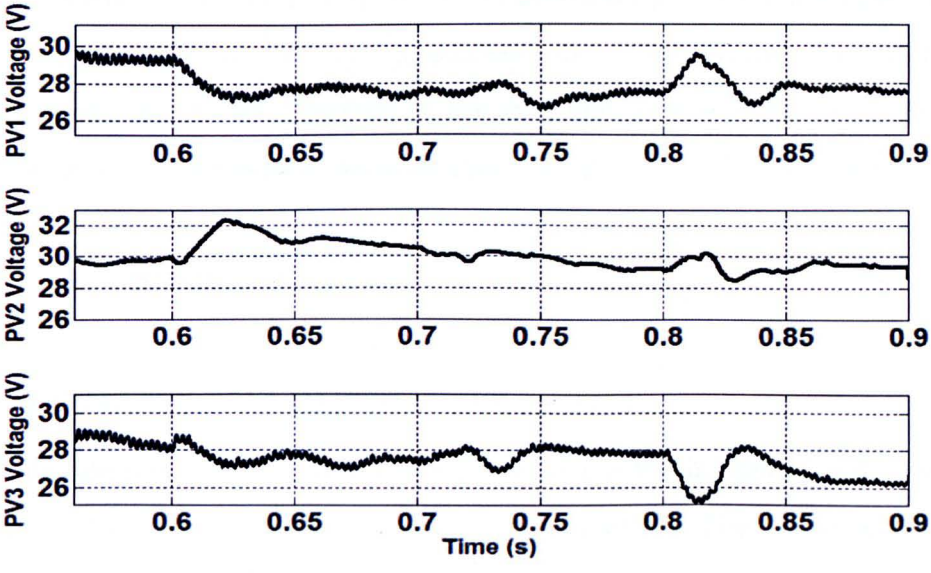

(b) Simulated voltage response and that predicted by model

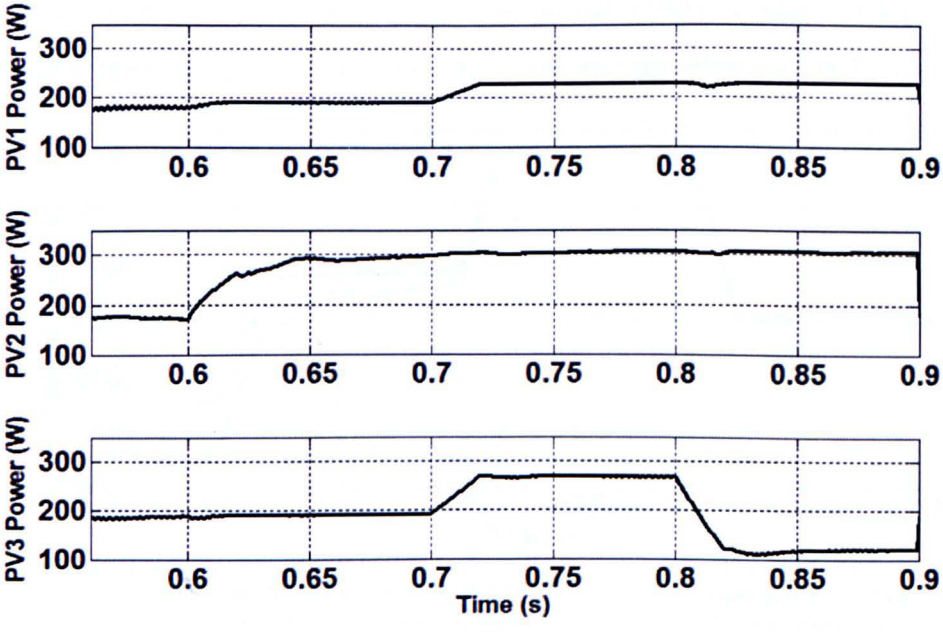

(c) Power obtained from the PV modules

Figure 5.17 Simulated responses for P&O based control for duty ratio regulation

for the modelling-based approach, the predicted MPP voltages from the P&O algorithm are used directly to regulate the converter duty ratios.

In addition, the PV voltage responses take an average time of 0.085 second to settle down to a steady-state value and hence comparing to the model-based control, the P&O method is slower in leading the PV voltages to those corresponding to MPPs. This also affects the total power output extracted, as shown in Figure 5.18. The power losses for all the shading conditions are summarized in Table 5.6. For the last two weather conditions (i.e. G_1 = 70 mW/cm^2, G_2 = 90 mW/cm^2, G_3 = 40 mW/cm^2 for the former and G_1 = 70 mW/cm^2, G_2 = 90 mW/cm^2, G_3 = 80 mW/cm^2 for the latter), the power extracted is almost equal to that when using the model-based control. The difference between them is larger for other weather conditions; i.e. about 31 W when $G_1 = G_2 = G_3$ = 60 mW/cm^2 and 9 W when $G_1 = G_3$ = 60 mW/cm^2, G_2 = 90 mW/cm^2.

5.6 Comparison with Bypass Diode System

This section compares the performance of the PV-integrated converter to the conventional system using only bypass-diode connection. For the three-PV module system, three diodes as illustrated in Figure 5.19 are connected in opposite polarity to the respective PV modules. The Ćuk step-up converter can be connected across its output terminal and is used to track the global MPPs. Under different shading conditions, the system power-voltage characteristics are displayed in Figure 5.20.

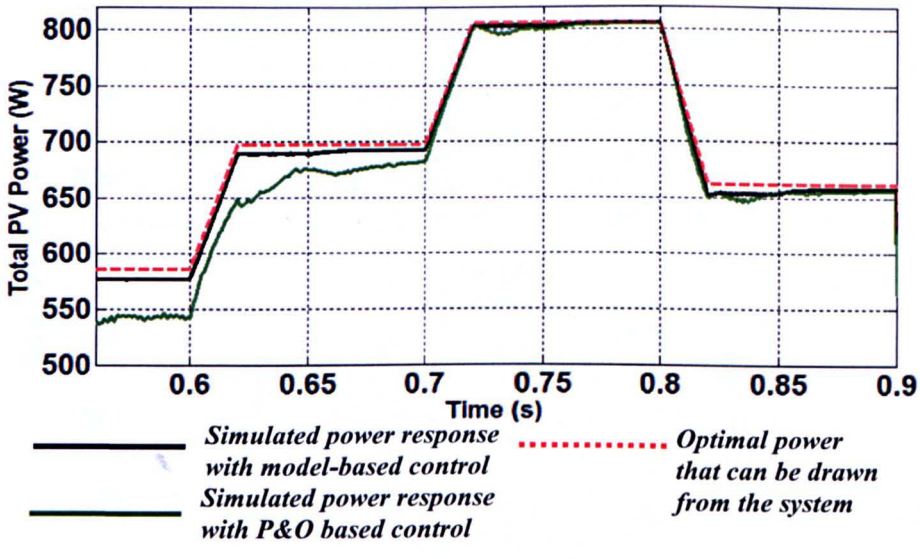

Figure 5.18 Comparison between the extracted power output using modelling-based control and that using P&O based control

Table 5.6 Maximum power available from the PV modules and the power extracted using different control methods

Cell Temperature	Solar Insolations (mw/cm^2)			Optimal power that can be drawn from the PV modules	Total power extracted using P&O method	Total power extracted using integrated converter
	G_1	G_2	G_3			
20° C	60	60	60	578.2 W	542.3 W	573.8 W
	60	90	60	692.1 W	678.2 W	687.1 W
	70	90	80	805.2 W	803.6 W	803.6 W
	70	90	40	658.0 W	655.0 W	655.9 W

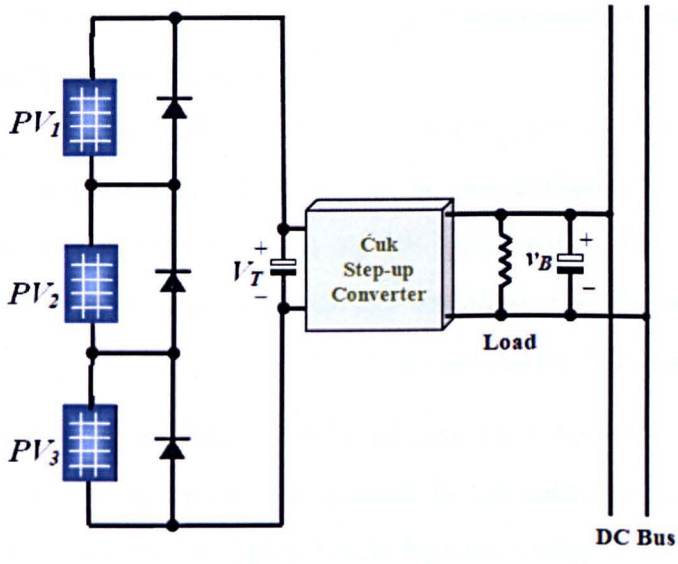

Figure 5.19 System configuration for a three-PV module system with bypass diode

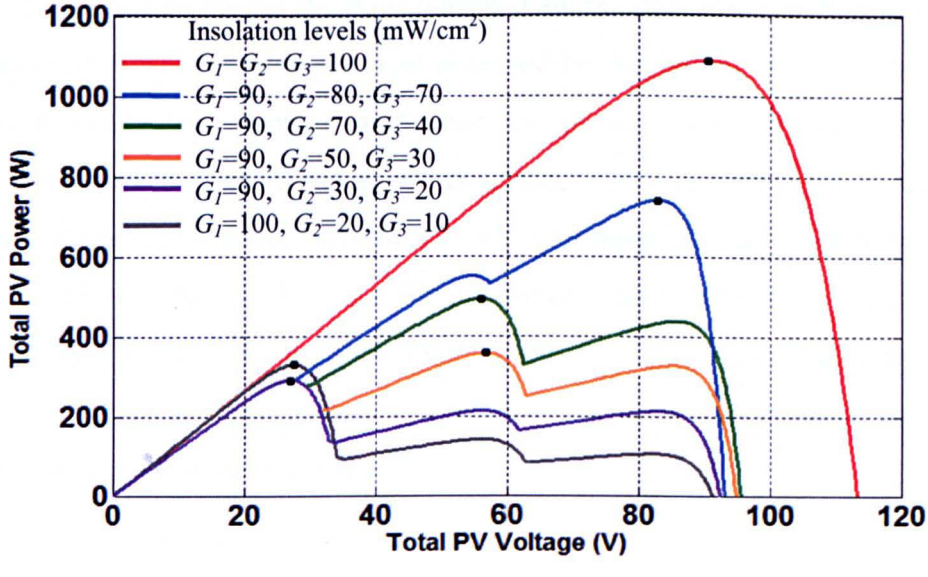

Figure 5.20 System power-voltage characteristics for a three-PV module system with bypass-diode connection

For different combinations of light conditions, there are three power peaks and for each of them, the location for the highest power peak as represented by a black dot is not limited within the 75 – 86 volt range. For instance under the shading condition when $G_1 = 70$ mW/cm^2, $G_2 = 90$ mW/cm^2, $G_3 = 40$ mW/cm^2, the highest peak power occurs when the PV voltage is equal to 56.18 V.

To implement the control for the MPP tracking, a three-stage P&O algorithm in [53] can be applied to firstly find all the power peaks and then set the global peak as the desired voltage reference for the terminal converter. A SIMULINK computer model is constructed and another MATLAB algorithm for P&O tracking is incorporated with a voltage perturbation set as 2.5 V. Note that the value now has been set at least ten times higher than those in the PV-integrated converter since this system requires a higher voltage search range.

Under the same shading conditions used for Section 5.4 and 5.5, the simulated response is depicted by the brown dotted line are shown in Figure 5.21. This can be compared to the the responses obtained using PV-integrated converter depicted by the black solid line. For both cases, the weather variations are illustrated in Figure 5.21(a) and the responses for PV voltage and power are shown in Figure 5.21(b).

Initially when they are uniformly irradiated with $G_1 = G_2 = G_3 = 60$ mW/cm^2, the total power output obtained for this system is the same as that of the PV-integrated converter. When the insolation levels become unequal, the power output of this system becomes lower than that of the PV-integrated converter. In particular the worst case occurs during the third partial shading condition (i.e. from $t = 0.8$ to $t = 0.9$ second), when the power output obtained by the former is about 160 W less than the latter. For all weather conditions, the power outputs obtained with both systems are listed in Table 5.7. Another downside for the conventional system is the terminal voltage fluctuation of within 25 – 85 volts range for each change in weather condition. This is due to the need for an iterative searching among the multiple power peaks. The PV-integrated converter, on the other hand, has substantially improved the system performance by only requiring a narrower operating voltage range; i.e. within 75 – 86 volt range.

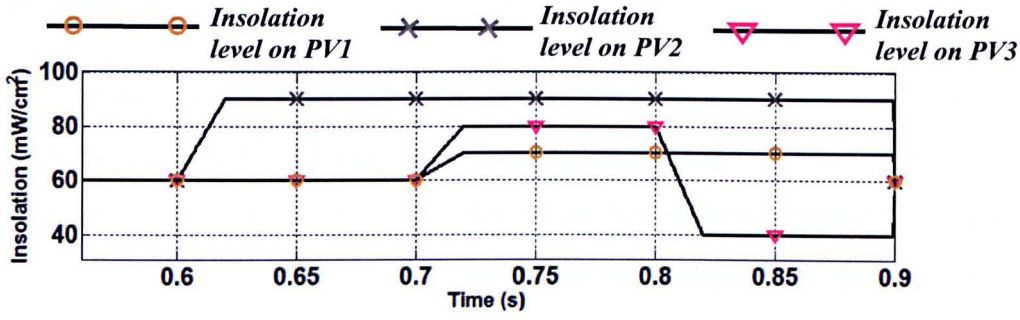

(a) Variation in solar insolation levels

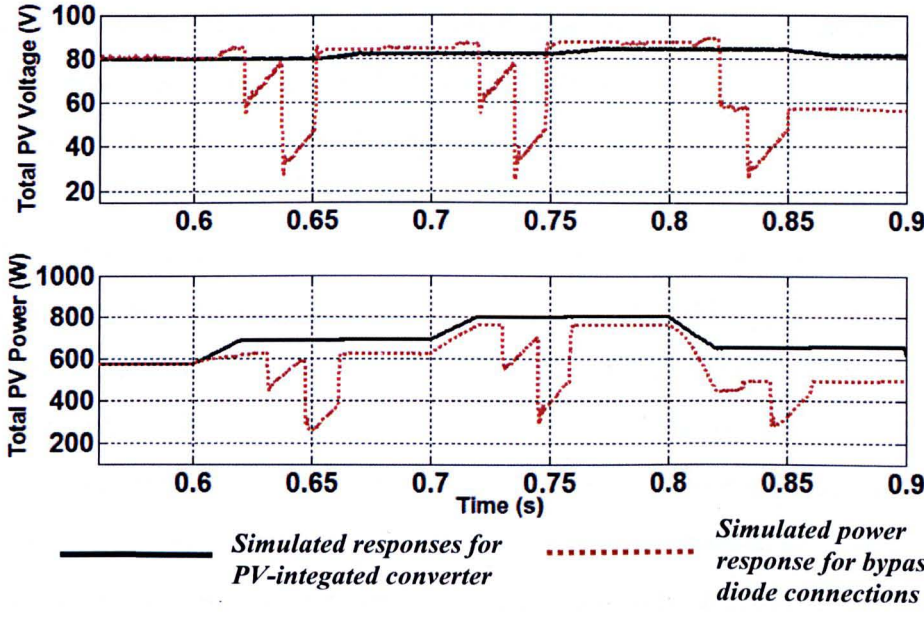

(b) PV voltage and power responses

Figure 5.21 Comparison between the responses for bypass-diode connection and those of PV-integrated converter

Table 5.7 Maximum power available from the PV modules, the power extracted using bypass diode and that using integrated converter scheme

Cell Temperature	Solar Insolations (mw/cm^2)			Maximum Power Available from the PV modules	Total Power Extracted using Bypass Diode	Total Power Extracted using Integrated Converter
	G_1	G_2	G_3			
20° C	60	60	60	578.2 W	576.4 W	573.8 W
	60	90	60	692.1 W	623.8 W	687.1 W
	70	90	80	805.2 W	764.2 W	803.6 W
	70	90	40	658.0 W	495.6 W	655.9 W

5.7 Summary

This chapter presented a detailed study of a PV-integrated converter system for maximum power point tracking under shading conditions. The structure and the operating principles of this system are described. For different shading conditions, appropriate operation modes for the converters are selected so that all the PV modules can operate optimally. A novel scheme for the operation mode selection has been developed: for systems having three or less modules, it is based on the solar insolation levels and otherwise it is determined by the optimal operating points for the PV modules. This system has been implemented using two different control techniques, namely, the modelling based approach and the P&O method for regulating the converters' duty ratios. The former offers faster transient and more stable steady-state responses than those of the latter. As demonstrated in this chapter, maximum power generation may not always be achieved using the P&O method. This can be explained by the evidence that the prediction PV optimal voltages are solely based on the on-line measurements of the voltage and current which are subject to continuous fluctuation. On the other hand, if the solar insolation and cell temperature measurements are available and the PV models have been accurately tuned, the modelling based approach can lead this converter system to MPP generation under any illumination conditions

This chapter has also demonstrated that under uniform illumination conditions, the power extracted using the proposed integrated converter scheme is equal to that using the conventional method of bypass diodes. However when there is inhomogeneous illumination between the modules, the former can keep all PV modules operating optimally and hence the power extracted is higher than that using the latter scheme. In particular, for the three-PV module system studied in this chapter, the integrated converter scheme increases the power output significantly by as much as 160 W or 32%.

Chapter 6

Artificial Intelligence Based Modelling and Control for PV

6.1 Introduction

As described in Chapter 5, the Perturbation and Observation method leads to continuous voltage oscillation around the maximum power points (MPPs). To avoid this problem, as discussed in Chapter 1, a model-based control technique can be used for MPP tracking in a PV system. This requires a model representing the relationship between the weather conditions and the PV electrical characteristics. Artificial intelligence techniques, such as neural networks, have been used to develop PV models [43]. The challenge in using this type of technique lies in establishing the appropriate model structure and tuning its parameters accurately using measured data.

The models obtained should satisfy the following:

1) high accuracy in representing the characteristics of a practical PV panel under all possible weather and load conditions

2) compact structure enabling its implementation in a single-chip microcontroller device,

3) adaptive in their structures and parameters as practical PV characteristics may change over time, or cells may be damaged, hence a fast tuning algorithm is necessary for re-designing the PV model.

To achieve all of the above, this chapter presents a PV model based on the Takagi-Sugeno type of Neuro-Fuzzy system. The modelling technique is based partially on the work in [101] where an efficient encoding scheme is also incorporated into the design. However a different training scheme, the Particle Swarm Optimisation (PSO) method is used. This has the potential to speed up the model training process. The modelling technique is tested through the re-construction of simulated and practical characteristics of a PV module. A scheme is described for applying the model to MPP tracking. The practical implementation of

the model on a dsPIC microcontroller is detailed in Chapter 7. The modelling technique was also used in Chapter 5 to assist the PV-integrated converter system to achieve the MPP generation. It is noted that a three PV-module system, for example, requires three models which are based on the three sets of weather measurements, respectively.

6.2 Model Structure

The Takagi-Sugeno (TS) neural-fuzzy model representing the PV characteristics is shown in Figure 6.1. This has three layers: input layer; middle hidden layer and; output layer.

6.2.1 Input Layer

The input layer to the model consists of a three-dimensional vector given as

$$\mathbf{x} = \begin{bmatrix} x_1 \\ x_2 \\ x_3 \end{bmatrix} = \begin{bmatrix} \text{Insolation} \\ \text{Temperature} \\ \text{PV Voltage} \end{bmatrix} \tag{6.1}$$

6.2.2 Hidden Layer

The sampled data for each input vector is passed on to the hidden layer. This consists of two networks, the premise network, and consequent network, as shown in Figure 6.1. The former performs the stage 1 function as described in section 1.5.2,

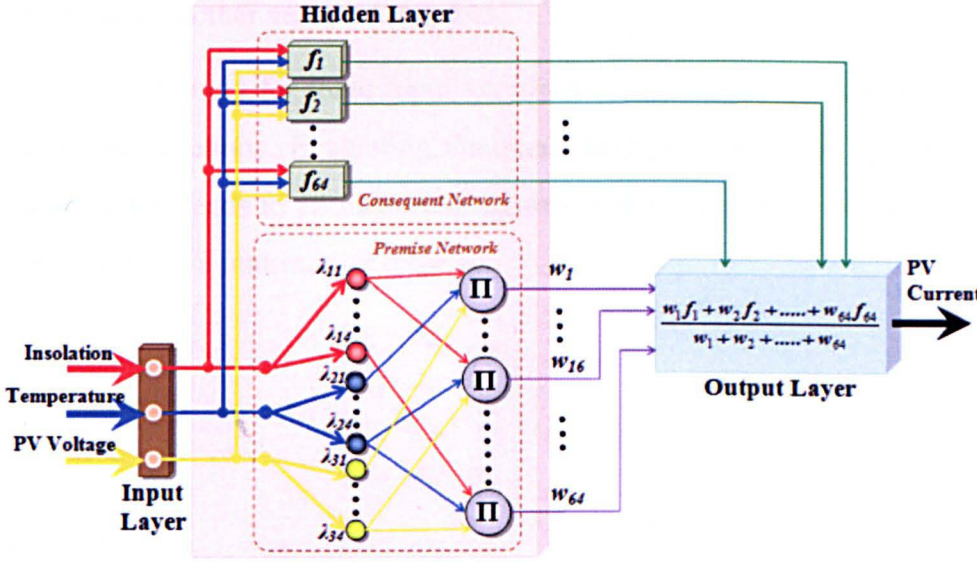

Figure 6.1 PV modelling using Neuro-Fuzzy network

i.e. the *Fuzzification Interface.* The output of this part is a set of weighting factors, w_i. The latter uses the input vector to implement a set of linear equations as expressed Equation 1.8, therefore, its output, is a set of function values f_k. The details of these two networks are described below.

6.2.2.1 Premise Network

The purpose of this network, as outlined above, is to partition the input space. This is obtained by using a grid-partitioning approach [68, 69]; i.e. for each of the three input variables shown in Equation 6.1, their samples are grouped into n membership functions (MF). In this model, the MFs are (characterized as) Gaussian functions and four are used for each input variable as shown in Figure 6.2, thus for input i, we have four MFs defined as

$$\lambda_{in} = \exp\left(-\frac{(x_i - \mu_{in})^2}{(\sigma_{in})^2}\right) \tag{6.2}$$

where λ_{in} gives the value of n-th MF for the i-th input variable, μ_{in} (n = 1 to 4) defines the corresponding mean value and σ_{in} the spread factor of the n-th Gaussian function. According to the numerical range of a specific input variable, the four sets of μ and σ values have to be estimated. Each of them defines a fuzzy band as shown in Figure 6.2(a) – 6.2(c), and for convenience four bands can be named as: LOW (L) for n = 1; MEDIUM LOW (ML) for n = 2; MEDIUM HIGH (MH) for n = 3; and HIGH (H) for n = 4. The number of bands is obviously a compromise between precision and complexity. In this thesis, four bands are used as these were found to work well by other authors [102, 103].

Accordingly for three input variables of a PV system, there are altogether 12 Gaussian functions. Evaluating Gaussian function values for each set of sampled input values leads to 12 numerical figures in the range from near 0 to 1 which may be grouped in a matrix, presented as

$$\mathbf{FL} = [\Lambda_1 \quad \Lambda_2 \quad \Lambda_3] = \begin{bmatrix} \lambda_{11} & \lambda_{21} & \lambda_{31} \\ \lambda_{12} & \lambda_{22} & \lambda_{32} \\ \lambda_{13} & \lambda_{23} & \lambda_{33} \\ \lambda_{14} & \lambda_{24} & \lambda_{34} \end{bmatrix} \tag{6.3}$$

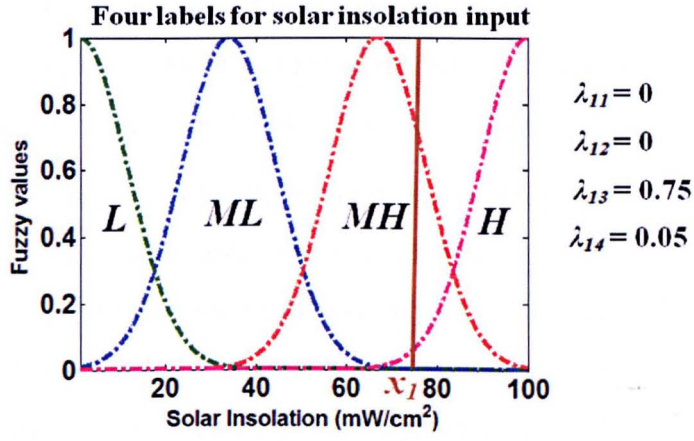

(a) MFs for solar insolation input

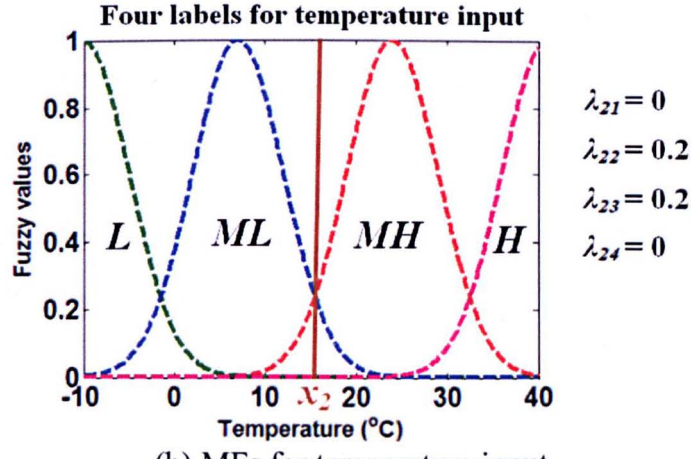

(b) MFs for temperature input

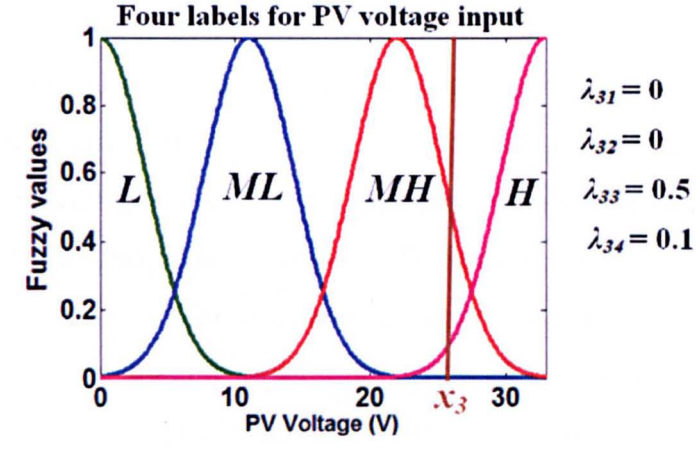

(c) MFs for PV voltage input

Figure 6.2 Example of allocation of fuzzy values

The column vector, consisting of four λ values for a given input variable, is referred to as that input sample's MFs. It is a set of real numbers, expressing the closeness of each input variable, to the mean value of each of its four Gaussian functions.

Based on the derived MFs, the second step in the premise network determines fuzzy rules. In this model with the use of grid partition, the fuzzy rules are represented as weighting factors which will be used in the second network. These are defined by combining the MF for one input variable, say insolation, with those for the other two input variables, namely the temperature and voltage. Thus there are 4 × 4 × 4 = 64 possible combinations. Each combination, consisting of three λ values, is referred to as the premise of a "fuzzy rule", the product of these λ values defines a weighting factor, namely,

$$w_r = (\lambda_{1a}) \times (\lambda_{2b}) \times (\lambda_{3c}) \tag{6.4}$$

where a, b, and c denote the index of the associated fuzzy band while r (1 to 64) indicates the r-th weighting factor or fuzzy rules out of 64 in total as listed in Table 6.1.

The example in Figure 6.2 illustrates how each of these elements can be allocated a value for a given input set; x_1 = 75 mW/cm^2, x_2 = 15°C and x_3 = 26 V. For insolation input, the corresponding Gaussian functions in both MH and H fuzzy bands have significantly non-zero values as can be seen in Figure 6.2(a), for those less than 10^{-5}, zero values are given. Thus the λ values for insolation input are 0, 0, 0.75 and 0.05, indicating that it is more appropriate to put this sample in MH band than in H band. Similarly, for a sampled PV voltage value, the corresponding λ values are 0, 0, 0.5 and 0.1. The non-zero values are for MH and H fuzzy bands. On the other hand, the temperature input value gives two non-zero Gaussian function values in ML and MH bands, leading to a set of λ values as 0, 0.25, 0.25 and 0. Therefore, the fuzzy factor matrix for this particular input vector is expressed as

$$\mathbf{FL} = \begin{bmatrix} 0 & 0 & 0 \\ 0 & 0.25 & 0 \\ 0.75 & 0.25 & 0.5 \\ 0.05 & 0 & 0.1 \end{bmatrix} \tag{6.5}$$

Consequently, the 60th fuzzy rule or weight factor, for instance, is w_{60} = 0.00125.

Table 6.1 Computation for the complete set of the fuzzy rule weights

Rule no.	*Rule weight, w_r*	*Rule no.*	*Rule weight, w_r*	*Rule no.*	*Rule weight, w_r*
1	$\lambda_{11} \times \lambda_{21} \times \lambda_{31}$	25	$\lambda_{12} \times \lambda_{23} \times \lambda_{31}$	49	$\lambda_{14} \times \lambda_{21} \times \lambda_{31}$
2	$\lambda_{11} \times \lambda_{21} \times \lambda_{32}$	26	$\lambda_{12} \times \lambda_{23} \times \lambda_{32}$	50	$\lambda_{14} \times \lambda_{21} \times \lambda_{32}$
3	$\lambda_{11} \times \lambda_{21} \times \lambda_{33}$	27	$\lambda_{12} \times \lambda_{23} \times \lambda_{33}$	51	$\lambda_{14} \times \lambda_{21} \times \lambda_{33}$
4	$\lambda_{11} \times \lambda_{21} \times \lambda_{34}$	28	$\lambda_{12} \times \lambda_{23} \times \lambda_{34}$	52	$\lambda_{14} \times \lambda_{21} \times \lambda_{34}$
5	$\lambda_{11} \times \lambda_{22} \times \lambda_{31}$	29	$\lambda_{12} \times \lambda_{24} \times \lambda_{31}$	53	$\lambda_{14} \times \lambda_{22} \times \lambda_{31}$
6	$\lambda_{11} \times \lambda_{22} \times \lambda_{32}$	30	$\lambda_{12} \times \lambda_{24} \times \lambda_{32}$	54	$\lambda_{14} \times \lambda_{22} \times \lambda_{32}$
7	$\lambda_{11} \times \lambda_{22} \times \lambda_{33}$	31	$\lambda_{12} \times \lambda_{24} \times \lambda_{33}$	55	$\lambda_{14} \times \lambda_{22} \times \lambda_{33}$
8	$\lambda_{11} \times \lambda_{22} \times \lambda_{34}$	32	$\lambda_{12} \times \lambda_{24} \times \lambda_{34}$	56	$\lambda_{14} \times \lambda_{22} \times \lambda_{34}$
9	$\lambda_{11} \times \lambda_{23} \times \lambda_{31}$	33	$\lambda_{13} \times \lambda_{21} \times \lambda_{31}$	57	$\lambda_{14} \times \lambda_{23} \times \lambda_{31}$
10	$\lambda_{11} \times \lambda_{23} \times \lambda_{32}$	34	$\lambda_{13} \times \lambda_{21} \times \lambda_{32}$	58	$\lambda_{14} \times \lambda_{23} \times \lambda_{32}$
11	$\lambda_{11} \times \lambda_{23} \times \lambda_{33}$	35	$\lambda_{13} \times \lambda_{21} \times \lambda_{33}$	59	$\lambda_{14} \times \lambda_{23} \times \lambda_{33}$
12	$\lambda_{11} \times \lambda_{23} \times \lambda_{34}$	36	$\lambda_{13} \times \lambda_{21} \times \lambda_{34}$	60	$\lambda_{14} \times \lambda_{23} \times \lambda_{34}$
13	$\lambda_{11} \times \lambda_{24} \times \lambda_{31}$	37	$\lambda_{13} \times \lambda_{22} \times \lambda_{31}$	61	$\lambda_{14} \times \lambda_{24} \times \lambda_{31}$
14	$\lambda_{11} \times \lambda_{24} \times \lambda_{32}$	38	$\lambda_{13} \times \lambda_{22} \times \lambda_{32}$	62	$\lambda_{14} \times \lambda_{24} \times \lambda_{32}$
15	$\lambda_{11} \times \lambda_{24} \times \lambda_{33}$	39	$\lambda_{13} \times \lambda_{22} \times \lambda_{33}$	63	$\lambda_{14} \times \lambda_{24} \times \lambda_{33}$
16	$\lambda_{11} \times \lambda_{24} \times \lambda_{34}$	40	$\lambda_{13} \times \lambda_{22} \times \lambda_{34}$	64	$\lambda_{14} \times \lambda_{24} \times \lambda_{34}$
17	$\lambda_{12} \times \lambda_{21} \times \lambda_{31}$	41	$\lambda_{13} \times \lambda_{23} \times \lambda_{31}$		
18	$\lambda_{12} \times \lambda_{21} \times \lambda_{32}$	42	$\lambda_{13} \times \lambda_{23} \times \lambda_{32}$		
19	$\lambda_{12} \times \lambda_{21} \times \lambda_{33}$	43	$\lambda_{13} \times \lambda_{23} \times \lambda_{33}$		
20	$\lambda_{12} \times \lambda_{21} \times \lambda_{34}$	44	$\lambda_{13} \times \lambda_{23} \times \lambda_{34}$		
21	$\lambda_{12} \times \lambda_{22} \times \lambda_{31}$	45	$\lambda_{13} \times \lambda_{24} \times \lambda_{31}$		
22	$\lambda_{12} \times \lambda_{22} \times \lambda_{32}$	46	$\lambda_{13} \times \lambda_{24} \times \lambda_{32}$		
23	$\lambda_{12} \times \lambda_{22} \times \lambda_{33}$	47	$\lambda_{13} \times \lambda_{24} \times \lambda_{33}$		
24	$\lambda_{12} \times \lambda_{22} \times \lambda_{34}$	48	$\lambda_{13} \times \lambda_{24} \times \lambda_{34}$		

6.2.2.2 Consequent Network

Following the TS model described in sub-section 1.5.2.2, this network computes a set of linear equations using the given input data set in Equation 6.1. Thus for the PV system these equations can be expressed in a vector form as

$$\mathbf{FR} = \begin{bmatrix} f_1 \\ f_2 \\ . \\ . \\ f_{64} \end{bmatrix} = \mathbf{C} \cdot \begin{bmatrix} x_1 \\ x_2 \\ x_3 \\ 1 \end{bmatrix} \tag{6.6}$$

and

$$\mathbf{C} = \begin{bmatrix} \mathbf{C}_1 \\ \mathbf{C}_2 \\ . \\ . \\ \mathbf{C}_{64} \end{bmatrix} = \begin{bmatrix} c_0^1 & c_1^1 & c_2^1 & c_3^1 \\ c_0^2 & c_1^2 & c_2^2 & c_3^2 \\ . & . & . & . \\ . & . & . & . \\ c_o^{64} & c_1^{64} & c_2^{64} & c_3^{64} \end{bmatrix} \tag{6.7}$$

where $\mathbf{C}$ is a 64 × 4 tall matrix containing 256 parameter coefficients, and $\begin{bmatrix} x_1 \\ x_2 \\ x_3 \\ 1 \end{bmatrix}$ is a column vector containing samples of all the input elements with a coefficient of '1' at the bottom row. Evaluation of Equation 6.6, gives a set of 64 f values, namely the rule outputs. These are then transferred to the output layer to calculate the PV current value.

6.2.3 Output Layer

In this layer 64 weight factors from the premise part and 64 f_r functions of the consequent part are multiplied to predict the model output, i.e. the sampled value of the PV panel current is presented as

$$I_{PV}^{*} = \frac{w_1 f_1 + w_2 f_2 + ... + w_{64} f_{64}}{w_1 + w_2 + ... + w_{64}} \tag{6.8}$$

which can also be written as

$$I_{PV}^{*} = \frac{\mathbf{Q\Gamma}}{\theta} \tag{6.9}$$

$\mathbf{\Gamma}$ is a column vector containing all the 256 parameter coefficients from the 64 f_r functions, hence is expressed as

$$\Gamma = \left[c_0^1 \quad c_1^1 \quad c_2^1 \quad c_3^1 \quad c_0^2 \quad c_1^2 \quad \ldots \quad c_3^{64}\right]^T \tag{6.10}$$

$\theta = \sum_{n=1}^{64} w_n$ represents the sum of all the weight factors; and **Q** is a 1 × 256 row vector containing the products between the input samples and the corresponding weighting factors, hence is given by

$$\mathbf{Q} = \left[w_1 x_1 \quad w_1 x_2 \quad w_1 x_3 \quad w_1 \quad w_2 x_1 \quad w_2 x_2 \quad \ldots. \quad w_{64}\right] \tag{6.11}$$

A simple visualisation of the operation of this model as expressed by Equation (6.8) is as follows. Imagine that the space of input variables is partitioned into cubical regions, i.e. by a grid of plane partitions. Associated with each region is a predicted point value of the target function (in this case the PV current) at a point near the centre of that region. The variation of the function near the point is approximated as linear, using a set of coefficients in **C**, which vary from region to region. A non-fuzzy scheme would assign the input vector definitely to one region and thus activate a particular point prediction corrected by the local linear approximation to the function variation. In the fuzzy scheme, the point is tested for its closeness to each region using the continuous variable *w* which will only be significant when the input vector is close to that region. A few *w* values can be significantly none zero, while they perform a continuously variable weighting of both the point values and the linear variation coefficients. Thus the scheme produces a predicted output value which is certain to be close to the local point values, with an interpolation between them that is smoother than linear. The discontinuities associated with the non-fuzzy assignment to regions are smoothed out.

6.3 Model Structure Optimization

As can be seen, the above described model has a total number of 12 MFs and 64 fuzzy rules, giving 76 model components in total. This structure may not be the optimum as some of these components may be redundant. In addition for 12 MFs there are 24 MF parameters (μ and σ). It is important to note that the design of an optimal TS Neuro-Fuzzy model involves finding a rule structure which has an adequate number of rule sets and fuzzy MFs, and an optimal set of MF parameters. The model, thus obtained, should satisfy three requirements; having a compact

structure, an interpretable set of rules and ultimately being accurate in predicting the output values based on the known input samples. While the third requirement is common to any modelling technique, the former two are specific for optimizing TS Neuro-Fuzzy models.

To ensure a compact Neuro-Fuzzy model it should have the least number of fuzzy rules and MFs. In the example of the PV model, the maximum number of MFs is fixed to 4 for each input variable, thus there are only 64 rule sets for three input variables. However in general with higher numbers of input variables, and hence MFs, and with using grid-partitioning scheme, the number of fuzzy rules increases, exploding exponentially such that it becomes too large to be handled efficiently. To optimise the number of MFs and fuzzy rules, an effective evaluation algorithm is defined and will be explained in Section 6.3.1.

On the other hand, an interpretable Neuro-Fuzzy model should have meaningful labels for its MFs; i.e. they should be not overlapping significantly and are separable, hence they can be allocated with meaningful symbols such as LOW, MEDIUM or HIGH. Obtaining an interpretable model requires selecting a proper set of MF parameters for each input variable to prevent overlapping. The scheme developed for this will be discussed in Section 6.3.2.

6.3.1 Scheme for Achieving Compactness

As explained above, this scheme is to eliminate invalid fuzzy rules and MFs, hence only useful ones are selected.

6.3.1.1 Selecting Valid Fuzzy Rules

This is done by defining a set of rule weight factors, called the chain links l_m, each of these chain links relates directly to a subset of fuzzy rules and hence its value can be set as a flag to switch in and out of the corresponding rules [101]. These chain links are defined as follows.

As discussed in Section 6.2.2, the combination of different MFs from different inputs forms a set of fuzzy rules. For the PV model all rules can be represented using a rule structure diagram as illustrated in Figure 6.3. It can be seen that each MF of the first input variable, the insolation, has a connection with every MF of the second input (temperature). Likewise, every MF of temperature has a connection with that

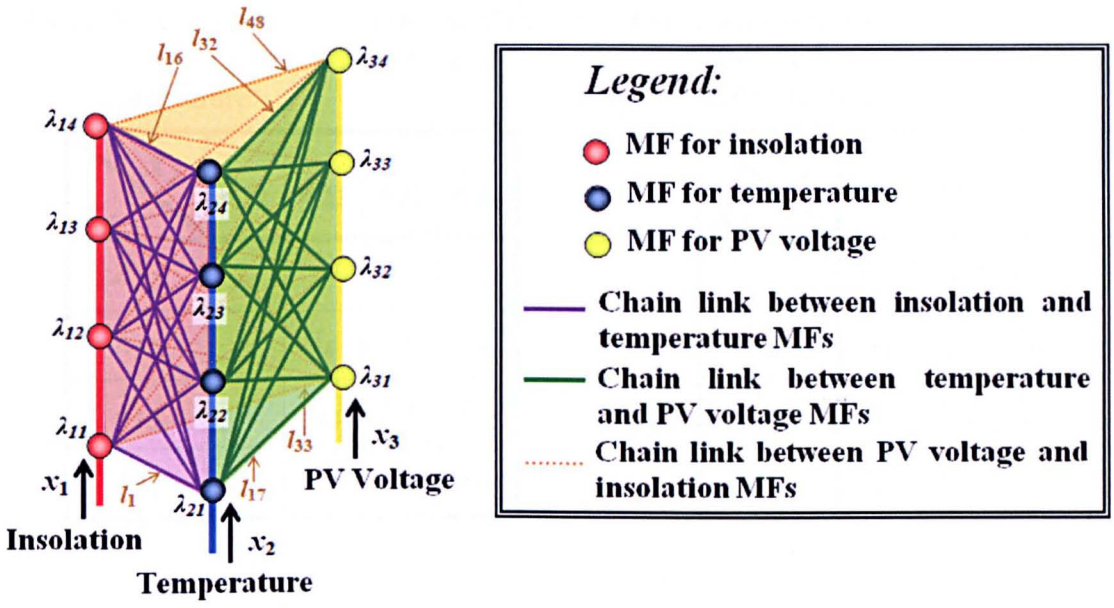

Figure 6.3 Rule structure diagram for the PV model

of the voltage. To form a closed-path, each MF of the voltage is connected back to the MFs of insolation. In total there are 48 connections - chain links which are listed in Tables 6.2 – 6.4. For instance, the chain link, between the second MF of solar insolation, λ_{12}, and the third MF of temperature, λ_{23}, is represented by l_7 and l_{47} is the chain link between λ_{34} and λ_{13}.

A rule relates to any three of these chain links by tracing through the closed path which starts and ends at the same MFs of any input. For example, the 64-th fuzzy rule is formed by λ_{14}, λ_{24}, and λ_{34} and this involves three chain links, l_{16}, l_{32} and l_{48}. Hence, all the fuzzy rules are defined by a set of the chain links which are listed in a vector given by

$$\mathbf{CL}=[l_1 \quad l_2 \quad \ldots \quad l_{16} \quad l_{17} \quad \ldots \quad l_{32} \quad l_{33} \quad \ldots \quad l_{48}] \tag{6.12}$$

The values of these chain links are set randomly (at least initially) between 0 and 1. A rule becomes inactive, or 'flagged out', when any of the three chain links have an l value less than 0.5. In that case, the corresponding fuzzy rule weight is set to zero and will not be used in the PV model to predict the output values.

It is worth highlighting that the chain links are only weight factors, with their values manually given, and then iteratively estimated. By flagging in and out some of the rules they determine the structure of the Neuro-Fuzzy model but are not used as a parameter set in the Neuro-Fuzzy model defined in section 6.2. The benefit of

Table 6.2 Chains linking between MFs of solar insolation and those of temperature

x_1 \ x_2	λ_{21}	λ_{22}	λ_{23}	λ_{24}
λ_{11}	l_1	l_2	l_3	l_4
λ_{12}	l_5	l_6	l_7	l_8
λ_{13}	l_9	l_{10}	l_{11}	l_{12}
λ_{14}	l_{13}	l_{14}	l_{15}	l_{16}

Table 6.3 Chains linking between MFs of temperature and those of of PV voltage

x_2 \ x_3	λ_{31}	λ_{32}	λ_{33}	λ_{34}
λ_{21}	l_{17}	l_{18}	l_{19}	l_{20}
λ_{22}	l_{21}	l_{22}	l_{23}	l_{24}
λ_{23}	l_{25}	l_{26}	l_{27}	l_{28}
λ_{24}	l_{29}	l_{30}	l_{31}	l_{32}

Table 6.4 Chains linking between MFs of PV voltage and those of solar insolation

x_3 \ x_1	λ_{11}	λ_{12}	λ_{13}	λ_{14}
λ_{31}	l_{33}	l_{34}	l_{35}	l_{36}
λ_{32}	l_{37}	l_{38}	l_{39}	l_{40}
λ_{33}	l_{41}	l_{42}	l_{43}	l_{44}
λ_{34}	l_{45}	l_{46}	l_{47}	l_{48}

using this set of factors for model structure optimization rather than directly using the rule set, is that it reduces the number of factors in the model tuning process significantly. In the PV model case, the number of chain links is 48 whereas the number of fuzzy rules is 64.

6.3.1.2 Selecting Valid Membership Functions

Similar to the above, another set of weight factors is set to store the validity information of the MFs, and is expressed as

$$\mathbf{FS} = \begin{bmatrix} m_{11} & m_{21} & m_{31} \\ m_{12} & m_{22} & m_{32} \\ m_{13} & m_{23} & m_{33} \\ m_{14} & m_{24} & m_{34} \end{bmatrix} \tag{6.13}$$

With their values set between 0 and 1, each element in matrix 6.13 determines whether the corresponding linguistic label is valid, hence the corresponding MF is

active. For example, if m_{23} is less than 0.5, the third MF for temperature input is de-activated and its fuzzy value, λ_{23} is not considered during the computation of w_r.

Again the elements of **FS** in Equation (6.13) are not parameters in the Neuro-Fuzzy model, they are only flags for switching in and out MFs. By changing their values iteratively, the structure of the model is varied.

Combining with the scheme in Section 6.3.1.1 for fuzzy rule selection, the MFs and fuzzy rules are switched in and out accordingly. However there are two special scenarios leading to further elimination of rules. The first is that some active rules are associated with all inactive MFs and therefore, the corresponding rule can be removed. The second scenario is that for the chain links among the rule weights, there may exist two or more closed paths along which the same active MFs are found. In this case, only one of the associated rules is considered whilst the others are discarded.

6.3.1.3 Design Example

The above described encoding schemes are applied to select the MFs and rules for a design example which has completely undergone a training process. The information about its chain links and the MFs validities are listed in Tables 6.5 – 6.8, respectively. Referring to all the chain links, there are 11 active fuzzy rules. However when the validities of the MFs are considered, it can be observed that the fuzzy rules associated with rule 8 are the same as those of rule 6, hence one of them will be discarded. The same condition also occurs between rules 56 and 54. Rules 36 and 44 are invalid because they have no active MFs and are also eliminated. As shown in Figure 6.4, there are 7 rule weights which only depend on the 4 MFs.

Table 6.5 Example chain links between MFs of solar insolation and those of temperature

x_1 \ x_2	λ_{21}	λ_{22}	λ_{23}	λ_{24}
λ_{11}	0.1	0.7	0.2	0.1
λ_{12}	0.2	0.8	0.3	0.8
λ_{13}	0.7	0.6	0.5	0.4
λ_{14}	0.3	0.7	0.2	0.9

Table 6.6 Example chains links between MFs of temperature and those of PV voltage

x_2 \ x_3	λ_{31}	λ_{32}	λ_{33}	λ_{34}
λ_{21}	0.3	0.9	0.1	0.5
λ_{22}	0.2	0.5	0.2	0.5
λ_{23}	0.3	0.1	0.6	0.6
λ_{24}	0.4	0.6	0.5	0.3

Table 6.7 Example chains link between MFs of PV voltage and those of solar insolation

x_3 \ x_1	λ_{11}	λ_{12}	λ_{13}	λ_{14}
λ_{31}	0.8	0.2	0.2	0.5
λ_{32}	0.9	0.8	0.4	1.0
λ_{33}	0.1	0.2	0.9	0.1
λ_{34}	0.5	0.1	0.6	0.8

Table 6.8 Example MFs validities for solar insolation, temperature and PV voltage

MFs	*Weight values*	*MFs*	*Weight values*	*MFs*	*Weight Values*
λ_{11}	*0.2*	λ_{21}	0.4	λ_{31}	0.4
λ_{12}	0.8	λ_{22}	0.8	λ_{32}	0.3
λ_{13}	0.3	λ_{23}	0.1	λ_{33}	0.9
λ_{14}	0.5	λ_{24}	0.2	λ_{34}	0.1

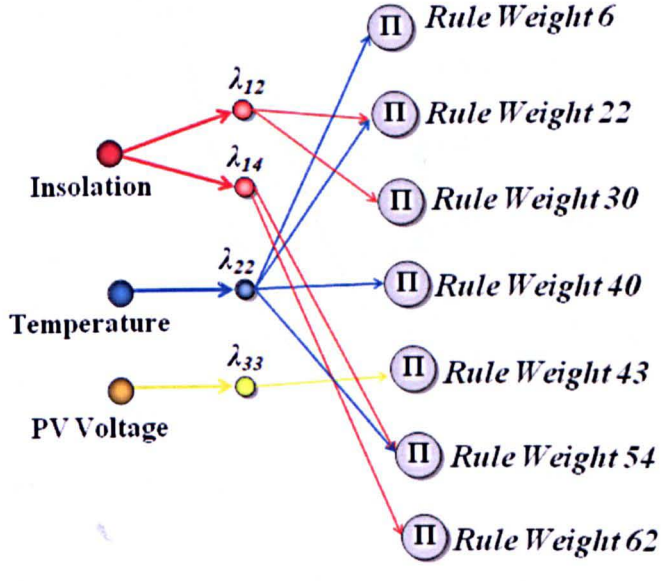

Figure 6.4 Resulting rule structure for the design example

6.3.2 Scheme for Achieving Model Interpretability

If a model is highly interpretable, MFs for each input are well- distributed and thus can be distinguishable from others. The concept of Model Interpretability can be illustrated by two examples of MFs designed using different optimization schemes shown in Figures 6.5(a) and 6.5(b). Before optimization is performed, the parameters of both models are initialized with random values. After optimization, the MFs of the model in Figure 6.5(b) are highly distinguishable and can still be allocated with meaningful labels like LOW, MEDIUM and HIGH. There is also a sufficient continuity from one MF to another. Thus a model is highly interpretable if any two MFs from an input variable do not excessively overlap each other, in other words, each MF has a reasonable gap between its adjacent counterparts.

To achieve this, a penalty function is used to evaluate amounts of overlap or gap among the MFs [101], this is calculated based on a constraint line ξ_{INT} which is used to specify the compromise between the continuity and overlapping of MFs. As illustrated by a design example in Figure 6.6, there are two intersecting points between the ξ_{INT} line, and an MF, one on the left and the other on the right. Based on these points, the distance between two MFs can be calculated, this can be explained by using the three examples shown in Figure 6.7.

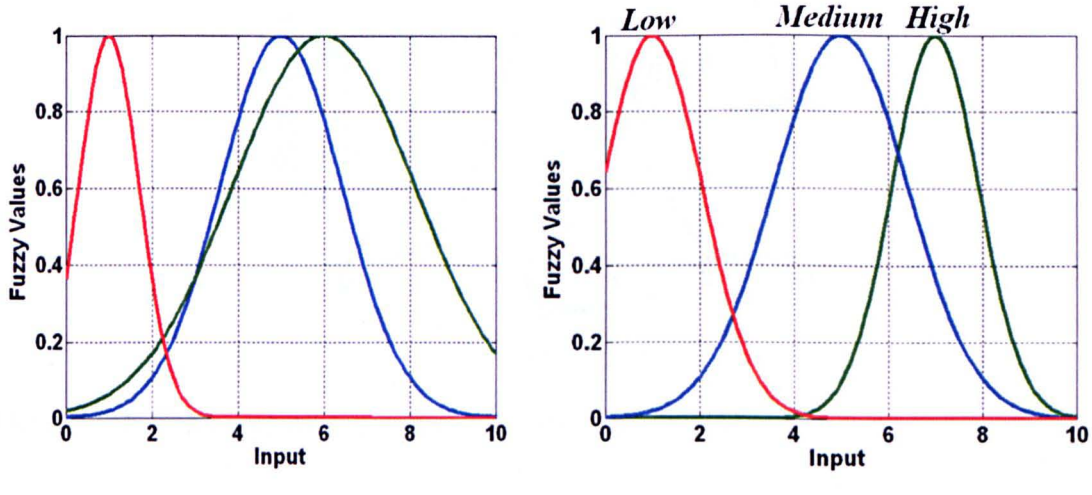

(a) Unevenly distributed MFs (b) Evenly distributed MFs

Figure 6.5 Examples of different distributions of MFs

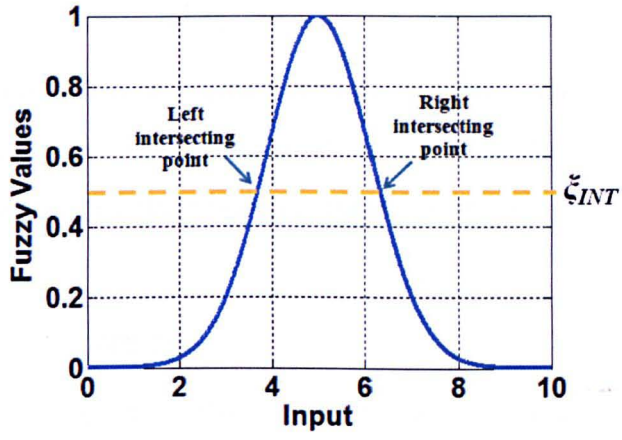

Figure 6.6 Definition of the constraint line used to evaluate gap and overlap of MFs

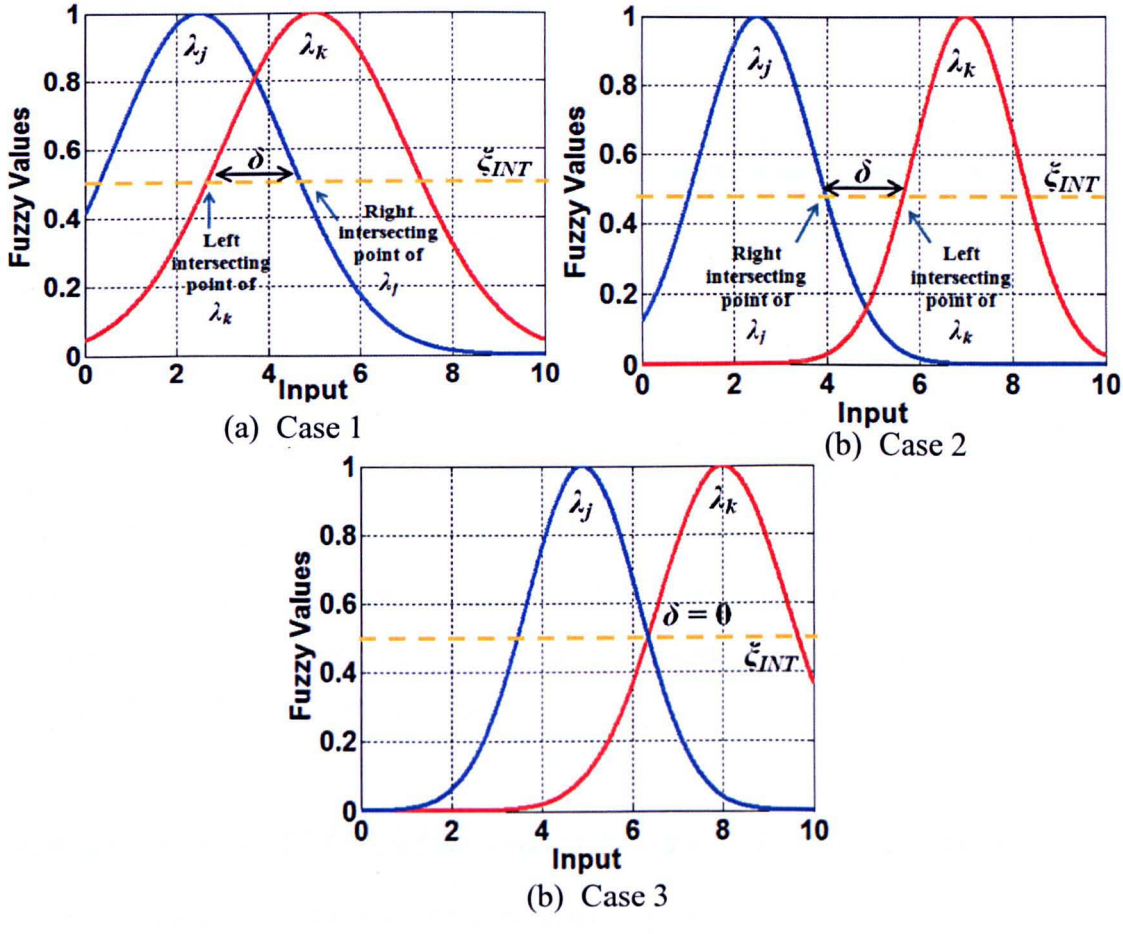

Figure 6.7 Examples of gap and overlap between two MFs

Case 1: Overlap between λ_j and λ_k

As shown in Figure 6.7(a), λ_j is situated to the left of λ_k and along the ξ_{INT} line, thus overlapping each other. The length of the overlap can be calculated by taking the distance, of δ between the right intersecting point of λ_j and the left intersecting point of λ_k.

Case 2: Gap between λ_j and λ_k

As shown in Figure 6.7(b), λ_j is still situated to the left of λ_k, but along the ξ_{INT} line, separate from each other. The length of the gap can be determined by taking the distance, of δ between the right intersecting point of λ_j and the left intersecting point of λ_k.

Case 3: No gap or overlap between λ_j and λ_k

As shown in Figure 6.7(c), there is no overlap between λ_j and λ_k along the ξ_{INT} line. In this case, the distance between them will be zero, which is highly desirable for model interpretability.

In the above three cases, the distances of the MFs are determined based on the constraint ξ_{INT} being set at 0.5. For other values of ξ_{INT}, it is also possible to obtain a zero distance between two MFs. These are demonstrated by another five design examples which are shown in Figures 6.8(a) – (e) respectively. As can be observed when ξ_{INT} deviates from the 0.5 line, the MFs become either indistinguishable or discontinuous throughout the input range. Therefore, the optimum value of ξ_{INT} at 0.5 will be used for this PV modelling.

6.4 Definition of Model Parameter Set and Fitness Function

As discussed in the preceding section an optimal PV model is assessed by three criteria: accuracy, compactness and interpretability. To achieve all of these, the following three elements are required; a parameter set which determines the structure and parameters of the model, a multi-objective fitness function encompassing all the three criteria and the Particle Swarm Optimization (PSO) algorithm to tune the parameter set for obtaining the optimal fitness function value. The former two are explained in this section, while tuning using PSO algorithm is discussed in section 6.5.

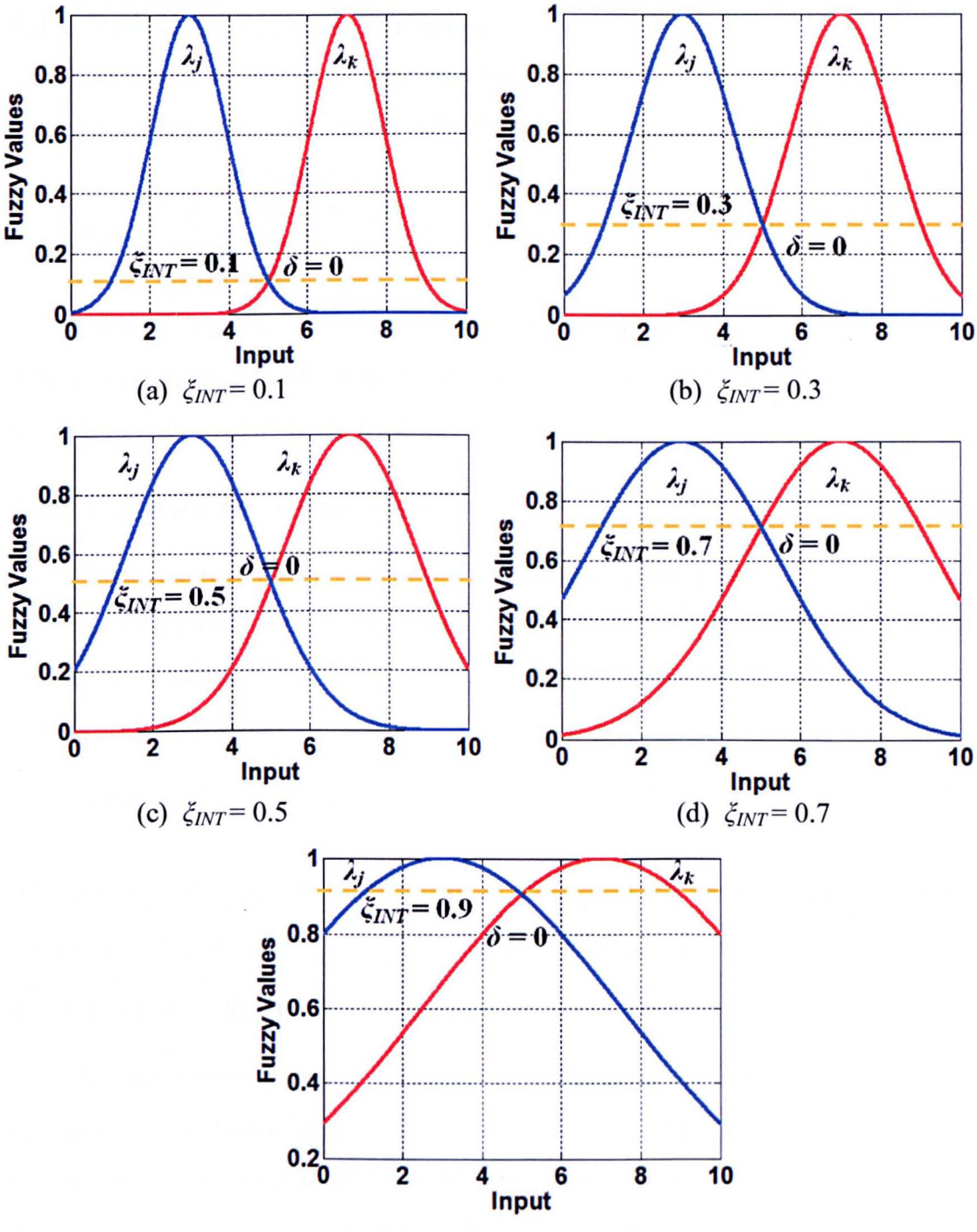

(a) $\xi_{INT} = 0.1$ (b) $\xi_{INT} = 0.3$

(c) $\xi_{INT} = 0.5$ (d) $\xi_{INT} = 0.7$

(e) $\xi_{INT} = 0.9$

Figure 6.8 Examples of gap and overlap between λ_j and λ_k with $\delta = 0$ for different ξ_{INT} values

6.4.1 Parameter Set to Be Estimated

The parameter set which specifies the model; and hence determines the model accuracy, compactness and interpretability, is given by

$$\Phi_p = \begin{bmatrix} \text{Centres of fuzzy sets} \\ \text{Spread - widths of fuzzy sets} \\ \text{Validities of rule chain links} \\ \text{Validities of fuzzy sets} \end{bmatrix} \tag{6.14}$$

$$= [\mu_{11} \ \ldots \ \mu_{34} \ \ \sigma_{11} \ \ldots \ \sigma_{34} \ \ l_1 \ \ldots \ l_{48} \ \ m_{11} \ \ldots \ m_{34}]^T$$

where in total, Φ_p has 84 elements which have been described in Sections 6.2 and 6.3. All of these will be tuned by PSO algorithm.

6.4.2 Criterion for Model Accuracy

When all the model parameters are known, a set of trial input samples is applied to the model and the predicted PV current is obtained. Repeating this for the whole set of samples, the accuracy of a PV model can be assessed from the mean square prediction error

$$\text{MSE} = \frac{1}{T_{sam}} \sum_{i=1}^{T_{sam}} \left(I_{PV}(i) - \hat{I}_{PV}(i) \right)^2 \tag{6.15}$$

where $I_{PV}(i)$ and $\hat{I}_{PV}(i)$ are the actual value of a PV current sample and that predicted by the model. T_{sam} is the total number of trial samples in the set.

6.4.3 Criterion for Model Compactness

A more compact model is desirable to minimise the usage of computational resources [101]. This is closely related to the number of MFs and rules required by the model in predicting the PV current. Before training is performed, the PV model described above has a maximum of 12 MFs and 64 fuzzy rules. After adjusting their validity vectors, the actual number of components being used may be reduced. The measure of model compactness can then be given by

$$\text{COMP} = \frac{1}{2}\left(\frac{T_{set}}{12} + \frac{T_{set}}{64} \right) \tag{6.16}$$

where T_{set} and T_{rule} are the number of active MFs and valid rules for the model.

6.4.4 Criterion for Model Interpretability

By normalizing the length of gap or overlap of MFs with the corresponding input range (i.e. D_1, D_2 and D_3 for insolation, temperature and PV voltage), the overall measure of interpretability can then be expressed as

$$\mathrm{INT_a} = \left(\frac{1}{P_1}\right)\sum_{n=1}^{P_1}\frac{\delta_n}{D_1} \quad \text{for insolation input;}$$

$$\mathrm{INT_b} = \left(\frac{1}{P_2}\right)\sum_{n=1}^{P_2}\frac{\delta_n}{D_2} \quad \text{for temperature input;}$$

$$\text{and} \quad \mathrm{INT_c} = \left(\frac{1}{P_3}\right)\sum_{n=1}^{P_3}\frac{\delta_n}{D_3} \quad \text{for PV voltage input.} \tag{6.17}$$

where P_1, P_2 and P_3 denote the available number of MF pairs which can be calculated using the combination equation, ${}_{\varsigma}C_2 = \frac{n!}{2(n!-2)}$ and ς is the number of active MFs for the corresponding input. δ_n is the distance between n-th pair of MFs. It should be noted that after an elimination process has been carried out, an input may only have one MF, in this case, the associated interpretability measure will have a zero value.

6.4.5 Overall Fitness Function

The overall fitness function of a model design will be used by the training algorithm to adjust the model parameters appropriately. This function is computed as the sum of all performance indices described above as shown in Table 6.9. MSE may have a widely varying range throughout the training. To narrow this range down, its value is expressed in logarithmic scale as

$$\mathrm{MA} = -K_A \times \log(\mathrm{MSE}) \tag{6.18}$$

Table 6.9 Evaluation of fitness function for PV modelling

Variable	Criteria	Prioritized Performance Indices
MA	Accuracy	$-K_A \times \log(\mathrm{MSE})$
MC	Compactness	$K_C \times [(1-\mathrm{COMP})]$
MI	Interpretability	$K_I \times \left[\frac{(1-\mathrm{INT_a})+(1-\mathrm{INT_b})+(1-\mathrm{INT_c})}{3}\right]$
Overall Fitness Function		FF = MA + MC + MI

On the other hand, the compactness measure is evaluated as

$$MC = K_C \times [(1 - COMP)] \tag{6.19}$$

which has a value ranging between 0 and 1. The value of 0 means that the model has all the 140 model components and 1 indicates that the model has the least number of components. The interpretability measure can also be evaluated as

$$MI = K_I \times \left[\frac{(1 - INT_a) + (1 - INT_b) + (1 - INT_c)}{3} \right] \tag{6.20}$$

which ranges between 0 and 1. It is worth noting that the average is taken over all the individual interpretability measures due to the inputs. K_A, K_C and K_I are the the weights for the respective measures. These constants can also be varied according to the training objectives. In particular for off-grid PV applications installed in remote areas, where costs become a major obstacle, K_C may be set higher so that a computationally simple model can be obtained. Conversely when precision has a higher priority for PV modelling, K_A can be increased further.

6.5 Training Scheme for PV Neuro-Fuzzy Model

The search for an optimum PV model using PSO algorithm starts by initializing 20 particles or in this case, 20 $\mathbf{\Phi}_p$ vectors (i.e. $\mathbf{\Phi}_1$, $\mathbf{\Phi}_2$, $\mathbf{\Phi}_3$, ..., $\mathbf{\Phi}_{20}$). The parameters in every $\mathbf{\Phi}_p$ vector are assigned initially with values randomly distributed within their desired ranges. Each $\mathbf{\Phi}_p$ vector potentially offers the optimum solution for the PV model.

The complete model training process involves two stages. In the first stage, a total of T_{sam} input-output data samples are used to estimate the linear parameters in $\mathbf{\Gamma}$ (in Equation (6.10)) and this can be achieved using least-square estimation method. The corresponding fitness function is then calculated based on Table 6.9. The estimation process and fitness function evaluation are performed for all $\mathbf{\Phi}_p$ vectors. The full detail for this stage of training is explained in Section 6.5.1.

Based on the calculated fitness functions, the second stage of training employs PSO algorithm to adjust the parameters for all $\mathbf{\Phi}_p$ vectors and this will be described in Section 6.5.2. Stages 1 and 2 will be performed iteratively until the defined maximum iteration is reached. At the end of the training process, the $\mathbf{\Phi}_p$ vector which offers the highest fitness function is chosen as the final specifications for the PV model.

6.5.1 Stage One: Recursive Least Square Estimation for Γ Matrix

If all the T_{sam} input data samples are known and the parameters in Φ_p vector are initialized first, the predicted output samples in the output layer can be written as

$$\mathbf{OP} = \Xi \cdot \Gamma \tag{6.21}$$

$\Xi = \begin{bmatrix} \mathbf{Q}_1/\theta_1 \\ \mathbf{Q}_2/\theta_2 \\ \vdots \\ \mathbf{Q}_n/\theta_n \\ \vdots \\ \mathbf{Q}_{Tsam}/\theta_{Tsam} \end{bmatrix}$ is a $T_{sam} \times 256$ tall matrix where each row has a **Q** vector (in Equation (6.11)) corresponding to each input data set, and θ_1, θ_2, ..., θ_{Tsam} are the sums of weighting factors for the respective input set. Γ is still the 256×1 column vector as defined in Equation (6.10) but its elements are unknown at the initial stage of the training.

Hence in this training stage, the output samples together with Ξ vector are used to estimate all the elements in Γ using the recursive least-square formula given as [102]:

$$\Gamma^n = \Gamma^{n-1} + \mathbf{S}_n \Xi_n{}^T \left({I_{PV}}^n - \Xi_n \Gamma^{n-1} \right) \tag{6.22}$$

and $$\mathbf{S}_n = \mathbf{S}_{n-1} - \frac{\mathbf{S}_{n-1} \Xi_n{}^T \Xi_n \mathbf{S}_{n-1}}{1 + \Xi_n \mathbf{S}_{n-1} \Xi_n{}^T} \tag{6.23}$$

where Ξ_n is the row vector corresponding to n-th row of Ξ; $\mathbf{S}_n$ is the covariance matrix [102] and at the initial stage, $\mathbf{S}_0 = \gamma \mathbf{I}$ where the value $\gamma = 4$ was found to work well by other authors [102, 103]. The derivation for this formula can also be found in the Appendix of this thesis.

The estimation technique starts by applying the first set of output samples to Equations (6.22) and (6.23) to update the vector Γ. This process is repeated with the next output sample set and a new Γ vector is obtained. This continues iteratively until n reaches the total number of sample sets and the final solution for Γ is the one which minimizes the value for the following cost function:

$$E = \frac{1}{2} \sum_{n=1}^{T_{sam}} \left({I_{PV}}^n - {\hat{I}_{PV}}^n \right)^2 \tag{6.24}$$

where E represents the sum of squared errors evaluated between the actual sampled I_{PV}^{n} from n-th data set and $\hat{I}_{PV}^{n}$, the model predicted value obtained by applying the model equation in (6.9).

The model accuracy is then evaluated using the Equation (6.15) while the parameters defined in $\mathbf{\Phi}_p$ are used to evaluate the compactness and interpretability of the model using Equations (6.16) and (6.17) respectively. The overall fitness function is then calculated according to Table 6.9. The above PV current prediction and model evaluation is repeated with all the 20 particles to obtain the values for their individual fitness functions.

6.5.2 Stage Two: Model Parameters Tuning Using PSO Algorithm

The resulting fitness function values for all the above 20 particles are used to improve the model performance using the PSO technique described in Chapter 1. In particular, personal best position, $pbest_p$ of a particle will only take the current values of $\mathbf{\Phi}_p$ if its current fitness function, $\mathbf{FF}_p[k]$ is greater than $\mathbf{FF}_p^{\,b}[k\text{-}1]$ which is the fitness function associated with its previous $pbest_p$. Hence at k-th iteration, the personal best position and its associated fitness function of each particle is updated respectively as

$$pbest_p[k] = \begin{cases} pbest_p[k-1] & \text{if } \mathbf{FF}_p[k] \le \mathbf{FF}_p^{\,b}[k-1] \\ \mathbf{\Phi}_p[k] & \text{if } \mathbf{FF}_p[k] > \mathbf{FF}_p^{\,b}[k-1] \end{cases}$$

$$\text{and} \quad \mathbf{FF}_p^{\,b}[k] = \begin{cases} \mathbf{FF}_p^{\,b}[k-1] & \text{if } \mathbf{FF}_p[k] \le \mathbf{FF}_p^{\,b}[k-1] \\ \mathbf{FF}_p[k] & \text{if } \mathbf{FF}_p[k] > \mathbf{FF}_p^{\,b}[k-1] \end{cases} \tag{6.25}$$

The particle which has the highest fitness function value is chosen as the overall best at the k-th iteration. Its fitness function, $\mathbf{FF}_o[k]$ is then compared to $\mathbf{FF}_g^{\,b}[k\text{-}1]$ which is the fitness function associated with the global best position at the previous iteration. If only the former is higher, then the position of the current overall best particle, $\mathbf{\Phi}_p^{\,o}[k]$ is chosen as current global best position. Hence at k-th iteration, the global best position for the swarm and its associated fitness function are updated respectively as

$$gbest[k] = \begin{cases} gbest[k-1] & \text{if } \mathbf{FF}_o[k] \le \mathbf{FF}_g^{\,b}[k-1] \\ \mathbf{\Phi}_p^{\,o}[k] & \text{if } \mathbf{FF}_o[k] > \mathbf{FF}_g^{\,b}[k-1] \end{cases}$$

$$\text{and} \quad \mathbf{FF}_g^{\,b}[k] = \begin{cases} \mathbf{FF}_g^{\,b}[k-1] & \text{if } \mathbf{FF}_o[k] \le \mathbf{FF}_g^{\,b}[k-1] \\ \mathbf{FF}_o[k] & \text{if } \mathbf{FF}_o[k] > \mathbf{FF}_g^{\,b}[k-1] \end{cases} \tag{6.26}$$

With the information of the above best positions, $\mathbf{\Phi}_p$ of each particle is adjusted using the PSO algorithm formula given as

$$\mathbf{\Phi}_p(k+1) = \mathbf{\Phi}_p(k) + \mathbf{V}_p(k+1) \tag{6.27}$$

where $\mathbf{V}_p(k+1)$ denotes the amount for parameter update and it can be obtained as

$$\mathbf{V}_p(k+1) = \Lambda_1 rand_1(k)\left[\mathbf{\Psi}_p(k) - \mathbf{\Phi}_p(k)\right] + \Lambda_2 rand_2(k)\left[\hat{\mathbf{\Psi}}(k) - \mathbf{\Phi}_p(k)\right] + \mathbf{\Omega}(k)\mathbf{V}_p(k) \tag{6.28}$$

where Λ_1 and Λ_2 are the acceleration coefficients. While they were allocated with a value of 2 according to the original application of PSO, their actual values can still be optimized for PV modelling. $rand_1$ and $rand_2$ are random values generated from a uniform distribution.

$\mathbf{V}_p(k)$ is also added into the search to provide a momentum for the previous update. This is controlled by the inertia factor, $\mathbf{\Omega}$ which is decreasing linearly with the iteration expressed as

$$\mathbf{\Omega}(k) = (\mathbf{\Omega}(0) - \mathbf{\Omega}(N_k))\frac{(N_k - k)}{N_k} + \mathbf{\Omega}(N_k) \tag{6.29}$$

where N_k is the maximum number of iterations for which the algorithm is executed, $\mathbf{\Omega}(0)$ is the initial inertia weight and $\mathbf{\Omega}(N_k)$ is the final inertia weight. By setting the inertia weights such that $\mathbf{\Omega}(0) > \mathbf{\Omega}(N_k)$, the training is prevented from being trapped within a sub-optimal region at the beginning of the tuning process, while at the end the model parameters can be finely tuned.

For the above training algorithm, there are four PSO parameters, namely, $\mathbf{\Omega}(0)$, $\mathbf{\Omega}(N_k)$, Λ_1, and Λ_2, which all need to be selected properly so that the model training is accurate and computationally efficient. This is done in the next section when this modelling technique is applied to a PV system.

When all the model parameters have been adjusted, the rule weights have to be re-calculated using Equation (6.4) and the linear parameters have to be updated using Equations (6.22) and (6.23) in order to obtain another set of new fitness function values. The training algorithm is carried out iteratively so that a set of particles with better solutions is generated continuously until the maximum iteration is reached. At the end of this process, the particle which gives the highest value for the fitness function will be used to determine the final structure for the PV model.

The above described PSO-trained PV model is illustrated by the flowchart in Figure 6.9. This algorithm is implemented in MATLAB M-file.

6.6 Application Example I: Re-constructing a Set of Simulated I-V Characteristics

In this section, the modelling technique described above is applied to generate three PV models with their structure optimized according to the different design priorities.

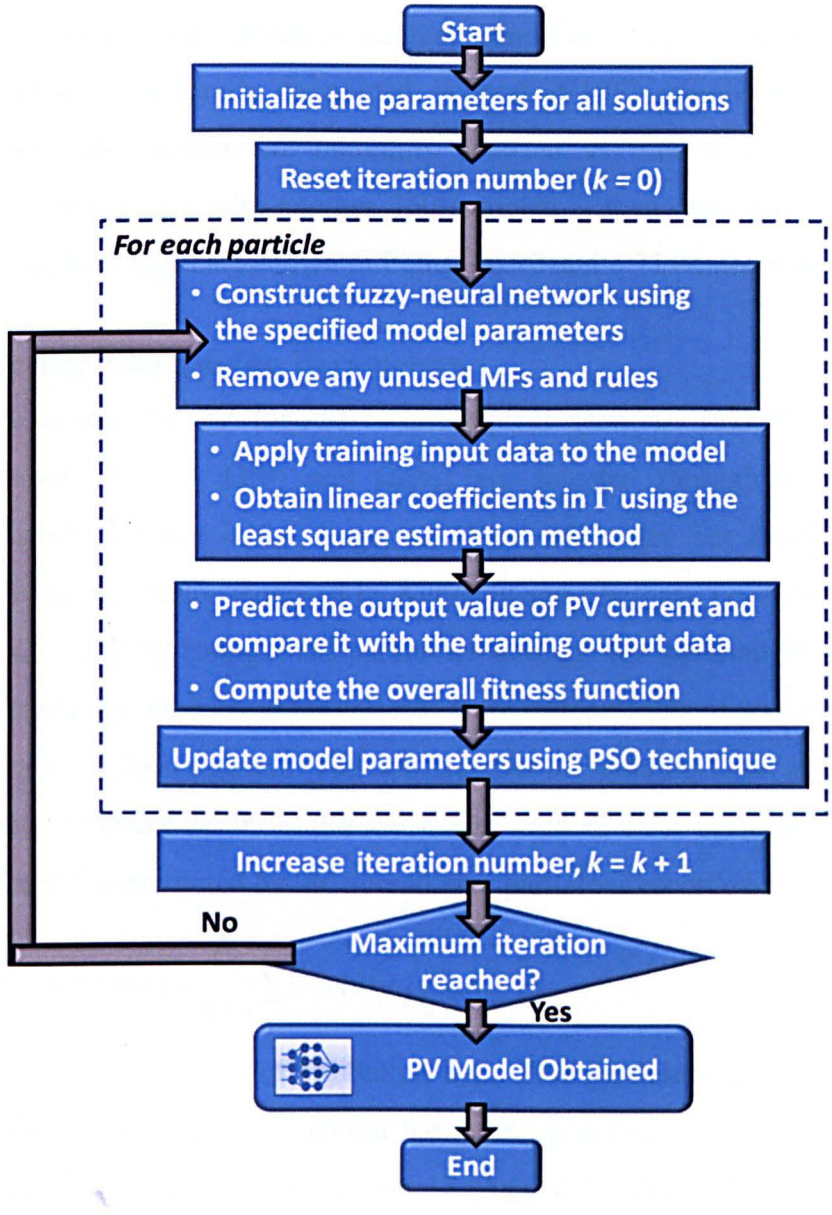

Figure 6.9 Flowchart for tuning the PV Neural-Fuzzy model

6.6.1 Design Specifications

A set of simulated PV data samples is taken, and it consists of model input-output data which are within the following ranges:

- Solar Insolation: 1 – 106 mW/cm^2
- Ambient Temperature: -15 – 45 °C
- PV Voltage: 13 – 42.7 V
- PV Current: 0-14.1 A

These represent 127 different weather conditions under which the voltage-current samples are uniformly distributed. A total of 1057 samples are created and out of these, 360 samples are randomly selected as training data. For model validation, a separate set with another 360 samples is then randomly created. The data clouds for both types are shown in Figures 6.10 and 6.11 respectively.

6.6.2 Selecting PSO Tuning Parameters

Before tuning the PV models in subsequent sections, four PSO parameter settings, namely Λ_1, Λ_2, $\Omega(0)$ and $\Omega(N_k)$ are selected through a pre-liminary simulation study. At the initial stage, all their values are set according to the algorithm design originally proposed by Kennedy and Eberhart; i.e. $\Lambda_1 = \Lambda_2 = 2$ and $\Omega(0) = \Omega(N_k) = 1$ [73]. Using these parameter settings, ten different PV models are generated separately. Each model is selected from different sets of 20 particles which potentially offer the best solution. The total number of iterations is set at 30 for every model tuning. At every iteration, the root-mean-squared error between the sampled PV current and that predicted by the overall best particle is recorded as

$$\text{RMSE (in Ampere)} = \sqrt{\frac{1}{T_v}\sum_{n=1}^{T_v}\left(I_{PV}(n) - \hat{I}_{PV}(n)\right)^2} \tag{6.30}$$

where T_v is the total samples of validation data. Five models with the lowest error values are then selected and throughout the tuning process, their error variations in logarithmic scale are depicted in Figure 6.12. As can be observed, the errors for all five models have not fully stabilized even after 25 iterations. For example moving from the 27th to 28th iteration, the error of one model can still vary by around 3.5 mA

at the highest. In addition, the errors of all the models are within a wide range between 0.331 mA and 82 mA at the end of the tuning process.

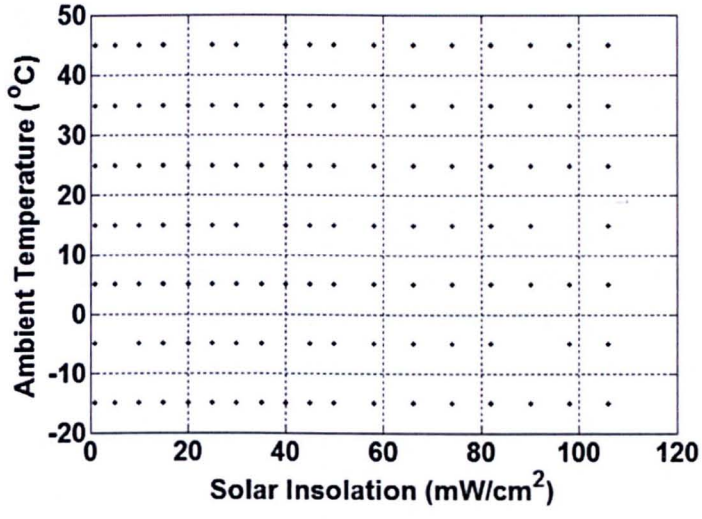

(a) Simulated solar insolation – temperature pair

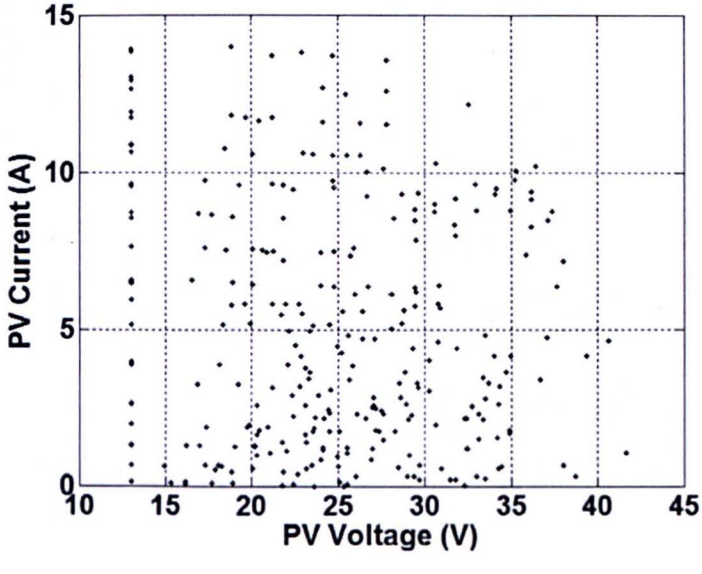

(b) Simulated PV voltage – PV current pair

Figure 6.10 Simulated sample data used for training the PV model

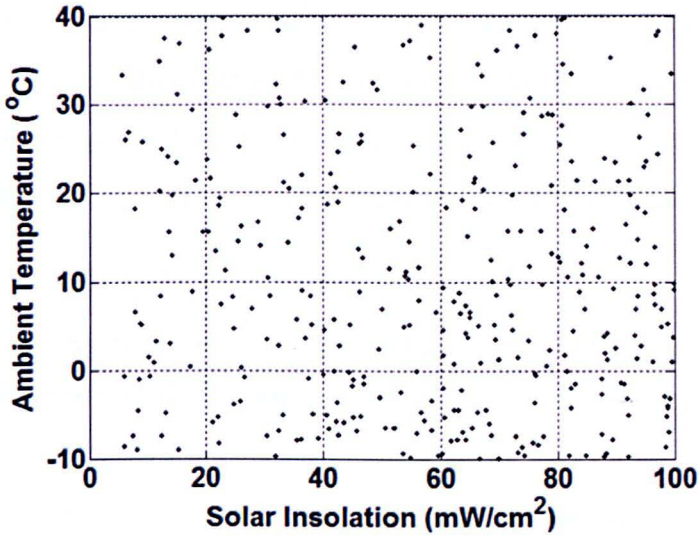

(a) Simulated solar insolation – temperature pair

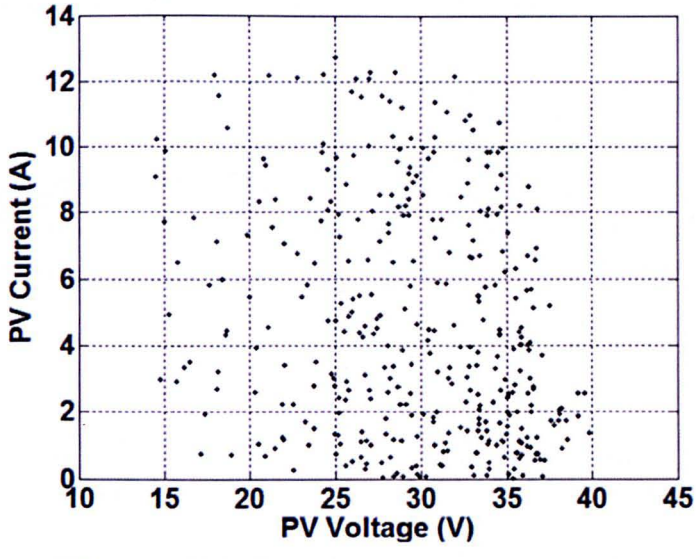

(b) Simulated PV voltage – PV current pair

Figure 6.11 Simulated sample data used for validating the PV model

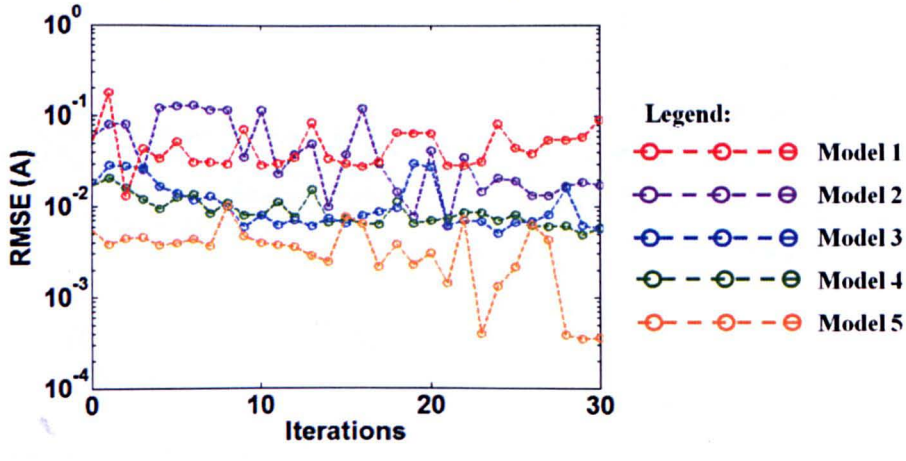

Figure 6.12 Error variations for the 5 best models using the conventional values for PSO design parameters, i.e. $\Lambda_1 = \Lambda_2 = 2$ & $\Omega(0) = \Omega(N_k) = 1$

These performances are set as the reference, and the parameters used are classified as Set 0. Six other sets of $\Lambda 1$, $\Lambda 2$, $\Omega(0)$, and $\Omega(N_k)$ are analyzed and their error variations are plotted in Figures 6.13(a) – (c), and Figures 6.14(a) – (c) respectively. The explanation for each of these is explained as follows:

6.6.2.1 Selecting $\Omega(0)$ and $\Omega(N_k)$ Values

With Λ_1 and Λ_2 fixed at 2, the above tuning process and error recording are repeated with three sets of $\boldsymbol{\Omega}(0) - \boldsymbol{\Omega}(N_k)$ values.

Set 1 : $\boldsymbol{\Omega}(0) = 1$ and $\boldsymbol{\Omega}(N_k) = 0$

Unlike Set 0, the errors tend only to fluctuate within the first 10 iterations as shown in Figure 6.13(a). After 10 iterations have elapsed, the errors begin to stabilize. At the end of the tuning process, the lowest error obtained is only 4.74 mA.

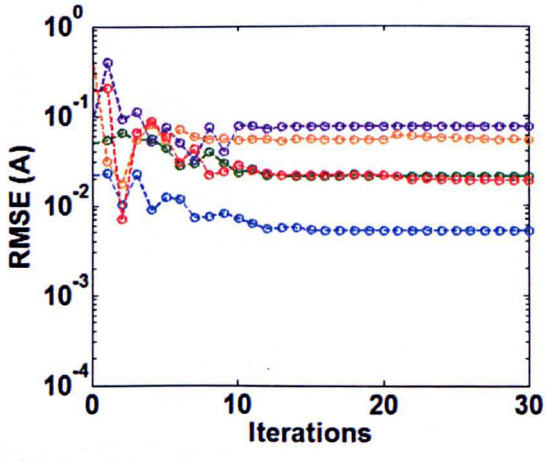

(a) Set 1: $\boldsymbol{\Omega}(0) = 1$ and $\boldsymbol{\Omega}(N_k) = 0$

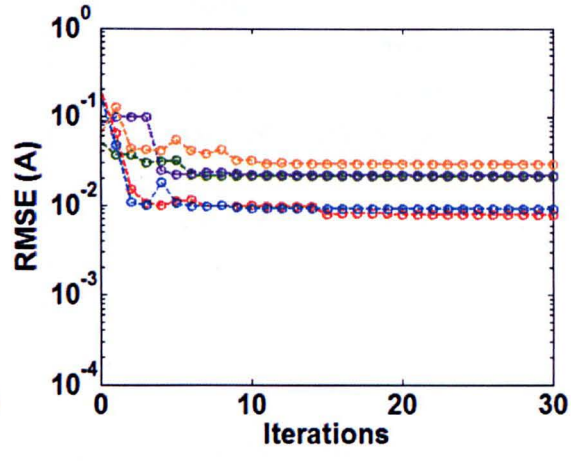

(b) Set 2: $\boldsymbol{\Omega}(0) = 0.5$ and $\boldsymbol{\Omega}(N_k) = 0$

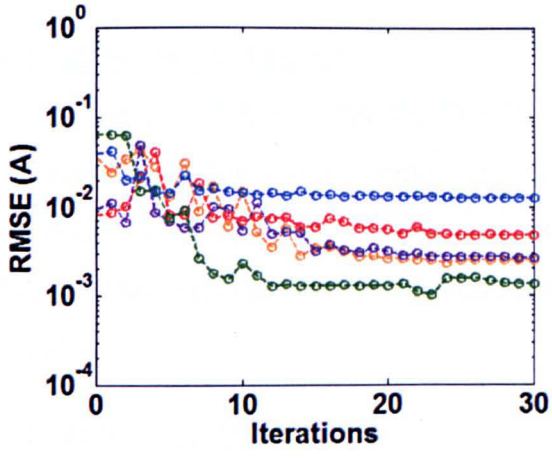

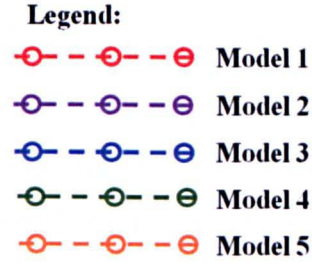

(c) Set 3: $\boldsymbol{\Omega}(0) = 1$ and $\boldsymbol{\Omega}(N_k) = 0.5$

Figure 6.13 Error variations for the 5 best models when setting Λ_1 and Λ_2 as 2 while varying the values for $\boldsymbol{\Omega}(0)$ and $\boldsymbol{\Omega}(N_k)$

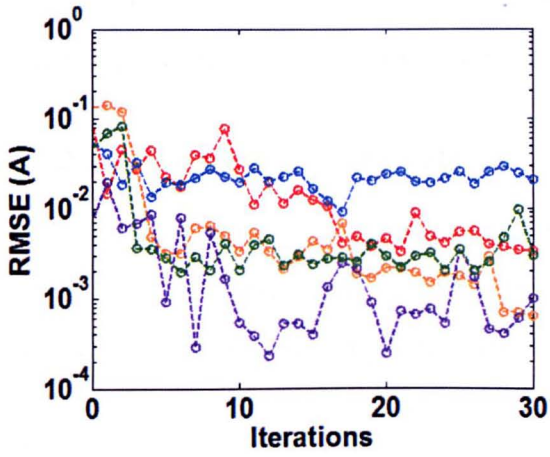

(a) Set 4: $\Lambda_1 = \Lambda_2 = 20$

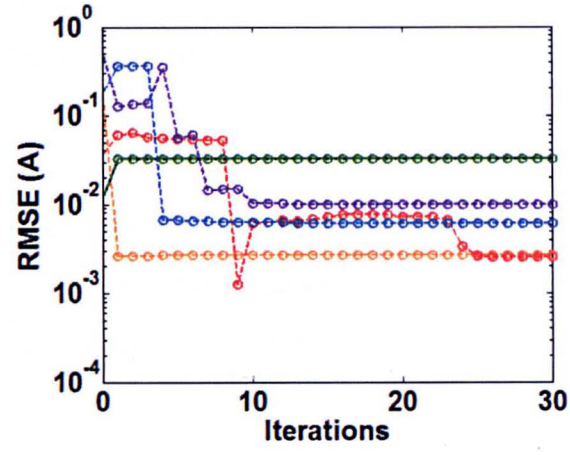

(b) Set 5: $\Lambda_1 = \Lambda_2 = 0.2$

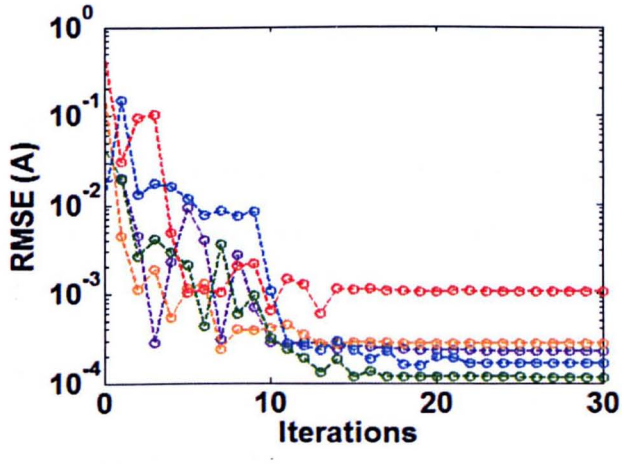

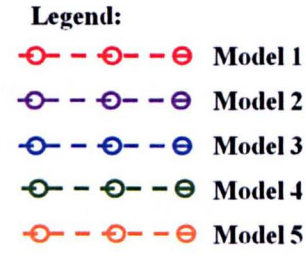

(c) Set 6: $\Lambda_1 = \Lambda_2 = 4$

Figure 6.14 Error variations for the 5 best models when setting $\mathbf{\Omega}(0) = 1$, $\mathbf{\Omega}(N_k) = 0.5$ while varying the values for Λ_1 and Λ_2

Set 2 : $\mathbf{\Omega}(0) = 0.5$ and $\mathbf{\Omega}(N_k) = 0$

All errors stabilize within the first 10 iterations as shown in Figure 6.13(b) and the errors of all the models only vary through a smaller range. However, their magnitudes at the end of the tuning process are still very high; i.e. the lowest being 9.8 mA. This indicates that the training has been trapped within the region of sub-optimal solutions.

Set 3: $\mathbf{\Omega}(0) = 1$ and $\mathbf{\Omega}(N_k) = 0.5$

As shown in Figure 6.13(c), there are still some variations towards the last 10 iterations of the tuning process but the magnitudes are much smaller than those of Set 0. In addition, the lowest error is 1.17 mA. This can be explained by the effect of

the greater inertia factor used throughout the process which, in turn, prevents the training from being trapped within the region of sub-optimal solutions.

6.6.2.2 Selecting Λ_1 and Λ_2 Values

From the previous analysis, the best performance for the error variation is when $\Omega(0) = 1$ and $\Omega(N_k) = 0.5$. Using these values, the tuning process and error recording are repeated using three different sets of Λ_1 and Λ_2 values.

Set 4 : $\Lambda_1 = \Lambda_2 = 20$

As shown in Figure 6.14(a), the errors do not stabilize even within the last 5 iterations, and their fluctuations are greater than those in Sets 1 to 3. Nevertheless, at the end of the tuning process, the lowest error obtained is around 0.643 mA.

Set 5 : $\Lambda_1 = \Lambda_2 = 0.2$

Similar to those in Set 1 but unlike Set 4, the errors fluctuate more in the beginning of the training process and stabilize towards the end as shown in Figure 6.14(b). After 30 iterations, the smallest error obtained is only 2.48 mA.

Set 6 : $\Lambda_1 = \Lambda_2 = 4$

As shown in Figure 6.14(c), this set, offers by far the best performance, since the error magnitudes at the end of the tuning are the lowest among all the previous sets; i.e. the lowest error is 0.114 mA. While the errors tend to fluctuate by a moderately large amount at the beginning of the tuning process, the fluctuation is then limited to a smaller amount of no more than 0.01 mA within the last 10 iterations. Hence, a total search area has been adequately explored to find the most optimum solution for the model.

The overall performances of Sets 1 – 6 are summarized in Table 6.10. It is worth noting, by this stage, that the values in Set 6 can still be tuned more finely by repeating the above selection processes. This is particularly necessary when they are applied to other subsequently models designed in this chapter.

6.6.3 Generating PV Models with Different Design Priorities

Three different sets of weight parameters for the design priorities are given in Tables 6.11 – 6.13. The main design priority for Model A is accuracy. Hence the

values for K_A, K_C and K_I have been set at 116, 3.9 and 6.5 respectively. For Model B, it is highly desirable to have a simpler model structure. Hence, K_A has been set to be at least 3 times lower than that in Model A, while others are maintained at a constant. Meanwhile, the design goal for Model C is to obtain a compact structure while its desired accuracy level is maintained. To achieve this, K_A is set to slightly higher than Set B; i.e at 58 while K_C and K_I values are the same as those in the previous sets. The PSO design parameters tuned in the previous section are applied to all the three model designs.

The maximum number of iterations for training each model is fixed at 30, and by average, the training procedure took about 97.8 seconds or 3.3 seconds per

Table 6.10 Performance indices of different sets of PSO tuning parameters

Set	PSO Tuning Parameters	Lowest Error	Iterations taken to settle down
0	$\Lambda_1 = \Lambda_2 = 2$, $\Omega(0) = \Omega(N_k) = 1$	0.331 mA	Unstable Response
1	$\Lambda_1 = \Lambda_2 = 2$, $\Omega(0) = 1$, $\Omega(N_k) = 0$	4.740 mA	12
2	$\Lambda_1 = \Lambda_2 = 2$, $\Omega(0) = 0.5$, $\Omega(N_k) = 0$	9.800 mA	9
3	$\Lambda_1 = \Lambda_2 = 2$, $\Omega(0) = 1$, $\Omega(N_k) = 0.5$	1.170 mA	15
4	$\Lambda_1 = \Lambda_2 = 20$, $\Omega(0) = 1$, $\Omega(N_k) = 0.5$	0.643 mA	Unstable Response
5	$\Lambda_1 = \Lambda_2 = 0.2$, $\Omega(0) = 1$, $\Omega(N_k) = 0.5$	2.48 mA	11
6	$\Lambda_1 = \Lambda_2 = 4$, $\Omega(0) = 1$, $\Omega(N_k) = 0.5$	0.114 mA	18

Table 6.11 Weight parameters for Model A

Parameters	Symbol	Values
Weights for fitness function	K_A	116.0
	K_C	3.9
	K_I	6.5

Table 6.12 Weight parameters for Model B

Parameters	Symbol	Values
Weights for fitness function	K_A	40
	K_C	3.9
	K_I	6.5

Table 6.13 Weight parameters for Model C

Parameters	Symbol	Values
Weights for fitness function	K_A	58
	K_C	3.9
	K_I	6.5

iteration to generate each model. A comparison among the three models can be made in Table 6.14. The structure size considers the numbers of MFs, fuzzy rules and the f_r functions used by the model. The overlap or gap between two MFs can be measured using Equation (6.17). The accuracy of the model, on the other hand, can be evaluated using the RMSE formula given in Equation (6.30). The performance of each model is explained as follows.

6.6.3.1 Model A: Accuracy-biased PV model

Based on the information from the final values of **FS** and **CL**, the model requires 41 rules which are based on 9 optimised MFs. This gives a total of 91 model components. As shown in Figure 6.15, the MFs for all three inputs tend to overlap with each other and this leads to a high value of around 23.9% for the average overlap between two MFs. Hence, it is not easy to give a unique label for either of them. However a small root mean square error (RMSE) of 0.2479 mA is achieved.

6.6.3.2 Model B: Size-biased PV model

The model requires 5 MFs and 7 fuzzy rules, leading to a total of 19 components, 10 times less than Model A. As demonstrated by the distributions of the input MFs in Figure 6.16, the average overlap between any two MFs is the lowest which is 3.58% and hence, each of them can be allocated with a linguistic label. However, the RMSE for this model is 28 mA which is about 100 times higher than that of Model A.

Table 6.14 Performance indices for Models A, B and C

Type of model	Total number of model components	Average overlap between two MFs	RMSE (Validation data)
Model A	91	23.9%	0.2479 mA
Model B	19	3.58%	28.000 mA
Model C	48	7.65%	1.400 mA

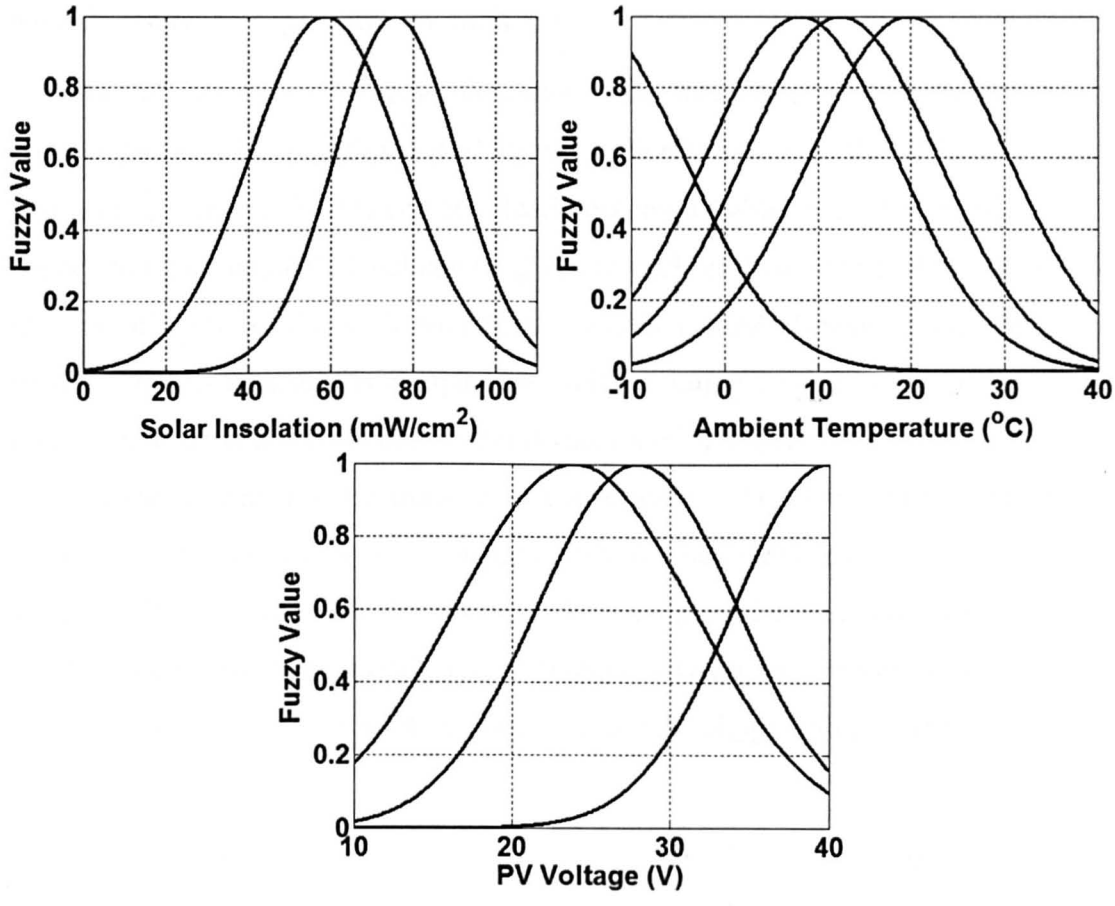

Figure 6.15 MFs of the three inputs for Model A

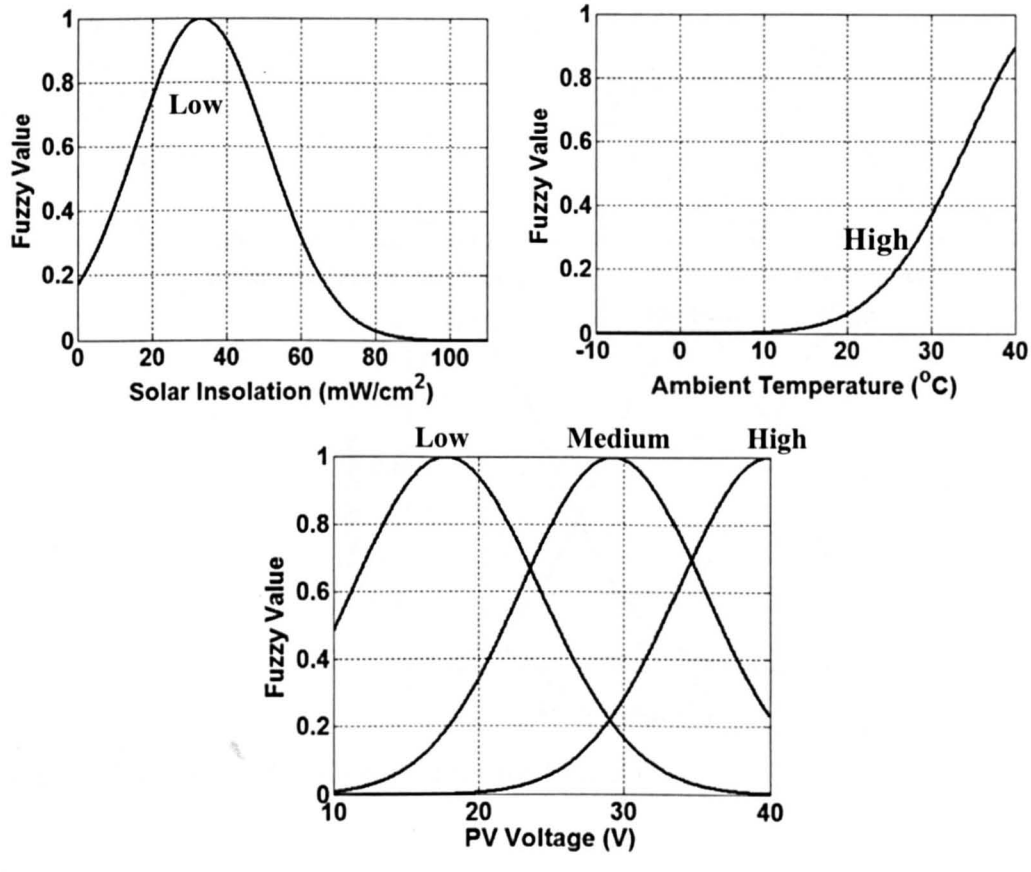

Figure 6.16 MFs of the three inputs for Model B

6.6.3.3 Model C: Optimum PV model

With 6 MFs and 21 fuzzy rules, this model has a total of 48 components and this number is at least half of that of Model A. Furthermore, all the MFs have quite a low overlap which is 7.65% and are clearly distinguishable, as shown in Figure 6.17; hence a unique linguistic label can be given to each of them. Meanwhile, the RMSE level is only 6 times that of Model A; i.e. around 1.4 mA. Hence, this model is still accurate and its structure is compact, as well as simple enough to be interpreted by users. The final structure of this model is illustrated in Figure 6.18.

Model C can also be used to re-construct the PV characteristic curves. To achieve this, the inputs for solar insolation and temperature are kept constant while a series of PV voltage samples (from 0 to the open-circuited voltage value) are iteratively applied to the model. The difference between two consecutive samples is set to be no more than 1% of the open-circuited voltage value. For every voltage

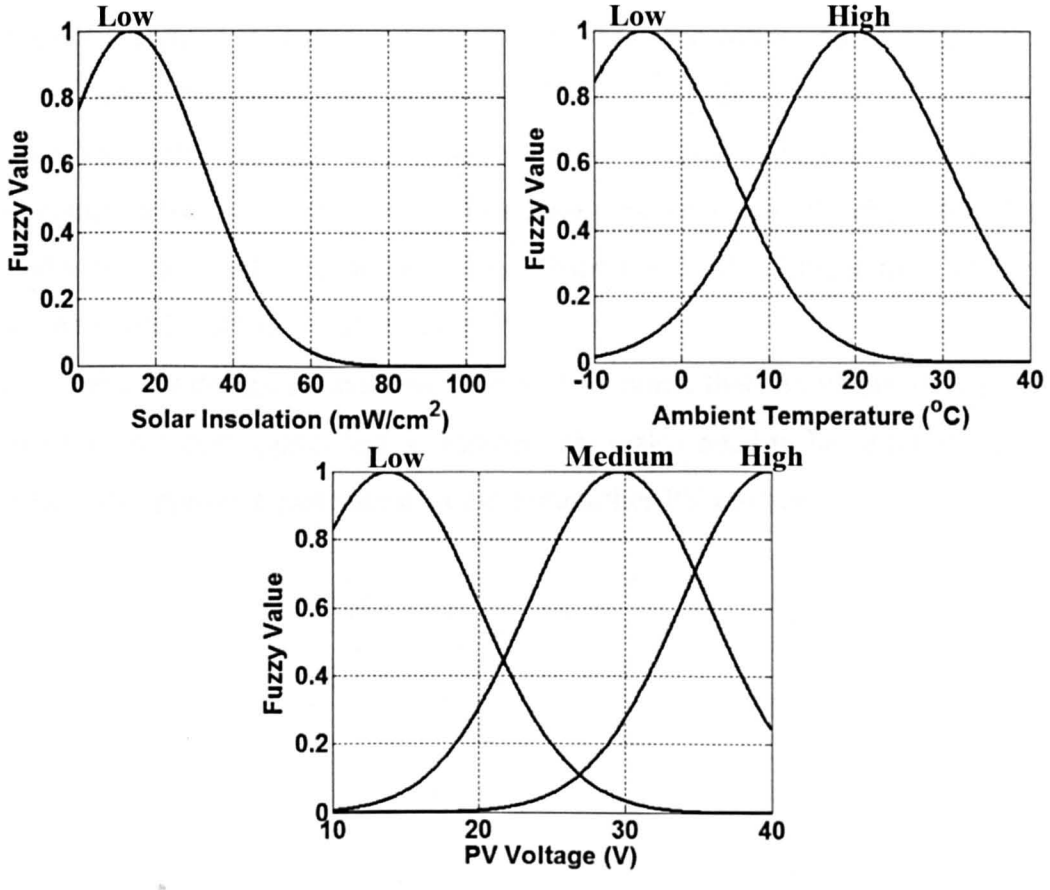

Figure 6.17 MFs of the three inputs for Model C

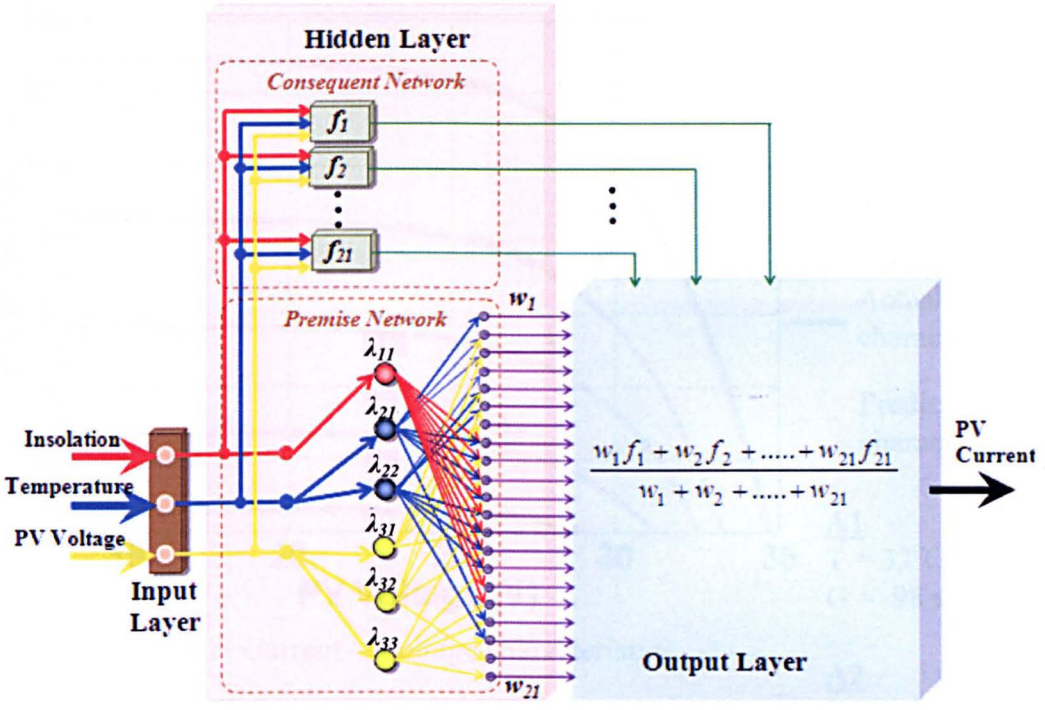

Figure 6.18 Optimally-tuned PV Neuro-Fuzzy model

level, the PV current is predicted and recorded. Using these voltage-current pairs, the I-V and P-V characteristics can be plotted for 5 sets of weather conditions as shown in Figure 6.19 where the red dashed lines denote the predicted characteristics which can be compared to the black solid lines that represent the PV characteristics simulated using the modelling technique in Chapter 2. Both of them fit relatively well and the RMSE obtained is still below 1%.

Like the PSO design parameters, it should be noted that the values of K_A, K_C and K_I differ from one application to another. They also need to be re-tuned when these values are applied to generate a model for another PV module.

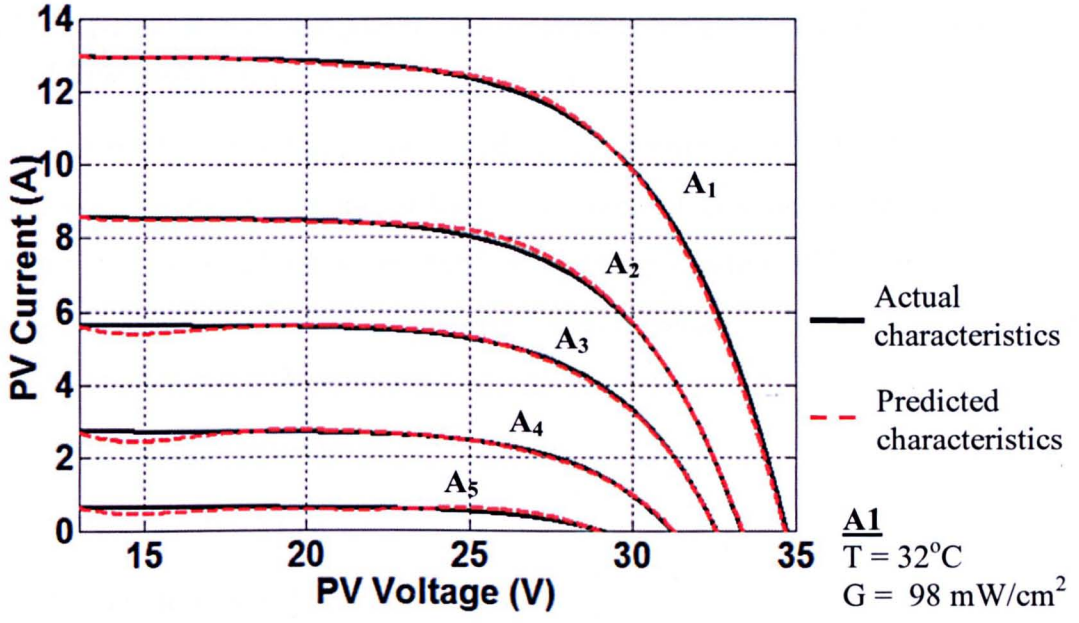

(a) Current – Voltage characteristics

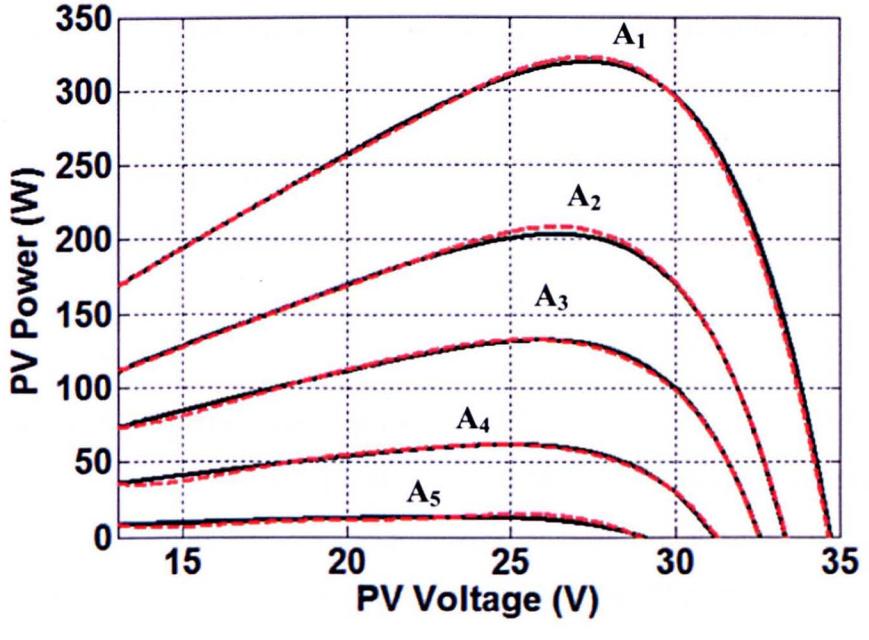

(b) Power –Voltage characteristics

Figure 6.19 Re-construction of simulated PV characteristics

6.7 Application Example II: Re-constructing a Set of Practical I-V Charateristics

The modelling technique proposed in this chapter is evaluated further through re-constructing the PV characteristics of a practical module at the University of Leeds. This is based on a Siemens M56 polycrystalline PV module with the following typical characteristics measured under insolation = 106.98 mW/cm^2 and ambient temperature = 25°C:

MPP voltage: 18.38 V

MPP current: 0.53 A

Maximum power: 9.8 W

Data samples were available as this PV module has been studied previously by the researcher in [83]. Of all the data collected, 604 data samples as shown in Figure 6.2 are set as the training data and they are within the following specified ranges:

Ambient Temperature: 18.59 – 34.32 °C

Solar Insolation: 34.70 – 135.25 mW/cm^2

PV Voltage: 10.05 – 19.03 V

PV Current: 0.02 – 0.91 A

6.7.1 I-V Curve Modelling

The PSO training procedure described in Section 6.5 is employed to generate a model to represent the relationship linking the weather conditions and the PV voltage to the corresponding current samples. The values for $\mathbf{\Omega}(0)$ and $\mathbf{\Omega}(N_k)$ are similar to those in the previous model designs. On the other hand for Λ_1 and Λ_2, a fine tuning is required prior to setting them to 2.8. The maximum number of iteration is still set to 30.

The training process took about 149.4 seconds or 4.98 seconds per iteration. The time is slightly longer than that in the previous application example due to the larger number of samples used for this model. By setting the values for K_A, K_C and K_I as 200, 4.9 and 6.7 respectively, an optimum model based on 8 MFs and 37 rules is obtained. The number of model components used is 82, which is higher comparing to the optimum model in Section 6.6.3.1. This can be explained by the

less even distribution of the actual samples, especially for the weather measurements, as can be observed in Figure 6.20. Nevertheless, only around 60 % of the maximum available rules and MFs are used, hence the model structure has been minimised.

As illustrated in Figure 6.21, the MFs are evenly distributed and the average overlap between two MFs is found to be at 0.141. Therefore, they can be allocated with unique linguistic labels; (i.e. LOW, MEDIUM or HIGH) for solar insolation as well as ambient temperature, and (i.e. LOW, HIGH) for PV Voltage. Using this

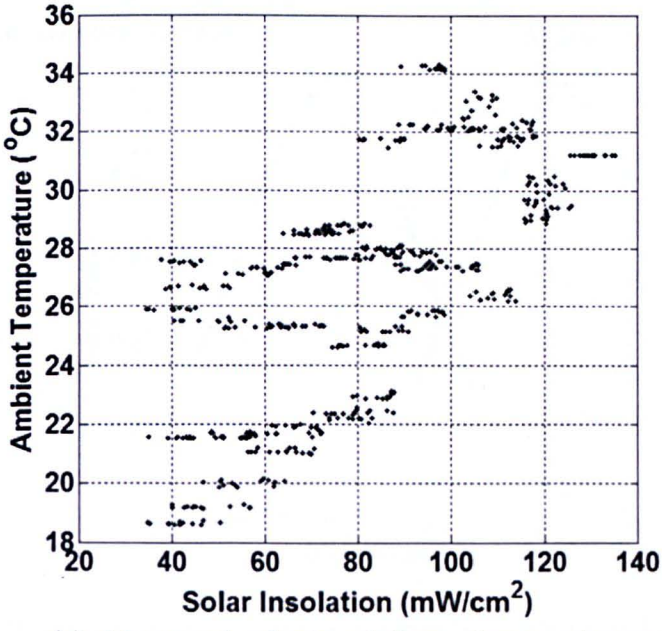

(a) Measured solar insolation – temperature pair

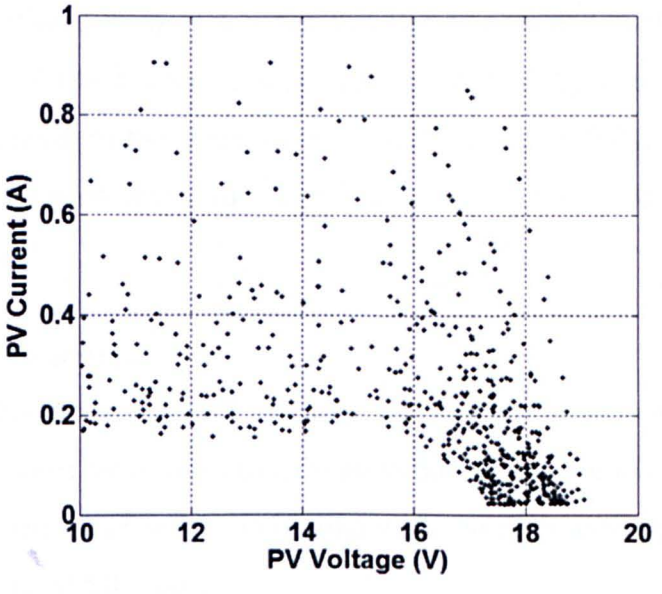

(b) Measured PV voltage – PV current pair

Figure 6.20 Practical sample data used for training the PV model

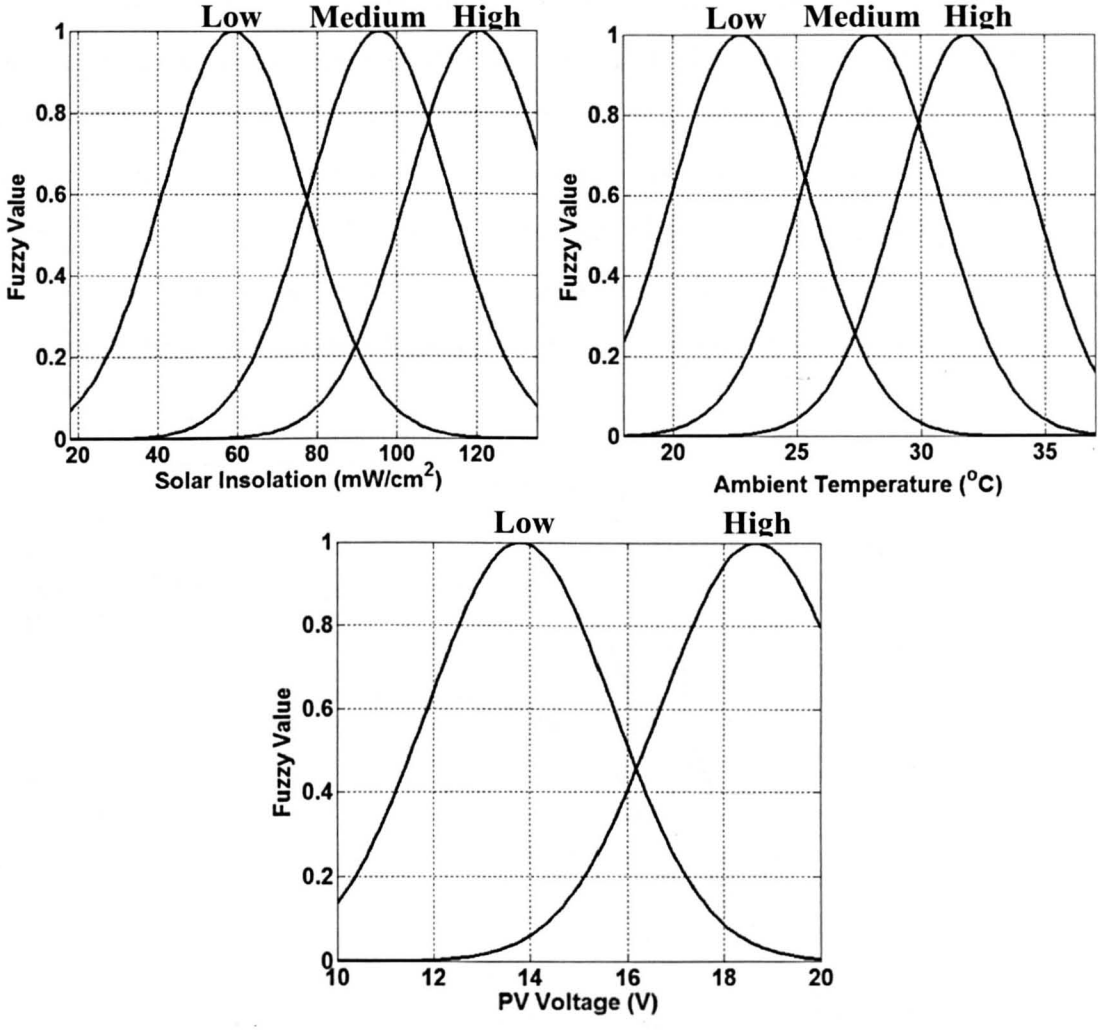

Figure 6.21 MFs of the three inputs for the practical PV model

model, the practical I-V characteristics can also be obtained as shown in Figure 6.22. The accuracy of the trained model can be verified by comparing its predicted characteristic curves to those measured from the practical PV module. It can be also observed that the predicted values match well with the actual data and an RMSE of 0.3 % is obtained.

6.7.2 MPP Prediction

To use this model for MPP tracking, the weather measurements and a series of PV voltage samples are applied iteratively to the model. For every voltage value, the PV current is computed and is multiplied with the corresponding voltage sample to obtain the predicted MPP power.

The model designed in the previous section is used to validate the MPP prediction accuracy for 40 different weather conditions. As illustrated in Figure 6.23,

the insolation-temperature changing pattern is plotted with the variation in the MPP power. The red dashed lines denote the predicted MPP while the black solid lines represent the actual MPP power. Note that the temperature for every I-V curve is the averaged value under which the corresponding practical I-V data were taken. For every weather condition, the model only takes about 15 msec to predict the entire range of I-V curve from which the corresponding MPP can be determined. As can also be observed, the model offers a high degree of accuracy with an RMSE of 3.6%.

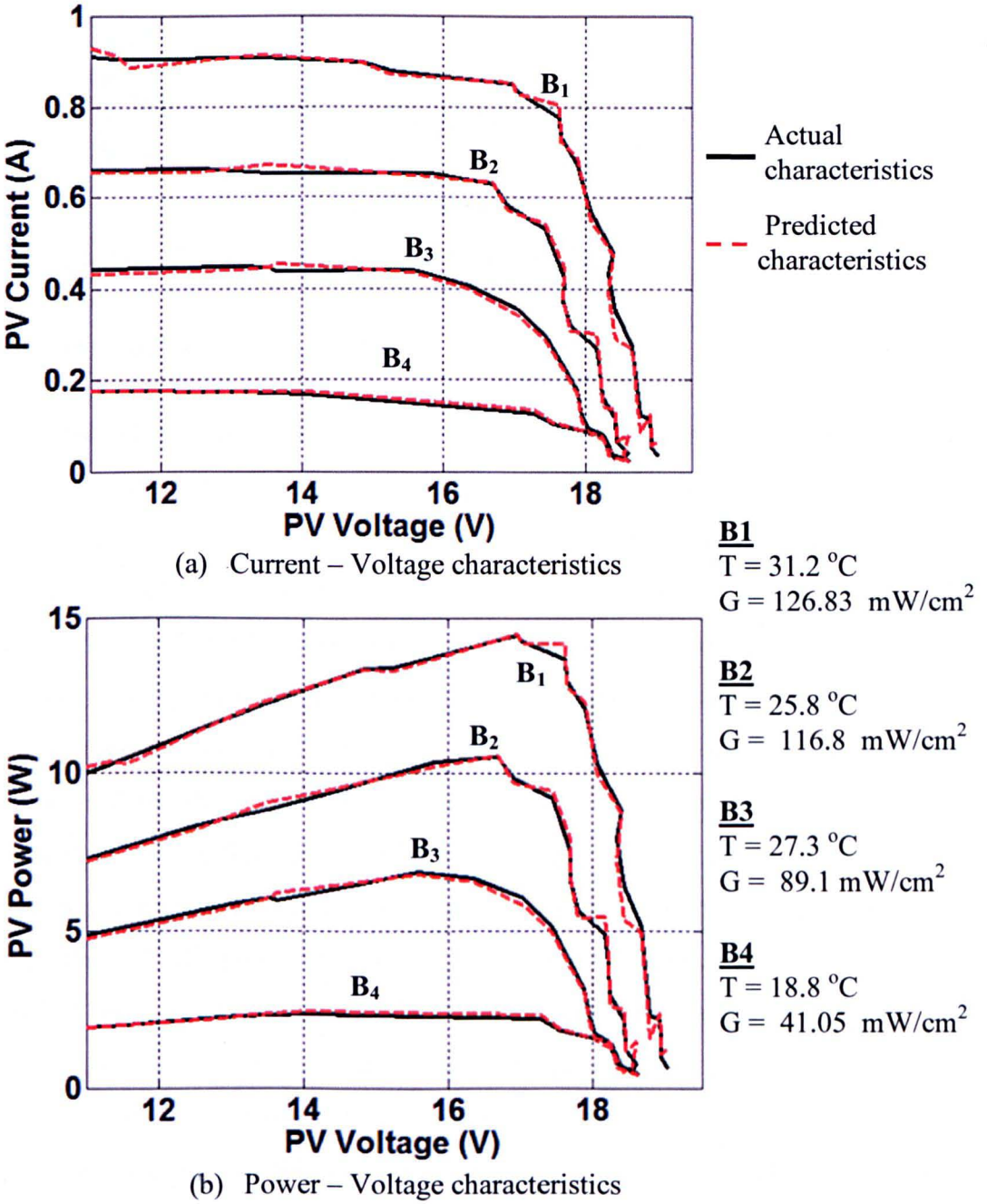

(a) Current – Voltage characteristics

(b) Power – Voltage characteristics

Figure 6.22 Reconstruction of practical PV characteristics

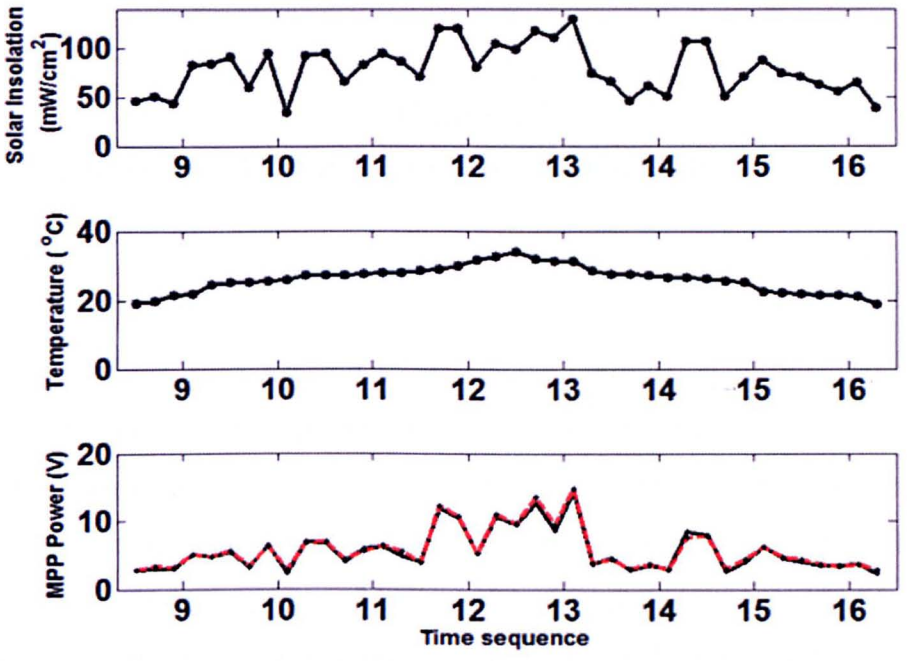

Figure 6.23 MPP prediction using PSO-based Neuro-Fuzzy model for PV

6.8 Summary

This chapter presented a Neuro-Fuzzy-network based model for representing PV characteristics the training scheme used is the particle-swarm-optimization algorithm. To achieve accuracy, compactness and high interpretability, the model structure should be optimized together with the model parameters. This has been obtained through minimizing a fitness function which incorporates all three criteria. Particle swarm optimization method used for the model training has been described for accurate and fast model training. The acceleration coefficients and the inertia factor used for the PSO training scheme have been selected such that the model parameters do not fluctuate significantly throughout the training process while the error between the predicted current and its actual value at the end of the process can be minimized. The proposed modelling technique has been applied to represent both a set of simulated and practical I-V characteristics. The resultant models fit well in both cases, and the training speed is fast. In particular for the practical system, the entire training process takes about 149 seconds which is about 170 seconds less than the Genetic-Algorithm (GA) based technique which has been used by the previous researcher in [83] for modelling the same PV module. The proposed model can be used to predict the MPP points and the error obtained in this case is 3.6% on average, which is about four times less than that using the GA model in [83].

Chapter 7
Experimental Implementation, Results and Discussions

7.1 Introduction

This chapter describes the experimental verification of the design scheme proposed in Chapter 3 through the construction of a practical DC-DC Ćuk step-down converter controlled by a dsPIC microcontroller. The experimental results are analyzed and compared to those obtained from the simulation. The second part of this chapter also presents the application of the PV model designed in Chapter 6 for tracking the maximum power point of a practical 20-Watt PV system. The general configuration for this experimental setup is shown in Figure 7.1. A practical Ćuk step-up converter links a 20-Watt PV generator to a DC load across which the voltage is held constant by a 30-volt DC power supply. The converter is then used to adjust the voltage across the PV so that maximum power points can be achieved for any weather conditions. This is performed by regulating the converter duty cycle according to the model-predicted MPP voltage as discussed in Chapter 6. The implementation for all the above is also described in this chapter.

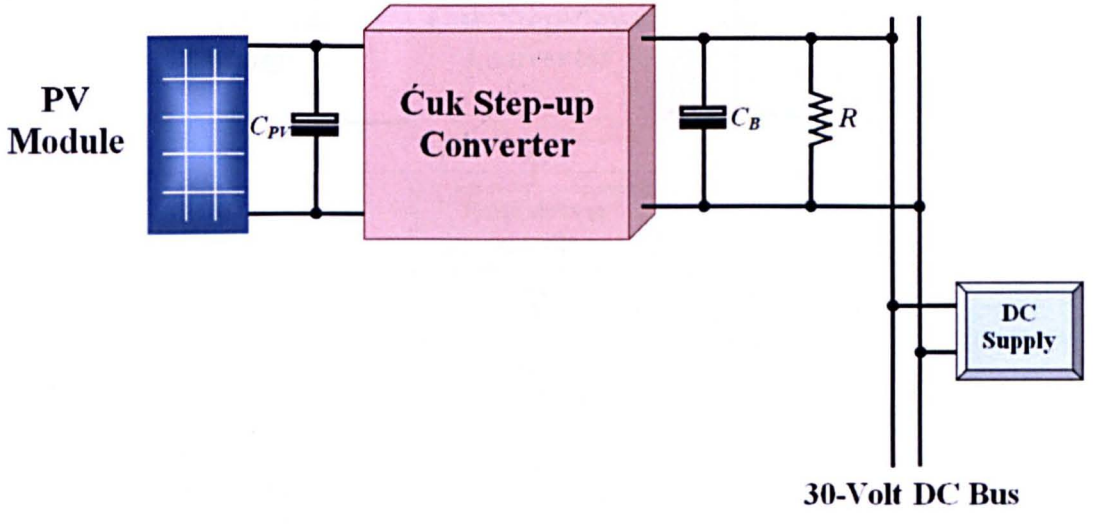

Figure 7.1 General configuration of a experimental setup for the PV energy system

7.2 Practical Ćuk Step Down Converter

Figure 7.2 shows the block diagram for the the experimental prototype designed for a practical Ćuk step-down converter. This includes a converter circuit which is used to regulate the voltage across a 180-Watt load, and a microcontroller circuit for generating the desired PWM signals. They are isolated by another interface circuit consisting of an opto-coupler and a gate driving circuit for the MOSFET.

7.2.1 Microcontroller Circuit Design

The operation of all the converters analyzed in this thesis is based on PWM control. In the converter prototype, the PWM signal is controlled by a dsPIC30F4013 device which is a type of Microchip Digital Signal Controller. The key features which make this device a desirable choice include the simple schemes available for generating PWM signals and the high computational capabilities of a digital signal processor (DSP) [105].

Figure 7.3 shows a block diagram of the PWM control implementation for this experimental prototype. The inputs to this block are the analogue signals which can be received from other sensors or defined by user for representing the desired value

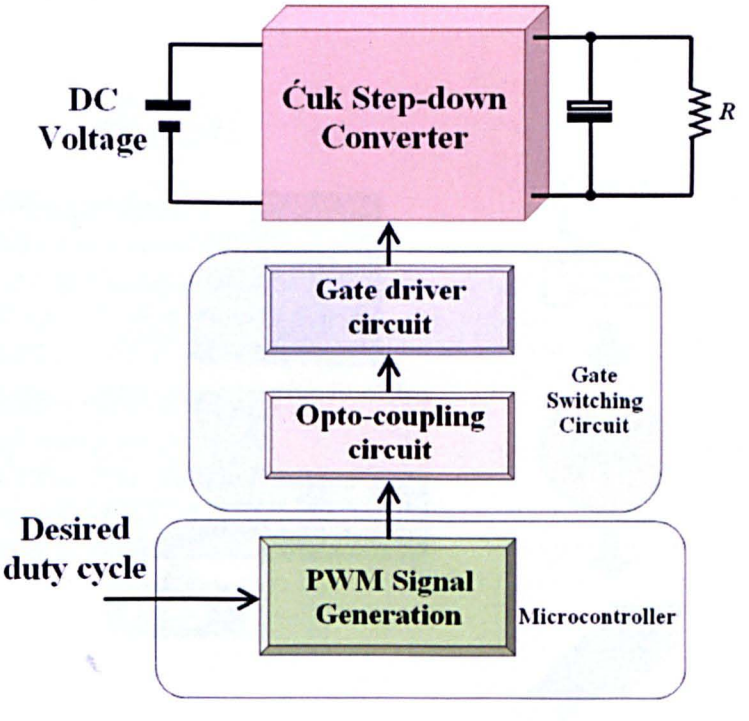

Figure 7.2 Configuration for a Ćuk step down converter and its associated PWM control circuit

of PWM duty ratio. They are then converted to a 12-bit digital number by the analogue-to-digital converter (ADC) and finally sent to the Output Compare Module to generate the appropriate PWM signal.

The process of implementing the PWM control on the device is summarized in the flowchart shown in Figure 7.4. Using MPLAB IDE software, a C program is written to initialize all variables used, configure the input/output pins and define the control tasks performed by the microcontroller. This program is debugged and compiled into machine code files before being uploaded into the device via MPLAB In-circuit Debugger 2 (ICD2).

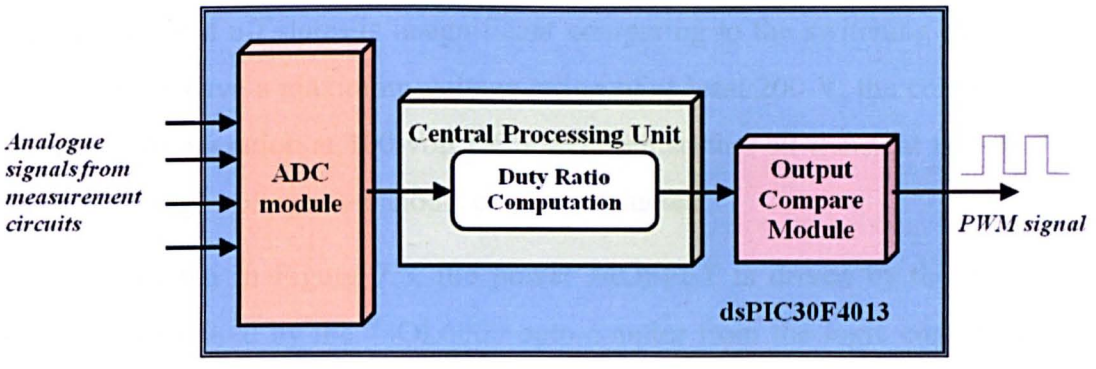

Figure 7.3 Block diagrams for PWM signal generation using dsPIC30F4013 microcontroller

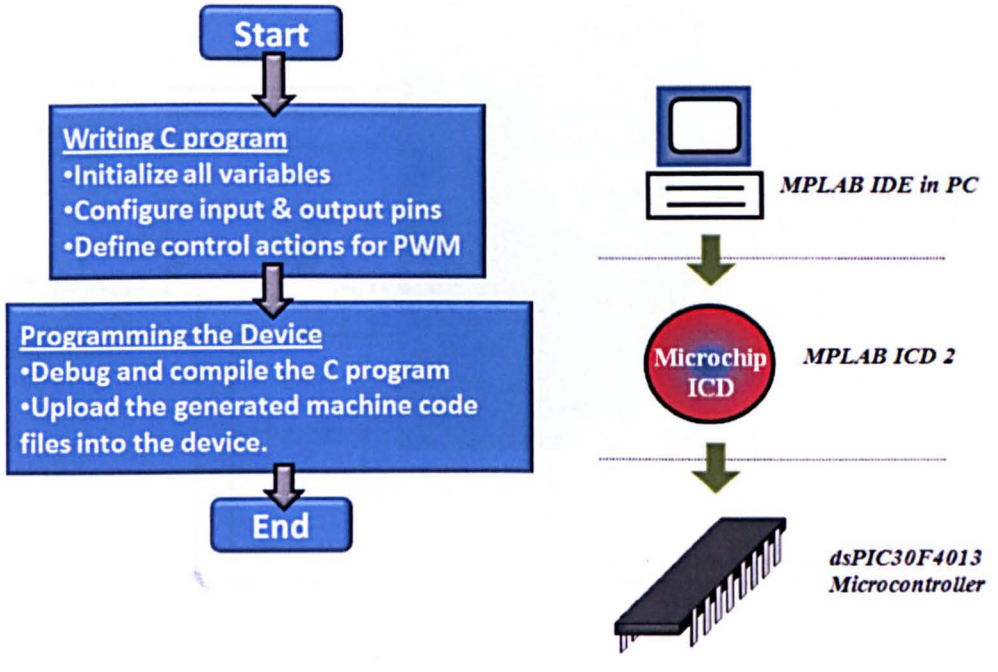

Figure 7.4 Flowchart for development process of PWM signal generation using dsPIC30F4013 microcontroller

External circuit connections to the programmed device are shown in Figure 7.5. This device is powered by a 5-volt supply. The analogue inputs are ranged from 0 to 5 volts. Hence, AV_{DD} and AV_{SS} are connected to the same supply via an external RC circuit which is used to remove unwanted noises from the ADC. A filter capacitor is also connected across all $V_{DD} - V_{SS}$ pins.

7.2.2 Power Electronics Devices and Switching Circuit Design

In this experimental prototype, the power switch and the power diode used are IRF640N N-channel power MOSFET and BY249 general purpose rectifier diode. The type of power MOSFET is selected so that the total time for it to transition between on and off states is insignificant comparing to the switching period. While both devices have a maximum voltage rating of at least 200 V, the converter output is limited to operation at 100-volt DC maximum so that all transient tests including those with high voltage overshoots can be conducted.

As shown in Figure 7.6, the power MOSFET is driven by the TD351 gate driver and isolated by the 74OL6000 opto-coupler from the logic control circuitry; they are powered by 15-volt and 5-volt isolated supplies respectively. The opto-coupler has a TTL output and hence, output V_{CC} is clamped at 5V by a zener

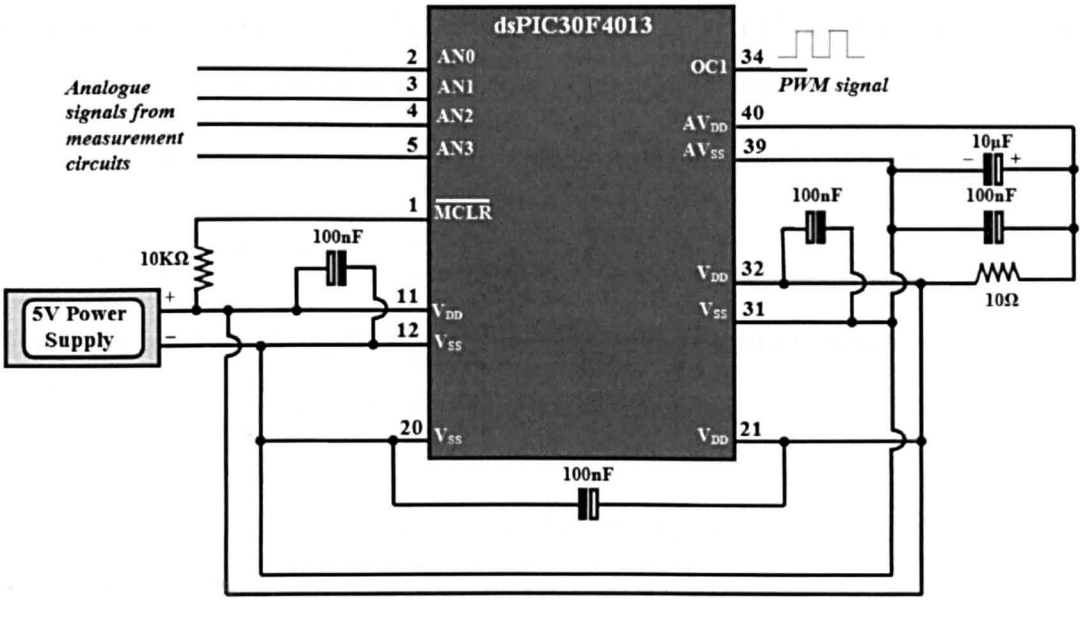

Figure 7.5 External circuit connections for dsPIC30F4013 micrcontroller

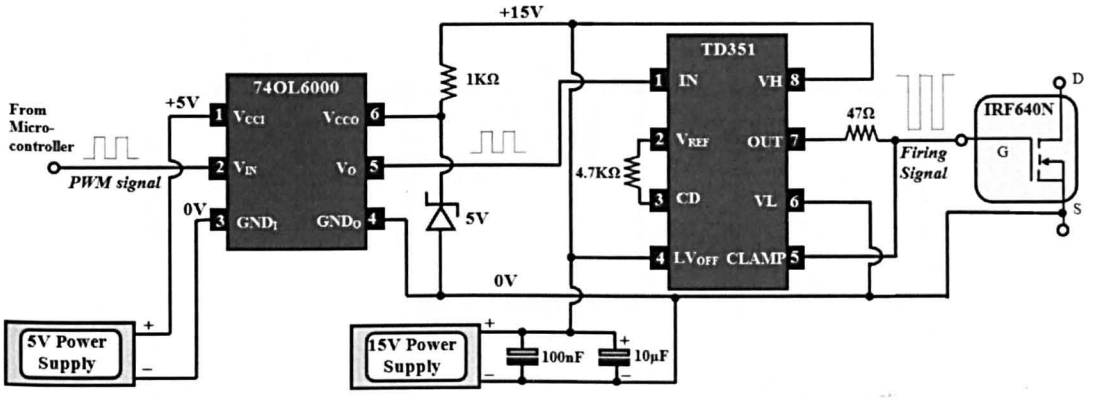

Figure 7.6 Gate switching circuit consisting an opto-coupler and a gate driver

diode. Decoupling has also been provided by having a 100 nF ceramic capacitor and a 10 μF electrolytic capacitor across the gate-drive supply [106]. The driver then interfaces with the MOSFET gate via a current limiting resistor of 47 Ω. To avoid the effect of unwanted noises on the PWM signal applied to the gate, a short link is required between MOSFET source and the driver ground.

7.2.3 Converter Circuit Design

A non-ideal Ćuk converter circuit shown in Figure 7.7 is used. This includes equivalent series resistance (ESR), r_{cn} and r_{co}, for the capacitor and the DC resistance (DCR), r_{L1} and r_{12}, for the inductors. This section describes the modification needed for the design equations of L_1 and C_o so that a practical Cúk step-down converter circuit can be accurately implemented.

For selecting L_1, r_{L1} causes a voltage drop and this can be written as

$$V_{rL1} = r_{L1} I_1 = K \frac{V_o}{R} r_{L1} \tag{7.1}$$

Thus the peak-to-peak input current during the switch turn-on period is now given as

$$\Delta i_1 = \frac{K}{L_1 f_s}\left[V_1 - V_o\left(1 + K\frac{r_{L1}}{R}\right)\right] \tag{7.2}$$

Factor r_{L1}/R can be determined according to the practical load resistance and practical inductor for the type of application considered. Thus for a given operating condition, L_1 can be determined based on the desired maximum value for Δi_1.

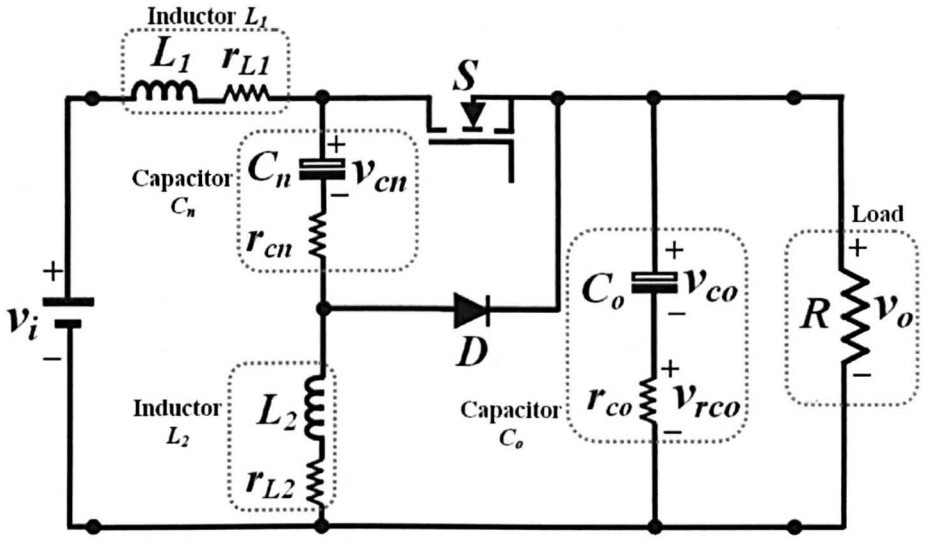

Figure 7.7 Ćuk step down converter circuit with non-ideal components

For selecting C_o the magnitude of the output voltage ripple is expressed as [107]

$$\Delta v_o = \Delta v_{co} + \Delta v_{rco} = \Delta i_o \left(\frac{1}{8 C_o f_s} + r_{co} \right) \tag{7.3}$$

where Δv_{co} and Δv_{rco} are the ripple voltage magnitudes generated by C_o and its ESR, r_{co}, respectively. Δi_o in (7.3) equals to $\Delta i_1 + \Delta i_2$ and Δi_2 is determined by the expression

$$\Delta i_2 = \frac{K}{L_2 f_s} \left[V_{cn} - V_o \left(1 + (1-K) \left(\frac{r_{L2} + r_{Cn}}{R} \right) \right) \right] \tag{7.4}$$

Substituting Δi_o in (7.3) by the sum of Δi_1 (Equation (7.2)) and Δi_2 (Equation (7.4)), we have

$$\Delta v_o = (\Delta i_1 + \Delta i_2) \left[\frac{1}{8 C_o f_s} + r_{co} \right] \tag{7.5}$$

Similar to the ideal case in Chapter 3, designing C_o according to Equation (7.5) is difficult since it requires both Δi_1 and Δi_2 . However C_o can be pre-evaluated using Equation (7.3) according to the required Δv_o, load R, switching frequency f_s and desired r_{co}. C_n and L_2 are then designed according to the design procedure in Section 3.4.2. With the L_2, Δv_o is evaluated and retuning of C_o and L_2 may be needed by using Equation (7.5) and the procedure in Section 3.4.2. The above process can be

repeated until Δv_o and the transient cost function E (Equation 3.30) are below the defined limits.

7.2.4 Practical Verification of the Converter Design Scheme

The converter prototype is powered by a 60-volt DC source, and according to the device ratings can deliver 180 W of power to the load. The ripple requirements for both input current and output voltage are $\leq 5\%$.

Based on the output voltage and input current ripple requirements, L_1 is initially set to 10 mH and C_o to 10.0 μF for $K = 0.5$. For L_2 and C_n, a set of cost function values is evaluated as described in Section 3.4.2. Figure 7.8 shows the variations of E value for C_n changing from 0.5 to 6.5 μF and L_2 from 0.75 to 3.5 mH using a 3-D plot as shown in Figure 7.8(a) and its corresponding plane view in Figure 7.8(b). In both diagrams, the E values are plotted against the ratios, C_n/C_o and L_2/L_1.

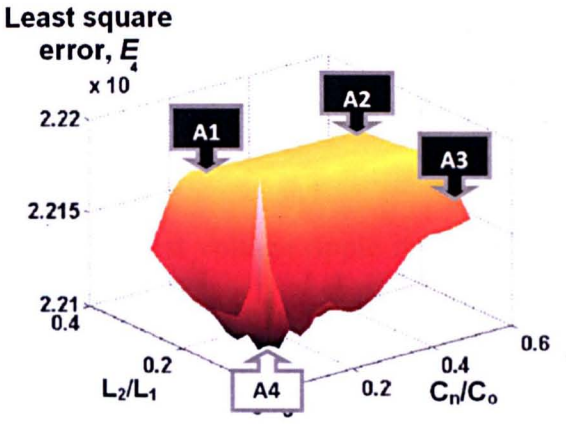

(a) 3-D plot

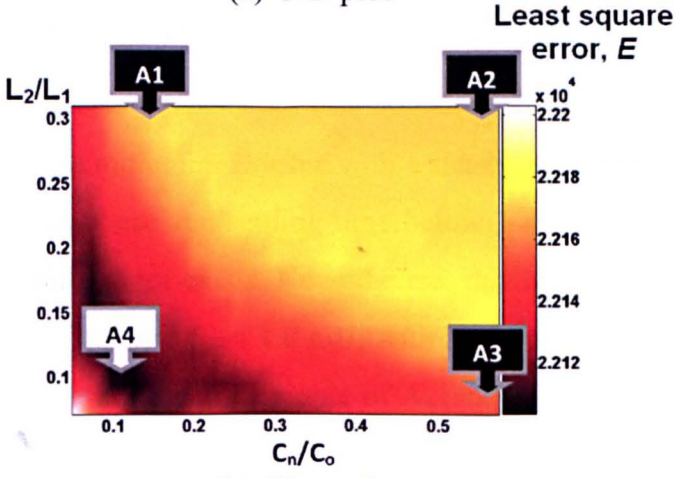

(b) Plane plot

Figure 7.8 Performance evaluation for a practical Ćuk step-down converter

As can be observed, E decreases with the reduction of both L_2 and C_n. In particular, the trough is where C_n/C_o lies between 0.075 to 0.14, i.e., C_n ranging from 0.75 to 1.4 μF, and L_2/L_1 between 0.08 to 0.15, i.e., L_2 ranging from 0.8 mH to 1.5 mH. The lowest E value in this case occurs at the point notated as A_5 with L_2 = 1.0 mH and C_n = 1.0 μF.

Using the four different sets of components in the practical converter circuit, chosen according to their E values as shown in Figure 7.8 at points A_1 to A_4, the corresponding transient and steady state responses are compared, by both simulation and experiment.

The measured output voltage responses for five different cases due to the same pattern of duty ratio change are shown in Figures 7.10 (a)-(d). The experimental waveforms are in close agreement with the simulated ones which are shown in 7.9(a)-(d).

For case A_1, L_2 = 6 mH and C_n = 2 μF. The steady state ripple magnitude is much smaller than the desired 5-percent. However, the transient response shows a large overshoot of 6 % and it takes a relatively long time of about 5.1 ms to settle into the steady state.

Case A_2 has the smallest voltage ripple magnitude. However the overshoot is above 7 % and it takes more than 5 ms to settle down. In addition, the E value is the highest among all the cases.

Case A_3 has a ripple magnitude of just below the 5% limit. The response is less oscillatory than the previous two cases and takes less time to settle down but it still has a high overshoot.

Case A_4 gives the minimum E value with a steady state ripple of within 5%, an adequately damped response and settling time below 3 ms. The trade-off for this is that an amount of undershoot exists. Nevertheless, this has the best performance of the four when C_n = 1.0 μF and L_2 = 1.0 mH, with both having about one tenth of C_o and L_1. In addition, the input current ripple of A_4 remains within the 5-percent limit as shown in Figure 7.11.

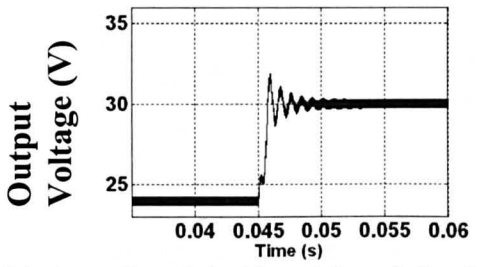

(a) $A_1 - C_n = 2.0$ μF and $L_2 = 3.0$ mH

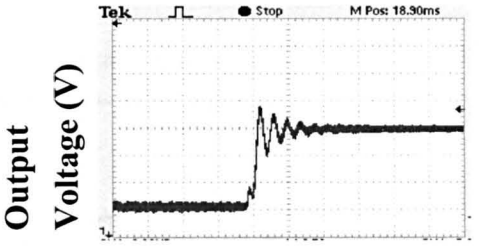

(a) $A_1 - C_n = 2.0$ μF and $L_2 = 3.0$ mH

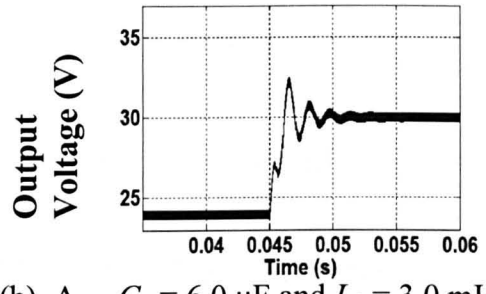

(b) $A_2 - C_n = 6.0$ μF and $L_2 = 3.0$ mH

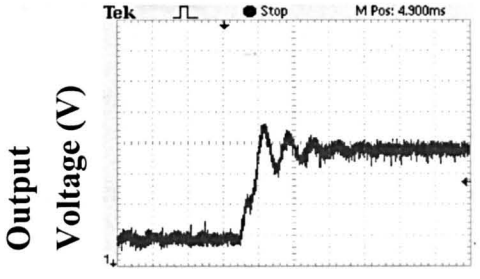

(b) $A_2 - C_n = 6.0$ μF and $L_2 = 3.0$ mH

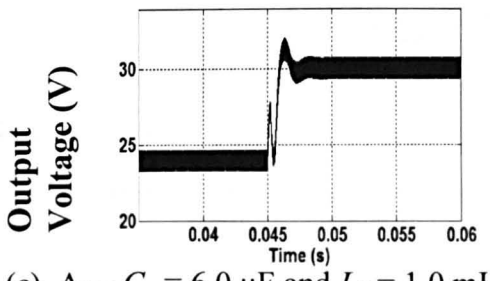

(c) $A_3 - C_n = 6.0$ μF and $L_2 = 1.0$ mH

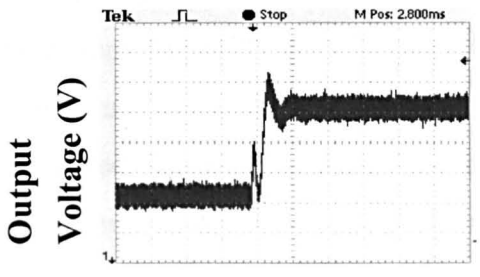

(c) $A_3 - C_n = 6.0$ μF and $L_2 = 1.0$ mH

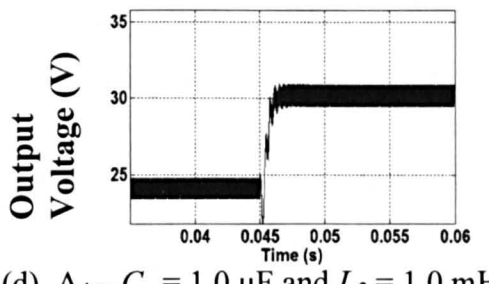

(d) $A_4 - C_n = 1.0$ μF and $L_2 = 1.0$ mH

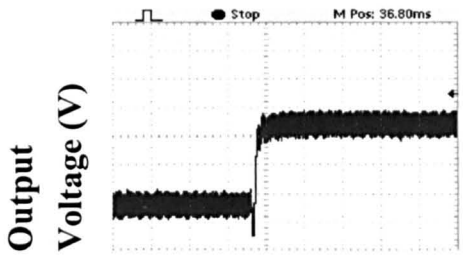

(d) $A_4 - C_n = 1.0$ μF and $L_2 = 1.0$ mH

Figure 7.9 Simulated transient responses due to duty ratio variation for various pairs of L_2 and C_n

Figure 7.10 Experimental transient responses due to duty ratio variation for various pairs of L_2 and C_n

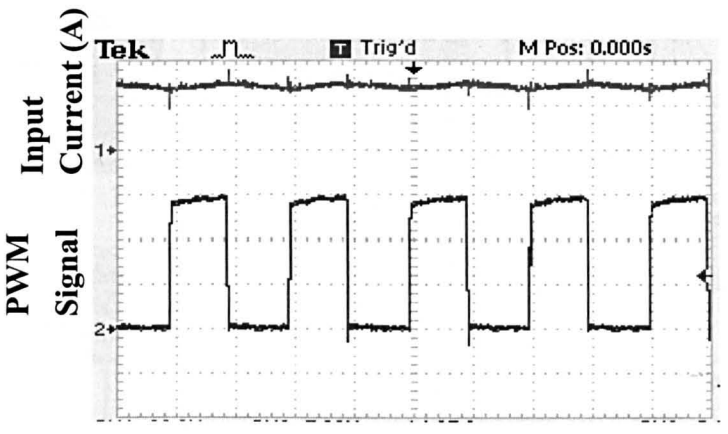

Figure 7.11 Experimental waveform of input current corresponding to PWM signal

7.3 Model-Based Control for a Practical PV Generator

Figures 7.12(a) and 7.12(b) illustrate the configuration and the photographic images of the experimental setup used for controlling the MPP of a PV generator. A number of sensory circuits are employed to measure the weather conditions under which the PV generator operates. The measured signals are then sent to the microcontroller which applies the modelling technique described in Chatper 6 to compute the optimal MPP voltage. A PWM with desired duty ratio is then generated by the microcontroller and used to regulate the input terminal voltage of the DC-DC Ćuk step-up converter. This section describes the implementation for this setup and the evaluation of the designed control scheme.

7.3.1 PV Generator and Solar Simulator

The 20-Watt PV module described in Chapter 6 is used for the setup shown in Figure 7.12. In this experimental work, the implemented PV model will be tested for various operating weather conditions. This is mainly limited by the unpredictable weather in UK. Hence, the Solar Simulator used by the author in [83] can be employed. As illustrated in Figures 7.13(a) and 7.13(b), the PV module is laid under this simulator having three rows of five 100-Watt daylight lamps. A dimmer is also included in the lighting circuit so that the irradiance level can be adjusted accordingly.

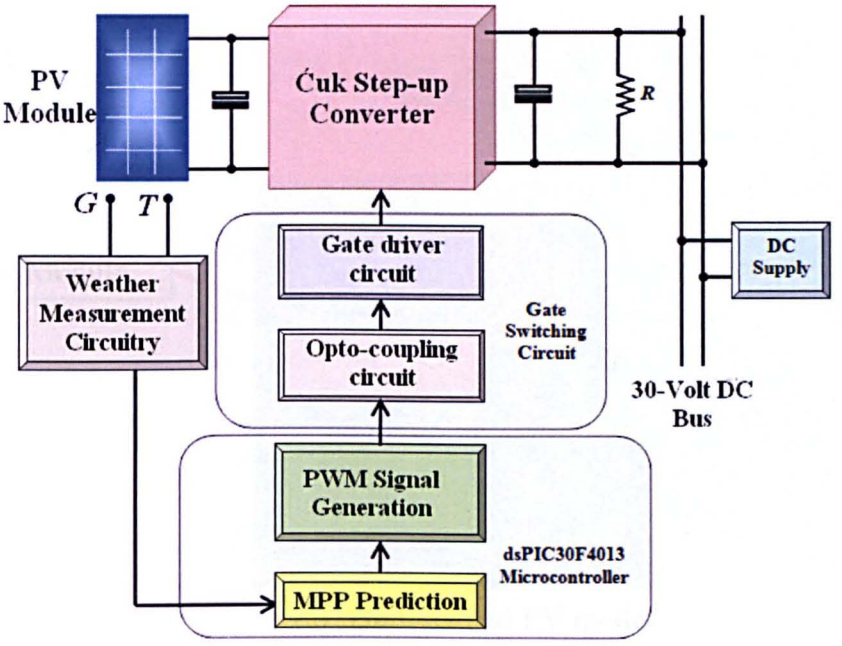

(a) Configuration for the experimental setup

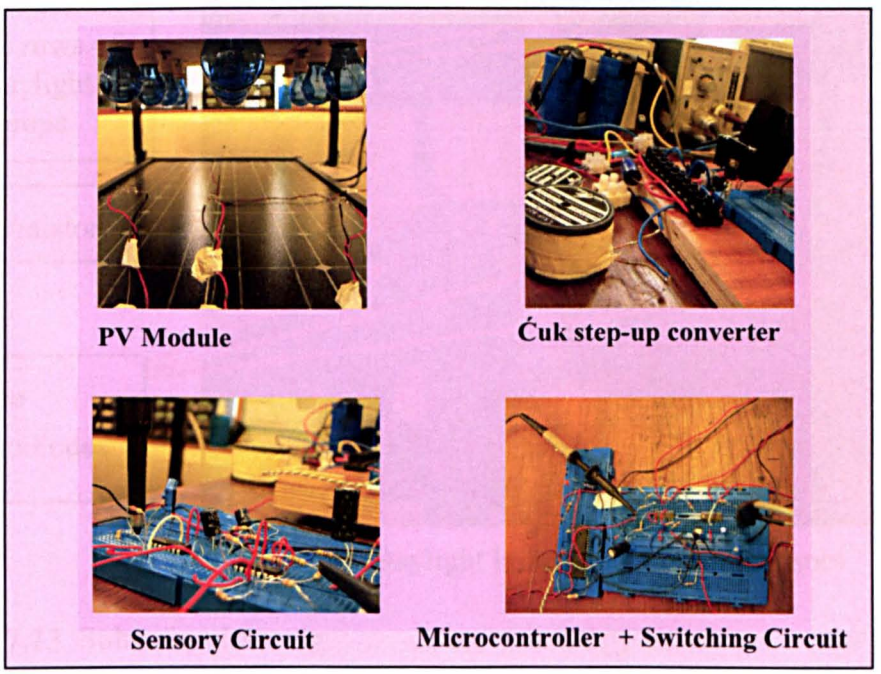

(b) Photographic images for the experimental setup

Figure 7.12 Experimental setup for the MPPT control of a practical PV module

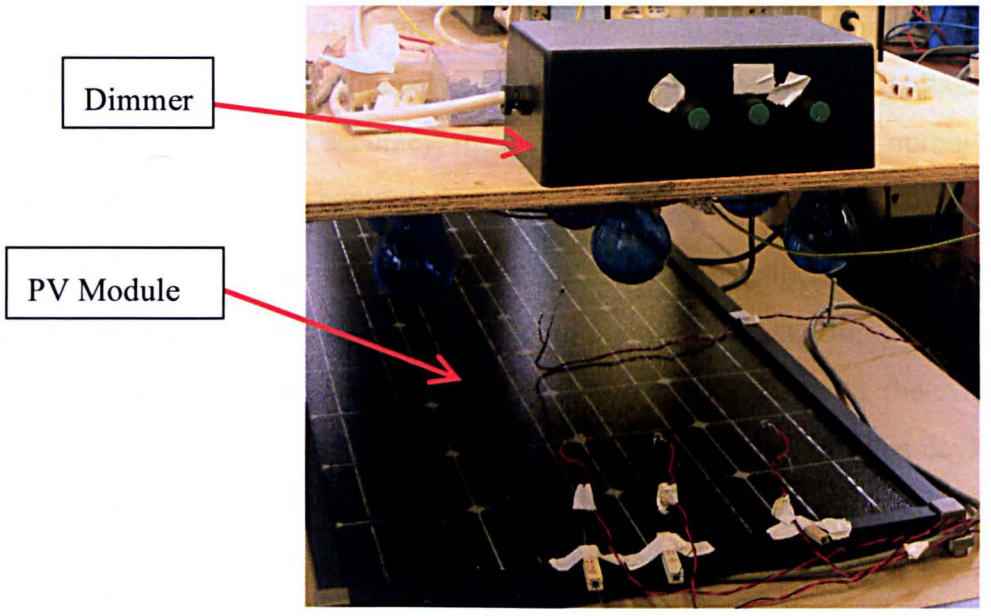

(a) Dimmer and PV module

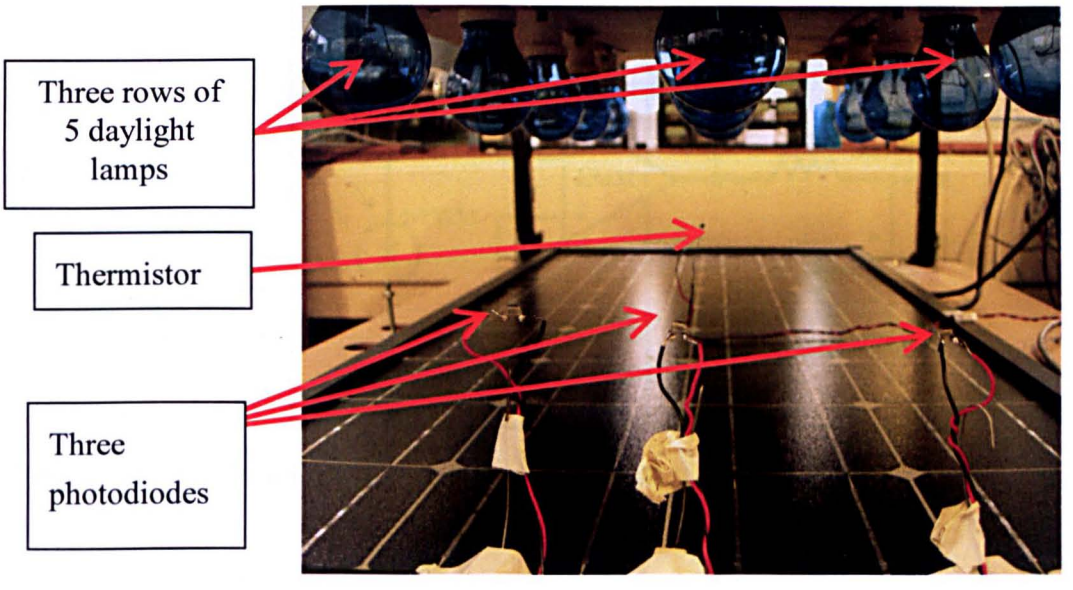

(b) Daylight lamps and weather sensors

Figure 7.13 Solar simulator rig

7.3.2 Weather Measurement Circuits

In order to evaluate the PV modelling scheme, two types of measurements are necessary; namely Light Intensity and Cell Temperature. Their sensors are mounted in the vicinity of the PV module as shown in Figure 7.13(b).

Three BPW34 Silicon PIN photodiodes are used to measure the light intensity level on the PV module. As shown in Figure 7.14, each photodiode is connected to an operational amplifier (op-amp) circuit which is used to limit the voltage to vary between only 0 and 5V (corresponding to the previously configured voltage range

for the ADC) [83]. While the induced-current from the photodiode changes according to the light intensity level, the op-amp output voltage varies proportionally. For higher accuracy, the average of the three sensors' output voltages is taken for the duty cycle computation.

An NTC thermistor is used to measure the cell temperature. As shown in Figure 7.15, the thermistor is connected to an amplifier based scaling circuit so that the operating cell temperature range (10 – 40°C) corresponds to the ADC input voltage range (0 – 5V). As the temperature rises, the resistance of this device drops [108] and hence, the voltages at the non-inverting terminal as well as the output of the op-amp are decreasing. The above measured signals from the weather sensory circuits are then fed to the microcontroller for MPP voltage prediction.

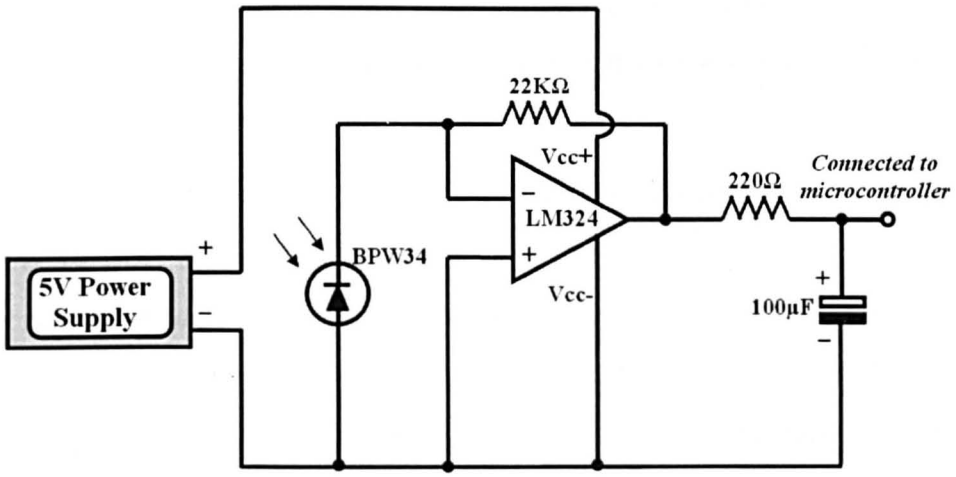

Figure 7.14 Light intensity measurement circuit

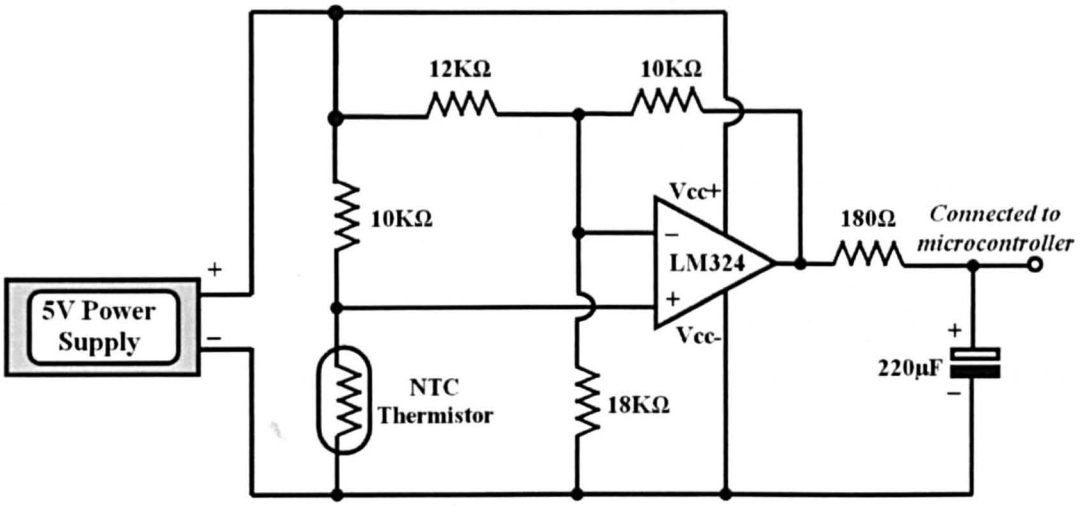

Figure 7.15 Cell temperature measurement circuit

7.3.3 Microcontroller-based Implementation of PV Model

Using the modelling technique designed in Chapter 6, the computation of PV current for the corresponding weather condition and PV voltage, involves numerous arithmetic operations. These computations can be performed by the dsPIC micrcocontroller using either its arithmetic logic unit (ALU) or the digital-signal-processing (DSP) based engine [109]. The latter is desirable as it works with variables expressed in the fixed-point number format which enables computation to be performed quickly while maintaining high accuracy. This format represents a real-valued variable by a signed 32-bit integer which in general can be expressed as $b_{31}b_{30}b_{29}.....b_{16}b_{15}.....b_1b_0$. There are two groups of bits in this integer. The first group consisting of the bits from b_{16} to b_{30} is used to represent the integer part of a real-valued number while its fractional part is represented by the other group of bits from b_0 to b_{15}. The most significant bit is b_{31} which has a value of 0 for a positive number and 1 for a negative number.

Therefore, the conversion of any variable into its equivalent fixed-point format can be done by multiplying it with $2^{16} = 65536$, and dividing by this factor for the reverse operation. For example, a variable having a real value of 15.0625 has the equivalent fixed point integer which can be expressed in the hexadecimal form as 000F 1000. A wide range of values can then be converted into this type of fixed-point form; i.e. from 2^{-16} to $(2^{15} - 2^{-16})$ for positive numbers, and from -2^{15} to -2^{-16} for negative numbers. This becomes the key attraction of the computation of numbers using the DSP engine unit in a microcontroller. In addition, the conversion process has a degree of precision since the value of any number converted back from its fixed-point form may differ by not more than 2^{-16} unit. Such an amount is negligible considering the ranges of voltage, temperature and solar insolation under which the PV system is operating.

The advantage of expressing a variable in fixed-point format over other methods which use floating-point form can also be demonstrated through a preliminary study focusing on a function, f given by

$$f = 1293.141592 \times a + 0.01 \tag{7.6}$$

where a has a range of values from 0.001 to 10. In this study, the function in Equation (7.6) is evaluated using both fixed-point as well as floating-point formats and a comparison can be made for the computational speed. To achieve this, the calculations were implemented and debugged in MPLAB IDE software. It can be observed from Table 7.1 that fixed-point computation takes equal amounts of time throughout the overall range of a values and is at least 5 times faster than that using floating point. This is because for a fixed point system, the in-built function, MAC, can be executed and hence, arithmetic operations including multiplication and addition can be carried out simultaneously.

To employ the DSP engine unit for computing the desired MPP voltage, all data including the model parameters and the inputs sampled by the ADC are firstly converted to the fixed-point format. By iteratively applying the PV model described in Chapter 6, a set of current-voltage pairs is obtained based on the given weather conditions. The voltage which gives the highest power is selected as the MPP voltage and its equivalent real value is used to compute the required duty ratio for the PWM signal. The above implementation of MPP control scheme on the dsPIC microcontroller is summarized in the flowchart as shown in Figure 7.16.

7.4 Verification of the Control Scheme

Using the experimental prototype, two tests were undertaken to demonstrate the accuracy and high performance of the MPP control using the modelling-based method as described in Chapter 6.

Table 7.1 Performance evaluation for fixed-point and floating-point calculations

Parameter *a*	**Time taken for fixed-point calculation**	**Time taken for floating-point calculation**
10.000	2.2 μs	13.1 μs
1.000	2.2 μs	12.9 μs
0.10	2.2 μs	11.6 μs
0.01	2.2 μs	10.6 μs
0.001	2.2 μs	9.8 μs

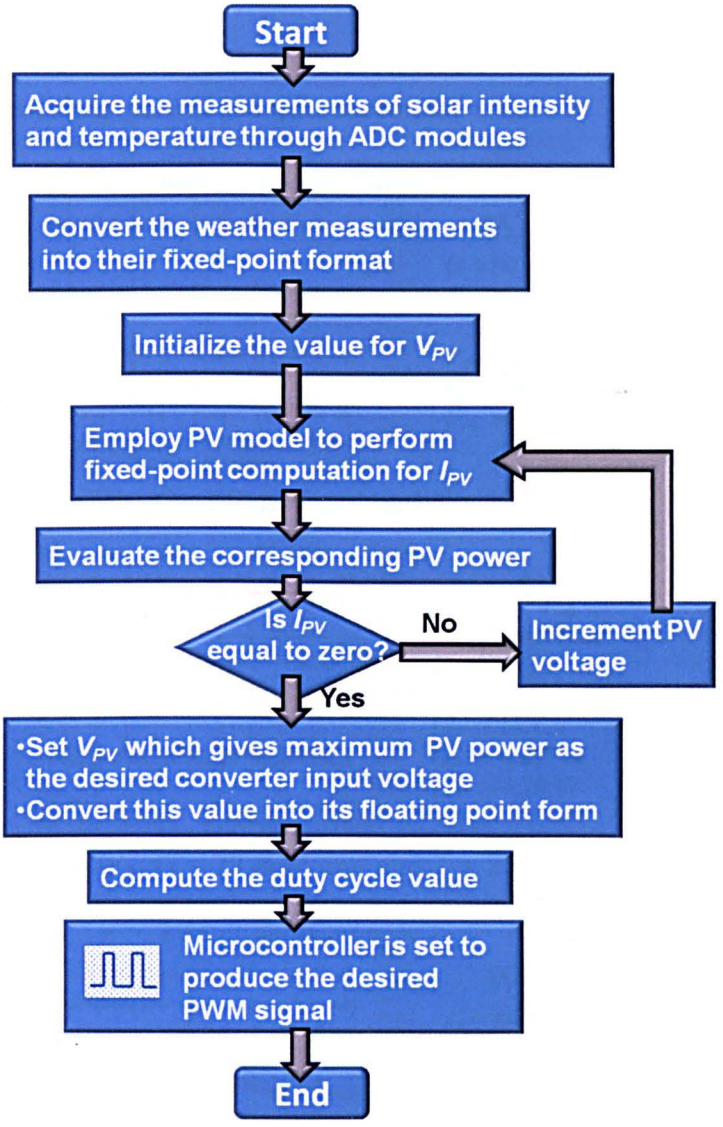

Figure 7.16 Flowchart for MPP voltage computation using PV model implemented on dsPIC microcontroller

7.4.1 Evaluation based on Accuracy

Figures 7.17(a), (b), (c) and (d) show the measured values of PV voltages, currents and powers under four different weather conditions. It can be observed from the experimental responses that a decrease in PV voltage, for instance, leads to an increase in current, conforming to the I-V characteristics of a typical PV module. The spikes present in the current and voltage responses are due to the fact that a high voltage is generated across the stray inductance (which can be found around the non-ideal connectors and power devices) as the MOSFET transitions between switch turn-on and turn-off states. For each weather condition, the mean values for the voltages, currents and powers over a switching period are listed to right side of the responses in Figure 7.17.

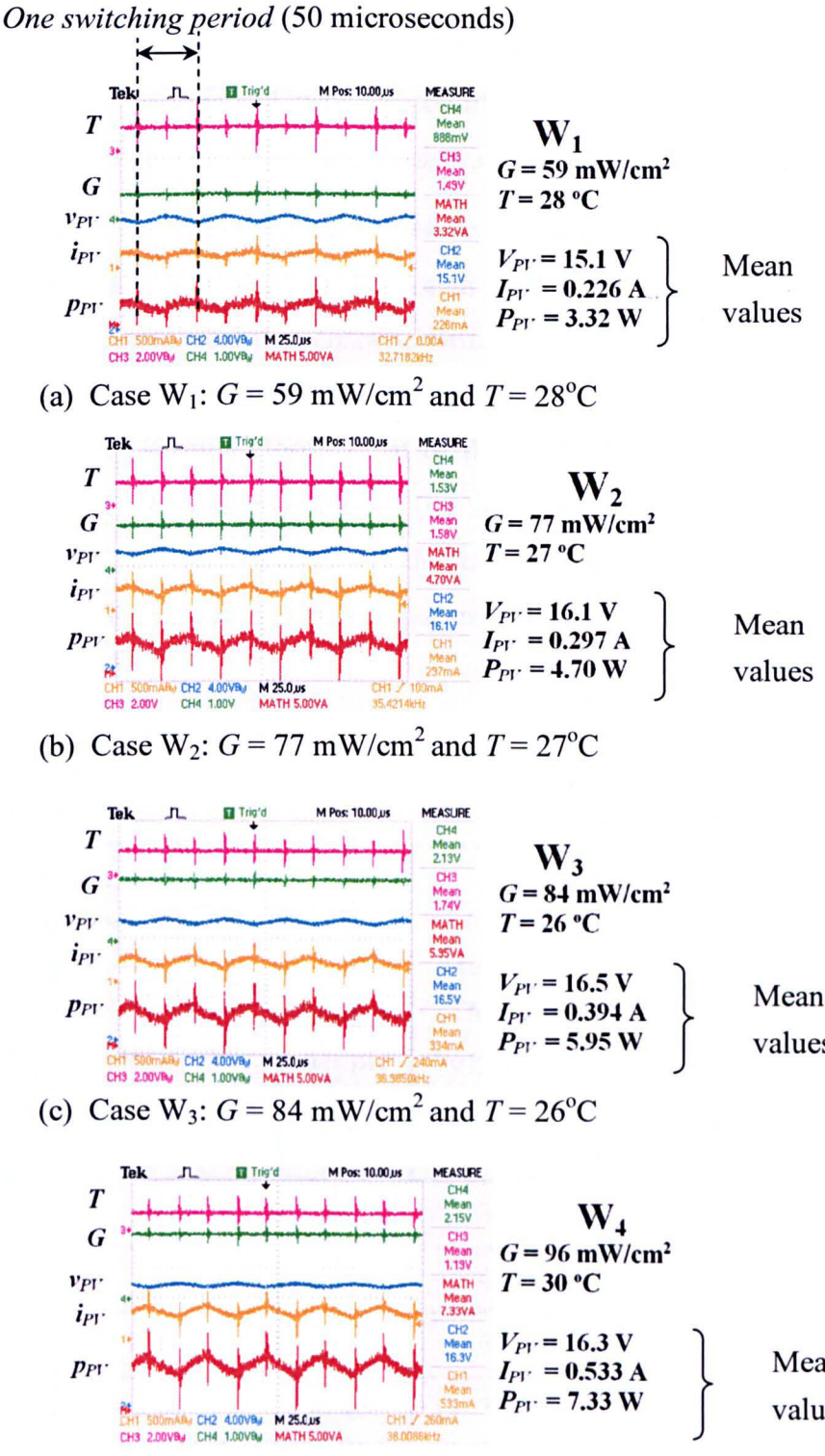

Figure 7.17 Steady-state responses of the PV generator with MPPT control under various weather conditions

The converter input capacitor (which is connected across the PV module) is chosen such that the steady-state PV voltage ripple requirement (i.e. below 7%) is satisfied and hence as listed in Table 7.2, the peak-to-peak ripples for v_{pv} are found to be less than 7% under all weather conditions. Note the voltage ripples were calculated based on the corresponding mean values of PV voltages.

In addition, the measured mean power values can also be compared to the values of the total power that can be drawn from the PV module. The latter are extracted from the practical P-V characteristics in Figure 7.18 which were obtained through the data collection in Chapter 6. As can be observed, the power extracted from the generator is quite close to that of the MPP level. The highest difference between them for all weather conditions (i.e. from W_1 to W_4) is 6% when the solar insolation is 96 mW/cm^2 and while the cell temperature is 30°C, the lowest difference is about 3.8% when the solar insolation is 59 mW/cm^2 and the cell temperature is 28 °C.

Table 7.2 Comparison between power extracted and the power available from the PV module

Weather Conditions		**PV Voltage Ripple (%)**	**Measured Mean Power (W)**	**Power that can be drawn from the PV module (W)**	**Power Loss (%)**
Solar Insolation (mW/cm^2)	**Cell Temperature (°C)**				
59	28	6.95	3.32	3.5	5.1
77	27	6.70	4.70	4.9	4.1
84	26	6.50	5.95	6.2	3.8
96	30	6.45	7.33	7.8	6.0

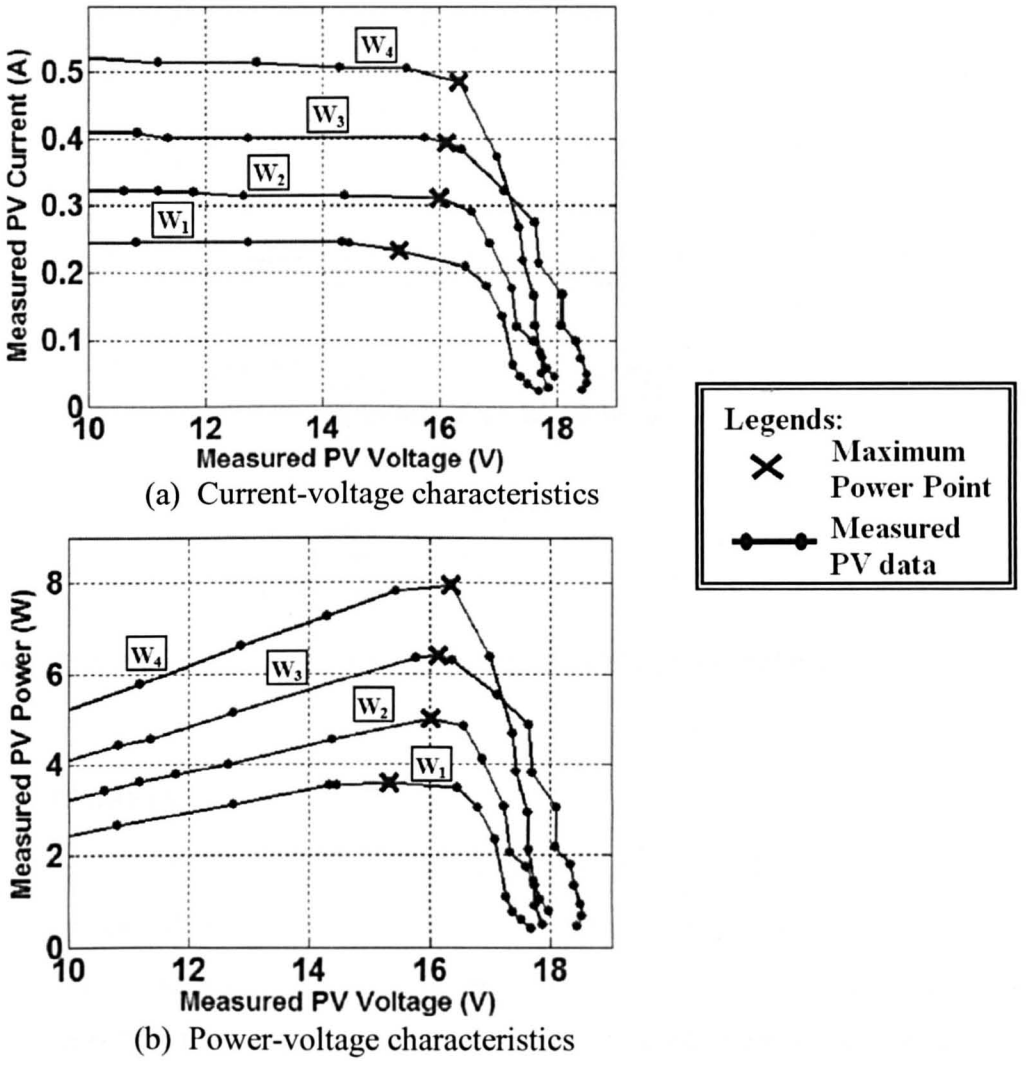

(a) Current-voltage characteristics

(b) Power-voltage characteristics

Figure 7.18 Electrical characteristics of the PV generator:

7.4.2 Evaluation based on Performance

Further tests are also performed for rapidly changing weather conditions. Figure 7.19 shows the response of the PV voltage when the light intensity is changing (from G_H = 96 to G_L = 55 mW/cm^2 and vice versa) at about every time interval of one second. This time interval is chosen considering the realistic variation of solar intensity [85]. During the transient response, there is a negligible overshoot and hence sufficient damping has been provided. In addition, the microcontroller can promptly respond to the weather change and hence quickly track the MPPs.

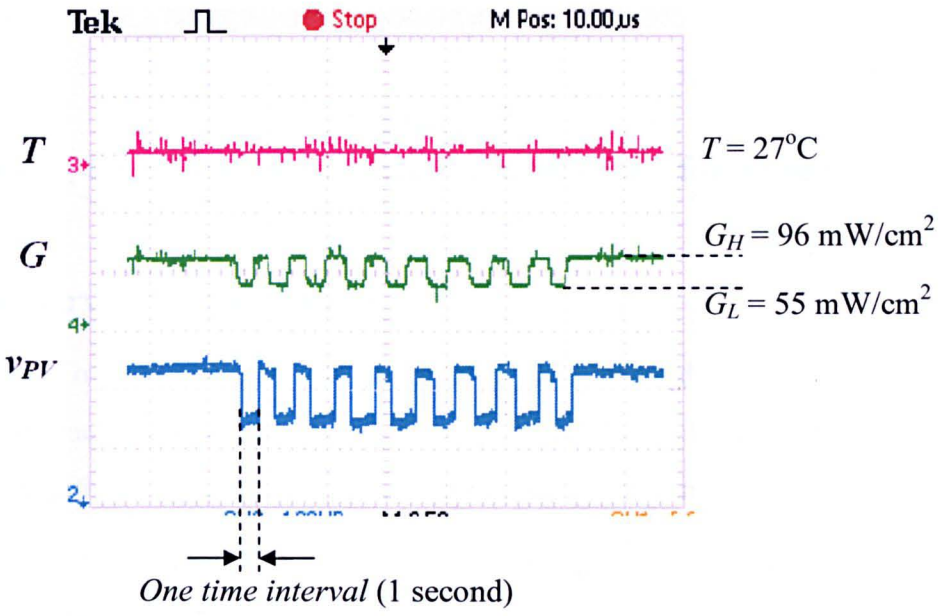

Figure 7.19 Response of PV voltage to rapidly changing weather conditions

7.5 Summary

A practical Ćuk step-down converter has been developed using the design scheme proposed in Chapter 3. Test results for four different sets of components have been shown and compare well with those from the simulation. It has been demonstrated that the steady state ripples for the input current and output voltage satisfy their defined limits.

The practical PV model based on a PSO plus Neural-Fuzzy network technique proposed in Chapter 6 has also been implemented practically on a dsPIC microcontroller. This model has been applied for predicting the desired operating point corresponding to the maximum power operation for a given weather condition. Based on this information, the microcontroller adjusts the duty ratio of the Ćuk step-up converter such that the MPP voltage across the PV module can be obtained. The model is tested for four different weather conditions, and on average, the difference between the maximum power extracted and that which can be drawn from the module is 0.27 W or 1.35% (based on its output power rating). In addition, it has been demonstrated that the maximum power prediction can be done sufficiently fast, so as to enable the PV to operate optimally, even under rapidly changing insolation conditions.

Chapter 8
Summary, Conclusions and Recommendations for Future Work

8.1 Summary and Conclusions

The aim of this research was to develop an integrated PV-converter system which can extract the maximum power from an array of PV modules under all types of weather conditions, particularly inhomogeneous distribution of irradiation.

This aim has been achieved successfully in that a novel integrated PV-Ćuk converter system has been proposed, and together with its model-based control scheme the proposed system offers an increase power output by up to 32%, compared to the conventional method of using bypass diodes. This thesis presented a detailed description of the major achievements and contributions made in this work, which are summarised as follows:

- A detailed understanding of a PV solar cell operating under homogeneous and inhomogeneous distributions of irradiation has been demonstrated. A complete simulation model has been developed for representing the electrical characteristics of a PV module. It has been demonstrated that bypass diodes can prevent potentially damaging power dissipation in a shaded module, but it has been shown that not all available solar power can be extracted from the system with this method.

- Various converter configurations and the schemes for controlling the MPP of multiple PV modules under partial shading conditions have been investigated. The PV-Ćuk converter was found to efficiently lead all PV modules to MPP generation, regardless of the inhomogeneous distribution of irradiation.

- A significant contribution to this work has been the development of a comprehensive control technique for the converters in the integrated system. This has not been seen in any previous literature report. In this thesis, the issue of selecting the operating modes for the integrated PV-Ćuk converters has been addressed for the first time by only using ambient weather conditions. The duty ratios of the converters are regulated using the modelling-based

approach, and a novel set of co-ordinated control strategies were presented for both the inner and terminal converters. Compared to the conventional method using the bypass diode, the output power extracted using the proposed scheme is increased by as much as 160 W or 32%.

- The application of the P&O algorithm to the MPP control for the integrated PV-Ćuk converters has been investigated. It has been shown that this method leads to a more oscillatory and slower voltage response than the proposed modelling-based technique.

- A comprehensive study of the Ćuk step-down and Ćuk step-up converters has been undertaken, deriving generalised transfer function models for two different operating modes; constant input voltage – variable output voltage, and variable input voltage – constant output voltage. The latter has been shown to exhibit a response that has a non-minimum phase feature when there is a switch duty ratio variation.

- A novel method for selecting the energy storage components in the Ćuk converters has been developed. This is based on minimising the time-integrated squared errors between the desired and actual output voltages, in addition to, suppressing the steady state current and voltage ripple percentages to below a desired level. A converter has been designed and tested experimentally, and the design procedure is shown to work well for both operating modes. However when controlling the terminal voltage of a PV panel, and to achieve both fast and well-damped MPP searching, the duty ratio of the converter can only vary within a narrow range determined by the I-V characteristics of the PV module under specific weather conditions.

- Based on the developed transfer function models, a phase lead-lag closed-loop controller has been developed for a Ćuk step-up converter. This shortened the transient interval of the input voltage responses for lower duty cycle values, while at the higher end of the duty ratio range, more damping can be added for the responses. The converter has been applied to the proposed PV system and since it has a fast and stable response, all operating conditions including rapidly changing weather variation can be analyzed and optimised.

- A novel technique has been applied for representing the PV characteristics using Particle-Swarm-Optimization applied to a Neuro-Fuzzy network. The developed PV model has a compact structure, an interpretable set of rules and ultimately is accurate in predicting the output values for given input samples. The proposed PV model has been applied for re-constructing a set of practical I-V characteristics and it has been shown to compare well with the measured values. The entire training process takes about 2 minutes and 29 seconds which is half the time taken by the genetic-algorithm based technique in the previous research to model the same PV module. The proposed model can also be used to predict MPP points and the errors obtained, on average, are about four times less than those using the previous genetic-algorithm-based model.
- The proposed PV model has been implemented practically on a dsPIC microcontroller and assessed through its application to the MPP control of a practical PV module. The difference between the actual power extracted from the module and the maximum possible is only 1.35% at most.

8.2 Recommendations for Future Work

Proposed future work on this subject is as follows:

- A PV module itself may be in homogenously irradiated and therefore, the power extracted may not be the maximum. The associated control design proposed in this thesis can be expanded to include the scheme for enabling the module to operate at its global maximum power point. This involves either re-designing of the artificial-intelligence model or the application of other MPP tracking algorithms.

- Other environmental conditions, humidity level, and wind speed which may affect the PV power output and can also be taken as inputs for the PV model designed in this thesis. In addition, the model could be expanded to consider information about the severity of the inhomogeneous irradiation on the PV module. After a period of time, the module can degrade and its electrical characteristics may change. Therefore, an online data logging system could be developed to implement online modelling. All the relevant algorithms can be incorporated into the microcontroller employed in this thesis.

- When there is a slight difference between the irradiances in two PV modules, the integrated Ćuk converters may operate in discontinuous conduction mode. Thus, the converter design and its control scheme could also consider the performance of this non-linear operation mode.

References

1. "Renewable Energy Scenario to 2040", European Renewable Energy Council, May 2004, Available: http://www.erec-enewables.org/documents/targets_2040/EREC_Scenario%202040.pdf.
2. Smits, F.M., "History of Silicon Solar Cells", IEEE Transactions on Electron Devices, Vol. 23, No. 7, July 1976, pp. 640 – 643.
3. Rauschenbach, H.S., "Electrical Output of Shadowed Solar Arrays", IEEE Transactions on Electron Devices, Vol. 18, No. 8, August 1971, pp. 483 – 490.
4. Wolf, M., "Outlook for Si Photovoltaic Devices for Terrestrial Solar-energy Utilization", Journal of Vacuum Science and Technology, Vol. 12, No. 5, September 1975, pp. 984 -999.
5. Bishop, J.W., "Computer Simulation of the Effects of Electrical Mismatches in Photovoltaic Cell Interconnection Circuits", Solar Cells, Vol. 25, No. 1, October 1988, pp. 73 – 89.
6. Ossenbrink, H., and Sample, T., "Results of 12 Years of Module Qualification to the IEC 61215 Standard And CEC Specification 503, 3rd World Conference on Photovoltaic Energy Conversion, May 2003, pp 1882 – 1887.
7. Van der Borg, N.J.C.M., and Jansen, M.J., "Energy loss due to Shading in a BIPV Application", , 3rd World Conference on Photovoltaic Energy Conversion, May 2003, 2220 – 2222.
8. Walker, G.R., and Sernia, P.C., "Cascaded DC-DC Converter Connection of Photovoltaic Modules", IEEE Transactions on Power Electronics, Vol. 19, No. 4, July 2004, pp. 1130 – 1139.
9. Walker, G.R., and Pierce, J.C., "Photovoltaic DC-DC Module Integrated Converter for Novel Cascaded and Bypass Grid Connection Technologies – Design and Optimisation", 37th IEEE Power Electronics Specialists Conference, June 2006, pp. 1 – 7.
10. Femia, N., Lisi, G., Petrone, G., Spagnuolo, G., and Vitelli, M., "Distributed Maximum Power Point Tracking of Photovoltaic Arrays: Novel Approach

and System Analysis", IEEE Transaction on Industrial Electronics, Vol. 55, No. 7, July 2008, pp. 2610 – 2621.

11. Erge, T., Hoffmann, V.U., and Kiefer, K., "The German Experience with Grid-connected PV-Systems", Solar Energy, Vol. 70, No. 6, 2000 pp. 479 – 487.

12. Quaschning, V., and Hanitsch, R., "Numerical Simulation of Current-Voltage Characteristics of Photovoltaic Systems with Shaded Solar Cells", Solar Energy, Vol. 56, No. 6, 1996, pp. 513 – 520.

13. Hassaine, L., Olias, E., Quintero, J., and Haddadi, M., "Digital Power Factor Control and Reactive Power Regulation for Grid-Connected Photovoltaic Inverter", Renewable Energy, Vol. 34, 2009, pp. 315 – 321.

14. Pregelj, A., Begovic, M., and Rohatgi, A., "Impact of Inverter Configuration on PV System Reliability and Energy Production", IEEE 24th Photovoltaic Specialists Conference, May 2002, pp. 1388 – 1391.

15. "Reliability Study of Grid Connected PV Systems – Field Experience and Recommended Design Procedure", Report IEA-PVPS T7-08: 2002, March 2002, (Available at: http://iea-pvps.org/products/download/rep7_08.pdf)

16. Ćuk, S., and Middlebrook, R.D., "A New Optimum Topology Switching DC-to-DC Converter", PESC' 77 Record, IEEE Power Electronics Specialists Conference 1977, pp. 160-179.

17. Massey, R. P., and Snyder, E. C., "High Voltage Single-Ended DC-DC Converter", PESC' 77 Record, IEEE Power Electronics Specialists Conference 1977, pp. 156-159.

18. Martins, D.C., de Abreu, G.N. and Barbi, I., "ZETA-GEPAE PWM Isolated DC/DC Converter Analysis", Proceedings of 1st COBEP '91, December 1991, pp. 154-159.

19. Mohan, N., Undeland, T.M., and Robbins, W.P., "Power Electronics: Converters, Applications and Design", John Wiley & Sons Inc., New York, USA, 2nd Edition, 1995.

20. Tymerski, R., and Vorperian, V., "Generation, classification and analysis of switched-mode, dc-to-dc converters by the use of converter cells", Conference Proceedings of INTELEC' 86, IEEE International Telecommunications Energy Conference, October 1986, pp. 181-195.

21. Zhang, Z., and Ćuk, S., "A High Efficiency 1.8kW Battery Equalizer", Conference Proceedings of APEC, 8th IEEE Applied Power Electronics Conference and Exposition, March 1993, pp. 221-227.

22. Zhang, Z., and Ćuk, S., "A High Efficiency 500 W Step-up Cuk Converter", Proceedings of IPEMC 2000, 3rd IEEE International Power Electronics and Motion Control Conference, Vol. 2, August 2000, pp. 909-914.

23. Pietkiewicz, A., and Tollik, D., "Small-signal Analysis of a Coupled-inductor Step-down Switching DC-DC Converter", Conference Proceedings of INTELEC '86, IEEE International Telecommunications Energy Conference, October 1986, pp. 241-246.

24. Pietkiewicz, A., and Tollik, D., " Current-mode Control in Coupled-inductor Step-down Switching DC-DC Converter", EPE Proceedings, 2nd European Conference on Power Electronics and Applications, Vol. 1, September 1987, pp. 447-451.

25. Xu, J., "Modelling and Analysis of Switching DC-DC Converter with Coupled-inductor", Conference Proceedings on Circuits and Systems, China 1991 International Conference on Circuits and Systems, Vol. 2, June 1991, pp. 717-720.

26. Babu, C.S., and Veerachary, M., "Predictive Valley Current Controller for Two Inductor Buck Converter", Proceedings of ISCAS '05, IEEE International Symposium on Circuits and Systems 2005, May 2005, Vol. 4, pp. 3075 – 3078.

27. Noguchi, T., Togashi, S., and Nakamoto, R., "Short-Current Pulse-Based Maximum-Power-Point Tracking Method for Multiple Photovoltaic-and-Converter Module System", IEEE Transactions on Industrial Electronics, February 2002, Vol. 49, No.1, pp. 217 – 223.

28. Myrzik, J.M.A, and Calais, M., "String and Module Integrated Inverters for Single-Phase Grid Connected Photovoltaic Systems – A Review", IEEE Bologna PowerTech Conference, Vol. 2, June 2003, pp. 1 – 8.

29. Kajihara, A., and Harakawa, T., "Model of Photovoltaic Cell Circuits under Partial Shading", Conference Proceedings of IEEE International Conference on Industrial Technology, December 2005, pp. 866 – 870.

30. Bratcu, A.I., Munteanu, I., Bacha, S., Picault, D., and Raison, B., "String and Module Integrated Inverters for Single-Phase Grid Connected Photovoltaic Systems – A Review", IEEE Bologna PowerTech Conference, Vol. 2, June 2003, pp. 1 – 8.

31. Zhang, H., Shan, L., Ren, J., Cheng, B.-D., and Zhang, H.-W., "Study on Photovoltaic Grid-Connected Inverter Control System", Conference Proceedings of PEDS 2009, International Conference on Power Electronics and Drive Systems, November 2009, pp. 210 – 212.

32. Enslin, J.H.R., Wolf, M.S., Snyman, D.B., and Swiegers, W., "Integrated Photovoltaic Maximum Point Tracking Converter", IEEE Transactions on Industrial Electronics, Vol. 44, No. 6, December 1997, pp. 769 – 773.

33. Salas, V., Olias E., Barrado, A., and Lazaro, A., "Review of the Maximum Power Point Tracking Algorithms for Stand-alone Photovoltaic Systems", Solar Energy Materials & Solar Cells, Vol. 90, No. 11, July 2006, pp. 1555 – 1578.

34. Phang, J.C.H., Chan, D.S.H. and Phillips, J.R., "Accurate Analytical Method for the Extraction of Solar Cell", Electronics Letter, Vol. 20, No. 10, May 1984, pp. 406 – 408.

35. Xiao, W.-D., Lind, M.G.J., Dunford, W.G., and Chapel, A., "Real-time Identification of Optimal Operating Points in Photovoltaic Power Systems", IEEE Transactions on Industrial Electronics, Vol. 53, No. 4, August 2006, pp. 1017 – 1026.

36. Hua, C., Lin, O., and Shen C., "Implementation of a DSP-controlled Photovoltaic System with Peak Power Tracking," IEEE Transactions on Industrial Electronics, Vol 45, pp. 99 – 107.

37. Bose, B.K., Szczeny, P.M., and Steigerwald, R.L., "Microcomputer control of a residential photovoltaic power conditioning system", IEEE Transactions on Industrial Applications, Vol. IA-21, September/October 1985, pp. 1182 – 1191.

38. Hussein, K., Muta, I., and Hoshino, T., "Maximum Photovoltaic Power Tracking: An An Algorithm for Rapidly Changing Atmospheric Condition", IEE Proceedings of Generation, Transmission and Distribution, Vol. 142, 1995, pp. 59 – 64.

39. Melit A., "Development of an Expert Configuration of Stand-Alone Power PV System Based on Adaptive Neuro-Fuzzy Inference Systems (ANFIS)", Conference Proceedings of MELECON 2006, IEEE Mediterranean Electrotechnical Conference, May 2006, pp. 893 – 896.

40. Melit, A., and Kalogirou, S.A., "Neuro-Fuzzy based Modeling for Photovoltaic Power Supply System", Conference Proceedings of PECON 2006, First International Power and Energy Conference, November 2006, pp. 88 – 93.

41. Chai, S-B., and Zhou, Y., "A Study on How to Help Back-propagation Escape Local Minimum", Conference Proceedings of Natural Computation, 3rd International Conference on Natural Computation, August 2007, pp. 62 – 66.

42. Al-Amoudi, A.O., and Zhang, L., "Application of Radial Basis Function Networks for Solar-Array Modelling and Maximum Power Point Prediction", IEE Proceedings of Generation, Transmission and Distribution, Vol. 147, pp. 310 – 316.

43. Zhang, L., and Bai, Y.F., "On-line Neural Network Training for Maximum Power Poitn Tracking of PV Power Plant", Transactions of the Institute of Measurement and Control, Vo. 39, No. 1, 2008, pp. 77 – 96.

44. Khosla, A., Kumar, S., and Ghosh, K.R., "A Comparison of Computational Efforts between Particle Swarm Optimization and Genetic Algorithm for Identification of Fuzzy Models", Annual Meeting of the North American Fuzzy Information Processing Society, June 2007. pp. 245 – 250.

45. Lin, C-L., Hsieh, S-T., Sun, T-Y., and Liu, C-C., "Cluster Distance Factor Searching by Particle Swarm Optimisation for Self-Growing Radial Basis Function Neural Network", Conference Proceedings on Neural Networks, IEEE International Joint Conference on Neural Networks, July 2006, pp 4825 – 4830.

46. Chatterjee, A., and Watanabe, K., "An Optimised Takagi-Sugeno Type Neuro-fuzzy System for Modelling Robot Manipulators", Neural Computing & Applications, Vol. 15, No. 1, March 2006, pp 55 – 61.

47. Khaehintung, N., Kunakorn, A., and Sirisuk, Phaophak, "A Novel Fuzzy Logic Control Technique tuned by Particle Swarm Optimization for

Maximum Power Point Tracking for a Photovoltaic System using a Current-mode Boost Converter with Bifurcation Control", International Journal of Control, Automation and Systems, 2010, Vol. 8, No. 2, pp. 289 – 300.

48. Chen, L.-R., Tsai, C.-H., Lin, Y.-L., , and Lai, Y.-S., "A Biological Swarm Chasing Algorithm for Tracking the PV Maximum Power Point", IEEE Transactions on Energy Conversion, June 2010, Vol. 25, No. 2, pp. 484 – 493.

49. Kuo, Y., Liang, T., and Chen, J., "Novel Maximum Power Point Tracking Controller for Photovoltaic Energy Conversion System", IEEE Transactions on Industrial Electronics, Vol. 48, 2001, pp. 594-601.

50. Gow, J.A., and Manning, C.D., "Development of a Photovoltaic Array Model for Use in Power Electronics Simulation Study," IEE Proceedings in Electric Power Applications, Vol. 146, 1999, pp. 193 – 200.

51. Ahmed, N.A., and Miyatake, M., "A Novel Maximum Power Point Tracking for Photovoltaic Applications under Partially Shaded Insolation Conditions", Electric Power Systems Research, Vol. 78, 2008, pp. 777 – 784.

52. Kobayashi, K., Takano, I., and Sawada, Y., "A Study on a Two Stage Maximum Power Point Tracking Control of a Photovoltaic System under Partially Shaded Insolation Conditions", IEEE Power Engineering Society General Meeting, Vol. 4, 2003, pp. 2612 – 2617.

53. Patel, H., and Agarwal, V., "Maximum Power Point Tracking Scheme for PV Systems Operating Under Partially Shaded Conditions", IEEE Transactions on Industrial Electronics, Vol. 55, No. 4, April 2008, pp. 1689 – 1698.

54. Hiyama, T., and Kitabayashi, K., "Neural Network based Estimation of Maximum Power Generation from PV module using Environmental Information", IEEE Transactions on Energy Conversion, Vol. 12, 1997, pp. 241 – 247.

55. Solodovnik, E.V., Liu, S., and Dougal, R.A., "Power Controller Design for Maximum Power Tracking in Solar Installations", IEEE Transactions on Power Electronics, Vol. 19, No. 5, September 2004, pp. 1295 – 1294.

56. Petrone, G., Spagnuolo, G., and Vitelli, M., "Analytical Model of Mismatched Photovoltaic Fields by Means of Lambert W-function", Solar Energy Materials & Solar Cells, Vol. 91, 2007, pp. 1652 – 1657.

57. McCulloch, W.S., and Pitts, W., "A logical Calculus of the Ideas Immanent in Nervous Activity", Bulletin of Mathematical Biology, Vol. 52, No. 1/2, 1990, pp 99 – 115.

58. Carpenter, G.A., "Neural Network Models for Pattern Recognition and Associative Memory", Neural Network, Vol. 2, 1989 pp. 243 – 257.

59. Rumelhart, D.E., Widrow, B., and Lehr, M.A., "The Basic Ideas in Neural Networks", Communications of the ACM, Volume 37, No. 3, March 1994, pp 87 – 92.

60. Buckley, J.J., and Hayashi, Y., "Hybrid Neural Nets Can be Fuzzy Controllers and Fuzzy Expert Systems", Fuzzy Sets and Systems Vol. 60, 1993, pp. 135 – 142.

61. Zadeh, L.A., "Outline of a New Approach to the Analysis of Complex System and Decision Processes", IEEE Transactions on Systems, Man and Cybernetics, Volume 3, No. 1, Jan 1973, pp 28 – 44.

62. Tomsovic, K., and Hoang, P., "Approaches for Evaluating Fuzzy Logic Based Power Syste Stabilization Control", Conference Proceedings of the 3rd International Workshop on Rough Sets and Soft Computing, November 1994, pp. 262 – 269.

63. Guo, R.-J., Xie, M., Ma, B.-R., and Chen, W.-L., "Fuzzy Set Model for Computerized Diagnosis System in Traditional Chinese Medicine", Approximate Reasoning in Decision Analaysis, North-Holland, Amsterdam, Netherlands, 1982, pp 283 – 287.

64. Reznik, L., "Fuzzy Controllers Handbook: How to Design Them, How They Work", Elsevier Science & Technology, UK, 1997.

65. Di Nuovo, A.G., Palesi, M., and Patti, D., "Fuzzy Decision Making in Embedded System Design", Conference Proceedings of Codesign and System Synthesis, October 2006, pp. 223 – 228.

66. Yasunobu, S., Miyamato, S., Takaoka, T., and Oshima, H., "Applications of Predictive Fuzzy Control to Automatic Train Operation Controller", Conference Proceedings of IEEE Industrial Electronics Society, 1984, pp. 657 – 662.

67. Castillo, O., and Melin, P., "Type-2 Fuzzy Logic: Theory and Applications", Springer, Berlin, Germany, 2008.

68. Mamdani, E.H., and Assilian, S., "An Experiment in Linguistic Synthesis with a Fuzzy Logic Controller", International Journal Man – Machine Studies, Vol. 7, 1975, pp. 1 – 13.

69. Sugeno, M., and Kang, G.T., "Structure Identification of Fuzzy Model", Journal of Fuzzy Sets and Systems, Vol. 28, 1988, pp. 15 – 33.

70. Ban, X.-J., Gao, X.-Z., Huang, X.-L., and Hang, Y., "Stability Analysis of the Simplest Takagi-Sugeno Fuzzy Control System Using Popov Critertion", International Journal of Innovative Computing, Information and Control, Vol 3, No. 5, October 2007, pp 1087 – 1096.

71. Wang, L.-X., "Adaptive Fuzzy Systems and Control: Design and Stability Analysis", PTR Prentice Hall, Englewood Cliffs, New Jersey, USA, 1994.

72. Yager, R.R., "Implementing Fuzzy Logic Controllers Using a Neural Network Framework", Fuzzy Sets and Systems, Vol. 48, 1992, pp 53 – 64,

73. Kennedy, J., and Eberhart, R.C., "Particle Swarm Optimization", Conference Proceedings on Neural Networks, Vol. IV, 1995, pp. 1942 – 1948.

74. Eberhart, R.C., and Shi, Y., "Particle Swarm Optimization: Developments, Applications and Resources", Conference Proceedings on Evolutionary Computation, 2001, pp. 81 – 86.

75. Engelbrecht, A.P., "Computational Intelligence: An Introduction", 2nd Edition, Wiley, Hoboken, New Jersey, USA, 2007.

76. Shi, Y., and Eberhart, R.C., "A Modified Particle Swarm Optimizer", Conference Proceedings of Evolutionary Computation, 1998, pp. 69 – 73.

77. John, V., and Ivekovic, S., "Articulated Human Motion Tracking with HPSO", Conference Proceedings on Computer Vision Theory and Applications, February 2009, Vol. 1, pp. 531 – 538.

78. Doctor, S., Venayagamoorthy, G.K., and Gudise, V.G., "Optimal PSO for Collective Robotic Search Applications", Congress on Evolutionary Computation, June 2004, Vol. 2, pp. 1390 – 1395.

79. Suganthan, P.N., "Particle Swarm Optimiser with Neighbourhood Operator", Conference Proceedings of Evolutionary Computation, 1999, pp 1958 – 1962.

80. Möller, H.J., "Semiconductors for Solar Cells", Artech House, Inc., Boston, USA, 1993.

81. Goetzberger, A., Knobloch, J., and Voss, B., "Crystalline Silicon Solar Cells", John Wiley & Sons, Ltd., Chichester, UK, 1994.

82. Andreev, V.M., "Photovoltaic Conversion of Concentrated Sunlight", John Wiley & Sons, Inc., New York, UK, 1997.

83. Bai, Y.-F., "Internet based Modelling and Control for Grid-Connected Photovoltaic Power Generation Systems Using Artificial Neural Networks", Ph.D thesis, University of Leeds, August 2003.

84. Vachtsevanos, G., and Kalaitzakis, K., "A Hybrid Photovoltaic Simulator for Utility Interactive Studies", IEEE Transactions on Energy Conversion, Vol. EC-2, No. 2, June 1987, pp. 227 – 231.

85. Markvart, T., "Solar Electricity", Wiley, Chichester, UK, 2nd Edition, 2000.

86. Hisamatsu, T., Kawasaki, O., and Matsuda, S., "Reverse Bias Characteristics, of Modules Made of Solar Cells with and without Integrated Bypass Function (IBF)", Conference Proceedings of PVSC, IEEE Conference on Photovoltaic Specialists, May 1997, pp. 251 – 254.

87. Kimber, R., Hill, R., and Pearsall, N.M., "Investigation of the Reverse Biasing of Solar Cells in a Space Array", Conference Proceedings of PVSC, IEEE Conference on Photovoltaic Specialists, Vol. 2, May 1990, pp. 1282 – 1287.

88. Lopez Pineda C.F., "Experimental Evaluation of Reverse Bias Stress Induced on Photovoltaic Modules for Different Configurations", Solar & Wind Technology, Vol. 3, No. 2, 1986, pp. 85 – 88.

89. Bishop, J.W., "Microplasma Breakdown and Hot-Spots in Silicon Solar Cells", Solar Cells, Vol. 26, 1989, pp. 335 – 349.

90. Hartman, R.A., Prince, J., and Lathrop, J.W., "Second Quadrant Effect in Silicon Solar Cells", Conference Proceedings of PVSC, IEEE Conference on Photovoltaic Specialists, 1980, pp. 119 – 122.

91. Silvestre, S., and Chouder, A., "Effects of Shadowing on Photovoltaic Module Performance", Progress in Photovoltaics: Research and Applications, 2008, Vol. 16, pp. 141 – 149.

92. Alonso-Garcia, M.C., and Ruiz, J.M., "Analysis and Modelling the Reverse Characteristic of Photovoltaic Cells", Solar Energy Materials & Solar Cells, Vol. 90, 2006, pp. 1105 – 1120.

93. Benda, V., Gowar, J., and Grant, D.A., "Power Semiconductor Devices – Theory and Applications", John Wiley & Sons, New York, USA, 1999.

94. Bird, J.O., "Engineering Mathematics", 5th Edition, Newnes, Oxford, UK, 2007.

95. Reinhard Hollaus, T., Zehetbauer, R., and Bednorz, K., "Solar Cell Module", United States Patent, No. 4456316, Jan 1986.

96. Sparkes, J.J., "Semiconductor Devices", 2nd Edition, Chapman & Hall, London, UK, 1994.

97. Middlebrook, R.D., and Ćuk, S., "A General Unified Approach to Modelling Switching Converter Power Stages", International Journal of Electronics, Vol. 42, No. 6, pp. 521 - 550.

98. Ogata, K., "Modern Control Engineering", 4th Edition, Prentice Hall, New Jersey, USA, 2002.

99. Dorf, R.C., and Bishop, R.H., "Modern Control Systems", 11th Edition, Pearson Prentice Hall, New Jersey, USA, 2008.

100. Majo, J., Martinez, L., Fossas, E., Poveda, A., Garcia de Vicuna, L., Guinjoan, F., and Sanchez, A.F., "Large-signal Control of a Bidirectional Coupled-Inductor Ćuk Converter via Pseudolinearization", Conference Proceedings on Midwest Symposium, 1990, Vol. 2, pp. 1107 – 1110.

101. Kim, M.-S., Kim, C.-H, and Lee, J.-J., "Evolving Compact and Intrepretable Takagi-Sugeno Fuzzy Models with a New Encoding Scheme", IEEE Transactions on Systems, Man and Cybernetics – Part B: Cybernetics, Vol. 36, No. 5, October 2006, pp. 1006 – 1023.

102. Jang, R.J.-S., "ANFIS: Adaptive-Network-Based Fuzzy Inference Systems", IEEE Transactions on Systems, Man, Cybernetics, May 1993, Vol. 23, No. 3, pp. 665 – 685.

103. Wannige, C.T., and Sonnadara, D.U.J., "Adaptiv Neuro-Fuzzy Traffic Signal Control for Multiple Junctions," Fourth International Conference on Industrial and Information Systems, December 2009, pp. 262 – 267.

104. Vítězslav, B.J., Gowar, J., and Grant, D.A., "Power Semiconductor Devices: Theory and Applications", John Wiley, New York, USA, 1994.

105. Zhang, W.-L., Yang, Y.-J., and Wang, J.-Q., "A dsPIC-based Excitation Control System for Synchronous Generator", Conference Proceedings on Mechatronics and Automation, 2007, pp. 3844 – 3848.

106. Datasheet for TD351 Advanced IGBT/MOSFFET Driver, STMicroelectronics, November 2004.

107. Mai, Y.-Y. and Mok, P.K.T.: "A constant Frequency Output-Ripple-Voltage-Based Buck Converter Without Using Large ESR Capacitor", IEEE Transactions on Circuits and Systems – II: Express Briefs, 2008, Vol. 55, No. 8, pp. 748 – 752.

108. Datasheet for NTC Thermistor, BC02, BCcomponents, Septmber 1998.

109. Datasheet for dsPIC30F3014/4013 High-Performance, 16-bit Digital Signal Controllers, Microchip, 2008.

110. Henderson, H.V., and Searle, S.R., "On Deriving the Inverse of a Sum of Matrices", SIAM Review, Vol. 23, No. 1, January 1981, pp. 53 – 60.

Appendix

Derivation of Equations

Considering a multi-input-single-output model (MISO), a total of N actual output samples can be expressed as

$$Y_N = [y(1) \quad y(2) \quad y(3) \quad \ldots \quad y(N)]^T \tag{A.1}$$

and the vector containing N sets of input samples is given by

$$Q_N = [q_1 \quad q_2 \quad q_3 \quad \ldots \quad q_N]^T \tag{A.2}$$

where q_k is a column vector representing a set of multi-dimensional inputs.

The outputs predicted by the model can be written as

$$\hat{Y}_N = Q_N \Gamma \tag{A.3}$$

where Γ is the parameter vector defining the relationship between the predicted output and the input samples.

The error between the model-predicted output and that of the actual sample can be evaluated using a cost function expressed as

$$J = \frac{1}{2}\sum_{k=1}^{n}\left(y(k) - q_k^T\Gamma\right)^T\left(y(k) - q_k^T\Gamma\right) \tag{A.4}$$

Differentiating Equation (A.4) with respect to Γ and setting the derivative to zero obtains

$$\sum_{k=1}^{n} q_k q_k^T \Gamma = \sum_{k=1}^{n} q_k y(k) \tag{A.5}$$

$\hat{\Gamma}_n$ is denoted as the value for Γ which leads to a minimum value of J in Equation (A.4) and it can be written as

$$\hat{\Gamma}_n = V_n^{-1}\sum_{k=1}^{n} q_k y(k) \tag{A.6}$$

where

$$V_n = \sum_{k=1}^{n} q_k q_k^T \tag{A.7}$$

At the next sample, Γ may have different value and hence, Equation (A.6) is re-written as

$$\hat{\Gamma}_{n+1} = V_{n+1}^{-1} \sum_{k=1}^{n+1} q_k y(k) \tag{A.8}$$

and the summation term in Equation (A.8) can be expressed as

$$\begin{aligned} &\sum_{k=1}^{n+1} q_k y(k) = \sum_{k=1}^{n} q_k y(k) + q_{n+1} y(n+1) \\ &= V_n \hat{\Gamma}_n + q_{n+1} y(n+1) + q_{n+1} q_{n+1}^T \hat{\Gamma}_n - q_{n+1} q_{n+1}^T \hat{\Gamma}_n \\ &= V_{n+1} \hat{\Gamma}_n + q_{n+1} \left[y(n+1) - q_{n+1}^T \hat{\Gamma}_n \right] \end{aligned} \tag{A.9}$$

where

$$V_{n+1} = V_n + q_{n+1} q_{n+1}^T \tag{A.10}$$

Substituting Equation (A.10) into Equation (A.8) gives

$$\hat{\Gamma}_{n+1} = \hat{\Gamma}_n + V_{n+1}^{-1} q_{n+1} \left[y(n+1) - q_{n+1}^T \hat{\Gamma}_n \right] \tag{A.11}$$

$(V_{n+1})^{-1}$ in Equation (A.11) can be simplified compared to the inversion formula proposed by Henderson and Searle which is given by [110]

$$(\mathbf{A} + \mathbf{BCD})^{-1} = \mathbf{A}^{-1} - \mathbf{A}^{-1}\mathbf{BC}\left(\mathbf{I} + \mathbf{DA}^{-1}\mathbf{BC}\right)^{-1}\mathbf{DA}^{-1} \tag{A.12}$$

and hence one yields

$$\begin{aligned} \mathbf{A} &= V_n \\ \mathbf{B} &= \mathbf{I} \\ \mathbf{C} &= q_{n+1} \\ \mathbf{D} &= q_{n+1}^T \end{aligned} \tag{A.13}$$

Defining S_{n+1} as $(V_{n+1})^{-1}$ gives

$$S_{n+1} = S_n - \frac{S_n q_{n+1} q_{n+1}^T S_n}{1 + q_{n+1}^T S_n q_{n+1}} \tag{A.14}$$

and Equation (A.11) can be re-written as

$$\hat{\Gamma}_{n+1} = \hat{\Gamma}_n + S_{n+1} q_{n+1} \left[y(n+1) - q_{n+1}^T \hat{\Gamma}_n \right] \tag{A.15}$$